



**NUMERICAL SIMULATION OF CORNEAL REFRACTIVE  
SURGERY BASED ON IMPROVED RECONSTRUCTION OF  
CORNEAL SURFACE**

Thesis submitted in accordance with the requirements of  
the University of Liverpool for the degree of

Doctor in Philosophy by

*Junjie Wang*

November 2015

# TABLE OF CONTENTS

List of figures .....	v
List of tables.....	xii
List of abbreviations.....	xv
Publications.....	xviii
Abstract.....	I
Chapter 1 Introduction.....	- 1 -
1.1 Preface.....	- 1 -
1.2 Scope of study.....	- 7 -
1.3 Aims and objectives .....	- 7 -
1.4 Thesis structure .....	- 8 -
Chapter 2 Literature review .....	- 10 -
2.1 Introduction.....	- 10 -
2.2 Structure and optics of the human eye .....	- 10 -
2.2.1 The eyeball.....	- 11 -
2.2.2 The cornea.....	- 12 -
2.2.3 Optics of the eye.....	- 18 -
2.3 Corneal topography fitting.....	- 22 -
2.4 Corneal topography matching.....	- 26 -
2.5 Refractive surgery .....	- 30 -
2.5.1 From da Vinci's codex to laser corneal refractive surgery .....	- 30 -
2.5.2 Other prospects of refractive surgery.....	- 35 -

2.6	Numerical simulation of refractive surgery .....	- 36 -
2.7	Concluding remarks .....	- 39 -
Chapter 3	Research methodology .....	- 42 -
3.1	Introduction .....	- 42 -
3.2	Topography fitting .....	- 42 -
3.2.1	Orthogonal polynomials.....	- 44 -
3.2.2	Computation of polynomial coefficients.....	- 51 -
3.2.3	Evaluation methods.....	- 57 -
3.3	Topography matching .....	- 58 -
3.3.1	Problem statement.....	- 60 -
3.3.2	Direct search (DS) method.....	- 64 -
3.3.3	Iterative closest point (ICP) algorithm.....	- 64 -
3.3.4	DS vs. ICP .....	- 69 -
3.3.5	Multi-view registration.....	- 69 -
3.4	Numerical simulation of refractive surgery .....	- 74 -
3.4.1	Model construction.....	- 75 -
3.4.2	Stress free configuration .....	- 81 -
3.4.3	Adjustment of the ablation depth.....	- 84 -
3.4.4	Definition of flap (for LASIK)/cap (for SMILE).....	- 91 -
3.4.5	Wound healing .....	- 93 -
3.4.6	Summary of the simulation steps .....	- 94 -
3.4.7	Mathematical simulation of LASIK.....	- 97 -

3.4.8	Simulation of tonometry .....	- 97 -
3.5	Concluding remarks .....	- 100 -
Chapter 4	Results of topography fitting.....	- 102 -
4.1	Introduction .....	- 102 -
4.2	OP vs. LS .....	- 103 -
4.3	Topography reconstruction .....	- 107 -
4.4	Topography prediction .....	- 116 -
4.5	Concluding remarks .....	- 123 -
Chapter 5	Results of topography matching.....	- 124 -
5.1	Introduction .....	- 124 -
5.2	Repeatability of clinical data.....	- 125 -
5.3	Data sets and evaluation methods .....	- 126 -
5.4	Simulated and quasi-clinical exercises.....	- 128 -
5.5	Clinical data .....	- 133 -
5.6	Benefits of multi-view registration .....	- 136 -
5.7	Concluding remarks .....	- 140 -
Chapter 6	Results of numerical simulation.....	- 141 -
6.1	Introduction .....	- 141 -
6.2	Structural study .....	- 142 -
6.3	Parametric study of wound healing.....	- 150 -
6.4	Effect of considering surgery-related stiffness changes.....	- 153 -
6.5	LASIK vs. SMILE .....	- 158 -

6.6	Tonometry .....	- 164 -
6.7	Concluding remarks .....	- 167 -
Chapter 7	Overall discussion and Conclusion .....	- 169 -
7.1	Introduction .....	- 169 -
7.2	Overall discussion .....	- 169 -
7.2.1	Topography fitting .....	- 169 -
7.2.2	Topography matching .....	- 178 -
7.2.3	Numerical simulation .....	- 184 -
7.3	Conclusions .....	- 194 -
7.4	Future research and recommendations .....	- 197 -
7.4.1	Topography fitting against noise in the map .....	- 197 -
7.4.2	Multi-view ICP (MICP) .....	- 198 -
7.4.3	Ablation profile .....	- 199 -
7.4.4	Local mesh refinement .....	- 199 -
7.4.5	Anisotropy of ocular tissue .....	- 199 -
7.4.6	Simulation of stromal wound .....	- 200 -
7.4.7	Layered structure of the cornea .....	- 202 -
7.4.8	Material properties of the sclera .....	- 202 -
References	.....	- 206 -

## LIST OF FIGURES

Figure 1-1. Focusing of light in ideal eye .....	- 2 -
Figure 1-2. A brief history of corneal refractive surgery .....	- 4 -
Figure 2-1. Five distinctive layers of the cornea.....	- 14 -
Figure 2-2. Typical behaviour of the cornea under tension with an initial matrix regulated phase followed by a higher stiffness collagen regulated phase .....	- 18 -
Figure 2-3. Representative dimensions and refractive indices of the eye.....	- 19 -
Figure 2-4. A schematic eye model showing light rays being refracted by ocular system and the shape of wavefront during the transmission .....	- 20 -
Figure 2-5. Actual wavefront shapes for different low order aberrations compared to the ideal shape and their corresponding images of a point object on the myopic, emmetropic and hyperopic planes .....	- 21 -
Figure 2-6. Actual wavefront shapes for different high order aberrations compared to the ideal shape and their corresponding images of a point object on the myopic, emmetropic and hyperopic planes .....	- 22 -
Figure 2-7. Schematic figures of the cut in LASEK/Epi-LASIK and LASIK.....	- 33 -
Figure 3-1. Typical corneal topography data plotted in 3D. Colours of individual points reflect their z coordinates.....	- 43 -
Figure 3-2. Shapes of the 1D Gegenbauer polynomials up to order 4.....	- 46 -
Figure 3-3. Shapes of the 1D Gaussian-Hermite polynomials up to order 4 .....	- 47 -
Figure 3-4. Effect of scaling factor on the shape of 1D Gegenbauer polynomials ....	- 47 -
Figure 3-5. Shapes of Legendre polynomials up to order 4.....	- 48 -
Figure 3-6. Shapes of ZPs up to order 4 .....	- 50 -
Figure 3-7. Shapes of OFMPs up to order 4 .....	- 51 -

Figure 3-8. Discrete points/pixels and the squares and/or triangles representation of the unit circle .....	- 54 -
Figure 3-9. Schematic diagram of topography registration .....	- 59 -
Figure 3-10. Three forms of correspondence mapping showing in the cross-section views of the surfaces .....	- 63 -
Figure 3-11. An idealised model generated by the VB programme .....	- 76 -
Figure 3-12. Schematic method of adopting clinical corneal topography and thickness.... .....	- 77 -
Figure 3-13. The change in geometry from the idealised model to a typical patient-specific model .....	- 78 -
Figure 3-14. A cross-sectional view of the eye model showing the regions with specific material properties .....	- 80 -
Figure 3-15. Stress-strain curves for the cornea and sclera .....	- 81 -
Figure 3-16. Model with an epithelial layer in blue.....	- 81 -
Figure 3-17. Schematic method to obtain the stress-free configuration of a linear strip model .....	- 83 -
Figure 3-18. Schematic description of steps to obtain the stress-free configuration .	- 84 -
Figure 3-19. Model with an ablation depth profile being isolated in a specific layer	- 85 -
Figure 3-20. The alternative approach to enable adjustment of ablation depth.....	- 85 -
Figure 3-21. Ablation sample points and their locations as shown on the anterior corneal surface of the model.....	- 87 -
Figure 3-22. Re-configured corneal nodes to fit the ablation boundary .....	- 88 -
Figure 3-23. Locations identified for adjustment of ablation depth as seen from the front of the cornea .....	- 90 -

Figure 3-24. An OCT image of a corneal cross section showing the boundary of flap.....	- 91 -
Figure 3-25. Plot of flap thickness in z-x and z-y cross-section and the 2 <sup>nd</sup> order Zernike expression of the flap thickness distribution .....	- 92 -
Figure 3-26. Dimensions of LASIK flap and SMILE cap and the corresponding cut sizes .....	- 93 -
Figure 3-27. Model with a wound healing layer in orange .....	- 94 -
Figure 3-28. Visual Basic programme used to generate idealised models .....	- 96 -
Figure 3-29. Graphical user interface under MATLAB environment that guides the patient-specific modelling of corneal refractive surgeries LASIK and SMILE-	- 96 -
Figure 3-30. Schematic method to model GAT, showing in an INTACT model.....	- 98 -
Figure 3-31. Temporal air-puff pressure profile over 30 ms and spatial distribution of the pressure across corneal surface.....	- 99 -
Figure 3-32. Schematic method to model CVS, showing in an INTACT model ....	- 100 -
Figure 4-1. Typical Pentacam topography data viewed from the top .....	- 103 -
Figure 4-2. Vibration of coefficients as evaluated by the LS method while using different Zernike orders.....	- 104 -
Figure 4-3. Discrete points and the squares and/or triangles representation of the unit circles.....	- 105 -
Figure 4-4. Absolute errors of the first and fifth Zernike polynomial coefficients and the root mean square error of all the first 6 coefficients.....	- 106 -
Figure 4-5. Reconstruction errors plotted against order for eight sets of polynomials, for one clinical anterior topography of a randomly chosen normal eye.....	- 108 -
Figure 4-6. Reconstruction errors of Gaussian-Hermite polynomials with different scaling factors .....	- 110 -



Figure 4-7. Mean reconstruction errors plotted for anterior normal corneal surfaces fitted by ZPs, PZPs, OFMPs and GHPs .....	- 112 -
Figure 4-8. Boxplots of reconstruction errors by OFMPs from order 8 to 12 for anterior normal, anterior keratoconic, posterior normal and posterior keratoconic corneal surfaces .....	- 113 -
Figure 4-9. Magnitudes of coefficients for ZPs up to order 10 for typical anterior normal, anterior keratoconic, posterior normal and posterior keratoconic corneal topographies.....	- 116 -
Figure 4-10. Mean reconstruction and prediction errors plotted for anterior normal corneal surfaces fitted by ZPs, PZPs, OFMPs and GHPs .....	- 117 -
Figure 4-11. Mean reconstruction and prediction errors by ZPs, PZPs, OFMPs and GHPs using different sub-sets of the original anterior normal corneal topography as reconstruction sets .....	- 118 -
Figure 4-12. Inflection orders of prediction curves and the corresponding prediction errors by ZPs, PZPs, OFMPs and GHPs.....	- 122 -
Figure 5-1. A typical central topography provided by Medmont E300, showing irregular peripheral shape .....	- 125 -
Figure 5-2. Repeatability tests of clinical height maps .....	- 126 -
Figure 5-3. Convergence of registration algorithms, simulated surface with no noise, $E_a$ vs. iteration. ....	- 129 -
Figure 5-4. Convergence of registration algorithms, simulated surface with no noise, $E_r$ vs. time.....	- 130 -
Figure 5-5. Convergence of ICP point-to-plane routines – noisy data .....	- 132 -
Figure 5-6. Registration outcomes of clinical maps for one collection .....	- 134 -
Figure 5-7. Area of the combined map. ....	- 136 -

Figure 5-8. Convergence of MICP registration.....	- 137 -
Figure 5-9. Individual alignment error between each pair of dynamic-to-static or dynamic-to-dynamic map along the convergence of the MICP registration..	- 139 -
Figure 6-1. Models in simulation 1 and 2 , showing different numbers of scleral rings .... .....	- 143 -
Figure 6-2. Cross-sectional views of models in simulation 2 with three layers and simulation 3 with two layers.....	- 143 -
Figure 6-3. Cross-sectional views of models used in simulations 1 and 5 .....	- 146 -
Figure 6-4. Top views of models used in simulations 1 and 5.....	- 147 -
Figure 6-5. Distributions of errors in surface fit with the clinical measurements for the 6 simulations.....	- 149 -
Figure 6-6. Average root mean square errors between 60 numerically predicted and clinically postoperative anterior corneal surfaces.....	- 151 -
Figure 6-7. A typical example of distribution of error in surface fit between the predicted and measured postoperative anterior corneal surfaces .....	- 152 -
Figure 6-8. Individual root mean square errors between 60 numerically predicted and clinically postoperative anterior corneal surfaces.....	- 153 -
Figure 6-9. Box plot of the RMSE for both numerical and mathematical simulations .....	- 154 -
Figure 6-10. Linear correlation between the refractive powers predicted by numerical and mathematical simulations, and the clinical refractive powers .....	- 156 -
Figure 6-11. Bland-Altman plots for predicted and measured refractive correction-	- 157 -
Figure 6-12. Cross section of inflated LASIK and SMILE models using one typical set of patient data.....	- 159 -

Figure 6-13. Top view of inflated LASIK and SMILE models using one typical set of patient data.....	- 160 -
Figure 6-14. Linear correlation of corneal apical rise and limbal rise in LASIK and SMILE models.....	- 161 -
Figure 6-15. Linear correlation of limbal rises in LASIK models between the right and left, superior and inferior limbal nodes.....	- 162 -
Figure 6-16. Linear correlation of limbal rises in SMILE models between the right and left, superior and inferior limbal nodes.....	- 162 -
Figure 6-17. Linear correlation of true IOP and estimated $IOP_{GAT}$ .....	- 165 -
Figure 6-18. Linear correlation of true IOP and estimated $IOP_{CVS}$ .....	- 165 -
Figure 6-19. Linear correlation of CCT and ratio between estimated $IOP_{GAT}$ and true IOP .....	- 166 -
Figure 6-20. Linear correlation of CCT and ratio between estimated $IOP_{CVS}$ and true IOP .....	- 167 -
Figure 7-1. The set of polynomials that achieves best prediction and the corresponding polynomial order for all topography maps .....	- 175 -
Figure 7-2. Mean reconstruction errors for maps with different radii and resolutions .....	- 177 -
Figure 7-3. Mean reconstruction and prediction errors for maps with different radii and resolution 0.2 mm .....	- 177 -
Figure 7-4. The influence of Zernike fitting on the performance of the ICP CP routine....	- 180 -
Figure 7-5. Alignment errors of two sets of Pentacam topographies.....	- 182 -
Figure 7-6. The maps in registration, shown in 3D.....	- 183 -
Figure 7-7. The maps in registration, shown in X-Y views.....	- 184 -

Figure 7-8. Estimated bending stiffness before and after LASIK surgery and their approximated linear relationships.....	- 189 -
Figure 7-9. Estimated membrane stiffness before and after LASIK surgery and their approximated linear relationships.....	- 189 -
Figure 7-10. Linear correlations between various fitting errors and the RMSE of numerically predicted and clinically measured anterior corneal topography within the central 3 mm radius.....	- 191 -
Figure 7-11. Vertical difference in anterior surfaces of LASIK and SMILE models for one eye.....	- 192 -
Figure 7-12. Displacement difference of anterior corneal surfaces between the models with edge-localised wound healing layers and the one with complete wound healing layer.....	- 201 -
Figure 7-13. Displacement difference of anterior corneal surfaces between the models with softer or stiffer scleral material properties and the one with reference material properties.....	- 204 -
Figure 7-14. Displacement difference of anterior corneal surfaces between the model with reduced equatorial and posterior scleral stiffness and the one with reference material properties.....	- 205 -

## LIST OF TABLES

Table 2-1. Commonly used corneal laser surgical procedures and their major advantages and disadvantages .....	- 34 -
Table 3-1. Orthogonal polynomials in Cartesian system .....	- 45 -
Table 3-2. Orthogonal polynomials in Polar system.....	- 49 -
Table 3-3. First order Ogden parameters of different regions of the eye.....	- 80 -
Table 4-1. Reconstruction errors of GPs with different scaling factors.....	- 109 -
Table 4-2. Reconstruction error for Zernike polynomials .....	- 111 -
Table 4-3. Reconstruction error for pseudo-Zernike polynomials.....	- 111 -
Table 4-4. Reconstruction error for Orthogonal Fourier-Mellin polynomials.....	- 111 -
Table 4-5. Reconstruction error for Gaussian-Hermite polynomials.....	- 112 -
Table 4-6. Inflection orders of prediction curves and the corresponding prediction and reconstruction errors by various polynomials for anterior normal corneal topography .....	- 119 -
Table 4-7. Inflection orders of prediction curves and the corresponding prediction and reconstruction errors by various polynomials for anterior keratoconic corneal topography .....	- 120 -
Table 4-8. Inflection orders of prediction curves and the corresponding prediction and reconstruction errors by various polynomials for posterior normal corneal topography .....	- 120 -
Table 4-9. Inflection orders of prediction curves and the corresponding prediction and reconstruction errors by various polynomials for posterior keratoconic corneal topography .....	- 121 -
Table 5-1. Rigid-body transformation by various methods. ....	- 131 -
Table 5-2. ICP point-to-plane transformations – noisy data .....	- 132 -
Table 5-3. Alignment error .....	- 135 -
Table 5-4. Horizontal dimension of combined map.....	- 135 -
Table 5-5. Vertical dimension of combined map.....	- 135 -

Table 5-6. Overall alignment error, dynamic-to-static error and dynamic-to-dynamic error .....	- 138 -
Table 6-1. Six model settings tested in an initial study.....	- 142 -
Table 6-2. Displacements and thickness values at three model nodes after an initial loading and stress-free configuration.....	- 144 -
Table 6-3. Surface fit with the clinical measurements for the 6 simulations.....	- 148 -
Table 6-4. Average root mean square errors between 60 numerically predicted and clinically postoperative anterior corneal surfaces.....	- 151 -
Table 6-5. Average root mean square errors for both numerical and mathematical simulations.....	- 154 -
Table 6-6. Average refractive powers computed using clinical and predicted corneal topographies.....	- 155 -
Table 6-7. Average refractive corrections obtained clinically and predicted numerically and mathematically.....	- 157 -
Table 6-8. Average corneal refractive powers computed using corneal topographies before and after application of IOP in LASIK and SMILE models.....	- 163 -
Table 6-9. Average IOP estimates by GAT and CVS using INTACT, LASIK and SMILE models.....	- 164 -
Table 7-1. Explicit expressions of ZPs in Cartesian system, LPs and GPs. ....	- 171 -
Table 7-2. Prediction errors by polynomial fitting and various standard interpolation methods for anterior normal corneal topography.....	- 173 -
Table 7-3. Prediction errors by polynomial fitting and various standard interpolation methods for anterior keratoconic corneal topography.....	- 173 -
Table 7-4. Prediction errors by polynomial fitting and various standard interpolation methods for posterior normal corneal topography.....	- 174 -
Table 7-5. Prediction errors by polynomial fitting and various standard interpolation methods for posterior keratoconic corneal topography.....	- 174 -
Table 7-6. Rigid-body transformation by DS method fulfilled by various optimisation algorithms.....	- 179 -

Table 7-7. Estimated bending stiffness before and after LASIK surgery and the changes presented by mean  $\pm$  1 standard derivation ..... - 187 -

Table 7-8. Estimated membrane stiffness before and after LASIK surgery and the changes presented by mean  $\pm$  1 standard derivation ..... - 188 -

Table 7-9. Surface fitting errors by Zernike polynomials for corneal topography, thickness maps, ablation depth data and flap thickness..... - 190 -

Table 7-10. Effect of edge-localised wound healing layer on the refractive power predicted by numerical model ..... - 201 -

Table 7-11. Effect of varying sclera material properties on the refractive power predicted by numerical model ..... - 203 -

Table 7-12. Effect of reduced stiffness in equatorial and posterior sclera on the refractive power predicted by numerical model ..... - 204 -

## LIST OF ABBREVIATIONS

1D	One-Dimensional
2D	Two-Dimensional
3D	Three-Dimensional
ALK	Automated Lamellar Keratoplasty
AP1	Applanation Pressure 1
AS	Active-Set
AT1	Applanation Time 1
C3D15H	15-Node Solid Elements, Hybrid with Linear Pressure
CCT	Central Corneal Thickness
CDP	Closest Discrete Point
CP	Closest Point
CPP	Contractive Projection Point
CVS	Corvis ST
DCT	Dynamic Contour Tonometry
DS	Direct Search
ECM	Extracellular Matrix
EGF	Epidermal Growth Factor
EM	Exact Moments
FE	Finite Element
FEA	Finite Element Analysis
FEM	Finite Element Method
GA	Genetic Algorithm
GAT	Goldmann Applanation Tonometer
GHPs	Gaussian-Hermite Polynomials
GPs	Gegenbauer Polynomials



GUI	Graphical User Interface
HGF	Hepatocyte Growth Factor
HOAs	High Order Aberrations
ICP	Iterative Closest Point or Iterative Corresponding Point
IL-1	Interleukin-1
INT	Interpolation Version of EM
INTACT	Model with Full Corneal Thickness
IOP	Intraocular Pressure
IP	Interior-Point
KGF	Keratinocyte Growth Factor
LASEK	Laser-Assisted Sub-Epithelial Keratectomy
LASIK	Laser-Assisted in situ Keratomileusis
LLS	Linearisation/Least-Squares
LM	Levenberg-Marquardt
LOAs	Low Order Aberrations
LPs	Legendre Polynomials
LS	Least Squares Estimation
MICP	Multi-ICP
MPC	Multi-Point Constraints
NM	Nelder-Mead
NS	Normal Shooting
OCT	Optical Coherence Tomography
OFMPs	Orthogonal Fourier-Mellin Polynomials
OP	Orthogonal Projection
ORA	Ocular Response Analyser
PCT	Peripheral Corneal Thickness
PDGF	Platelet-Derived Growth Factor

PGs	Proteoglycans
PRK	Photorefractive Keratectomy
PS	Pattern Search
PSO	Particle Swarm Optimisation
PZPs	Pseudo-Zernike Polynomials
QN	Quasi-Newton
RBFs	Radial Basis Functions
RK	Radial Keratotomy
RMS	Root Mean Square
RMSE	Root Mean Square Error
RMSEs	Root Mean Square Errors
SA	Simulated Annealing
SMILE	Small-Incision Lenticule Extraction
SQP	Sequential Quadratic Programming
SVD	Singular Value Decomposition
TGF- $\beta$	Transforming Growth Factor $\beta$
TNF- $\alpha$	Tumour Necrosis Factor $\alpha$
TPs	Tchebichef Polynomials
VB	Visual Basic
VK	Videokeratography
VS	Vertical Shooting
ZOA	Zeroth Order Approximation
ZPs	Zernike Polynomials

## PUBLICATIONS

Co-first author in publication 2

- 1 J. Wang, A. Elsheikh, P. G. Davey, W. Wang, F. Bao, and J. E. Mottershead, “Corneal topography matching by iterative registration,” *Proc IMechE Part H: J Engineering in Medicine*, vol. 228, no. 11, pp. 1154, Nov 1, 2014.
- 2 F. Bao, J. Wang, J. Huang, Y. Yu, M. Deng, L. Li, A. Yu, Q. Wang, P. Davey, and A. Elsheikh, “Effect of Misalignment between Successive Corneal Videokeratography Maps on the Repeatability of Topography Data,” *Plos One*, vol. 10, no. 11, pp. 18, Nov, 2015.
- 3 F. Bao, Z. Huang, J. Huang, J. Wang, M. Deng, L. Li, A. Yu, Q. Wang, and A. Elsheikh, “Clinical Evaluation of Methods to Correct Intraocular Pressure Measurements by the Goldmann Applanation Tonometer, Ocular Response Analyzer, and Corvis ST Tonometer for the Effects of Corneal Stiffness Parameters,” *J Glaucoma*, Dec 24, 2015.

# **Numerical simulation of corneal refractive surgery based on improved reconstruction of corneal surface**

Junjie Wang

## **ABSTRACT**

The human eye is a fine optical system whose performance heavily relies on its dominant refractive component, the cornea. Slight imperfection in the cornea may result in significant refractive errors and decline in sharpness of vision. In addition to conventionally used prescription glasses and contact lenses, corneal refractive surgery has now become reliable method to permanently correct the refractive state of the cornea. Nowadays, millions of corneal refractive procedures are performed worldwide each year, however the outcome is not ideal, largely due to the lack of understanding of corneal biomechanical response to surgical procedures. This study aims to establish a predictive finite element (FE) model to assist the planning of future refractive surgery while taking account of corneal biomechanical properties.

The study involves corneal topography analysis to obtain convenient representation of the corneal shape for creation of eye-specific models and a series of numerical simulation addressing corneal response to surgical procedures such as Laser-Assisted in situ Keratomileusis (LASIK) and Small-Incision Lenticule Extraction (SMILE), and to external pressures such as tonometry pressures caused by Goldmann applanation tonometer (GAT) and Corvis ST (CVS).

The topography analysis includes studies on fitting and matching. In the topography fitting, a collection of orthogonal polynomials are employed to fit the corneal topography and they are assessed in terms of reconstruction of measured points and prediction of unmeasured locations, latter of which concerns the overfitting risks and has not been well

addressed in previous literature. Better fitting techniques, compared to the commonly used Zernike polynomials, are found. In the topography matching part, methods are assessed and further developed to match multiple corneal topographies collected from different viewpoints to obtain a combined map that covers the entire cornea. This study is to overcome the limitations of commonly used topographers that provide corneal topography with insufficient coverage of the cornea. In comparison to existing methods, the further developed matching method in this study is able to combine the topographies very fast (in a few seconds) with high levels of accuracy.

The outcome of topography analysis has helped build representative eye-specific FE models that fit the shapes of the eyes (undergoing LASIK surgery) measured clinically. These models closely simulate the LASIK procedure by considering the creation of corneal flap and its separation from the rest of the cornea, thickness reduction caused by laser ablation and wound healing after the surgery. The simulation is believed to be more patient-specific as it adopts not only the patient-specific corneal topography but also the patient-specific flap and ablation information which is not well captured in the published studies. The models are shown to be able to predict the clinical postoperative surgical outcome accurately. Comparison between LASIK and SMILE procedures indicates their similar visual outcomes but the LASIK procedure is revealed to be more invasive to the cornea. Subsequent simulation on tonometry has observed clear influence of LASIK and SMILE procedures on the tonometric estimates of intraocular pressure (IOP). With the cornea thickness thinned after surgery, the IOP estimates are significantly smaller than their true values, which is consistent with clinical findings.

# CHAPTER 1

## INTRODUCTION

---

### 1.1 PREFACE

The eyes are the window to your soul.

-William Shakespeare

Visual perception or vision is possibly our most important sense; it delivers the colours and orders of the outside world to our inner soul by seeing. Eyes are the indispensable organs for the formation of visual perception and act as the windows to our souls.

The human eye is a fine optical system whose performance heavily depends on its ability to form sharp images for the outside world onto the retina. This involves refracting light by the cornea and lens; the cornea as the first refractive component offers approximately 70% of the whole refractive power of the eye [1]. While light can be expressed as a bundle of rays or waves, the refracting process in the eye can be considered as focusing of light rays or equivalently converging of light wavefront, which is the shape of the light waves that are all in-phase. The wavefront as a matter of course is always perpendicular to the light rays.

In an ideal eye (Figure 1-1), the incoming light rays (essentially parallel when the eye is relaxed and focusing on far objects) are convergently refracted by the cornea and allowed, through the opening of the pupil (whose size is controlled by the iris), to reach the lens, by which the light rays are refracted again and become focused when they eventually strike the retina. Meanwhile, the shape of the wavefront is changed from plane to sphere

whose centre is located on the retina. Moreover the lens, although offers much less refractive power in the relaxed eye, can change its shape to add more refractive power when that is needed to focus light from near objects, this process is called accommodation (Figure 1-1, B). The focused light is then detected by light-sensitive cells panelled on the retina and converted to neural signals, which are transmitted to the brain through the optic nerve to form vision.

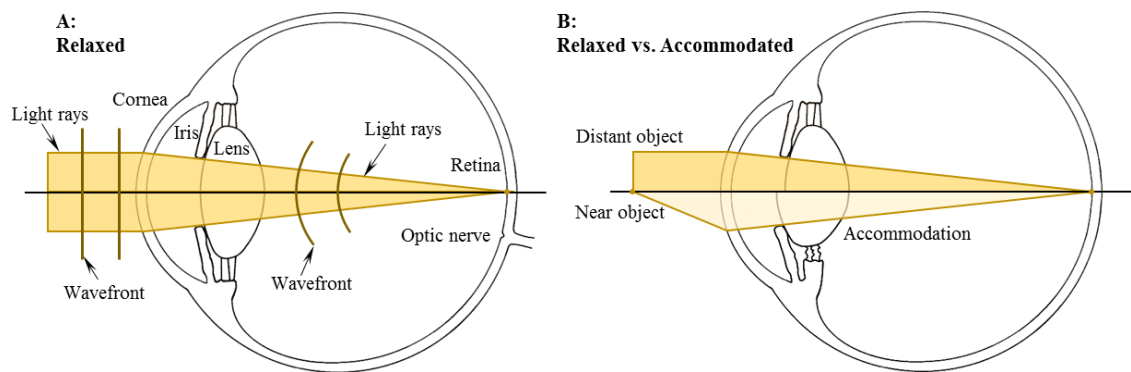


Figure 1-1. Focusing of light in ideal eye. **A.** The eye is relaxed (no accommodation) and focusing on distant object such the incoming light rays from that object are essentially parallel; **B.** The lens can change to more curved shapes and thus offer appropriate accommodative power when the eye needs additional refractive power to focus light rays from near objects.

In real eyes however, perfect focusing never occurs. On one hand, the perfect spherical wavefront as in the ideal eye does not converge to an infinitesimal point but a finite-sized spot because of light diffraction, which is a fundamental property of waves when they pass an aperture (e.g. the pupil). The finite-sized spot is called the Airy disk, however it is too small to introduce noticeable blurring. On the other hand, the perfect spherical wavefront never exists in real eyes, the difference between the actual wavefront and the spherical wavefront that is found in the ideal eye is called wavefront aberration, which is usually decomposed into low order aberrations (LOAs) and high order aberrations (HOAs). While trivial LOAs and HOAs create negligible visual effects in normal eyes (normal vision), correction is needed in eyes with significant amount of LOAs and HOAs.

The LOAs are the commonly known refractive errors including negative defocus – myopia (short-sightedness or near-sightedness), positive defocus – hyperopia (long-sightedness or far-sightedness) and astigmatism. In defocus or myopia and hyperopia, the converging wavefront is still spherical but its centre locates either in front of or beyond the retina, while in astigmatism, the wavefront has an asymmetric shape so that single focus is never achievable. Among all the refractive errors, myopia is now the commonest refractive error and it is effecting millions of individuals worldwide. It is even estimated that 2.5 billion individuals will be affected by myopia throughout the world by 2020 [2]. Further, the global prevalence of myopia is high and increasing, this situation is especially serious in eastern Asia, which is believed to be related to the increasing educational pressures and life-style changes [3]. Compared to LOAs, HOAs on average only contribute 10% to the overall ocular aberration, nevertheless their deleterious effect on visual performance is now known to be not negligible thanks to the rapid development in wavefront-related technologies, and this negative effect can be significant when the pupil is dilated for instance at night [4].

The first description of refractive errors (LOAs) dates back to as early as the time of Leonardo da Vinci [5] and these vision abnormalities have been efficiently corrected with optical treatments such as prescription glasses and contact lenses for centuries. Recently, corneal refractive surgery that aims to correct refractive errors by altering the shape of the dominant ocular refractive component, the cornea, has become a reliable substitution for the optical methods (Figure 1-2). There are now many forms of corneal refractive surgery including incisional procedures such as Keratotomy and Radial Keratotomy (RK), laser-based surface procedures such as Photorefractive Keratectomy (PRK), Laser-Assisted Sub-Epithelial Keratectomy (LASEK) and Epithelial Laser-Assisted in situ



Keratomileusis (Epi-LASIK) and lamellar procedures such as Laser-Assisted in situ Keratomileusis (LASIK) and Small-Incision Lenticule Extraction (SMILE).

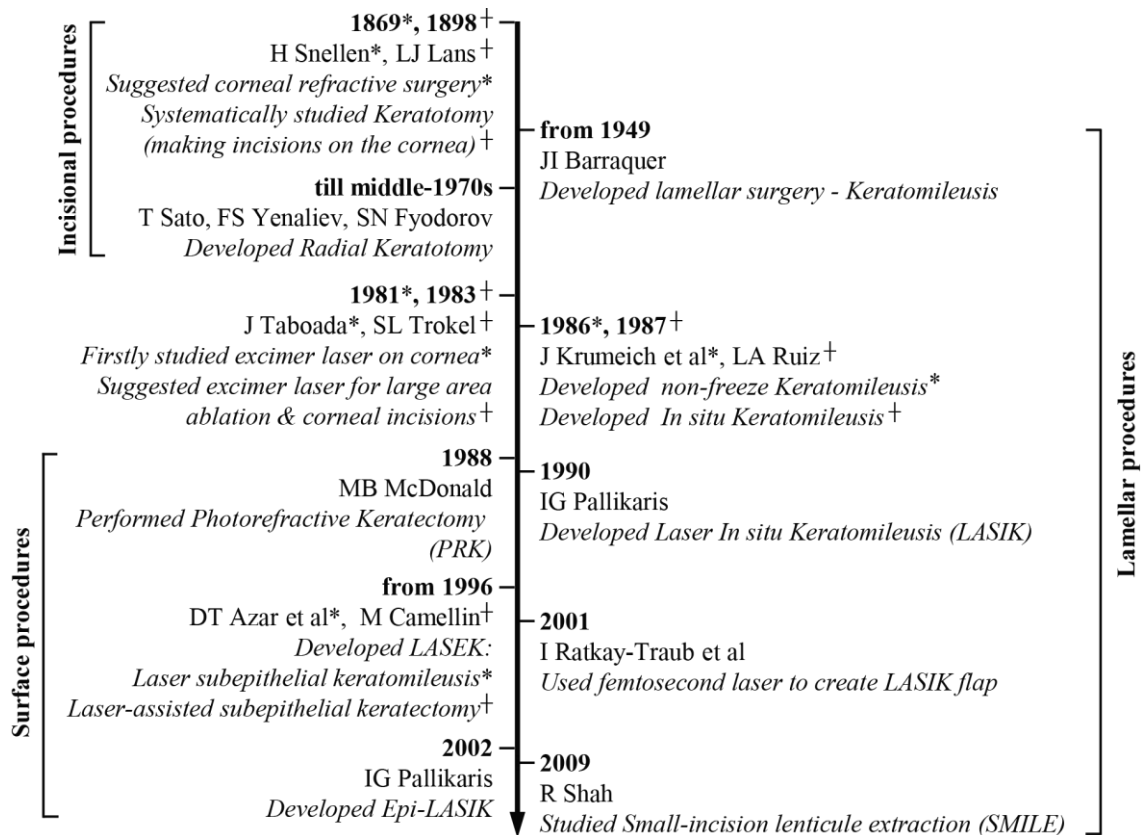


Figure 1-2. A brief history of corneal refractive surgery (more details will be included in Chapter 2)

While the incisional procedures are more or less abandoned now, the laser-based procedures are reported to result in similar visual outcomes after corneal healing [6]. PRK is the first laser-based corneal refractive surgery form, which involves removal of the corneal epithelium. The associated pain and slow visual recovery have made the procedure less popular now. On the other hand, owing to its relative comfort and rapid postoperative recovery, the LASIK has enjoyed growing popularity and has been successful in helping millions get rid of spectacles and contact lenses during the last two decades, achieving over 95% patient satisfaction [7]. In the LASIK procedure, a 100-200 micron thick flap of corneal tissue is cut and lifted up before an amount of tissue beneath the flap is removed with the excimer laser. The flap is then replaced for natural healing.

The newer SMILE procedure, on the other hand, has omitted the creation of the flap. It uses femtosecond laser to cut a corneal lenticule inside the intact bulk of the cornea and only makes a small incision (also by the same laser) on the anterior cornea to extract the lenticule. In this way, SMILE achieves the same outcome as LASIK but better preserves the corneal integrity which is advantageous to maintain the mechanical resistance of the cornea. Details of the steps of PRK, LASIK and SMILE procedures can be found from Zeiss website (<http://www.zeiss.com>).

By designing customised ablation profiles, the corneal refractive surgery in theory is able to correct both LOAs and HOAs and achieve supernormal vision (compared to normal vision) that reaches the limitation of diffraction [8]. Nevertheless, this target of supervision has never been achieved so far. In addition, while patient satisfaction of refractive surgery is quite high, there are always various degrees of discrepancy between attempted and achieved visual corrections in all surgical forms. The discrepancies and failure to achieve supervision are not explained by the attempted laser ablation, but are believed to be possibly related to the biomechanical reaction of the cornea to the surgery [9, 10]. As the remaining cornea after the surgery will have a reduced thickness, its deformation under internal eye pressure (intraocular pressure or IOP) will change leading to a new modified topography. Lack of understanding of corneal biomechanics has meant that the analysis of the procedure and the determination of the thickness of tissue to be removed are based on average corneal properties. Significant variations in corneal thickness or material behaviour would therefore lead to failure to fully correct refractive errors and may make re-treatment necessary.

With the gradual improvement in understanding of corneal biomechanics and the development of finite element method (FEM), we are now able to numerically simulate

the reaction of the eye following various forms of corneal surgery. The numerical modelling of refractive surgery can also help predict the surgical outcome and provide a way to assist the design of more accurate and realistic surgical plans that take full account of corneal biomechanical properties. This will involve building eye-specific models based on clinical data.

The necessary clinical data are typically collected preoperatively when the patient is being diagnosed and these data provides important measurements that determine the geometrical shape of the eye such as the anterior corneal topography, corneal thickness map and axial length. In addition, the eye-specific ablation depth profile can be obtained from the surgical instrument and this is essential to simulate the tissue removal in the numerical modelling. Unfortunately, all these data are generally exported as discrete points set and are not directly usable in the eye-specific numerical modelling, meaning that topography fitting techniques are generally needed to analytically represent the data for convenient use.

Further, the cornea shape cannot be wholly measured in a single observation because of limitations in current topography instrumentation and measurement techniques, which are also known to have reduced accuracy particularly towards the corneal periphery, making the topography measurement in the peripheral region considerably less reliable. This has meant that a single topography map can hardly provide adequate information of the cornea, increasing the difficulty of building representative eye-specific numerical model. To address this problem, topography matching or registration techniques are again needed to combine multiple topography maps for the same eye but collected from different viewpoints, providing a complete corneal topography and enabling the construction of accurate patient-specific numerical models.

## **1.2 SCOPE OF STUDY**

New knowledge and achievements in medical imaging technology, biomechanical and biochemical engineering, computer engineering and laser technology have enabled researchers in ocular community to better understand the nature of the human eye and provide enhanced care of ocular vision. This thesis mainly deals with corneal image/topography analysis and biomechanical modelling of refractive surgery.

Corneal topography is of great importance in characterisation of corneal shape, diagnosis of corneal disease and planning of refractive surgery. There are now quite a few instruments that can reliably measure corneal topography but unfortunately the output is often in a discrete form and the coverage of the measurements is limited. As a result, in most applications additional manipulations are needed, which are covered in this thesis as the first topic – topography analysis (topography fitting and matching). The purpose of topography analysis is to obtain an adequate and convenient representation of the cornea, which is essential for construction of patient-specific numerical models and enables the numerical analysis of refractive surgery, which is the second main concern of this thesis.

## **1.3 AIMS AND OBJECTIVES**

This research aims to establish a predictive finite element model acting as an assisting tool for planning of future refractive surgery. This finite element model should adopt patient-specific ocular shape with the help of topography analysis and be able to closely simulate the reaction of the cornea following the surgery and thus accurately predict the surgical outcome obtained clinically. The objectives of this research can then be divided into the following three aspects.

- *Topography fitting*: A set of orthogonal polynomials are used to fit corneal topography, the accuracy and reliability of these polynomials are compared and the capability of these fitting techniques in predicting surface information at locations that lay between the measured points are assessed.
- *Topography matching*: A set of approaches that match multiple corneal topographies collected from different viewpoints are assessed and further developed, aiming to provide a combined topography map which covers the entire cornea surface.
- *Numerical simulation of corneal refractive surgery*: Numerical models that simulate the LASIK refractive surgery form are developed using patient-specific data. The reaction of the cornea to the surgical procedures is predicted and compared to the clinical outcomes. The newer SMILE procedure is also developed numerically and compared to the LASIK procedure. In addition, the effect of LASIK and SMILE procedures on tonometry (method to measure intraocular pressure) is numerically studied.

#### 1.4 THESIS STRUCTURE

This thesis aims to provide a clear overview of the research programme including its aim and objectives, methods, major results and main conclusions. The thesis is organised as follows:

- Chapter 1 introduces the background of this research, the scope of the study and brief outline of the aim and objectives of this study.
- Chapter 2 reviews summarily earlier research on the human eye and its optics, analytical fitting models of corneal topography, methods of topography matching and image registration, common refractive surgery forms, and numerical simulation techniques of eye surgeries.

- Chapter 3 outlines the research methodologies adopted in this study including topography fitting, topography matching and numerical simulation of refractive surgery.
- Chapter 4 and Chapter 5 present the results of topography analysis, which includes both topography fitting and topography matching. The results are presented in the same logical order as in the methodology. The fitting polynomials are compared in terms of reconstruction and prediction errors. The achievements of topography matching are then presented.
- Chapter 6 shows the outcome of numerical simulation of refractive surgery, which is compared to the clinical outcome. The influence of surgical procedures on measuring intraocular pressure is also presented.
- Chapter 7 provides an overall discussion of the study and its main conclusions, in addition to a number of recommendations for future work.

## **CHAPTER 2**

### **LITERATURE REVIEW**

---

#### **2.1 INTRODUCTION**

A great deal of literatures can now be found in research of corneal structure and biomechanics, representation analysis of corneal topography and numerical modelling of ocular (especially corneal) behaviour under internal/external forces and following surgical procedures. These previous studies aimed to better understand the nature of the human eye including its structure and biomechanical properties, efficiently represent and reconstruct the corneal surfaces, precisely predict ocular response to external applications and reliably change the state of the eye for medical and health purposes.

This chapter firstly gives a brief review of previous publications on the geometric and optical structures of the human eye. Studies related to topography fitting and matching from both image processing and ocular communities are then reviewed and discussed. This is followed by a brief review of the history of corneal refractive surgery and its current achievements and limitations. In the last part of this chapter, previous studies on the numerical simulation of refractive surgery are reviewed, where limitations and gaps in some existing numerical modelling studies are discussed.

#### **2.2 STRUCTURE AND OPTICS OF THE HUMAN EYE**

In addition to the brief introduction of ocular structure and optics in Chapter 1, this section summarises the main anatomical components of the human eye and its optics. Considering the dominant role of the cornea and the focus of the thesis, the layered cornea and its geometrical and biomechanical properties are reviewed in a greater depth.

### 2.2.1 The eyeball

The human eye is a complex structure, ‘a pressurised and thick-walled shell that has an internal and external musculature, a remarkably complex internal vascular system, dedicated fluid production and drainage tissues, and a variety of specialised fluid and solute transport systems’ [11]. In general, it is composed of three coats enclosing three transparent media and structures [1]. These ocular components are either vital to maintain the shape of the eyeball, or responsible to supply and nourish the eye, or essential for the formation of sharp image.

The outermost coat is called fibrous tunic or corneoscleral envelop, of which the anterior sixth is the transparent cornea; the white and opaque sclera constitutes the posterior five-sixths. The transitional region that connects the cornea and sclera is called the limbus. The middle coat, known as vascular tunic or uvea, is comprised from behind forwards of the choroid, ciliary body and the iris, which presents near its centre a rounded aperture, the pupil. The innermost coat is the neural tunic or better known as retina. The fibrous corneoscleral coat confines the intraocular pressure (IOP) and determines precisely the optical geometry of the visual apparatus. The uveal circulation in the middle coat not only provides the source of the intraocular fluid but also nourishes the non-vascularised retina, which consists of numerous receptors and neurons for initial processing of visual information. This information is delivered to the brain for vision formation through the optic nerve [1].

Within the eyeball, there lie three transparent media, namely the aqueous humour, the crystalline lens and the vitreous body. The aqueous humour is continuously replenished; it is a clear and colourless fluid secreted by the ciliary processes in the ciliary body. This fluid moves inwards, scouring the lens, then anteriorly through the pupil to polish the



cornea, and finally drains out of the eye through the angle formed by the iris and cornea [11]. This circulation of the aqueous humour is responsible for creating the IOP. The crystalline lens (also frequently called the lens), which separates the aqueous humour and vitreous body, is located just behind the iris and suspended by ligament known as ciliary zonule, which attaches to the ciliary muscle of the ciliary body. The shape of lens can change through alterations in tone of the ciliary muscle to enrich the refractive power of the lens [11], which is known as accommodation and helpful for seeing nearside objects as illustrated earlier in Figure 1-1B. The vitreous body is stagnant and this gel-like transparent humour accounts for about four-fifth of the eyeball [12]. Although the vitreous body is relatively inert compared to the aqueous humour, it is quite porous thus able to transmit the IOP throughout the interior of the eye [11]. The mean IOP value in normal population is about 15 or 16 mmHg with standard deviation of about 3 mmHg [11, 13]. The range of normal IOP was reported to be related to age, sex, diabetes and geographical locations but the correlations were not explicitly agreed among the literatures [13-20]. It should be noted that IOP is a dynamic physiologic measurement, exhibiting remarkable diurnal and nocturnal variations which could be plus or minus 3.5 mmHg [21, 22]. Meanwhile, the difference between systolic and diastolic blood pressure creates circadian fluctuation in the IOP with the heart rate, which is quantified by the ocular pulse amplitude and normally has mean value of 3 mmHg [23, 24].

### **2.2.2 The cornea**

As the transparent layer covering the front of the eye, the cornea is the outmost ocular component. In addition to its roles of maintaining the ocular shape and acting as a natural barrier [25], the cornea is also responsible to provide about 70% of refractive power of the eye [1]. Therefore, understanding of the cornea is of great scientific and clinical significance.

### *Corneal geometry*

Geometrically as looking from the front, the cornea appears elliptical, averagely measuring 11.7 mm wide horizontally and 10.6 mm vertically, while from the back, the shape is circular, measuring 11.7 mm in diameter. This difference in shapes is due to the greater superior and inferior overlap of the sclera and conjunctiva than laterally [1]. The normal cornea has a shape as prolate ellipsoid, meaning it flattens towards the periphery [26]. The anterior and posterior surfaces of the cornea are not concentric as the cornea has non-uniform thickness distribution, being about 0.52 mm (0.46 to 0.67 mm) at its centre and about 0.67 mm (0.65 to 1.1 mm) close to the corneoscleral junction, making the central radius of curvature of the anterior surface 7.8 mm (6.8 to 8.5 mm) and 6.5 mm (6 to 7 mm) for the posterior surface [27].

The performance of the cornea heavily relies on its ability to maintain a perfect shape for light refraction. The knowledge of the shape, which can be characterised by the corneal axial and tangential curvatures, refractive power and elevation map [28], is essential for characterising ocular aberrations [29, 30], detecting corneal irregularities [31], modelling of the cornea [32] and the ablation planning of refractive surgeries [33]. Nowadays, a great number of devices are able to accurately measure the 3D corneal topography in vivo, including those Placido disc-based devices such as Keratron and Medmont [34], those slit-imaging technologies based such as Orbscan (horizontal/translational slit-scanning) and Pentacam (rotational Scheimpflug imaging) [35], and most recently those based on combined technologies such as Galilei and Sirius [36].

### *Anatomy and physiology of the cornea*

Histologically as shown in Figure 2-1, it has been well established that the cornea comprises five distinctive layers, namely from anterior to posterior, the continuous

regrowing epithelium, the Bowman's layer, the fibrous and strong stroma, Descemet's membrane and the endothelium. Additionally, a novel, well-defined and strong layer may exist in the pre-Descemet's cornea according to a recent study [37]. This newly discovered layer is named after the leader of this study as Dua's layer, however debate and criticism still exist both on the existence and eponyms of such layer [38, 39].

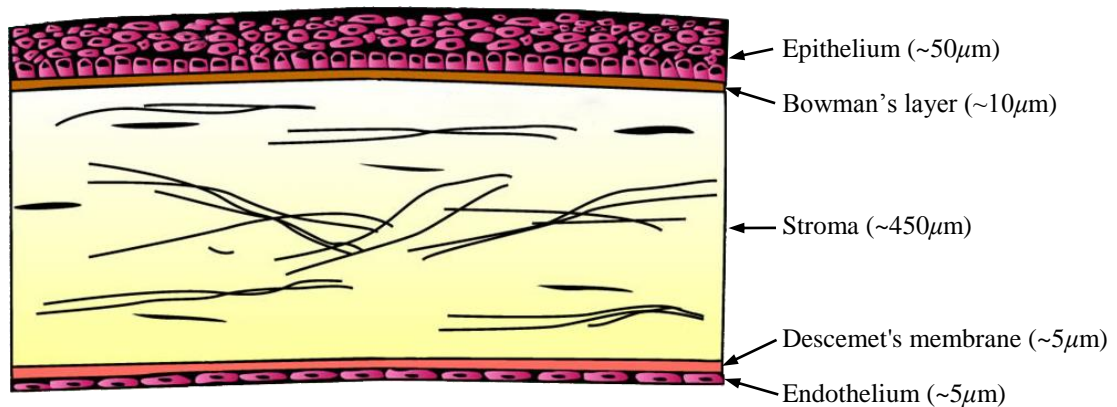


Figure 2-1. Five distinctive layers of the cornea

The collagenous stroma makes up almost 90% of the entire cornea thickness and dominates the overall biomechanical properties of the cornea [1]. Its form and function are predominantly defined by the extracellular matrix (ECM) which is rich in collagens and interspersed with keratocytes [40]. The collagens in the stroma are mainly type I, although types V, VI and XII are also present [41].

The human stroma consists of over 300 stromal lamellae, each forming a plate of collagen fibrils which are produced by keratocytes lying between the lamellae. The collagen fibrils inside the lamella are regularly spaced and connected by proteoglycans (PGs), forming a hexagonal arrangement of the fibrils [42]. The regular arrangement is hypothesised to induce minimal light scattering and thus is crucial for corneal transparency [40]. Moreover, there are evidences that other ECM components such as keratocytes are involved in creating corneal transparency by producing water-soluble proteins – ‘corneal

crystallins' [43]. The corneal transparency is also affected by hydration in the cornea which is maintained in a relatively deturgescenced state (78% water content) by the endothelial layer through a pump-leak process where leakage from the aqueous humour to the corneal layers is counteracted by the water pumping out through endothelial cells [44, 45].

The fibres of each lamella in the stroma are parallel with each other, but at right angles to those lying in nearby lamellae. The stromal lamellae are superimposed one on another and there exists remarkable anteroposterior lamellar interweave in the anterior stroma, making it more compact thus stronger in the anterior than the posterior [46]. The tighter rigidity in the anterior cornea is demonstrated to be particularly important to maintain the corneal curvature [47]. The preferential orientation of lamellae is along inferior-superior or nasal-temporal direction in the central cornea, which then appears to run circumferentially around the limbus where the cornea and sclera meet [48]. This change in lamellae orientation from central to peripheral cornea is believed to be helpful to maintain the corneal curvature as well [41].

The corneal integrity can be interrupted by any trauma, which trigger a series of cellular and molecular injury responses in the corneal layers with an evolutionary purpose of restoring the natural function of the cornea [49]. The injury responses are triggered in sequences and many processes can take place simultaneously and co-regulate in many ways. These complex wound healing processes are mediated by cytokines and various growth factors, and can involve many elements, among which the keratocyte apoptosis, keratocyte necrosis, keratocyte proliferation, migration of inflammatory cells, and myofibroblast generation are frequently present and best characterised [50].

Upon most injuries, the first disruption occurs in the epithelium which initiates epithelial–stromal healing interactions. The epithelial cells undergo immediate disappearance of hemidesmosomes, creation of cell membrane extensions and increase in mitochondrial energy production, which are followed by cell migration and spreading to cover the wounded side [51], before cell proliferation and stratification that re-establishes the multicellular layers of the epithelium [52]. In the stroma, keratocytes apoptosis occurs beneath the damaged epithelium areas and it is mediated by proapoptotic molecules and cytokines released mainly by the epithelial cells; these can include interleukin-1 (IL-1), Fas ligand, and tumour necrosis factor  $\alpha$  (TNF- $\alpha$ ) [53]. Subsequently, the surviving keratocytes are activated and begin to migrate and proliferate, probably mediated by platelet-derived growth factor (PDGF) [54]. These activated keratocytes produce relatively small amount of ECM [40] but they seem to play a decisive role in producing or helping produce growth factors such as epidermal growth factor (EGF), hepatocyte growth factor (HGF) and keratinocyte growth factor (KGF), which are helpful for the epithelial re-establishment [53]. Depending on the integrity of the epithelial basal membrane, cells known as myofibroblasts may derive from keratocytes in response to transforming growth factor  $\beta$  (TGF- $\beta$ ) which is produced by the epithelial cells and allowed to diffuse into the stroma following disruption of epithelial basal membrane [55]. Myofibroblasts trigger collagen and ECM remodelling and cause contraction of the repairing tissue, however these cells have reduced transparency and the resulting collagen and ECM are disorganised and opaque, causing high level of light scattering and reflection, and thus reduction in corneal transparency [56]. Eventually, when the levels of TGF- $\beta$  are reduced due to the recovery of epithelial basal membrane, IL-1 triggers apoptosis of myofibroblasts [57], which allows a regularisation process to take place, attempting to restore regular diameter and arrangement of the stromal fibrils, and thus the

corneal transparency [58]. The thickness and material properties undergo continuous changes during the wound healing process which can last from months to years [59]. These long-term changes in particular can lead to overcorrection, undercorrection and regression in surgical refractive procedures such as those that will be discussed later in this chapter. It has been widely agreed that understanding of the cascade of corneal wound healing events and processes is indispensable to improve the predictability and safety of refractive surgery [50, 59-61].

### *Corneal biomechanics*

Determined by its microstructure, the cornea has material properties including hyperelasticity, viscoelasticity and anisotropy [62]. With hyperelasticity, the cornea exhibits nonlinear material behaviour, reflected by a nonlinear stress-strain curve [63]. The hyperelastic property of the cornea makes the single Young's Modulus (or elastic modulus  $E$ ) inadequate to represent the overall corneal elastic material. However, as shown in Figure 2-2, the cornea does behave linearly under low pressure because of the dominant bearing role of corneal matrix; as the pressure increases, the stiffer collagen fibril layers becomes taut and dominant in tension bearing, resulting in significant elevation in corneal stiffness [25]. In addition, the cornea was observed to be stiffening with age [64]. This stiffness increase with age may partially due to the increase in collagen fibril diameter with age [65] but the increased cross-linking of collagen in older cornea is thought to contribute significantly more in corneal stiffening [64, 66].

Viscoelasticity and anisotropy are another two essential material properties of the cornea, the first indicates the elasticity of the cornea is time and loading rate dependent, while the latter means the cornea behaves differently in different directions [67, 68]. Like all soft tissues, the corneal viscoelasticity is mainly due to its highly hydrated nature. Moreover,

it is now clear that the mechanical anisotropy of the cornea is largely determined by the varying orientation of the fibrils.

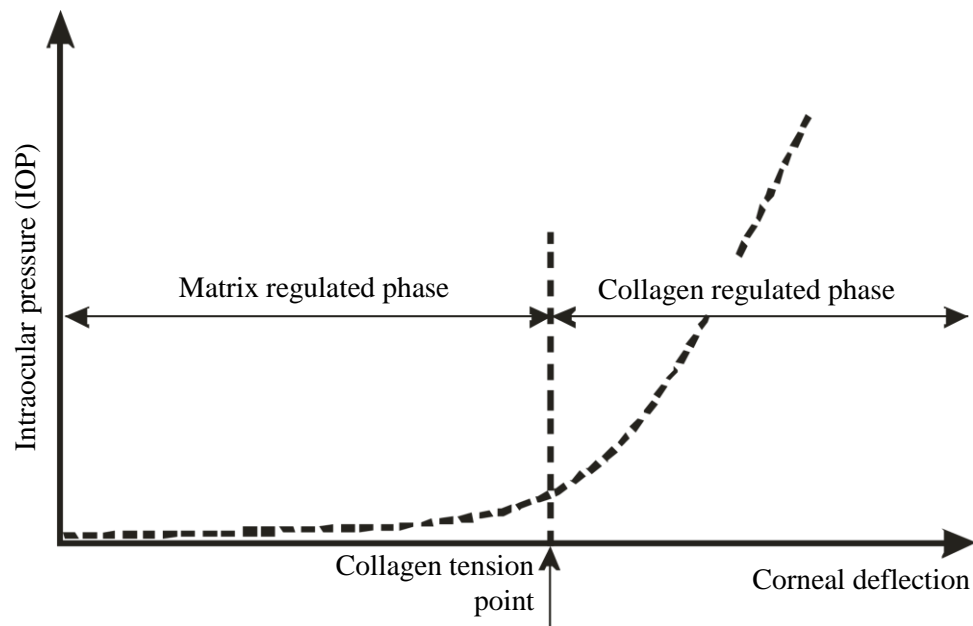


Figure 2-2. Typical behaviour of the cornea under tension with an initial matrix regulated phase followed by a higher stiffness collagen regulated phase [25]

### 2.2.3 Optics of the eye

Clear vision relies on the ocular capability of refracting and focusing the incoming light rays on the retina. The two ocular components that are responsible for this refraction are the cornea and the lens.

The refraction of light is caused by the difference in refractive indices of the transmission media and enlarged if the boundary of the media is right curved. Quantitatively, the refractive power is measured in inverse metre ( $m^{-1}$ ) or equivalently dioptre ( $D$ ) and it can be computed by  $(n'-n)/R$  where  $n$  and  $n'$  are the refractive indices on the incident and refracted sides, and  $R$  is the radius of the transmission boundary [69]. In the case of human eye, as shown in Figure 2-3 with representative dimensions and refractive indices, the change of refractive indices is greatest when light passes through the anterior corneal surface, leading to a refractive power of 48.2  $D$ . The total refractive power of the cornea

is about 42  $D$  because of a slight reduction in refractive index from the cornea (1.376) to the aqueous humour (1.336), which results in a negative refractive power caused by the posterior corneal surface of  $-6.2 D$ . Being different from the cornea, the lens has remarkably varying refractive index from the nuclear region to the cortex region. It is thus not straightforward to estimate its refractive power by simple formula above as done for the cornea. Collectively, the equivalent refractive power of the lens is estimated slightly above 20  $D$  [70]. Although this makes the lens contribute significantly less refractive power to the optical system, being about 30% of the entire ocular refractive power, the lens can add accommodative power when the eye needs additional power to focus light from near objects. This accommodative power (or amplitude of accommodation) is greatest at birth, being 15-16D, but declines to 8D at around age 25 years and to 2D or less at 50 years [1].

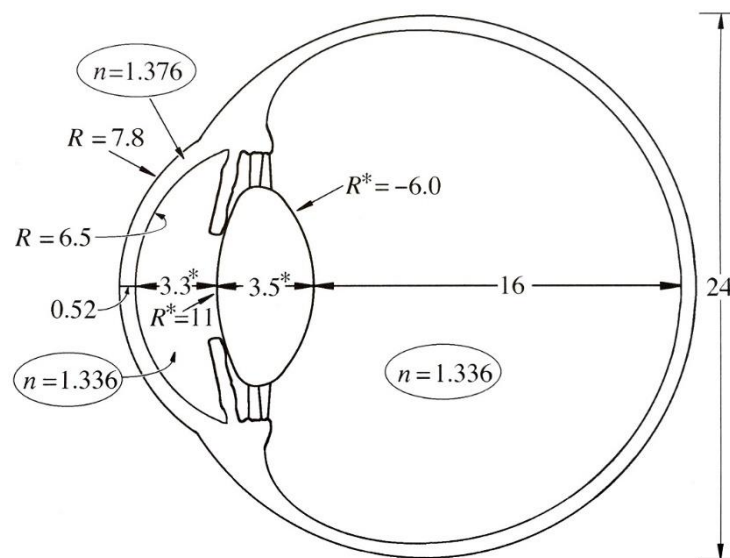


Figure 2-3. Representative dimensions ( $mm$ ) and refractive indices of the eye. The starred values are for relaxed eye (no accommodation). The refractive index of the lens is not constant and is greatest in the nuclear (central) region, being 1.406, and least in the cortex (peripheral) region, being 1.386 at the edge of the lens [69].

The mismatch between the actual refractive power of an individual eye and the right power that it needs to focus the light precisely on the retina, results in blurred vision.



Conventionally, this mismatch is quantified by refractive errors including myopia, hyperopia and astigmatism as introduced in Chapter 1. But more recently, wavefront aberration has become widely used to quantify the optical imperfection of the eye. This benefits from advances in physical optics where light is regarded as waves rather than a bundle of rays as in geometrical optics [71]. The wavefront, as its name applies, is the front surface of the light waves that are all in-phase and this surface is always perpendicular to the light rays as shown in Figure 2-4 or earlier Figure 1-1 in Chapter 1. Ideally, the wavefront, before it strikes the retina, should be a sphere with its centre located on the retina. The difference between the actual wavefront and the ideal wavefront is called the wavefront aberration.

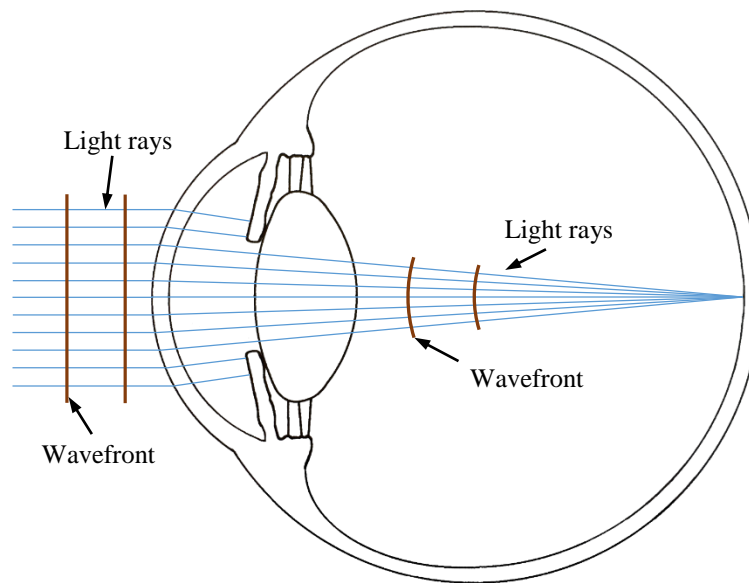


Figure 2-4. A schematic eye model showing light rays being refracted by ocular system and the shape of wavefront during the transmission

While the shape of the wavefront aberration can be arbitrary, it can be broken into ordered components including low order aberrations (LOAs) and high order aberrations (HOAs) [72]. In addition to but without repeating the details given in Chapter 1, Figure 2-5 and Figure 2-6 have shown the effects of various wavefront aberrations on the image formed on the retina (emmetropic plane (E)) as well as on the myopia (M) and hyperopia (H)

planes [73]. In a normal eye, the image of a point source object on plane E would be a small spot called Airy disk caused by light diffraction only [74]; while in an aberrated eye, such image can range from a blob to an arbitrary shape. It should be noted that wavefront aberrations are caused by imperfect shapes of both the cornea and the lens, and the discussion above has emphasised the overall wavefront of the whole eye. Moreover, it is evident that there exists compensation between cornea and lens to cancel out each other [75, 76].

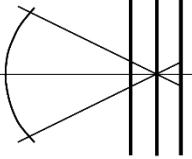



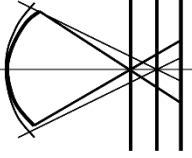


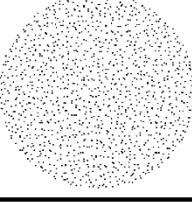
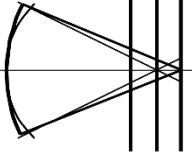
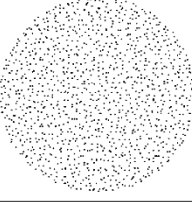


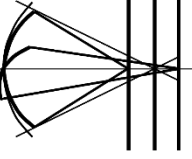


	M E H	M	E	H
Emmetropia				
Myopia				
Hyperopia				
Astigmatism				

Figure 2-5. Actual wavefront shapes for different low order aberrations compared to the ideal shape and their corresponding images of a point object on the myopic, emmetropic and hyperopic planes [73]

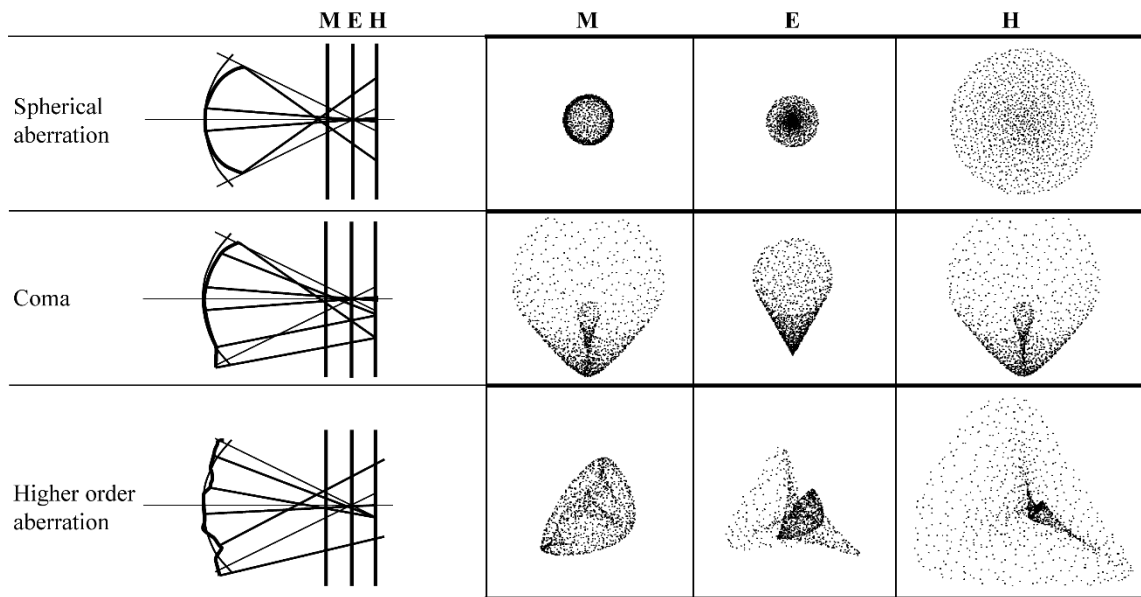


Figure 2-6. Actual wavefront shapes for different high order aberrations compared to the ideal shape and their corresponding images of a point object on the myopic, emmetropic and hyperopic planes [73]

Nowadays, wavefront analysis has become a crucial part in modern refractive surgery for the planning of laser ablation because it allows more accurate vision correction [77]. In this analysis, an aberrometer or wavefront sensor is employed to measure the shape of the wavefront expressed as wavefront aberration [78]. Further, the shape of the wavefront is usually fitted by the set of orthogonal Zernike polynomials to display the characteristic components [71, 79]. Zernike polynomials are also employed frequently to represent the corneal topography [80], and the resulting Zernike representation of the corneal topography can be used to indirectly determine the wavefront aberration [29]. The fitting of corneal topography to polynomials like Zernike polynomials is the topic of the next section.

### 2.3 CORNEAL TOPOGRAPHY FITTING

Although the corneal surfaces, including anterior and posterior surfaces, can now be reliably observed, they are normally exported as sets of discrete points. A crucial step before their applications is fitting of these discrete points to analytical surface. Historically, the corneal topography has been fitted to ellipsoid surface [81], spline

functions [82-84], Taylor series expansion [85]. Besides, the orthogonal Zernike polynomials (ZPs) [79], now as the standard for reporting optical aberrations [86], are also widely used as fitting techniques for corneal height data [80], having advantages over non-orthogonal polynomials such as explicit physical meaning of the polynomial features and independence among the polynomial terms. However, the ZPs, although being used frequently by ophthalmologists in their every-day work, have been reported to explain the topography features incompletely and fail to give all the information that affects visual acuity, which may lead to imperfections or mistakes of clinical diagnosis and treatment [34, 87]. This is particularly true when fitting irregular corneal topography because the 2D ZPs exhibit global features which are too smooth to detect local irregularities.

Subsequent works on fitting corneal topography have introduced other orthogonal polynomials such as pseudo-Zernike polynomials (PZPs) [88], continuous and discrete Tchebichef polynomials (TPs) [89, 90]. Also, the idea of combining several techniques to fully capture all shapes (both globally and locally) has been introduced by Martinez-Finkelshteinl, et al. [91], where the author proposed using both standard radial polynomials and radial basis functions (RBFs) to fit the corneal height data. This idea is well followed by Espinosa, et al. where the so called ‘zonal’ and ‘modal’ fitting strategies both based on ZPs are combined [92].

Similarly, orthogonal polynomials have been more extensively investigated in image processing community. Except for the aforementioned polynomials, other polynomials such as Gegenbauer polynomials (GPs) [93], Legendre polynomials(LPs) [94], Gaussian-Hermite polynomials (GHPs) [95], Orthogonal Fourier-Mellin polynomials (OFMPs) [96] have been used as kernels of image moments which relevantly turn out to be coefficients in the polynomial decomposition [97]. Superior performance of image reconstruction

based on some of these polynomials compared to the conventional ZPs has been demonstrated [96, 97].

The core step in representation of corneal topography by the expansion of polynomials is the determination of coefficients of the polynomial terms, which later allows reconstruction of the surface and thus the assessment of the representation quality. There are mainly two methods that are routinely implemented to obtain these coefficients. The first method takes advantage of the orthogonality of the polynomials such that the coefficients can be directly computed as the projection of the surface onto the polynomials. In other words, the coefficient is the inner product of the surface function and the polynomial function [98]. Unfortunately when continuous polynomials are used as in most cases, this inner product, which is a two-dimensional integration, cannot be computed straightforward but only approximated because the continuous or at least piecewise continuous surface function is unknown [94, 99]. In fact, it is the goal of polynomial fitting to achieve such explicit expression/function of the surface that is initially expressed by means of discrete points. The problems of determining coefficients for continuous polynomials had immediately motivated researchers in image processing community to employ discrete orthogonal polynomials such as discrete Tchebichef polynomials [100, 101], Krawtchouk polynomials [102], Hahn polynomials [103] and some other candidates [104]. Using discrete polynomials to decompose arbitrary surfaces can avoid certain inevitable errors introduced during the evaluation of the continuous polynomial coefficients, which rapidly popularised the research based on discrete polynomials in pattern recognition, character identification and other related fields. Nevertheless, the representation by expansion of discrete polynomials has the fundamental difficulty to predict points that lay between the measured locations. In other words, evaluating new points based on the discrete polynomials is somehow impossible,

while this is sometimes the main goal of fitting corneal topography to analytical surface. Therefore, using discrete polynomials to fit corneal topography is not considered in this thesis.

Instead of orthogonal projection as discussed above, the common used method in the ocular community is simply based on least-square estimation. Using the same sampling locations (i.e. x and y coordinates), the continuous polynomials are sampled and the process of determining polynomials coefficients become solving a linear equation system in least-square sense [98]. This method is relatively more straightforward and accurate in terms of reconstruction error. Nevertheless, the coefficients are obtained by mere optimisation and thus may not always reflect the exact ones because the orthogonal property of the polynomials are not taken into account. Further, a direct consequence is that the coefficient for a certain polynomial term may vary when other terms are added or subtracted, which would never take place using orthogonal projection techniques.

A common process in topography fitting or image reconstruction is to map the topography/image to the domain of the orthogonal polynomials [105], which is usually done by scaling the x and y coordinates of the map. The domain of polynomials is usually unit circle or square; the corneal topography map, on the other hand, is often exported as measurements at points within a circular region in consistency with the nature of the cornea. Mapping circular corneal topography to square domain may have two major difficulties: 1) If the map is scaled to be fully covered by the polynomial domain (i.e. the map is inscribed with the square domain), blank region in the four corners will erroneously effect the fitting performance because of the sudden change in shape from curved to flattened (e.g. the corners); 2) If the map is scaled such that the circular map area circumscribes the square domain, the sudden change in shapes is avoided but

significant portion of the original maps will be discarded. Nevertheless, if least-square method is employed to evaluate the polynomials coefficients, the orthogonality does not have to be maintained such that a circular portion of the square polynomials can be extracted and used to represent the surface.

## 2.4 CORNEAL TOPOGRAPHY MATCHING

The corneal topography cannot be wholly measured in a single observation because of limitations in current topography instrumentation and measurement techniques [106], which are also known to have reduced accuracy particularly towards the corneal periphery, making the topography measurement in the peripheral region considerably less reliable [34, 107]. In some applications such as fitting of scleral contact lenses [108] and planning and numerical simulation of eye surgery, both interpolated and extrapolated data are commonly used, running the risk of overestimating corneal height in the periphery [109]. An accurate representation of topography that covers the entire corneal surface and beyond into the anterior sclera is desirable and particularly important in evaluation of post-cross linking surgical eyes of keratoconics that require monitoring of outcome and fitting of large diameter contact lenses that cover the sclera – corneal junction and anterior sclera. A complete corneal topography also allows the construction of accurate patient-specific finite element models for biomechanical modelling of the human eye [110]. The topography matching study of this thesis is to address this need through an assessment and further development of methods that have the potential to provide a complete corneal topography.

As introduced earlier, the corneal topography is commonly measured using videokeratography (VK) instruments such as the Pentacam, Orbscan and Medmont. Single measurement maps using VK instruments have limited reliable coverage, normally

8-9 mm, with the peripheral measurements being less reliable than the central due to the quality of signal obtained tangentially versus perpendicularly. To overcome this disadvantage, the whole corneal surface can be covered in portions by directing the patient to central focusing point and a number of eccentric targets, thus a set of topography maps can be captured for central and several peripheral portions of corneal surface. However, the maps are in disparate coordinate systems and cannot be combined easily without additional manipulation since their relative directions are not precisely known. Therefore, reliable topography combination techniques are needed to bring together all the maps (central and peripheral) into a common, global coordinate system based on accurate overlapping information.

Relatively few publications are available in the ocular community on topography combination. Earlier studies either concentrate on conducting rigid-body transformation while minimising the height difference between individual maps within the overlapping region by a non-linear optimisation method [111], or determine the magnitude of this transformation by using the characteristics of the videokeratography [112]. Both methods are only validated by numerical simulation. One notable example is the method developed by Franklin et al. [109] where the point corresponding to the centre of the central map is located in the peripheral topography by testing all possible points within a candidate region. This is done by, for each point in the candidate region, shifting and rotating the peripheral map until the normal of the current candidate point shares the same direction as the centre point of the central map. The candidate point that minimises the difference between the central and transformed peripheral maps in the overlapping portion is sought. This procedure defines the required lateral shift and rotation of the peripheral map that enables the combination of the central and peripheral maps.



Franklin et al. [109] remarked that variability of axial radius of curvature was less than height-data variability, especially at the periphery. They chose to use the differences of axial radii of curvature as the alignment criterion. This approach seems not to be straightforward because axial curvature measurements depend on the videokeratography axis and represent curvatures only along the meridians, while ignoring shape properties in other directions [113]. To form the alignment criterion preferred by Franklin et al., the axial radius of curvature map must be computed based on the measured height map. The same authors reported that it took an hour to complete the matching task for one pair of central and peripheral maps on a standard desktop computer at that time and that their software required significant optimisation to be useful in clinical practice.

Compared to the limited number of publications on combining ocular topography maps, more literature exists in the image processing field on algorithms aimed at aligning views of an object taken from different viewpoints [114-116]. Among these, the Iterative Closest Point or Iterative Corresponding Point (ICP) algorithm has become the dominant method for image registration of three-dimensional objects since its introduction by Chen and Medioni [117], Besl and McKay [118], in the 1990s. In ICP routines, the surface or map usually consists of a cloud of three-dimensional points sampled on the surface of an object. The corneal topography is such a cloud of points, making the ICP algorithm also applicable to corneal topography combination. Modifications and improvements have been introduced in subsequent studies to make the ICP faster, more robust and accurate by optimising the analysis steps or introducing additional properties of the surfaces, such as slopes or curvatures, into the standard ICP procedure [119].

The ICP algorithm is available in several variants. When applied to match central and peripheral corneal topographies, it essentially consists of minimising an objective

function that defines the distance between sets of points of measured maps on the same surface observed from different viewpoints (central and peripheral). When there are two peripheral maps or more, one question raised that how to deal with or take use of the connective information between the peripheral maps themselves. On one hand, aligning the peripheral maps to the central map individually without consideration of their relative information will have big chance to introduce inconsistencies among the peripheral maps. On the other hand, newly added maps may bring in information that could improve the registrations of the previously registered maps [120]. The matching of multiple maps is coined as multi-view registration.

Compared to pair-wise registration, the multi-view registration is more complex and the proposed methods of doing so are diverse. The naturally extended approaches from ICP aim to consider all the peripheral maps simultaneously by integrating the connective information of the peripheral maps into the error metrics of the original ICP algorithms as firstly attempted by Stoddart and Hilton [121] using a gradient descent algorithm. In the same direction, Benjema and Schmitt [122] extended Besl's algorithm to solve multi-view registration problem using quaternions, while Neugebauer [123] gave a multi-view version of Chen and Medioni's approach by using either Newton-Taylor algorithm after special assumption of the world coordinates system and linearisation of the error metric or Levenberg-Marquardt algorithm directly [124], resulting in smoother convergence. A more detailed review refers to Huber [125], where the author preferred the point-to-plane based approach of Neugebauer. Corresponding to the ICP algorithm, the multi-view registration method is called Multi-ICP (MICP) method in this thesis and it is developed in this thesis based on Neugebauer's approach.

In contrast to the approach stated above to handle all transformation at the same time, another quite different approach was proposed recently by Sharp [126] to refine the multi-view transformations ending up with a more uniform global error distribution. This approach form circles according to the connective information of views (maps) and force the product of all transformation matrices belonging to one circle to be identity, i.e. a view or map should return to its original position after a circular traveling. By doing so, this method minimises the error between coordinate frames but may not always distribute the alignment error correctly [127]. This method will not be considered in this thesis for simplicity consideration.

## **2.5 REFRACTIVE SURGERY**

In ophthalmology, refractive surgery has an incomparable and fruitful history. From the substitution of normal prescriptive spectacles and contact lens to the demand of supervision or supernormal vision [128], refractive surgery has become not only a life-improving procedure but also a cosmetic routine. In general, refractive surgery is any eye surgery employed to improve the refractive state of the eye and all the modalities now available can be categorised into incisional, thermal, excimer laser ablation and intraocular [129]. Further, refractive surgery can be operated on both the cornea and the crystalline lens, leading to cornea-based refractive surgery and lens-based refractive surgery, respectively [130]. In this thesis only corneal refractive surgery is considered.

### **2.5.1 From da Vinci's codex to laser corneal refractive surgery**

The first known description of refractive errors dates back to the early 16<sup>th</sup> century when Leonardo da Vinci contemplated the possible source of visual disturbances [5]. While the vision abnormalities had been successfully corrected with spectacles and contact lens for centuries [131], the history of corneal refractive surgery, so to speak, only began in 1869

when Dutch ophthalmologist Herman Snellen (after whom the visual acuity chart Snellen chart was named) suggested possible surgical correction of corneal astigmatism by making incisions across the steep meridian of the cornea [132, 133]. This procedure, termed keratotomy, was systematically studied by another Dutch ophthalmologist Leendert Jan Lans almost 30 years later in 1898 [134] and following this line radial keratotomy (RK, making radial incisions to the anterior cornea to correct myopia and astigmatism) was finally developed in the middle-1970s after trials and experiments of over 70 years [135-141]. Unfortunately, the outcomes of RK were undesirable [142-144]. Combined with the regressive visual acuity and infection, this form was soon replaced by newer laser-based procedures [145].

Being different from making incisions in RK, lamellar surgery – keratomileusis (meaning ‘carving’ of the ‘cornea’) was theorised in 1949 by Colombian ophthalmologist José Ignacio Barraquer, who also invented the microkeratome and cryolathe in his successive works [146, 147]. This procedure, in its mature form, involved dissecting the central anterior cornea using the microkeratome, freezing the dissected corneal disk before attaching it to the cryolathe for fixation, lathing the stromal surface and suturing the reshaped disk back to the living cornea after thawing [148]. Although the results of Barraquer’s freeze keratomileusis were also disappointing largely due to the difficulty of operation and severe damage to the corneal tissue caused by the freezing process [149-151], subsequent refinement and improvement such as non-freeze cut [152-154] and in situ keratomileusis (or automated lamellar keratoplasty (ALK)) [155] had gathered speed for an evolution.

The next step was the arrival of excimer laser, which brought the refractive surgery to a new era, Table 2-1. In the early 1980s, pioneer studies on corneal tissue reaction to this

laser [156, 157] and attempts to improve the accuracy of RK incisions [158, 159] made scientists and ophthalmologists quickly realise that large area ablation could be performed in the central cornea using excimer laser rather than just incisional cut. This gave birth to the first laser corneal refractive surgery form photorefractive keratectomy (PRK) with excellent visual outcomes [160, 161] and later soon the most successful form laser in situ keratomileusis (LASIK) motivated by ALK, with additional advantages over PRK such as rapid visual recovery, less or no postoperative pain [162, 163].

The fence that distinguishes PRK and LASIK and their performance is the way they apply laser ablation. In PRK, the epithelium is scraped away to allow laser ablation of stroma, however the regrowing of the epithelial cells postoperatively is rather slow and the associated pain can even reach a point when narcotic agents are needed [145]. Another major disadvantage of PRK is corneal haze caused by the healing process [164, 165]. LASIK avoids all of these complications owing to its way of ablating the stroma beneath a corneal flap as described earlier in Chapter 1. Because the central epithelium is kept almost intact except for the cutting edge of the flap, the effect of wound healing is minimised such that the patient could feel less or no pain and the postoperative visual improvement is usually immediate. Nevertheless, although rare, LASIK has its unique flap-related complications such as incomplete cut, buttonhole and free cap during the procedure, and displacement of the flap, epithelial ingrowth, diffuse lamellar keratitis and induced ectasia postoperatively [166, 167].

To avoid the disadvantages of PRK and LASIK, modern corneal refractive surgery has been extended in two major lines – surface procedures and lamellar procedures. The first involves combining advantages of PRK and LASIK, leading to LASEK (Laser-Assisted Sub-Epithelial Keratectomy) [168] and Epithelial Laser-Assisted in situ Keratomileusis

(Epi-LASIK) [169], in which the epithelium is fashioned as the LASIK flap with the help of alcohol solution (LASEK) or mechanically with a modified microkeratome (Epi-LASIK) for a more complete separation; the ablation on the other hand is still applied to the immediate anterior stromal surface as happened in PRK [168, 169]. By preserving at least partial epithelium, these new surface procedures are reported to have significantly reduced the postoperative pain and haze, but the visual outcomes remain similar [170]. The difference in flap creation in LASEK/Epi-LASIK and LASIK is shown in Figure 2-7.

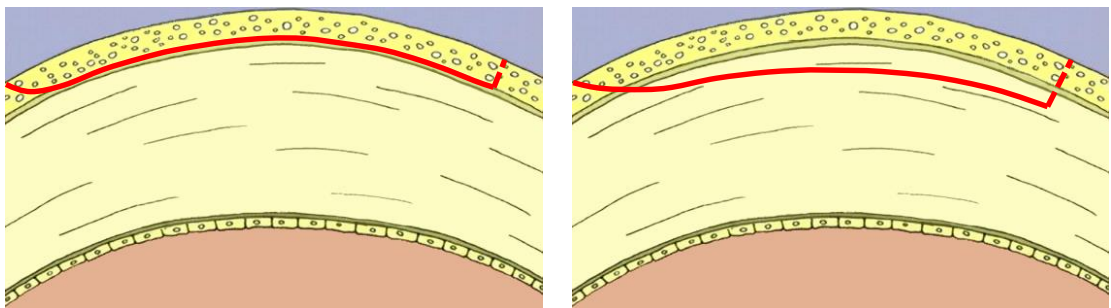


Figure 2-7. Schematic figures of the cut in LASEK/Epi-LASIK (left) and LASIK (right)

With the surgical applications of femtosecond laser stimulating another surge in the history of refractive surgery [171], femtosecond laser based LASIK (femtosecond-LASIK) [172] and most recently Small-Incision Lenticule Extraction (SMILE) [173] are made available in the lamellar procedure direction. Incredible accuracy and property that this laser can transmit through the clear cornea with no damage and only breaks down the tissue when the laser beam is focused [174, 175], have quickly gained femtosecond laser popularity. The flap created by femtosecond laser is smoother and with improved safety and thickness predictability which is essential for subsequent excimer laser ablation [176]. While the absolute superiority of femtosecond-LASIK over the conventional LASIK in terms of visual outcomes and safety are still not certain [177, 178], the most recent completely femtosecond laser based SMILE has indeed largely overcome major flap-related complications of LASIK [179]. In SMILE, a corneal lenticule is created in the

bulk of the cornea and only a small incision is made in the anterior surface to extract such lenticule. In this way, the corneal integrity is maximally preserved and this is advantageous to maintain the mechanical resistance of the cornea [180].

In Table 2-1, commonly used corneal laser surgical procedures are summarised with their major advantages and disadvantages, indicating none is perfect. However, it should be noted that, although LASIK has unique flap complications, it remains the most successful and popular form worldwide thanks to its excellent visual outcomes, rapid visual recovery and ultimate postoperative comfort.

Table 2-1. Commonly used corneal laser surgical procedures and their major advantages and disadvantages

	Advantages	Disadvantages
PRK	<ul style="list-style-type: none"> <li>▪ Excellent visual outcome with over 80% of eyes achieving refractive outcome within 1.0 D [181] after stabilisation which may take over 6 months</li> <li>▪ Preferable for eyes with thin corneas and large pupils which make LASIK difficult</li> </ul>	<ul style="list-style-type: none"> <li>• Intense postoperative pain especially within the first 24 hours</li> <li>• Slow visual recovery which may take weeks, making simultaneous operations on both eyes impractical</li> <li>• High risks of corneal haze</li> </ul>
LASIK	<ul style="list-style-type: none"> <li>▪ Excellent and possibly slight better visual outcome than PRK with over 90% of eyes achieving long-term post-LASIK refractive outcome within 1.0 D [182]</li> <li>▪ Rapid visual recovery (a few hours)</li> <li>▪ Extreme comfort with less or no pain</li> <li>▪ Have been performed for 20 years and widely accepted</li> </ul>	<ul style="list-style-type: none"> <li>• Unique intraoperative and postoperative flap complications (rating from 0.3% to 5.7% [183, 184]) such as free cap, incomplete flap, buttonholed flap, opaque bubble layer created by femtosecond laser, epithelial ingrowth, diffuse lamellar keratitis</li> <li>• Highest risk to induce ectasia among all surgical forms (still very rare though)</li> <li>• Not suitable for eyes with thin corneas, flat corneas</li> </ul>
LASEK	<ul style="list-style-type: none"> <li>▪ Similar visual outcome compared to PRK and LASIK</li> <li>▪ Theoretically less recovery time, haze and pain than PRK</li> </ul>	<ul style="list-style-type: none"> <li>• No significant improvements over PRK in terms of recovery time, haze and pain</li> <li>• Potential damage to epithelial cells and integrity due to alcohol usage</li> </ul>
Epi-LASIK	<ul style="list-style-type: none"> <li>▪ Similar visual outcome compared to PRK, LASIK and LASEK</li> <li>▪ Less recovery time and less significant haze than PRK and LASEK</li> <li>▪ Better preservation of epithelial integrity</li> </ul>	<ul style="list-style-type: none"> <li>• High rate of failure in creating epithelial flap (33% as reported in [185])</li> </ul>
SMILE	<ul style="list-style-type: none"> <li>▪ Excellent visual outcome and comfort comparable to LASIK</li> <li>▪ Able to treat thin corneas and safer to treat high myopia</li> <li>▪ Less compromise of corneal integrity compared to LASIK</li> </ul>	<ul style="list-style-type: none"> <li>• Not suitable to treat hyperopia and very low myopia for now</li> <li>• Difficult for retreatment</li> <li>• Slower visual recovery than LASIK</li> <li>• More expensive and still experiencing a learning curve</li> </ul>

### 2.5.2 Other prospects of refractive surgery

Except for the advances in modern surgical forms as stated above, other technology such as laser platforms, eye tracking system and wavefront analysis technology have also played important roles in the development of corneal refractive surgery [186, 187]. Wavefront analysis in particular has enhanced the customised design of ablation profile. Conventionally, the profiles for the corrections of ordinary refractive errors (low order aberrations) including myopia, hyperopia and astigmatism were computed based on the Munnerlyn formula [188], but soon this was reported to increase high order aberrations [189, 190] and also potentially disrupt the compensational balance between the cornea and the lens [191]. With the development of recent wavefront sensing and analysis techniques, this negative effect can now be minimised or optimised [192]. In addition, wavefront-based ablation profile claims to correct the overall aberration in the eye and targets supernormal vision that reaches the limitation of light diffraction [8]. Nevertheless, this target of supervision has never been achieved, largely due to the still imperfect understanding of corneal biomechanical reaction following the surgery and the wound healing process which further alters the corneal biomechanics gradually, increasing the unpredictability of the surgical outcomes [10].

Even though the average satisfaction rate for LASIK has scored over 95% in both general and physician populations [7, 193], the large number of LASIK procedures performed worldwide, being over 35 million till 2010 [194], leads to a dissatisfied patient population of over 1.5 million till 2010, which would be well beyond 2 million till now. This may have costed over 3 billion pounds if the average cost of LASIK is taken as 1500 pounds. Common reasons for dissatisfaction include residual refractive error, night vision symptoms [7], both of which may be due to the inconsideration of corneal biomechanical response to surgical applications. Moreover, surgical induced ectasia, although happened



rarely, can even put a threat of blindness and induce the need of corneal transplantation [195]. To predict and improve the surgical outcomes, and reduce complications, significant amount of research is still needed to understand the corneal biomechanical responses to surgical applications such as LASIK and SMILE. An essential part of doing so is the finite element analysis (FEA), which is the practical application of finite element method (FEM) firstly coined by Clough in 1960 [196].

## **2.6 NUMERICAL SIMULATION OF REFRACTIVE SURGERY**

Originating from solving complex structural problems in civil and aerospace engineering, FEM has become an utmost important numerical technique for finding approximate solutions to partial differential equations in complex structures. The FEM adheres the concept of 1) dividing the continuum into a finite number of parts or elements and 2) assembling all elements to achieve the solution of the complete system [197].

In ocular community, the past three decades saw a rapid growth in the use of FEM to understand and predict the ocular response to various conditions including but not limited to refractive surgery [63, 198-211], impact and injuries [212-214], diseases (especially keratoconus [215-218]) and tonometry [219-223]. Combined with some optimisation algorithms, FEM is also used as an important approach to determine essential model parameters such as coefficients of various material models that are employed in the finite element models [224-230].

During the last three decades, the accuracy and representation of the natural conditions of the eye has been remarkably improved, thanks to the advances in videokeratography and better understanding of corneal biomechanical properties. Corneal finite element models that adopt in vivo topography [200, 203, 204, 207, 215, 216] and material models representing corneal hyperelasticity, anisotropy and viscoelasticity [223, 231-233] have

become common, overcoming the drawbacks of some models (especially earlier models) based on analytical corneal shape [63, 210, 211, 227, 234-238] and assuming linear elastic and isotropic corneal material properties [209-211, 239]. Further, the rapid increase in computing power has enabled large complex models such as 3D whole-eye models to be solved quickly. The whole-eye model, which eliminates the need to specify boundary conditions at the limbus as done in cornea-only models [110, 199, 201], was favoured and claimed necessary in some studies to provide closer representation of the actual corneal behaviour [202, 240, 241].

By far most of finite element models were developed with applications in refractive surgery, among which LASIK and SMILE procedures are of great interest in this thesis. Deenadayalu, et al developed a 3D whole-eye finite element model to study the refractive change caused by the creation of LASIK flap [200]. They considered the hinged flap as a crack on the anterior surface of the cornea; spring elements were used to model the interaction between the flap and the residual stromal bed. Corneal thickness reduction caused by laser ablation however was not addressed. Roy, et al also developed a whole-eye LASIK model but it was in 2D [202]. The biomechanical behaviour of the cornea after reducing its thickness was studied. In their model, the LASIK flap was modelled hingeless and connected to the residual stromal bed but assigned softer material properties compared to the stroma. The ablation profile which determines the corneal thickness reduction was computed by the classic Munnerlyn formula [188]. Roy and Dupps created a patient-specific model using clinical measured corneal topography and used an inverse analysis approach to estimate the overall elastic reduction of the postoperative cornea by varying corneal elastic properties in their models and matching the simulated and clinical outcomes [203]. An enhanced ablation profile [192] was adopted while the cut of flap was neglected. The same group recently conducted numerical studies comparing the

LASIK and SMILE procedures, suggesting SMILE was generally safer for laser correction [206]. A thin wound healing layer was considered to connect the LASIK flap or SMILE cap to the residual stroma. Although the models adopted in vivo topography, clinical validation of these models were not provided.

Tonometry is an important procedure to estimate the intraocular pressure (IOP) and the instrument used to do so is known as a tonometer [242, 243]. There are now a handful of commercially available tonometers such as Goldmann tonometer (GAT), dynamic contour tonometry (DCT), ocular response analyser (ORA) and most recently Corvis ST (CVS), among which GAT is currently the gold standard for IOP measurement [244-247]. A common principle of these tonometers is to apply static (GAT, DCT) or dynamic (ORA, CVS) pressure onto the cornea and use the deforming information of the cornea to estimate the IOP. Factors such as corneal thickness, corneal curvature and age were reported to influence the accuracy of the estimates by various tonometers [248, 249]. Finite element models were thus employed to study the influence of these factors and correct the formula of various tonometers that convert information of corneal deformation to IOP reading [199, 220, 250, 251]. One remarkable example is the numerical study conducted by Elsheikh, et al [252], who developed a correction equation for GAT which was demonstrated to be superior over some earlier correction equations [253]. Similar numerical study was recently done by Joda, et al to develop correction equation for the very new CVS [254].

The IOP measurements of eyes after various refractive surgeries were reported, by many clinical studies, to be significantly smaller than the preoperative readings [255-259]. This is believed to be caused by the reduced corneal thickness and altered overall corneal stiffness which changes the deformation behaviour of the postoperative cornea. Till now,

finite element modelling of tonometry applied on eyes after refractive surgery such as LASIK and SMILE is lacking.

## **2.7 CONCLUDING REMARKS**

The human eye is a complex organ and biologic system with fluid perpetually flowing inside to create intraocular pressure and maintain its geometry that is precisely shaped to focus light. It is also a fine and adaptive dynamic system, which automatically adjusts the size of the pupil according to the light intensity and tunes the shape of the crystalline lens to refine the angles of light rays that have been refracted by the cornea. As the front components of the eye, the transparent cornea contributes about 70% of the entire ocular refractive power. This fact has made the cornea the most focused research object.

Unfortunately, as any real system does, the ocular optic system often has imperfections. One of them is wavefront aberration, which prevents the light rays from being focused sharply on the retina. The low order aberrations such as myopia, hyperopia and astigmatism were realised centuries ago, but it is only until recently that high order aberrations are investigated thanks to the advances in both optics and wavefront-sensing technology. To correct these optical aberrations, prescription glasses and contact lenses are commonly used. The existence and amount of the optical aberrations are determined by the shapes of optical components especially the cornea, which makes the imaging of corneal shape essential for diagnosis of refractive disorders and necessary for fitting of contact lenses.

Various videokeratography techniques and instruments are now available to reliably measure the corneal topography and thickness but the measurements are usually given in form of 3D point sets. Topography fitting are often needed to express these discrete point sets as analytical surfaces, among which the orthogonal Zernike polynomials have been

favoured by most researchers. However, notable number of research has suggested other polynomials for representing corneal topography for better performance and there are more candidates that have not been introduced into the ocular community.

Another problem in measuring corneal surface is that a single observation usually cannot cover the entire cornea accurately with the peripheral measurements being less reliable. A few studies have been published to overcome this problem by combining topographies that are collected from different viewpoints. The same cornea is measured several time but from different angles such that the obtained topographies, as a whole, can cover the whole cornea. An optimisation algorithm is typically needed to bring these topographies together but by far the existing methods proposed within the ocular community have had limited success. The approaches in image processing community however are promising.

A convenient corneal representation that covers the corneal surface adequately is desirable for building finite element models for corneal refractive surgery, a reliable substitution of glasses and contact lenses. Even though the concept of corneal refractive surgery was suggested more than a century ago, the outcomes of earlier procedures were not promising, largely due to the lack of understanding of corneal biomechanics. As the surgery involves cutting into the cornea, the corneal stiffness is weakened and the wound healing process will also gradually change the corneal stiffness. These factors have meant discrepancies between the expected and achieved outcomes. It is now obvious that planning of refractive surgery with consideration of corneal biomechanics is essential to achieve predictive surgical outcomes.

During the past three decades, finite element method has been used extensively to study the biomechanical behaviour of the cornea and its reaction to refractive surgery. Thanks to the advances in corneal topography and increased understanding of corneal

biomechanical properties, the finite element models nowadays can reflect corneal hyperelasticity, viscoelasticity and anisotropy, and reliably simulate surgical forms such as LASIK and SMILE. However, there are still research to be done to validate these models with clinical outcomes and extend them to study new problems that have been observed clinically such as reduction in IOP readings of eyes after refractive surgeries.

## **CHAPTER 3**

### **RESEARCH METHODOLOGY**

---

#### **3.1 INTRODUCTION**

This thesis is mainly concerned with reconstruction of corneal surface from topographic measurements and using the reconstructed representation to build patient-specific finite element (FE) models of LASIK and SMILE corneal refractive surgical procedures. In the reconstruction of corneal surface, focus is on topography fitting and analytical models to explicitly express the corneal surface. This is followed by a topography matching study that adopts and further develops methods that register and combine corneal topography maps collected from different viewpoints and covering the entire corneal surface. In last part of the study, on numerical simulation of corneal refractive surgery, an accurate way to simulate and predict the outcomes of the LASIK and SMILE is sought, which is employed later to study the influence of surgical procedures on tonometry. The methods for each of these three topics are highlighted in this chapter.

#### **3.2 TOPOGRAPHY FITTING**

The topography data exported from commonly used videokeratography instruments is typically expressed as  $x$ ,  $y$  and  $z$  coordinates of regularly-spaced discrete points on corneal surface as shown in Figure 3-1.

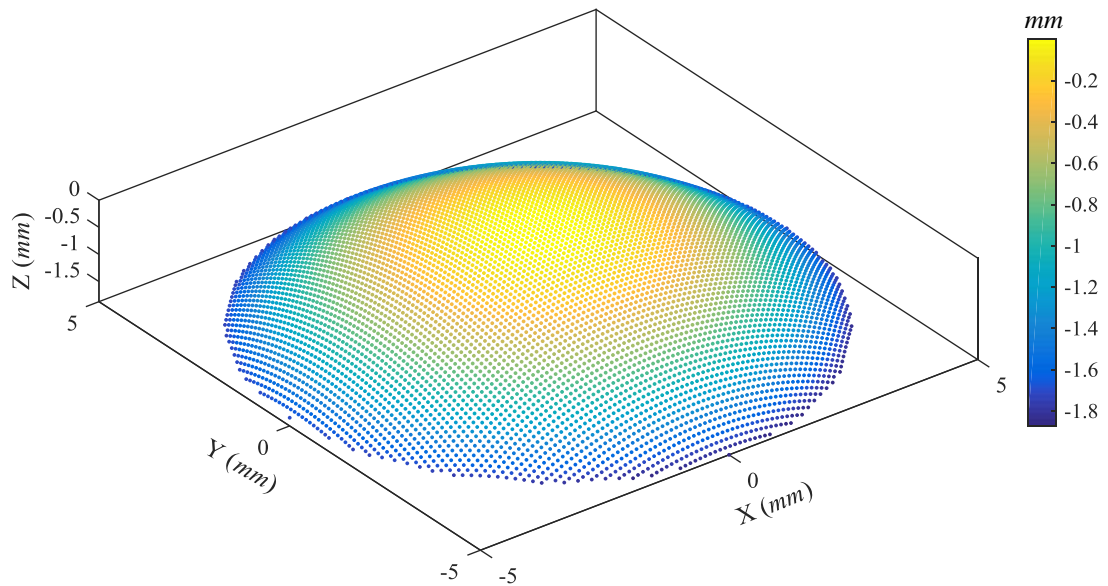


Figure 3-1. Typical corneal topography data plotted in 3D. Colours of individual points reflect their z coordinates.

The goal of topography fitting is to derive an expression  $z = Z(x, y)$  that represents the points set analytically such that the z value of any point on the surface can be determined by its x and y coordinates. This is typically done by fitting the points set to analytical models such as an ellipsoid or various sets of orthogonal polynomials. With the simple ellipsoid model being able to give a rough representation of corneal topography, it has limited ability to capture surface irregularity. Orthogonal polynomials on the other hand can be employed to fit complex shapes with high order modes. The set of orthogonal Zernike polynomials is one such family and it has been routinely used for reporting optical aberrations and representing corneal topography data. The set of orthogonal polynomials is said to be complete if it exactly represents arbitrary surface  $Z(x, y)$  such that

$$Z(x, y) = \sum_{p=1}^{\infty} a_p W_p(x, y) \quad (3.1)$$



where  $W_p(x, y)$  is the  $p$ th polynomial term with coefficients  $a_p$  indicating the contribution of each polynomial term to the whole surface. It should be noted that a complete set of orthogonal polynomials usually consists of infinite terms while in practice only a finite number of these terms are used and sufficient to fit  $Z(x, y)$  to an acceptable level of accuracy. Also, this finite number needs to be limited to avoid overfitting. As a result, if  $P$  polynomial terms are used, Equation (3.1) becomes

$$Z(x, y) = \sum_{p=1}^P a_p W_p(x, y) + \varepsilon(x, y) \quad (3.2)$$

where  $\varepsilon(x, y)$  is the truncation error. In this thesis, some of the popular orthogonal polynomials in ocular topography and image processing fields are studied and their abilities to fit corneal height data are assessed.

### 3.2.1 Orthogonal polynomials

There are numerous two-dimensional (2D) orthogonal polynomials defined in either rectangular or circular domains, with the former being defined in Cartesian coordinates and often obtained by production of one-dimensional (1D) polynomials along  $x$  and  $y$  axes, while the latter is defined in a polar system made of radial and angular components. The basics of the most commonly used orthogonal polynomials are highlighted in this section.

#### *Orthogonal polynomials in Cartesian coordinates*

Being constructed by 1D polynomials in two directions, the orthogonal 2D polynomials in Cartesian system usually have the form:

$$W_p(x, y) = R_n(x)R_m(y) \quad (3.3)$$

where  $n$  and  $m$  are the orders of 1D polynomials and  $p$  is the single-number index of the set of 2D polynomials, corresponding to each combination of  $n$  and  $m$ . In the current study, Legendre polynomials (LPs), Gegenbauer polynomials (GPs) and Gaussian-Hermite polynomials (GHPs) are considered in this category and their expressions are listed in Table 3-1. The orthogonality property of these polynomials follows:

$$\int_{\Omega} R_n(x)R_{n'}(x)w(x)dx = C_n\delta_{nm}, \quad (3.4)$$

where  $\int$  denotes integration,  $n$  and  $n'$  are the different orders of the polynomials,  $\delta_{nm}$  is the Kronecker symbol,  $C_n$  is the normalisation constant,  $w(x)$  is the weight function and  $\Omega$  is the domain for different polynomials (Table 3-1).

Table 3-1. Orthogonal polynomials in Cartesian system

	LPs	GPs	GHPs
$R_n(x)$	$\sum_{s=0}^n \frac{(-1)^{(n-s)/2}(n+s)!x^s}{2^n s! \left(\frac{n-s}{2}\right)! \left(\frac{n+s}{2}\right)!}$ , where $n-s = \text{even}$	$\sum_{s=0}^{\lfloor \frac{n}{2} \rfloor} \frac{(-1)^s \Gamma(n-s+\alpha) 2^{n-2s} x^{n-2s}}{s!(n-2s)! \Gamma(\alpha)}$ , $\alpha > -0.5$	$G_n \sum_{s=0}^{\lfloor \frac{n}{2} \rfloor} \frac{(-1)^s n! 2^{n-2s}}{s!(n-2s)!} \left(\frac{x}{\sigma}\right)^{n-2s} e^{-\frac{x^2}{2\sigma^2}}$ , $G_n = \frac{1}{\sqrt{2^n n! \sigma \sqrt{\pi}}}$ , and $\sigma > 0$
$C_n$	$\frac{1}{(2n+1)}$	$\frac{2\pi \Gamma(n+2\alpha)}{2^{2\alpha} n!(n+\alpha)[\Gamma(\alpha)]^2}$	1
$w(x)$	1	$(1-x^2)^{\alpha-0.5}$	1
$\Omega$	$[-1,1]$	$[-1,1]$	$[-\infty, \infty]$
$P$	$\frac{(n+1)(n+2)}{2}$	$\frac{(n+1)(n+2)}{2}$	$\frac{(n+1)(n+2)}{2}$

Both GPs and GHPs have scaling factors, being  $\alpha$  and  $\sigma$ , respectively, which change the polynomials from local to global features and vice versa. The effect of these scaling factors on the shapes of GPs and GHPs are shown in Figure 3-2 and Figure 3-3. The change between local and global features are more obvious for GHPs but this is dimmed for GPs because the big change in magnitude. In Figure 3-4, the 1D GPs of order 4 with

different scaling factor values are normalised by their maximal magnitudes (shown in Figure 3-2) to make the scaling effect prominent. It should be noted that the set of LPs is a special case of GPs when  $\alpha = 0.5$ . The shapes of the low order 2D Legendre polynomials are shown in Figure 3-5. The single-number index  $p$  in Equation (3.3) counts from the first row in Figure 3-5 and from left to right at each row.

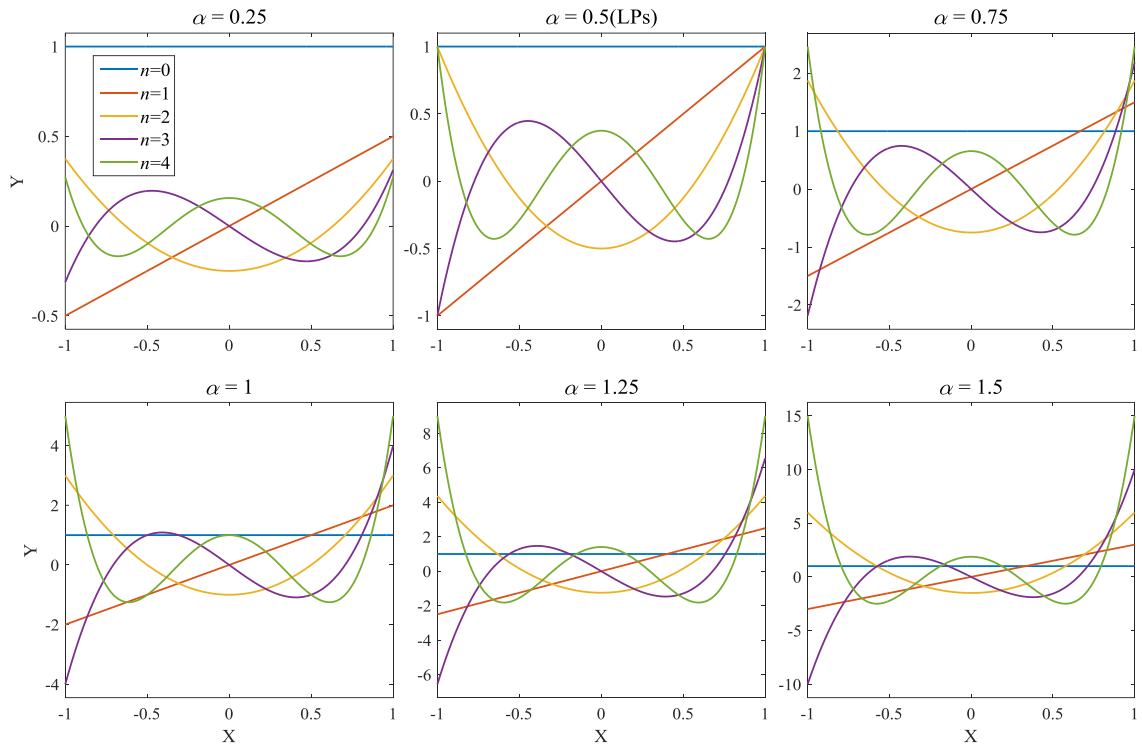


Figure 3-2. Shapes of the 1D Gegenbauer polynomials up to order 4

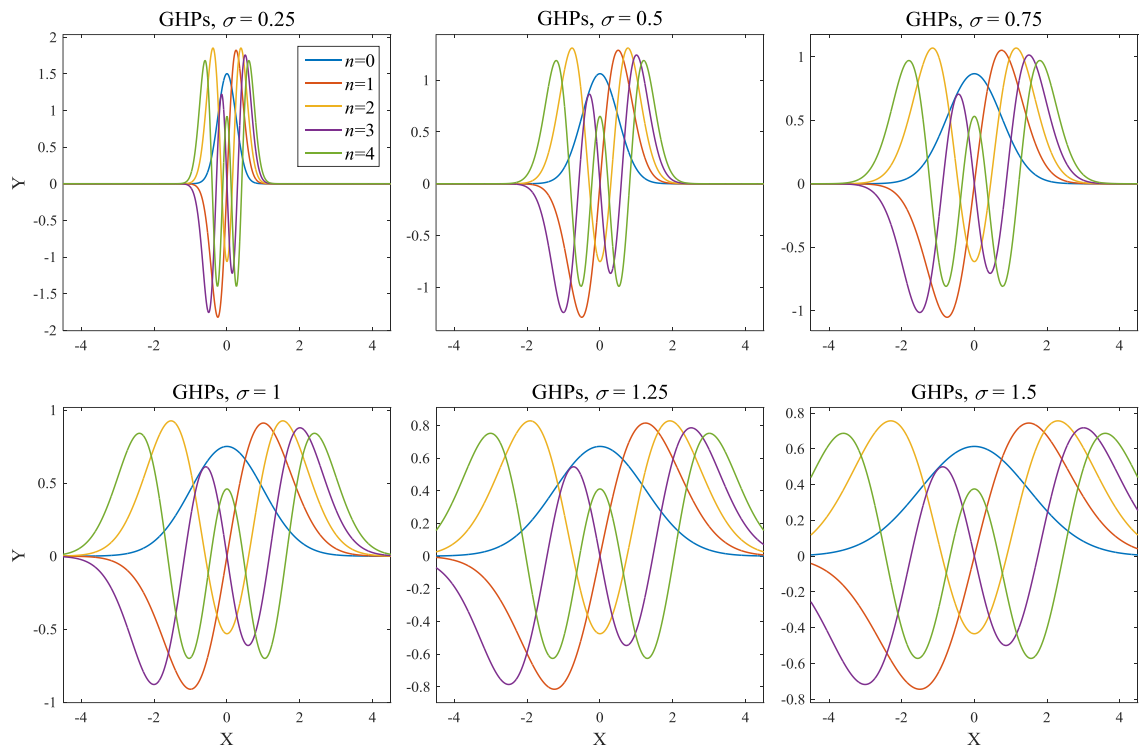


Figure 3-3. Shapes of the 1D Gaussian-Hermite polynomials up to order 4

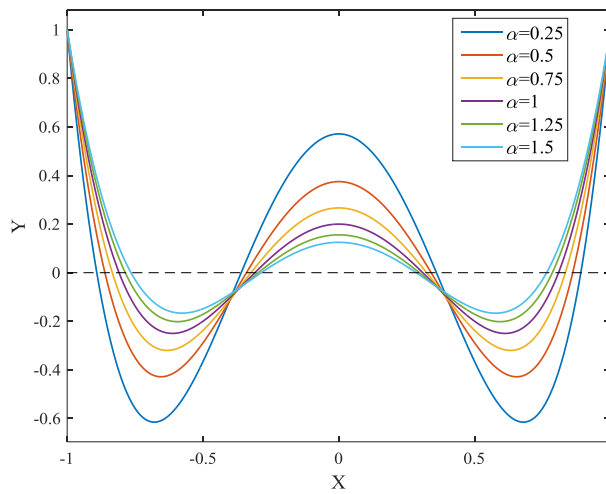


Figure 3-4. Effect of scaling factor on the shape of 1D Gegenbauer polynomials. The curves are for order 4 and they are normalised by their maximal values as shown in Figure 3-2

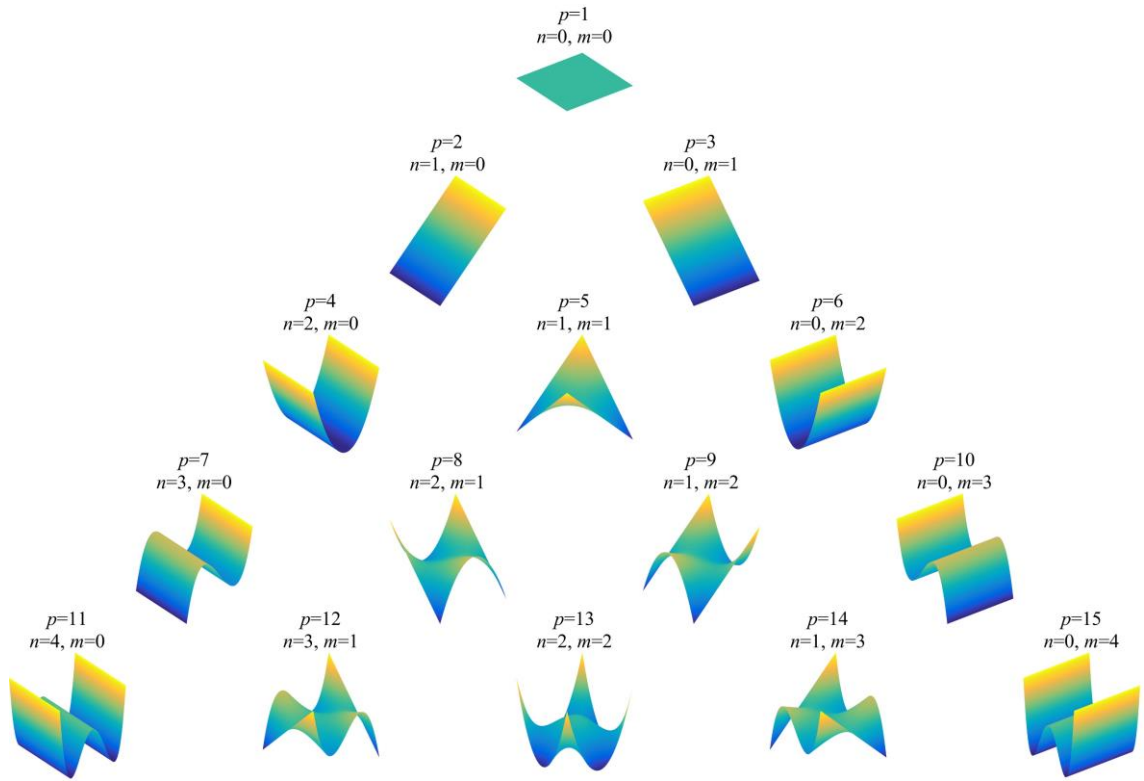


Figure 3-5. Shapes of Legendre polynomials up to order 4

### *Orthogonal polynomials in polar coordinates*

The well-known Zernike polynomials and the closely related pseudo-Zernike polynomials are orthogonal on the unit circle. These two-dimensional polynomials, now expressed in polar form  $W_p(r, \theta)$ , are formed by radial polynomials and angular trigonometric functions:

$$W_p(r, \theta) = \begin{cases} R_n^m(r) \cos(m\theta), & m > 0 \\ R_n^m(r) \sin(|m|\theta), & m < 0 \\ R_n^m(r), & m = 0 \end{cases} \quad (3.5)$$

where  $R_n^m(r)$  is the radial polynomial with order  $n$  ( $n = 0, 1, 2, \dots$ ) and angular frequency  $m$ . The angular components are either sine or cosine functions determined by the sign of  $m$ . For each  $n$ ,  $m$  may have multiple values as given in Table 3-2 and each combination of  $n$  and  $m$  determines a polynomial mode. Similarly, rather than indexing by  $n$  and  $m$ ,

these 2D modes can also be numbered by a single index  $p$ .  $W_p(r, \theta)$  is orthogonal on the unit circle due to the orthogonality of trigonometric functions on  $[0, 2\pi]$  as well as that of the radial polynomials on  $[0, 1]$  expressed as:

$$\int_0^1 R_n^m(r) R_n^m(r) r dr = C_n \delta_{mm}, \quad (3.6)$$

where there is no weight function compared to Equation (3.4).

Table 3-2. Orthogonal polynomials in Polar system with  $r \in [0, 1]$ . For OFMPs,  $m$  is not related to  $n$ .

	ZPs	PZPs	OFMPs
$R_n^m(r)$ or $R_n(r)$	$\sum_{s=0}^{\frac{n- m }{2}} \frac{(-1)^s (n-s)! r^{n-2s}}{s! \left(\frac{n+ m }{2} - s\right)! \left(\frac{n- m }{2} - s\right)!}$	$\sum_{s=0}^{n- m } \frac{(-1)^s (2n+1-s)! r^{n-s}}{s! (n+ m +1-s)! (n- m -s)!}$	$\sum_{s=0}^n \frac{(-1)^{n+s} (n+1+s)! r^s}{s! (n-s)! (s+1)!}$
$C_n$	$\frac{1}{(2n+1)}$	$\frac{1}{(2n+1)}$	$\frac{1}{(2n+1)}$
$m$ related to $n$	$ m  \leq n$ and $n -  m  = \text{even}$	$ m  \leq n$	/
$P$	$\frac{(n+1)(n+2)}{2}$	$(n+1)^2$	$(n+1)(2n+1)$

Also orthogonal on the unit circle are other polynomials such as Orthogonal Fourier-Mellin polynomials (OFMPs) which use radial polynomials that are independent with the frequency  $m$ . The advantage of OFMPs is that the frequency may have more values leading to more modes for a given order compared to Zernike and pseudo-Zernike polynomials. The two-dimensional form of OFMPs may be written as:

$$W_p(r, \theta) = \begin{cases} R_n(r) \cos(m\theta), & m > 0 \\ R_n(r) \sin(|m|\theta), & m < 0 \\ R_n(r), & m = 0 \end{cases} \quad (3.7)$$

and the orthogonality of radial polynomials changes to

$$\int_0^1 R_n(r)R_{n'}(r)rdr = C_n \delta_{nm} \quad (3.8)$$

In addition, Gegenbauer polynomials including their special case Legendre polynomials can be shifted by replacing  $x$  with  $2r-1$  such that they obey the same orthogonality property as in Equation (3.8) and thereby used as the radial kernels in Equation (3.7). The first few features of the conventional ZPs and the newer OFMPs are shown in Figure 3-6 and Figure 3-7. It is obvious that without the constrained relation between  $m$  and  $n$ , the OFMPs have significantly more terms for the same order. The rule of counting the single-number index  $p$  for ZPs and OFMPs are also illustrated in Figure 3-6 and Figure 3-7.

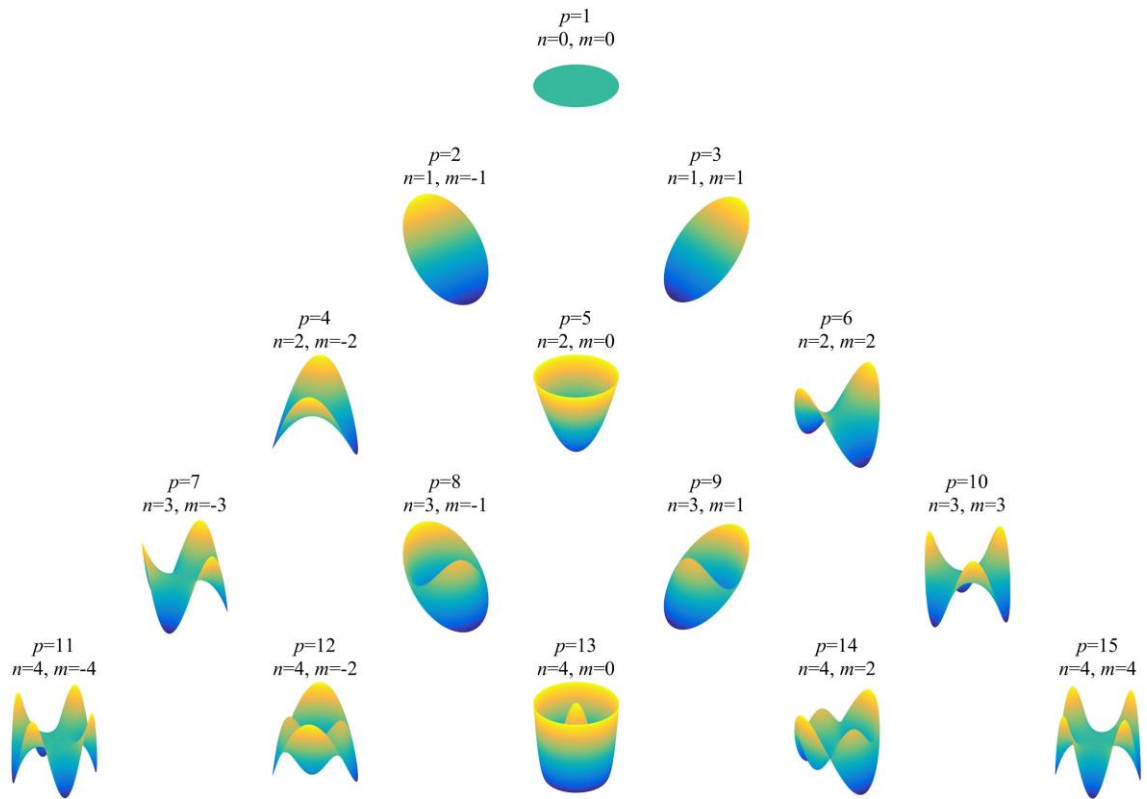


Figure 3-6. Shapes of ZPs up to order 4

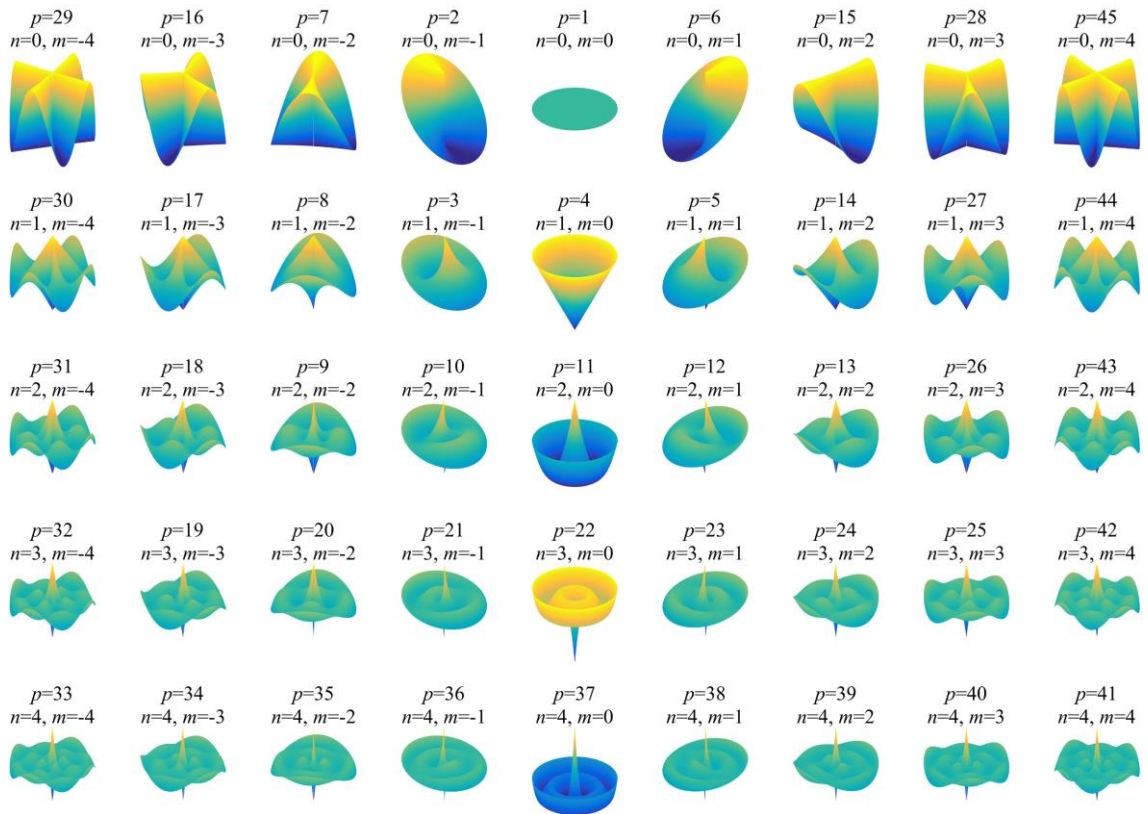


Figure 3-7. Shapes of OFMPs up to order 4

### 3.2.2 Computation of polynomial coefficients

The core step in fitting an arbitrary surface to a set of polynomials is the calculation of the coefficient value for each polynomial term. The methods for this calculation can be broken down into two categories using the orthogonality property, and the least squares estimation. It should be noted that a common process before the calculation of coefficients is to scale the topography into a unit circle or square to coincide with the domains of the orthogonal polynomials. This can be achieved by simply dividing the x and y coordinates of the data points with the maximal radius of the map.

#### *Orthogonal projection (OP)*

Using orthogonal polynomials to represent a target surface leads to minimal or no redundancy, also the independence among all the polynomial terms enables the coefficients to be evaluated separately and directly by projecting the surface awaiting for



decomposition onto each polynomial. Imagine that the target surface is represented as

$$Z(x, y) = \sum_{p'=1}^{\infty} a_{p'} W_{p'}(x, y), \text{ the projection of } Z(x, y) \text{ onto the } p\text{th Cartesian polynomial}$$

$W_p(x, y)$  will be

$$\iint_{\Psi} Z(x, y) W_p(x, y) w(x) w(y) dx dy \quad (3.9)$$

where  $\Psi$  is the 2D domain of  $W_p(x, y)$ , determined by  $\Omega$  which is the domain of the 1D polynomial.

By substituting  $Z(x, y)$  with  $\sum_{p'=1}^{\infty} a_{p'} W_{p'}(x, y)$ , Equation (3.9) becomes

$$\begin{aligned} & \iint_{\Psi} \left[ \sum_{p'=1}^{\infty} a_{p'} W_{p'}(x, y) \right] W_p(x, y) w(x) w(y) dx dy \\ &= \sum_{p'=1}^{\infty} a_{p'} \iint_{\Psi} W_{p'}(x, y) W_p(x, y) w(x) w(y) dx dy \end{aligned} \quad (3.10)$$

Considering the orthogonality of the polynomials,  $\iint_{\Psi} W_{p'}(x, y) W_p(x, y) w(x) w(y) dx dy$  is

zero when  $p' \neq p$  such that the summation in Equation (3.10) deduces

$$\begin{aligned} & \iint_{\Psi} Z(x, y) W_p(x, y) w(x) w(y) dx dy \\ &= a_p \iint_{\Psi} W_p(x, y) W_p(x, y) w(x) w(y) dx dy \\ &= a_p \int_{\Omega} R_n(x) R_n(x) w(x) dx \int_{\Omega} R_m(y) R_m(y) w(y) dy \\ &= a_p C_n C_m \end{aligned} \quad (3.11)$$

It is now obvious to derive the equation to compute the coefficient for the  $p$ th polynomial as follows:

$$a_p = \frac{1}{C_n C_m} \iint_{\Psi} Z(x, y) W_p(x, y) w(x) w(y) dx dy \quad (3.12)$$

Following similar derivation above, it is easy to obtain the following solution for polar cases

$$a_p = \begin{cases} \frac{1}{\pi C_n} \iint_{\Psi} Z(r, \theta) W_p(r, \theta) r dr d\theta, m \neq 0 \\ \frac{1}{2\pi C_n} \iint_{\Psi} Z(r, \theta) W_p(r, \theta) r dr d\theta, m = 0 \end{cases} \quad (3.13)$$

However, Equations (3.12) and (3.13) are hard to execute because the expression of  $Z(x, y)$  or  $Z(r, \theta)$  is unknown beforehand. This problem was discussed extensively in the image processing community when computing image moments [94, 99]. The easiest and most direct approach, sometimes called zeroth order approximation (ZOA) method, is to replace the double integral with double summation such that, for example, Equation (3.12) becomes

$$a_p = \frac{1}{C_n C_m} \sum_{d=1}^D \lambda_d Z(x_d, y_d) W_p(x_d, y_d) \quad (3.14)$$

where  $Z(x_d, y_d)$  refers to the  $d$ th pixel,  $\lambda_d$  is the finite area of the  $d$ th pixel and  $D$  is the number of valid pixels in this calculation. The weight functions have been omitted for simplicity. This solution is illustrated in Figure 3-8A, where the pixels of a square image are scaled and mapped to unit square ( $x \in [-1, 1]$  and  $y \in [-1, 1]$ ) and only those resulting pixels with middle points that lay inside the unit circle ( $r \in [-1, 1]$  and  $\theta \in [0, 2\pi]$ ) are kept. There are however pixels (dashed and with green middle points) that sit partly inside the unit circle, and empty areas usually exist where no pixel occupies (shown as colour-filled areas in Figure 3-8A). In this study, this problem is overcome by discarding incomplete

pixels and triangulating the empty areas after introducing new points on the edge of the unit circle as shown in Figure 3-8A. These new boundary points are necessary for the triangulation of empty regions and determined using existing x and y coordinates inside the unit circle. The calculations of terms in Equation (3.14) on the newly introduced triangles need height (z values) information at the triangle centres and this information is obtained by interpolation methods such as the Biharmonic Spline interpolation [260]. Consequently, the subscript  $d$  in Equation (3.14) now means the  $d$ th triangles or squares as shown in Figure 3-8A. It is worth noting that the point in the middle of each pixel corresponds to the discrete measurement point when corneal topography is concerned.

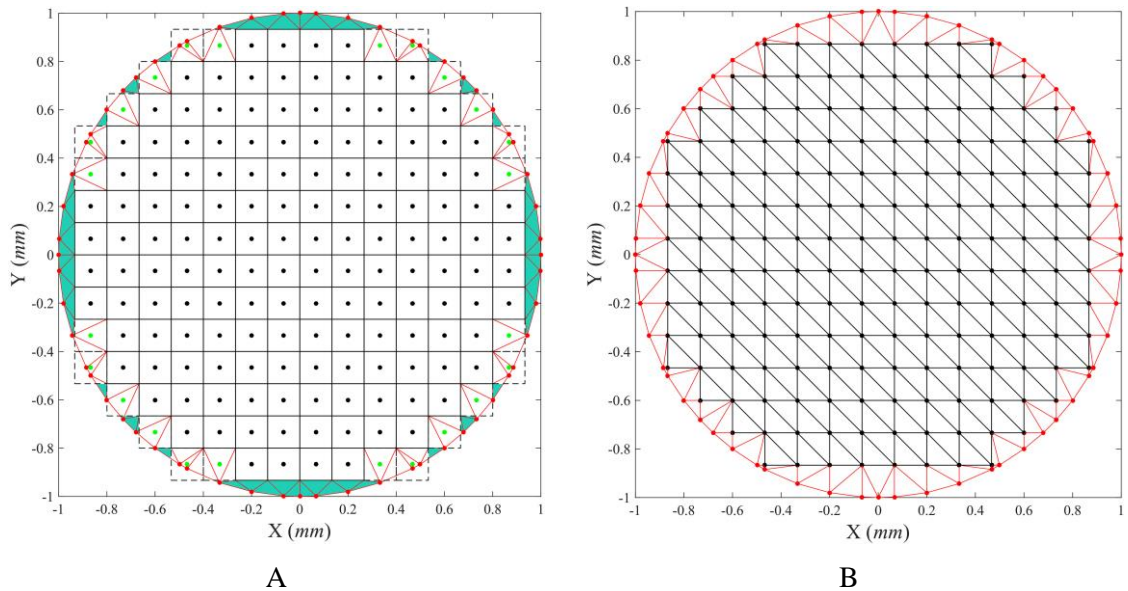


Figure 3-8. Discrete points/pixels and the squares and/or triangles representation of the unit circle

The ZOA method equivalently breaks the continuous polynomials into piecewise constant functions in the same fashion of the image that the polynomials have constant values within the finite area of the image pixels. It is expected that this method may not be accurate enough especially when the image size is small. An improved approach uses the same partition of the unit circle as the ZOA but avoids discretisation of polynomials by explicitly computing the double integral on each finite sub-domain of triangles or squares.

$$a_p = \frac{1}{C_n C_m} \sum_{d=1}^D Z(x_d, y_d) g_p(x_d, y_d), \text{ and} \quad (3.15)$$

$$g_p(x_d, y_d) = \iint_{\Psi_d} W_p(x, y) dx dy \quad (3.16)$$

where  $\Psi_d$  is the sub-domain occupied by the  $d$ th triangle or square, again the weight functions have been omitted. The image moments computed by Equation (3.15) are often called “Exact Moments”, so this second approach is called the exact moments (EM) method. The EM approach is naturally extended to an interpolation version (INT) where the image or surface  $Z$  is approximated as piecewise linear or higher order function based on its pixels/measurements [99]. Equation (3.12) is then broken into

$$a_p = \frac{1}{C_n C_m} \sum_{d=1}^D H_p(x_d, y_d), \text{ in which} \quad (3.17)$$

$$H_p(x_d, y_d) = \iint_{\Psi_d} Z_d(x, y) W_p(x, y) dx dy \quad (3.18)$$

where  $Z_d(x, y)$  is a linear or higher order 2D polynomials approximation of  $Z(x, y)$  on  $\Psi_d$ . Similarly but differently from the proposed version in Kotoulas, et al [99], the partition of the unit circle in Figure 3-8B is adopted in this study for INT method and  $Z(x, y)$  is approximated linearly. Using the original pixels/points and same boundary points in Figure 3-8A, the unit circle is triangulated and on each triangle the linear approximation  $Z_d(x, y) = E_d x + F_d y + G_d$  is achieved directly from the three vertices so that Equation (3.18) can be rewritten as:

$$H_p(x_d, y_d) = E_d e_p(x_d, y_d) + F_d f_p(x_d, y_d) + G_d g_p(x_d, y_d) \quad (3.19)$$

$$\text{where } e_p(x_d, y_d) = \iint_{\Psi_d} x W_p(x, y) dx dy, \quad (3.20)$$

$$f_p(x_d, y_d) = \iint_{\Psi_d} y W_p(x, y) dx dy \quad (3.21)$$

and  $g_p(x_d, y_d)$  is defined by Equation (3.16).

When the expressions in all the double integrals above are known, it is possible to derive the explicit solution of these integrals as proposed for example in Liao, et al for Zernike polynomials [261] and Hosny for Gaussian-Hermite polynomials [262]. In this paper however, for the sake of simplicity, the double integrals above are solved numerically by a MATLAB built-in function *quad2d* which involves vectorisation of the integrands [263], and indeed all methods mentioned in this study are implemented under MATAB environment (MATLAB, The MathWorks, Inc., Natick).

#### *Least squares estimation (LS)*

The topography reconstruction problem in Equation (3.2) may be also cast as an optimisation problem. Given that the measurements have  $D$  points, the  $d$ th measurement point follows

$$Z(x_d, y_d) = \sum_{p=1}^P a_p W_p(x_d, y_d) + \varepsilon_d \quad (3.22)$$

Considering all the  $D$  points, a linear equation system can be constructed and its matrix form is:

$$\mathbf{Z} = \mathbf{W}\mathbf{a} + \boldsymbol{\varepsilon} \quad (3.23)$$

where  $\mathbf{Z}$  is a  $D$ -element column vector consisting of all the measurements,  $\mathbf{W}$  is a  $D \times P$  matrix with each column having  $z$  values sampled from the continuous polynomials using the same  $x$  and  $y$  coordinates of the original measurements,  $\mathbf{a}$  is a  $P$ -element column vector of the polynomial coefficients, while the last term  $\boldsymbol{\varepsilon}$  is the error vector. The reconstruction problem reduces to finding the optimal  $\mathbf{a}$  such that the error vector  $\boldsymbol{\varepsilon}$  is minimised in a least-squares sense. Such least-squares solution can be achieved as:

$$\hat{\mathbf{a}} = (\mathbf{W}^T \mathbf{W})^{-1} \mathbf{W}^T \mathbf{Z} \quad (3.24)$$

### 3.2.3 Evaluation methods

In the current research, two methods are available to compute the coefficients of the polynomials; one benefits the orthogonality of the polynomials but needs additional approximations while the other regards the fitting as an optimisation problem and ignores the orthogonal properties of the polynomials. It is necessary to assess the flexibility and accuracy of these two methods and this can be done by fitting an analytically known surface to the set of polynomials and compare the obtained coefficients to the actual ones that are known beforehand.

Further for the actual corneal topographic maps, once the coefficients are obtained, the reconstructed surface can be computed using the same  $x$  and  $y$  coordinates of the original data points by

$$\hat{Z}(x, y) = \sum_{p=1}^P \hat{a}_p W_p(x, y) \quad (3.25)$$

The difference between the reconstructed and original maps can be quantified by the following root mean square error (RMSE)

$$e_r = \sqrt{\frac{\sum_{d=1}^D (\hat{Z}(x_d, y_d) - Z(x_d, y_d))^2}{D}} \quad (3.26)$$

and this error is called reconstruction error.

Considering the main purpose of topography fitting is to estimate locations on the cornea that are not measured, the reliability of various orthogonal polynomials in predicting the unmeasured locations must be assessed. In practice, the reconstruction of the map can be done using only part of the points in the original map, leading to an explicit expression as given by Equation (3.25). This expression can be subsequently used to predict the locations of the rest of the original points by substituting their x and y coordinates into Equation (3.25). The RMSE computed using these predicted points and their original correspondences is thus called prediction error which quantifies the prediction reliability of the polynomials.

The combination of reconstruction and prediction errors is not only useful to assess the abilities of various orthogonal polynomials, but also necessary to monitor the potential risk of overfitting. The results for this topic are presented in Chapter 4 and discussed in Chapter 7.

### 3.3 TOPOGRAPHY MATCHING

The topography fitting seeks an analytical representation of the discrete topography data. The achieved representation enables convenient application such as interpolating locations that are not measured. Nevertheless this representation usually covers small areas of the cornea. Fortunately, although a single observation cannot reliably cover the entire cornea, the surface can be measured in parts, commonly resulting in central and peripheral maps. In this study, datasets are taken from three patients using the Medmont

E300, a Placido-based machine, with multiple central and peripheral maps measured in each case. The central map is observed from the front when the patient looks at a centred target, and the peripheral maps (superior, inferior, temporal, nasal) are captured by directing the patient to decentred targets, while ensuring sufficient overlap with the central map.

The central and peripheral maps, although overlapping, are in different coordinate systems, making their combination impossible without additional manipulation, which is known as registration where a spatial transformation is found by matching the overlapping region of the central and peripheral maps. An example of this process is illustrated in Figure 3-9. The central map in red and the peripheral map in blue, while in their own coordinate system, both have limited coverage and exhibit similar shapes and orientations before any matching is applied. By considering the coordinate system of central map as a world coordinate system, a spatial transformation  $\mathbf{T}$  of the peripheral map is sought such that once the peripheral map is moved by this transformation the difference in shape with the central map within the overlapping area is minimised. The portion of the peripheral map that is not overlapping with the central map therefore enlarges the coverage of the measurements.

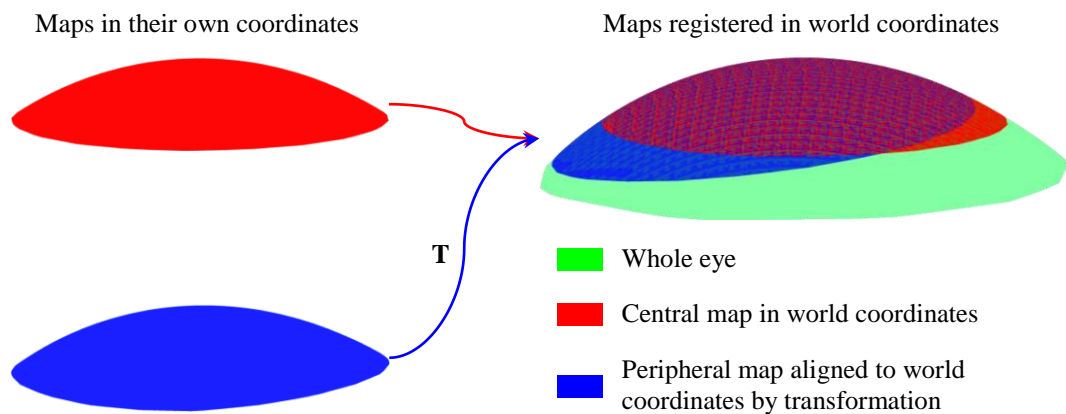


Figure 3-9. Schematic diagram of topography registration



In this thesis the ICP algorithm, familiar in the image processing community, is combined with the truncated Zernike polynomial series representation of corneal topography. The suitability of this approach for the problem of matching partial views of corneal topography is then assessed. The extension of this process to multi-view registration is also explored. The next section begins with a statement of the topography registration problem and includes theoretical principles of several variants of the ICP technique, including closest-point, point-to-point and point-to-plane routines. The extension from ICP algorithm to multi-view registration is explained in the last part of this section.

### 3.3.1 Problem statement

The registration problem is to find the coordinate transformation  $(\mathbf{R}, \mathbf{t})$  that matches two surfaces,  $\mathbf{Q}$  and  $\mathbf{P}$  (also known as height or elevation maps), each defined by discrete sets of data points  $(\mathbf{q}_i \in \mathbf{Q}; i = 1, 2, \dots, n)$  and  $(\mathbf{p}_j \in \mathbf{P}; j = 1, 2, \dots, m)$  with  $n$  and  $m$  being the numbers of points of  $\mathbf{Q}$  and  $\mathbf{P}$ , respectively. If the surface  $\mathbf{Q}$  is static (red surface in Figure 3-9), then the dynamic surface  $\mathbf{P}$  (blue surface in Figure 3-9) must undergo an extrinsic rotation  $\mathbf{R}$  about the origin of the fixed coordinate system and translation  $\mathbf{t}$  in order to achieve the required registration. Thus,

$$\bar{\mathbf{p}}_j = \mathbf{R}\mathbf{p}_j + \mathbf{t} \quad (3.27)$$

where the overbar denotes the transformed data points in terms of coordinates  $x, y, z$  and all data points  $j = 1, 2, \dots, m$  are required to undergo the same transformation. The rotation matrix is given by,

$$\mathbf{R} = \mathbf{R}_z \mathbf{R}_y \mathbf{R}_x \quad (3.28)$$

where,

$$\begin{aligned}
\mathbf{R}_x &= \begin{bmatrix} 1 & 0 & 0 \\ 0 & \cos\vartheta_x & -\sin\vartheta_x \\ 0 & \sin\vartheta_x & \cos\vartheta_x \end{bmatrix}, \\
\mathbf{R}_y &= \begin{bmatrix} \cos\vartheta_y & 0 & \sin\vartheta_y \\ 0 & 1 & 0 \\ -\sin\vartheta_y & 0 & \cos\vartheta_y \end{bmatrix}, \\
\mathbf{R}_z &= \begin{bmatrix} \cos\vartheta_z & -\sin\vartheta_z & 0 \\ \sin\vartheta_z & \cos\vartheta_z & 0 \\ 0 & 0 & 1 \end{bmatrix}
\end{aligned} \tag{3.29}$$

$\vartheta_x, \vartheta_y, \vartheta_z$  are Tait-Bryan angles and the translation vector is:

$$\mathbf{t} = (t_x \ t_y \ t_z)^T \tag{3.30}$$

where “ $T$ ” denotes matrix transposition.

It can be seen that the process of registration becomes that of determining  $\mathbf{r} = (\vartheta_x \ \vartheta_y \ \vartheta_z \ t_x \ t_y \ t_z)^T$ , which is generally straightforward if there is a unique correspondence between every  $\mathbf{q}_i$  and  $\mathbf{p}_j$ , such that

$$\mathbf{q}_i = \mathbf{R}\mathbf{p}_j + \mathbf{t} \tag{3.31}$$

is satisfied exactly.

The difficulty is that although the two surfaces are identical in their overlapping area, except for the required unknown transformation, the points  $\mathbf{q}_i$  and  $\mathbf{p}_j$  generally occupy different locations on the surfaces and, in the case of corneal topography the two surfaces in question are overlapping views of the same surface observed from different viewpoints.

The problem of lack of correspondence may be addressed by representing the target (static) surface as a continuous function. One such approach, as studied in the topography fitting

section, is the sequence of 2D Zernike polynomials. Thus the third coordinate  $z$  is given by a linear combination of Zernike polynomials such that the static surface is analytically expressed as

$$\mathbf{Q}(x, y) = \sum_{p=1}^P a_p Z_p(x, y) \quad (3.32)$$

where  $Z_p(x, y)$  is the  $p$ th Zernike polynomial and  $a_p$  is the coefficient that depends upon the surface to be represented.

Having defined the continuous static surface  $\mathbf{Q}(x, y)$  the points  $\mathbf{q}_i$  are unknown. There are a number of possible strategies for determining such points. These include: (a) the Closest Point (CP) approach; and (b) various ‘shooting’ methods whereby a ray is projected in a predetermined direction (usually vertical or normal to dynamic surface points  $\mathbf{p}_j$ ) to intersect the static surface  $\mathbf{Q}(x, y)$  thereby defining the points  $\mathbf{q}_i$ . The simplest approach is Vertical Shooting (VS), whereby every point  $\mathbf{q}_i$  is determined immediately from the  $x, y$  coordinates of each corresponding point  $\mathbf{p}_j$ , i.e.  $\mathbf{q}_i = \mathbf{Q}(x_j, y_j)$ . The Normal Shooting (NS) approach requires an iterative solution for the determination of the  $\mathbf{q}_i$ . Park and Subbarao [264] proposed a technique based on multiple applications of vertical shooting and backward projection onto the normal, known as the Contractive Projection Point (CPP) method. Determining the closest point to  $\mathbf{p}_j$  on  $\mathbf{Q}(x, y)$  is a nonlinear problem related to the number of terms in the Zernike representation (3.32). An alternative is to find the Closest Discrete Point (CDP), which relies entirely on the measured data without interpolation by the truncated series of Zernike polynomials.

The three methods of correspondence mapping are illustrated in Figure 3-10 where the surfaces are registered but vertical distances are magnified for the purposes of explaining the different techniques. During CDP mapping, every dynamic point is paired with a closest static point, however those pairs containing points on the boundary of static surface should be rejected [265], because, as shown in Figure 3-10, such pairs will force the dynamic surface to be erroneously dragged to the left and vertically upwards. Also, for the two shooting strategies, there will be dynamic points that cannot be paired with any points on the static surface because no intersections can be found for points that lie outside the overlapping region.

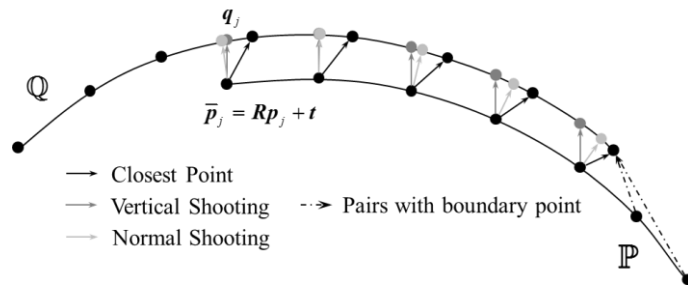


Figure 3-10. Three forms of correspondence mapping showing in the cross-section views of the surfaces

The task of determining  $\mathbf{r} = (\mathcal{G}_x \ \mathcal{G}_y \ \mathcal{G}_z \ t_x \ t_y \ t_z)^T$  may be cast as a nonlinear optimisation problem:

$$\min_r \left( \sum_{j=1}^m \|\mathbf{R}\mathbf{p}_j + \mathbf{t} - \mathbf{q}_j\|^2 \right), \quad (3.33)$$

where the subscript  $j$ , now on both  $\mathbf{q}_j$  and  $\mathbf{p}_j$ , denotes a corresponding pair. There are two main problems in this optimisation. On one hand, only if the correct transformation  $(\mathbf{R}, \mathbf{t})$  is provided can the ideal corresponding points  $\mathbf{q}_j$  be located by any of the three mapping strategies. On the other hand,  $\mathbf{q}_j$  is necessary for the minimisation (3.33) to seek

the desirable transformation. There are two main optimisation approaches, the Direct Search (DS) method and the Iterative Corresponding Point (ICP) algorithm.

### 3.3.2 Direct search (DS) method

The minimisation (3.33) may be achieved by a direct search, similar to that proposed by Lau, et al. [111]. It demands a search of the six-dimensional space of the rigid-body

transformation of the dynamic surface until  $\sum_{j=1}^m \|\mathbf{R}\mathbf{p}_j + \mathbf{t} - \mathbf{q}_j\|^2 \leq \text{tol}$ , where ‘tol’ denotes

an acceptably small tolerance. There are quite a few optimisation algorithms that can be employed to do this minimisation. For instance, this can be achieved by the widely-used Nelder-Mead (NM) simplex algorithm [266, 267], which uses only the values of the function without numerical or analytic gradients. Other more enhanced options such as Quasi-Newton Method, and the Sequential Quadratic Programming (SQP) algorithm [268] will be discussed in the final chapter of this thesis (Chapter 7).

### 3.3.3 Iterative closest point (ICP) algorithm

There are two versions of the ICP algorithm, the point-to-point and the point-to-plane forms. The point-to-point algorithm does not require an initial estimate of the unknown rotation and translation  $(\mathbf{R}, \mathbf{t})$  whereas the point-to-plane approach allows greater flexibility by letting the two surfaces slide over each other.

#### *Point-to-point error metric*

Point-to-point ICP solutions have been proposed based on singular value decomposition (SVD) [269], unit quaternions [270], orthonormal matrices [271], and dual quaternions [272]. Eggert et al. [273] provided a comparison of these essentially similar techniques, including an evaluation of numerical accuracy and robustness, and concluded that the

difference between them was small. The SVD-based solution is described in this study, based on the singular value decomposition of the cross-covariance matrix of the two point sets. By referring the points of correspondence to the centroids of the two surfaces it is found that determination of the rotation matrix can be separated from the translation, which is determined in a second calculation after the rotation matrix has been found.

Let the centroids of the static and the dynamic maps at the  $\ell$ th iteration be defined as  $\mathbf{q}_{c,\ell}$  and  $\mathbf{p}_{c,\ell}$  respectively,

$$\mathbf{q}_{c,\ell} = \frac{1}{m} \sum_{j=1}^m \mathbf{q}_{j,\ell} \quad \text{and} \quad \mathbf{p}_{c,\ell} = \frac{1}{m} \sum_{j=1}^m \mathbf{p}_j \quad (3.34)$$

then the location of other points relative to the centroids are given by,

$$\tilde{\mathbf{q}}_{j,\ell} = \mathbf{q}_{j,\ell} - \mathbf{q}_{c,\ell} \quad \text{and} \quad \tilde{\mathbf{p}}_j = \mathbf{p}_j - \mathbf{p}_{c,\ell} \quad (3.35)$$

and the displacement of the centroid of the transformed dynamic map from the centroid of the static map is,

$$\tilde{\mathbf{t}}_\ell = \mathbf{R}_\ell \mathbf{p}_{c,\ell} + \mathbf{t}_\ell - \mathbf{q}_{c,\ell} \quad (3.36)$$

Successive substitution of equations (3.35) and (3.36) into equation (3.33) then leads to the definition of an objective function,

$$\begin{aligned} f_\ell(\mathbf{R}_\ell, \mathbf{t}_\ell) &= \sum_{j=1}^m \left\| \mathbf{R}_\ell (\tilde{\mathbf{p}}_j + \mathbf{p}_{c,\ell}) + \mathbf{t}_\ell - (\tilde{\mathbf{q}}_{j,\ell} + \mathbf{q}_{c,\ell}) \right\|^2 \\ &= \sum_{j=1}^m \left\| (\mathbf{R}_\ell \tilde{\mathbf{p}}_j - \tilde{\mathbf{q}}_{j,\ell}) + \tilde{\mathbf{t}}_\ell \right\|^2 \\ &= \sum_{j=1}^m \left\| \mathbf{R}_\ell \tilde{\mathbf{p}}_j - \tilde{\mathbf{q}}_{j,\ell} \right\|^2 + 2\tilde{\mathbf{t}}_\ell \sum_{j=1}^m (\mathbf{R}_\ell \tilde{\mathbf{p}}_j - \tilde{\mathbf{q}}_{j,\ell}) + m \left\| \tilde{\mathbf{t}}_\ell \right\|^2 \end{aligned} \quad (3.37)$$

It can be seen that the second right-hand term of equation (3.37) is zero because both  $\sum_{j=1}^m \tilde{\mathbf{p}}_j = 0$  and  $\sum_{j=1}^m \tilde{\mathbf{q}}_{j,\ell} = 0$ . The third term is nonnegative, so in order to minimise equation (13),  $\tilde{\mathbf{t}}_\ell$  should vanish, which means the centroids of the transformed dynamic map and static map would be identical. The problem now reduces to the minimisation of the first term to obtain the rotation,

$$\tilde{f}_\ell(\mathbf{R}_\ell) = \sum_{j=1}^m \|\mathbf{R}_\ell \tilde{\mathbf{p}}_j - \tilde{\mathbf{q}}_{j,\ell}\|^2 \quad (3.38)$$

The optimal rotation matrix  $\mathbf{R}_\ell$  can be formed by the components of the SVD of the cross-covariance matrix of the two point sets [269, 274]:

$$\sum_{j=1}^m \tilde{\mathbf{p}}_j \tilde{\mathbf{q}}_{j,\ell}^T = \mathbf{U} \mathbf{\Lambda} \mathbf{V}^T \quad (3.39)$$

and the optimal rotation may be expressed in the form of an orthonormal matrix (Arun et al. [269]),

$$\mathbf{R}_\ell = \mathbf{V} \mathbf{U}^T \quad (3.40)$$

However,  $\det(\mathbf{V} \mathbf{U}^T) = -1$ , denotes a reflection rather than rotation, a problem that was overcome by Umeyama [274] who added a correction term,

$$\mathbf{R}_\ell = \mathbf{V} \mathbf{S} \mathbf{U}^T; \quad \mathbf{S} = \text{diag}(1, 1, \dots, 1, \det(\mathbf{V} \mathbf{U}^T)) \quad (3.41)$$

so that  $\det(\mathbf{R}_\ell) = 1$ . Once the rotation matrix is obtained, the translation vector can be computed by setting  $\tilde{\mathbf{t}}_\ell = 0$  in equation (3.36), which leads to

$$\mathbf{t}_\ell = \mathbf{q}_{c,\ell} - \mathbf{R}_\ell \mathbf{p}_{c,\ell} \quad (3.42)$$

*Point-to-plane error metric.*

The point-to-plane error metric minimises the projection of  $\mathbf{R}\mathbf{p}_j + \mathbf{t} - \mathbf{q}_j$  onto the unit normal vector  $\mathbf{n}_j$  (normal to the static surface at point  $\mathbf{q}_j$ ). Should  $\mathbf{n}_j^T (\mathbf{R}\mathbf{p}_j + \mathbf{t} - \mathbf{q}_j) = 0$ , there will be no projection of  $\mathbf{R}\mathbf{p}_j + \mathbf{t} - \mathbf{q}_j$  onto the normal, which indicates that  $\mathbf{p}_j$  lies at a tangent to the static surface at point  $\mathbf{q}_j$ . In this way the surfaces are permitted to slide over each other.

Unlike the point-to-point metric, a starting estimate is necessary and an optimisation approach may be applied as:

$$\min_{\mathbf{r}} \left( \sum_{j=1}^m \left\| \mathbf{n}_j^T (\mathbf{R}\mathbf{p}_j + \mathbf{t} - \mathbf{q}_j) \right\|^2 \right) \quad (3.43)$$

and implemented using the Levenberg-Marquardt (LM) algorithm, which provides an iterative solution, already shown to have high accuracy in solving ICP point-to-plane error metrics [275].

However, an alternative is available that has been shown to be robust to variability in starting values, does not depend upon optimisation, but approaches the solution iteratively using linearisation in the vicinity of an initial estimate  $\mathbf{r}_0 = (\mathcal{g}_x \ \mathcal{g}_y \ \mathcal{g}_z \ t_x \ t_y \ t_z)_0^T$  [117].

The rotation matrices  $\mathbf{R}_x$ ,  $\mathbf{R}_y$  and  $\mathbf{R}_z$  defined previously by equation (3.29) become,

$$\mathbf{R}_x = \begin{bmatrix} 1 & 0 & 0 \\ 0 & 1 & -\mathcal{g}_x \\ 0 & \mathcal{g}_x & 1 \end{bmatrix}, \mathbf{R}_y = \begin{bmatrix} 1 & 0 & \mathcal{g}_y \\ 0 & 1 & 0 \\ -\mathcal{g}_y & 0 & 1 \end{bmatrix}, \mathbf{R}_z = \begin{bmatrix} 1 & -\mathcal{g}_z & 0 \\ \mathcal{g}_z & 1 & 0 \\ 0 & 0 & 1 \end{bmatrix} \quad (3.44)$$

so



$$\mathbf{R} = \mathbf{R}_z \mathbf{R}_y \mathbf{R}_x = \begin{bmatrix} 1 & -\mathcal{G}_z & \mathcal{G}_y \\ \mathcal{G}_z & 1 & -\mathcal{G}_x \\ -\mathcal{G}_y & \mathcal{G}_x & 1 \end{bmatrix} \quad (3.45)$$

and at the  $\ell$ th iteration,

$$\mathbf{R}_\ell = \mathbf{R}_{\ell-1} + \Delta \mathbf{R}_\ell \mathbf{R}_{\ell-1}, \text{ where } \Delta \mathbf{R}_\ell = \begin{bmatrix} 0 & -\Delta \mathcal{G}_z & \Delta \mathcal{G}_y \\ \Delta \mathcal{G}_z & 0 & -\Delta \mathcal{G}_x \\ -\Delta \mathcal{G}_y & \Delta \mathcal{G}_x & 0 \end{bmatrix}_\ell \quad (3.46)$$

and,

$$\mathbf{t}_\ell = \mathbf{t}_{\ell-1} + \Delta \mathbf{R}_\ell \mathbf{t}_{\ell-1} + \Delta \mathbf{t}_\ell, \text{ where } \Delta \mathbf{t}_\ell = \begin{pmatrix} \Delta t_x & \Delta t_y & \Delta t_z \end{pmatrix}_\ell^T \quad (3.47)$$

An objective function may be written as:

$$f_\ell(\Delta \mathbf{R}_\ell, \Delta \mathbf{t}_\ell) = \sum_{j=1}^m \left\| \mathbf{n}_\ell^T \left( (\mathbf{I} + \Delta \mathbf{R}_\ell) \mathbf{p}_{j,\ell-1} + \Delta \mathbf{t}_\ell - \mathbf{q}_j \right) \right\|^2 \quad (3.48)$$

and re-cast in the form,

$$f_\ell(\Delta \mathbf{r}_\ell) = \sum \left\| \begin{pmatrix} (p_y n_z - p_z n_y) \\ (p_z n_x - p_x n_z) \\ (p_x n_y - p_y n_x) \\ n_x \\ n_y \\ n_z \end{pmatrix}^T \begin{pmatrix} \Delta \mathcal{G}_x \\ \Delta \mathcal{G}_y \\ \Delta \mathcal{G}_z \\ \Delta t_x \\ \Delta t_y \\ \Delta t_z \end{pmatrix} + (n_x \ n_y \ n_z) \begin{pmatrix} p_x - q_x \\ p_y - q_y \\ p_z - q_z \end{pmatrix} \right\|^2 \quad (3.49)$$

where the subscripts  $j$  and  $\ell$  (on the right hand side) have been omitted for simplicity.

Then re-writing in compact form, equation (3.49) becomes:

$$f_\ell(\Delta \mathbf{r}_\ell) = \sum \left\| \mathbf{a}^T \Delta \mathbf{r}_\ell + \mathbf{n}_\ell^T (\mathbf{p}_\ell - \mathbf{q}) \right\|^2 \quad (3.50)$$

and  $\Delta \mathbf{r}_\ell$  may be determined by least-squares approximation,

$$\Delta \mathbf{r}_\ell = \left( \sum \mathbf{a} \mathbf{a}^T \right)^{-1} \left( \sum \mathbf{a} (\mathbf{n}^T (\mathbf{p}_\ell - \mathbf{q})) \right) \quad (3.51)$$

### 3.3.4 DS vs. ICP

The DS objective function is highly nonlinear and involves a local search in the region of the initial values  $\mathbf{r}_0 = (\mathcal{G}_x \ \mathcal{G}_y \ \mathcal{G}_z \ t_x \ t_y \ t_z)_0^T$  using the Nelder-Mead algorithm. The point-to-point ICP algorithm does not require an initial estimate  $\mathbf{R}_0, \mathbf{t}_0$  and there is no requirement for linearisation, as with the point-to-plane ICP approach. The point-to-plane ICP algorithm is the most flexible technique because the dynamic and static surfaces are permitted to slide over each other. This overcomes the ‘hard’ convergence properties of the DS algorithm. However, the point-to-plane method is linearised about the initial values and therefore a reasonably accurate initial approximation is required. There is no guarantee of convergence with the DS or ICP routines and a global minimum may not be found. Nevertheless, the ICP method remains very robust and quite insensitive to initial values as will be demonstrated in Chapter 5.

### 3.3.5 Multi-view registration

The DS method and the ICP algorithm described above are only concerned with a pair of surfaces. When multiple peripheral topographies are collected to ensure sufficient coverage of the cornea, they are registered to the central topography one by one. This piece-wise manner of registration, however, may introduce inconsistencies among the peripheral topographies when they are brought into registration. On the other hand, these inconsistencies may be useful to further refine the positions of peripheral topographies. The multi-view registration developed in this study aims to address this problem, using a

multi-view extension of the point-to-plane ICP variant proposed by Neugebauer [123].

This method is henceforth called the MICP algorithm.

The error metric for the MICP algorithm is enlarged to include distances between dynamic map and static map, and among the dynamic maps. For description convenience, the error metric enclosed in Equation (3.43), which considers only a pair of maps, is now called the dynamic-to-static part and denoted  $f_u$ . For each dynamic map, similarly with minimisation (3.43),  $f_u$  may be expressed as:

$$f_u(\mathbf{R}_u, \mathbf{t}_u) = \sum_{j=1}^{m_u} \left\| \mathbf{n}_j^T (\mathbf{R}_u \mathbf{p}_{u,j} + \mathbf{t}_u - \mathbf{q}_j) \right\|^2 \quad (3.52)$$

where  $\mathbf{p}_{u,j}$  is the  $j$ th point on the  $u$ th dynamic map, which has  $m_u$  points. In addition, for each pair of dynamic maps, a dynamic-to-dynamic part  $f_{uv}$  is added and given as

$$f_{uv}(\mathbf{R}_u, \mathbf{t}_u, \mathbf{R}_v, \mathbf{t}_v) = \sum_{j=1}^{m_u} \left\| (\mathbf{R}_v \mathbf{n}_{v,j})^T [(\mathbf{R}_u \mathbf{p}_{u,j} + \mathbf{t}_u) - (\mathbf{R}_v \mathbf{p}_{v,j} + \mathbf{t}_v)] \right\|^2 \quad (3.53)$$

where  $\mathbf{n}_{v,j}$  is the surface normal at dynamic point  $\mathbf{p}_{v,j}$ . The error metric of MICP now becomes:

$$f(\mathbf{R}_1, \mathbf{t}_1, \dots, \mathbf{R}_U, \mathbf{t}_U) = \sum_{u=1}^U \left( f_u + \sum_{v \neq u} f_{uv} \right) \quad (3.54)$$

in which  $U$  is the number of dynamic maps. The optimisation problem is now enlarged to deal with more variables

$$\min_{\mathbf{r}} \sum_{u=1}^U \left( f_u + \sum_{v \neq u} f_{uv} \right) \quad (3.55)$$

where  $\mathbf{r} = (\mathbf{r}_1, \dots, \mathbf{r}_u, \dots, \mathbf{r}_U)^T$  with  $\mathbf{r}_u = (\mathcal{G}_{u,x} \ \mathcal{G}_{u,y} \ \mathcal{G}_{u,z} \ t_{u,x} \ t_{u,y} \ t_{u,z})^T$ .

Compared with Equation (3.43), Equation (3.55) is harder to solve theoretically because even after linearisation, Equation (3.53) has high order terms that are impossible to be segregated. However, when the transformation is small, dropping high order terms may be feasible. After replacing the rotation matrices with their linearised correspondences and omitting the high order terms afterwards, Equations (3.52) and (3.53) become:

$$f_u(\mathbf{r}_u) = \sum_{j=1}^{m_u} \left\| \hat{\mathbf{M}}_{u,j}^T \mathbf{r}_u + \mathbf{N}_{u,j} \right\|^2 \quad (3.56)$$

$$f_{uv}(\mathbf{r}_u, \mathbf{r}_v) = \sum_{j=1}^{m_{uv}} \left\| \hat{\mathbf{W}}_{uv,j}^T \mathbf{r}_u - \hat{\mathbf{W}}_{uv,j}^T \mathbf{r}_v + \mathbf{V}_{uv,j} \right\|^2 \quad (3.57)$$

with

$$\hat{\mathbf{M}}_{u,j} = \begin{pmatrix} \mathbf{p}_{u,j} \times \mathbf{n}_j \\ \mathbf{n}_j \end{pmatrix}, \text{ and } \hat{\mathbf{W}}_{uv,j} = \begin{pmatrix} \mathbf{p}_{u,j} \times \mathbf{n}_{v,j} \\ \mathbf{n}_{v,j} \end{pmatrix} \quad (3.58)$$

and

$$\mathbf{N}_{u,j} = \mathbf{n}_j^T (\mathbf{p}_{u,j} - \mathbf{q}_j), \text{ and } \mathbf{V}_{uv,j} = \mathbf{n}_{v,j}^T (\mathbf{p}_{u,j} - \mathbf{p}_{v,j}) \quad (3.59)$$

By adopting the following assembly

$$\mathbf{M}_{u,j} = \begin{pmatrix} 0 \\ \vdots \\ 0 \\ \hat{\mathbf{M}}_{u,j} \\ 0 \\ \vdots \\ 0 \end{pmatrix} \left. \begin{array}{l} \left. \vphantom{\hat{\mathbf{M}}_{u,j}} \right\} 6u-5 \\ \left. \vphantom{\hat{\mathbf{M}}_{u,j}} \right\} 6u \end{array} \right\} , \text{ and } \mathbf{W}_{uv,j} = \begin{pmatrix} 0 \\ \vdots \\ 0 \\ \hat{\mathbf{W}}_{uv,j} \\ 0 \\ \vdots \\ 0 \end{pmatrix} \left. \begin{array}{l} \left. \vphantom{\hat{\mathbf{W}}_{uv,j}} \right\} 6u-5 \\ \left. \vphantom{\hat{\mathbf{W}}_{uv,j}} \right\} 6u \end{array} \right\} - \begin{pmatrix} 0 \\ \vdots \\ 0 \\ \hat{\mathbf{W}}_{uv,j} \\ 0 \\ \vdots \\ 0 \end{pmatrix} \left. \begin{array}{l} \left. \vphantom{\hat{\mathbf{W}}_{uv,j}} \right\} 6v-5 \\ \left. \vphantom{\hat{\mathbf{W}}_{uv,j}} \right\} 6v \end{array} \right\} \quad (3.60)$$

Equations (3.56) and (3.57) become:

$$f_u(\mathbf{r}_u) = \sum_{j=1}^{m_u} \|\mathbf{M}_{u,j}^T \mathbf{r} + \mathbf{N}_{u,j}\|^2 \quad (3.61)$$

$$f_{uv}(\mathbf{r}_u, \mathbf{r}_v) = \sum_{j=1}^{m_u} \|\mathbf{W}_{uv,j}^T \mathbf{r} + \mathbf{V}_{uv,j}\|^2 \quad (3.62)$$

with  $\mathbf{r}$ , as given earlier, being a vector that contains all the transformation parameters of peripheral maps. It is now possible to deduce the solution of minimisation (3.55) as:

$$\mathbf{r} = - \left( \sum_{u=1}^U \sum_{v \neq u} \sum_{j=1}^{m_u} \mathbf{W}_{uv,j} \mathbf{W}_{uv,j}^T + \sum_{u=1}^U \sum_{j=1}^{m_u} \mathbf{M}_{u,j} \mathbf{M}_{u,j}^T \right)^{-1} \cdots \quad (3.63)$$

$$\left( \sum_{u=1}^U \sum_{v \neq u} \sum_{j=1}^{m_u} \mathbf{W}_{uv,j} \mathbf{V}_{uv,j} + \sum_{u=1}^U \sum_{j=1}^{m_u} \mathbf{M}_{u,j} \mathbf{N}_{u,j} \right)$$

It should be noted that both linearisation and omission of high order terms are applied to derive the solution (3.63), and this may be impractical and even problematic in certain circumstance. Instead of the above derivation, Equation (3.55) can be directly solved by using Levenberg-Marquardt algorithm and this has been shown to be efficient [123].

The MICP approach can include the relative information among all maps, but as the objective function becomes much more complex, the convergence of the algorithm may

be much slower than the pair-wise version. The slower solution process may benefit from an acceleration method first proposed by Besl et al. [118] based on line search theory, which extrapolates the next iteration by monitoring the movement of the algorithm in the solution space. To apply this method, the progress of the ICP algorithm or now the MICP algorithm may be considered as a journey in the transformation space. Letting  $\mathbf{r}_\ell$  denotes the total transformation vector at the  $\ell$ th iteration; one may define the change in the current iteration from the previous one as:

$$\Delta_\ell = \mathbf{r}_\ell - \mathbf{r}_{\ell-1} \quad (3.64)$$

$\Delta_\ell$  basically indicates in which direction the algorithm is moving. The angle between the last two directions is:

$$\varphi_\ell = \cos^{-1} \left( \frac{\Delta_\ell \cdot \Delta_{\ell-1}}{\|\Delta_\ell\| \|\Delta_{\ell-1}\|} \right) \quad (3.65)$$

The idea behind extrapolation is that if the algorithm has moved in almost the same direction during the last few iterations, as is the case when both  $\varphi_\ell$  and  $\varphi_{\ell-1}$  are sufficiently small (e.g.  $10^\circ$ ), it may move in this direction further. Instead of solving a minimisation, an increment  $\nu$  may be obtained based on the behaviour of the previous several movements, which is used to update the current transformation [118]:

$$\mathbf{r}_{\ell+1} = \mathbf{r}_\ell + \nu \frac{\Delta_\ell}{\|\Delta_\ell\|} \quad (3.66)$$

The detailed method to obtain this increment is omitted here and referred to [118], and the potential of this accelerating method is presented in Chapter 5.

### 3.4 NUMERICAL SIMULATION OF REFRACTIVE SURGERY

The topography reconstruction studies presented above aim to provide a convenient surface representation, which is important for the creation of patient-specific numerical models of refractive surgeries, where corneal topography for each eye is used to determine the geometry of the finite element model. 60 sets of data have been collected from 30 patients who have undergone LASIK surgery for myopic correction at Wenzhou Medical University, China. The patients include 15 male and 15 female aged from 21 to 41 years ( $27.44 \pm 4.88$ ). The collected data include corneal anterior and posterior topographies, corneal thickness maps, axial length and IOP measurements taken before and after the surgical procedure. The corneal topographies and thickness maps are provided by Pentacam topographer, the axial lengths are measured by an A-scan ultrasound device (Compuscan UAB 1000; Storz Inc., St. Louis, MO, USA), and the IOP values are measured with a dynamic contour tonometer (DCT; SMT Swiss Microtechnology AG, Switzerland). Information on the size and depth of the flap and the depth of removed tissue by laser ablation is also obtained from the laser instrument manufacturer, allowing the development of finite element (FE) modelling of the surgical procedure.

The simulation process is divided into several steps. First, an idealised model composed of the cornea, limbus and sclera is generated using average ocular dimensions. Second, clinical data representing the geometry of each eye is used to build an eye-specific model. This is done by changing the coordinates of nodes in the idealised model to meet the patient-specific data including corneal topographies and thickness and ocular axial length. Zernike polynomials are employed to fit the topography and thickness maps and to enable simple integration with the rest of the idealised model. A stress-free configuration step is then carried out to obtain a relaxed model corresponding to the state of the eye with zero

intraocular pressure (IOP). The removal of tissue as would be done in the refractive surgery by laser ablation is then simulated and finally the resulting model is inflated by full IOP to achieve the simulated postoperative eye.

The software package used in the FE analysis was Abaqus (Abaqus, SIMULIA, Dassault Systèmes), which is well-known for its stable nonlinear analyses. However the models are not generated in the Abaqus environment. In this study, a Visual Basic (VB) programme, based on the modelling strategies in [110], was written to construct the idealised model and the manipulation of the models to fit clinical data was conducted in MATLAB. This latter step includes fitting of clinical data, building clinical models, navigating the Abaqus FE analysis, and conducting post-processing tasks.

### **3.4.1 Model construction**

#### *Geometry and mesh*

The idealised model generated by the VB programme is shown in Figure 3-11. The shape of the cornea is determined by its anterior surface, central corneal thickness (CCT) and peripheral corneal thickness (PCT). The anterior corneal topography is represented by an ellipsoid that is flatter in the periphery and the corneal thickness at any location is linearly interpolated based on CCT and PCT. The sclera on the other hand has a spherical external shape. Based on an earlier experimental evidence, the scleral thickness is made equal to PCT at the limbus, decreasing to 0.8PCT at the equator, then increasing to 1.2PCT at the posterior scleral pole [276].

The model is meshed using 15-noded solid elements (C3D15H) arranged in rings across the ocular surface and in layers across the thickness. The C3D15H element is a second-order (quadratic) triangular prism with nodes both at the corners and in the middle of each edge. The boundary conditions of the model are set as follows; the polar nodes along the



z axis are restrained against displacement in the x and y directions, while the equatorial nodes are prevented from movement in the z direction. To prevent the model from rigid-body rotation around the z axis, the equatorial nodes in the x-z plane are fixed in the y direction as well.

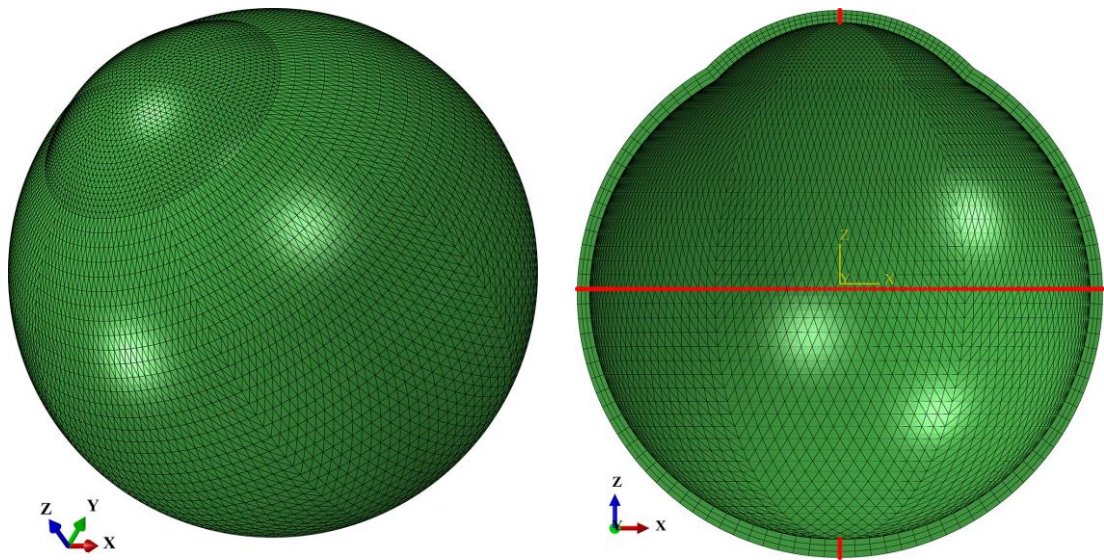


Figure 3-11. An idealised model generated by the VB programme. The model is rotationally symmetric. The right figure shows a cross section of the model where the coordinate system is plotted in yellow. The equatorial and polar nodes are marked as red points. In this idealised model, 25 and 45 rings are used in the cornea and the sclera, respectively; the corneal and scleral thickness is broken into 3 layers, resulting in 44100 elements.

Based on the mesh structure of the idealised model and using the same coordinates system and boundary conditions, the patient-specific model adopts the clinical measurements by only changing the coordinates of nodes. This involves modifying corneal shape to fit patient-specific measurements and stretching the sclera to suit the clinical axial length. The anterior corneal topography and the corneal thickness map for each eye are fitted to Zernike polynomials up to order 10, which allows easy calculation of node coordinates at any location and the corresponding thickness. The coverage of the topography and thickness map however is limited. The reliable measurements usually only adequately cover the central 8mm region in diameter and unfortunately in this study, multiple measurements of peripheral topography maps were not available, making topography

matching impractical. This situation has meant extrapolation in both anterior topography and thickness map were needed. Further, the Zernike expression, once obtained, is only useful to predict locations that are located inside its orthogonal radius and any extrapolation outside such radius will be problematic.

To solve the extrapolation problem for the anterior corneal topography, the best ellipsoid is found for each topography in addition to its Zernike expression, this best-fit ellipsoid has relatively worse representation of the clinical measurements but is ideal for extrapolation purpose. In the final method as shown in Figure 3-12, the central 8mm region adopts the Zernike expression, and the region outside 10mm reaching to the limbus is predicted based on the best fit ellipsoid, a transition region from 8mm to 10mm is used to smoothly connect these two regions.

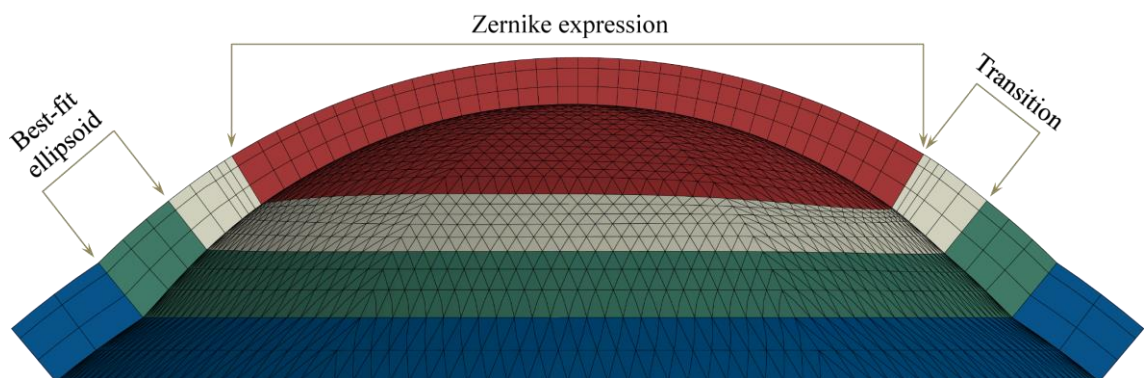


Figure 3-12. Schematic method of adopting clinical corneal topography and thickness

For the thickness map, the above technique of combining Zernike expression and best-fit ellipsoid equation is not suitable because an ellipsoid is too simple to represent the corneal thickness distribution. Instead, the extrapolation in corneal thickness is conducted as follows. First, the peripheral corneal thickness of the limbal ring is predicted by linear extrapolation of the available thickness measurements. Because of the asymmetric shape of the clinical thickness map, these extrapolated thickness values will be different. In the current study, their mean value has been adopted as a single value of PCT for the sake of

simplicity. The corneal thickness that is outside the Zernike expression radius is then interpolated linearly based on the available clinical data inside the Zernike radius and the predicted PCT at the limbal ring.

Once the nodes of anterior corneal surface and their associated thickness values are determined, the posterior nodes can be obtained by applying the thickness along the directions of surface normals, which are determined either by the Zernike expression or finite difference method. The next step is to stretch the sclera to meet the actual axial length for each eye and this is done by simply changing the vertical coordinates of the scleral nodes. The change in geometry from the idealised model to a patient-specific model is illustrated in Figure 3-13.

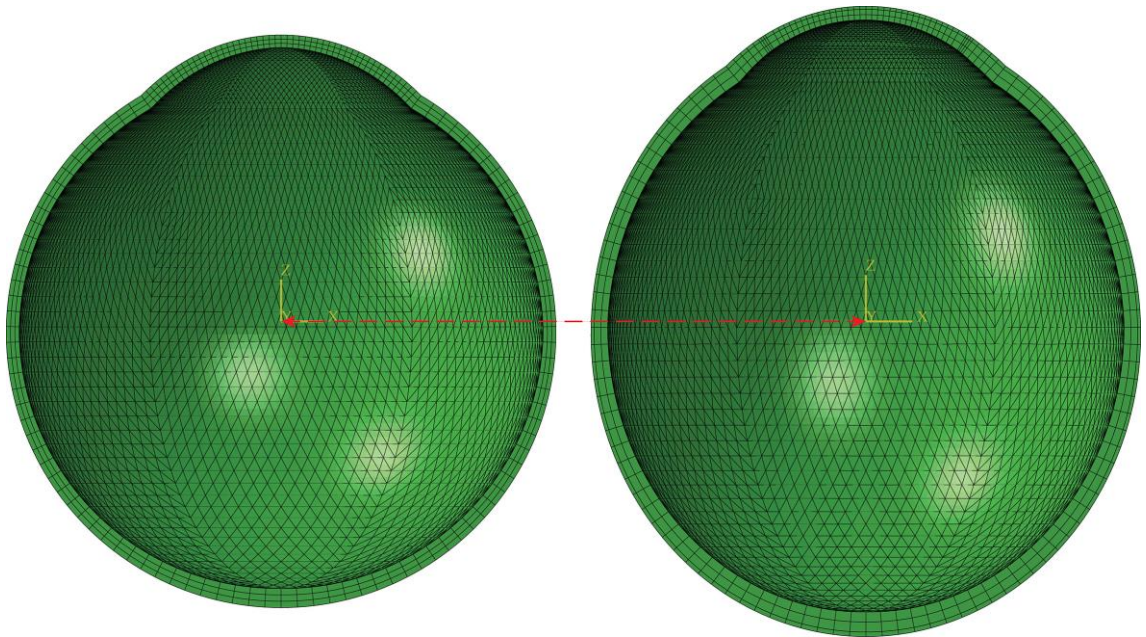


Figure 3-13. The change in geometry from the idealised model to a typical patient-specific model after adopting clinical data including corneal topography, corneal thickness map and axial length

### *Regional material properties*

The model incorporates an isotropic Ogden material model [277] that represents the hyperelastic and incompressible nature of the cornea and sclera:

$$U = \sum_{i=1}^N \frac{2\mu_i}{\alpha_i^2} (\bar{\lambda}_1^{\alpha_i} + \bar{\lambda}_2^{\alpha_i} + \bar{\lambda}_3^{\alpha_i} - 3) + \sum_{i=1}^N \frac{1}{D_i} (J_{el} - 1)^{2i} \quad (3.67)$$

where  $U$  is the strain energy potential,  $\bar{\lambda}_i = J^{-\frac{1}{3}}\lambda_i$  with  $J$  being the total volume strain and  $\lambda_i$  being the principal stretch,  $\mu_i, \alpha_i$  and  $D_i$  are material constants and the  $D_i$  values determine the compressibility of the material, which are chosen as zeros in this study to account for the nearly incompressibility of the cornea and sclera. The material parameters  $\mu_i, \alpha_i$  have been obtained through an inverse modelling exercise based on experimental data for the cornea [64] and the sclera [276] of age 50. In these inverse modelling exercises, representative numerical models of the cornea and sclera are built. For each model, an optimisation process is carried out to find the optimal material parameters that lead to the best fit between the output from the numerical model and the experimental data, e.g. load-deformation curve [278]. The optimisation problem in the inverse modelling is solved by a combination of customised Python codes and the optimisation software HEEDS (Red Cedar Technology, Michigan, USA).

The cornea has a single material definition while the sclera is divided into three regions as shown in Figure 3-14. In addition, the material properties of the limbus are kept the same as the anterior sclera.

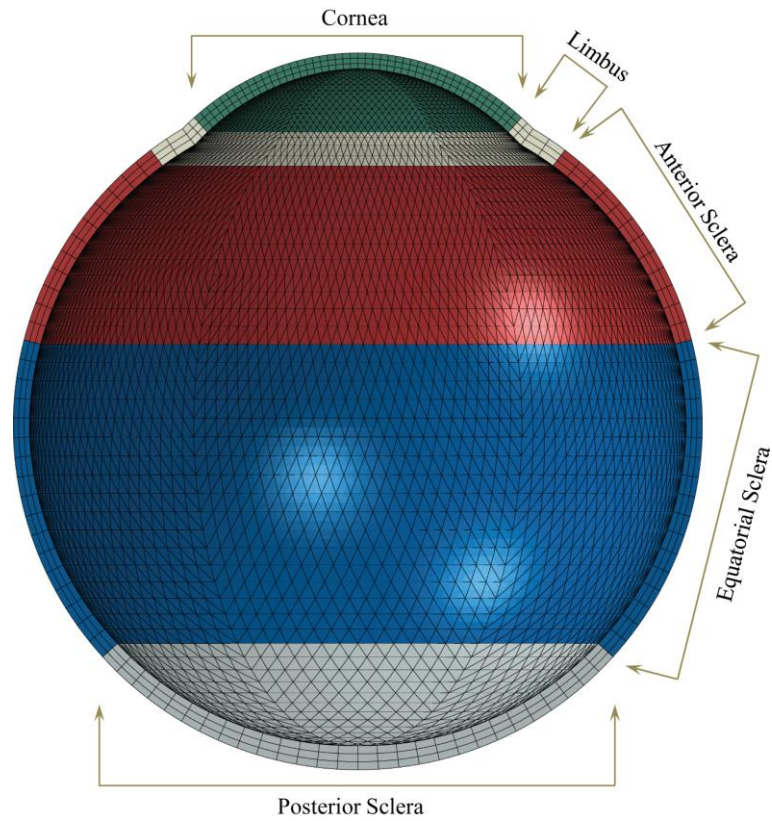


Figure 3-14. A cross-sectional view of the eye model showing the regions with specific material properties

The material parameters for all regions are given in Table 3-3. The cornea is softer than the sclera and the stiffness of the sclera decreases from the anterior to the posterior region. Reference can be made to Figure 3-15, which shows the stress-strain relations for the cornea and sclera under uniaxial loading based on the  $\mu$  and  $\alpha$  values given in Table 3-3.

Table 3-3. First order Ogden parameters of different regions of the eye

Regions	Material parameters	
	$\mu_1$	$\alpha_1$
Cornea	0.0541000	110.4
Anterior sclera	0.2709105	150.0
Equatorial sclera	0.1806070	150.0
Posterior sclera	0.1332790	150.0

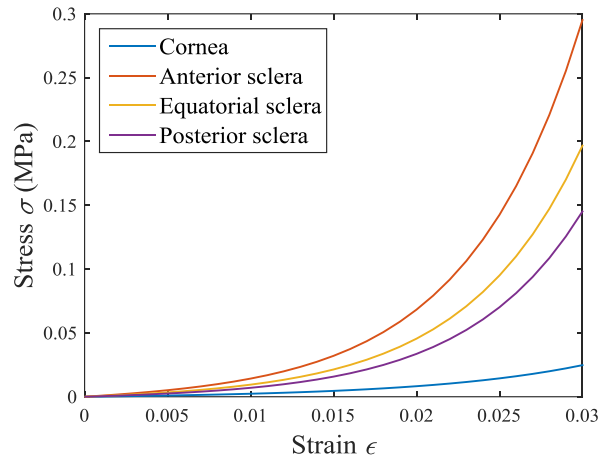


Figure 3-15. Stress-strain curves for the cornea and sclera

The epithelial layer of the corneal is much softer than the stroma and thus contribute little to the overall corneal stiffness [279], this fact is taken into account in the model by creating a superficial thin layer which is 50  $\mu\text{m}$  in thickness and has 10% of the cornea stiffness ( $10\% \mu_1$ ). The enhanced model with a separate layer representing the epithelium is shown in Figure 3-16.

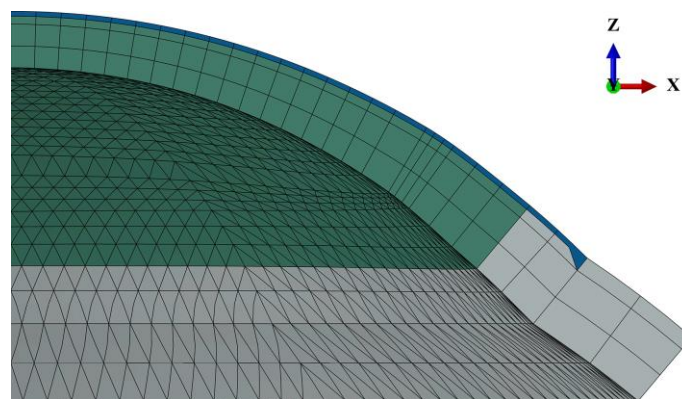


Figure 3-16. Model with an epithelial layer in blue

### 3.4.2 Stress free configuration

The patient-specific model at this point has adopted the clinical geometry, which has been measured in vivo in a stressed condition under IOP. This has meant there is a need to derive the stress-free configuration of the model which exhibits geometry with zero IOP. In this study, an efficient iterative approach proposed by Pandolfi and Holzapfel [238] is

used and this approach has been shown to be sufficiently accurate in [280]. If the initial model with measured (stressed) shape has nodal coordinates  $\mathbf{X}_0$ , the target of the stress-free configuration is to find a model with nodal coordinates  $\mathbf{X}$  which would match with  $\mathbf{X}_0$  after undergoing nodal displacements  $\mathbf{u}$  caused by the application of IOP, that is

$$\mathbf{X}_0 = \mathbf{x} = \mathbf{X} + \mathbf{u} \quad (3.68)$$

The unknown configuration  $\mathbf{X}$  is found iteratively (Figure 3-18), where the procedure begins by applying the IOP to the initial model with  $\mathbf{X}_0$  coordinates using non-linear finite element analysis and this leads to the nodal displacements  $\mathbf{u}_0$ , which is used to compute the first estimate of  $\mathbf{X}$  as

$$\mathbf{X}_1 = \mathbf{X}_0 - \mathbf{u}_0 \quad (3.69)$$

Now imagine a strip model that has a linear material behaviour, the subtraction in Equation (3.69) will derive its exact stress-free configuration as shown in Figure 3-17. Nevertheless, the same is not true for a model with hyperelastic material definition as in the current study. The consequence is that if the IOP is applied again to configuration  $\mathbf{X}_1$ , there is bound to exist a difference between the resulting configuration denoted  $\mathbf{x}_1 = \mathbf{X}_1 + \mathbf{u}_1$  with the target configuration  $\mathbf{X}_0$ . This difference is used to compute the error estimate:

$$e_1 = \|\mathbf{x}_1 - \mathbf{X}_0\| = \|\mathbf{X}_1 + \mathbf{u}_1 - \mathbf{X}_0\| \quad (3.70)$$

where  $\|\cdot\|$  denotes the Euclidean norm and a new stress-free estimate is approximated using the new nodal displacements as:

$$\mathbf{X}_2 = \mathbf{X}_0 - \mathbf{u}_1 \quad (3.71)$$

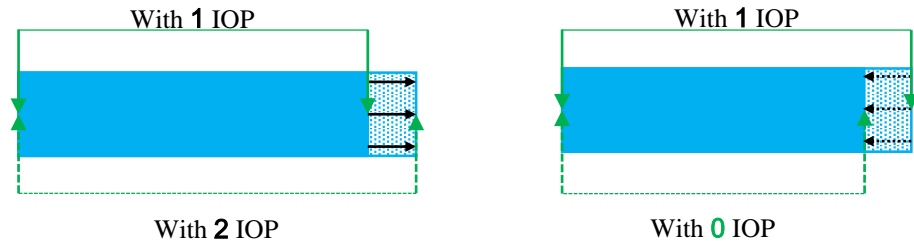


Figure 3-17. Schematic method to obtain the stress-free configuration of a linear strip model

Based on this new estimate, the procedure continues by carrying out another finite element analysis and using the resulting nodal displacements to compute a new error estimate. In the  $k$ th iteration, the stress-free estimate is given by

$$\mathbf{X}_k = \mathbf{X}_0 - \mathbf{u}_{k-1} \quad (3.72)$$

and the error estimate is calculated by

$$e_k = \|\mathbf{x}_k - \mathbf{X}_0\| = \|\mathbf{X}_k + \mathbf{u}_k - \mathbf{X}_0\| \quad (3.73)$$

The iterative process is illustrated in Figure 3-18 and it is generally terminated when the magnitude of  $e_k$  becomes smaller than a pre-set tolerance. In this study however, 3 iterations have been used in all cases and the final errors had magnitudes of less than  $10^{-5}$  mm.



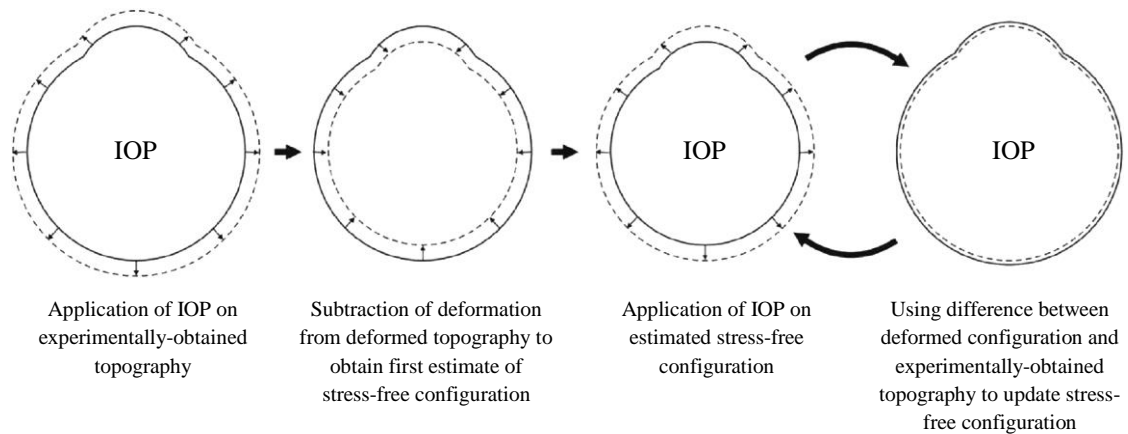


Figure 3-18. Schematic description of steps to obtain the stress-free configuration [280]

### 3.4.3 Adjustment of the ablation depth

The photoablation that is used to remove corneal tissue in the corneal refractive surgery is applied to the stressed cornea in vivo. Nevertheless, modelling tissue removal in a stressed model or when the finite element analysis is running is rather hard. Instead, the tissue removal in this study is done on the stress-free model by changing the corneal thickness according to the clinical ablation profile. Moreover, because the clinical ablation profile is designed using topography and/or wavefront data in vivo with the eye in a stressed state, an adjustment process of the ablation depth is included. Its purpose is to achieve a new ablation depth profile that is suitable for the stress-free configuration. This is done by marking the location and depth of the ablation and monitoring its changes during the stress free configuration process. The easiest way to do so is to introduce a new layer for the tissue that is going to be removed as shown in Figure 3-19. An alternative approach may be possible to only identify the location of this layer (more specifically, its posterior surface) but without adding it to the model (Figure 3-20), the nodal displacements corresponding to this layer then can be interpolated from the nearby nodes. Both approaches are able to estimate the location and shape of the ablation depth profile in the relaxed model (stress-free configuration). This profile is expected to be

thicker than the clinical measurements because after removing the IOP, the thickness of the whole cornea is expected to increase.

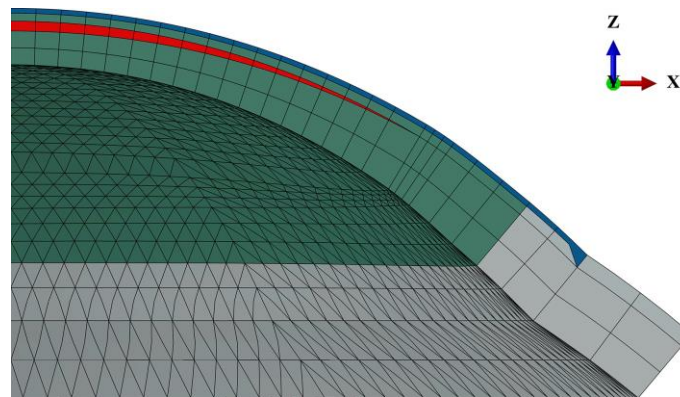


Figure 3-19. Model with an ablation depth profile being isolated in a specific layer (red)

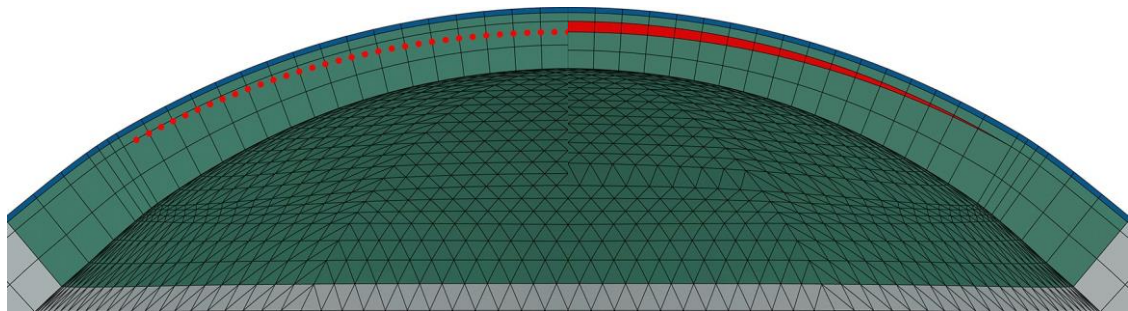


Figure 3-20. The alternative approach to enable adjustment of ablation depth (left), compared to the approach where an ablation layer is included as shown in Figure 3-19. Additional points are located in the left model to identify the **posterior surface** of the ablation depth. It should be noted that the thickness distribution across layers is different in these two models because of the different ways in handling ablation layer.

Because the actual ablation formula could not be obtained from the laser instrument manufacturer, the study had to rely on limited ablation depth data given at about 90 points across the ablation surface. The ablation profile has an asymmetric shape and the ablation depth decreases from the centre to the periphery. The points do not cover a complete circular region as shown in Figure 3-21. To closely adopt this data, the ablation thickness values are fitted to low order Zernike polynomials ( $n = 4$ ), to allow easy prediction of ablation depth at un-sampled locations and reasonable estimation of the ablation boundary, Figure 3-21. However this boundary is often not perfectly circular, which

introduces the need to reconfigure the corneal nodes to coincide with non-circular ablation boundary if a new layer is to be added (Figure 3-22). To do the nodal re-arrangement, an additional ablation boundary (yellow in Figure 3-22), on which the ablation depth has pre-set value, is also obtained through the Zernike expression of the ablation depth. This pre-set value is necessary to control the thickness of peripheral elements in the ablation layer, whose cross-sectional shapes are triangles. This ablation boundary is called minimal ablation boundary.

The nodal re-arrangement is only carried out in the central cornea till the flap boundary that defines the size of corneal flap (9 mm in diameter, Figure 3-22) as will be described in the next section. The gap between the ablation boundary and flap boundary is used to smoothly transit the corneal rings from uncircular shapes in the central area to circular shapes beyond the flap boundary.

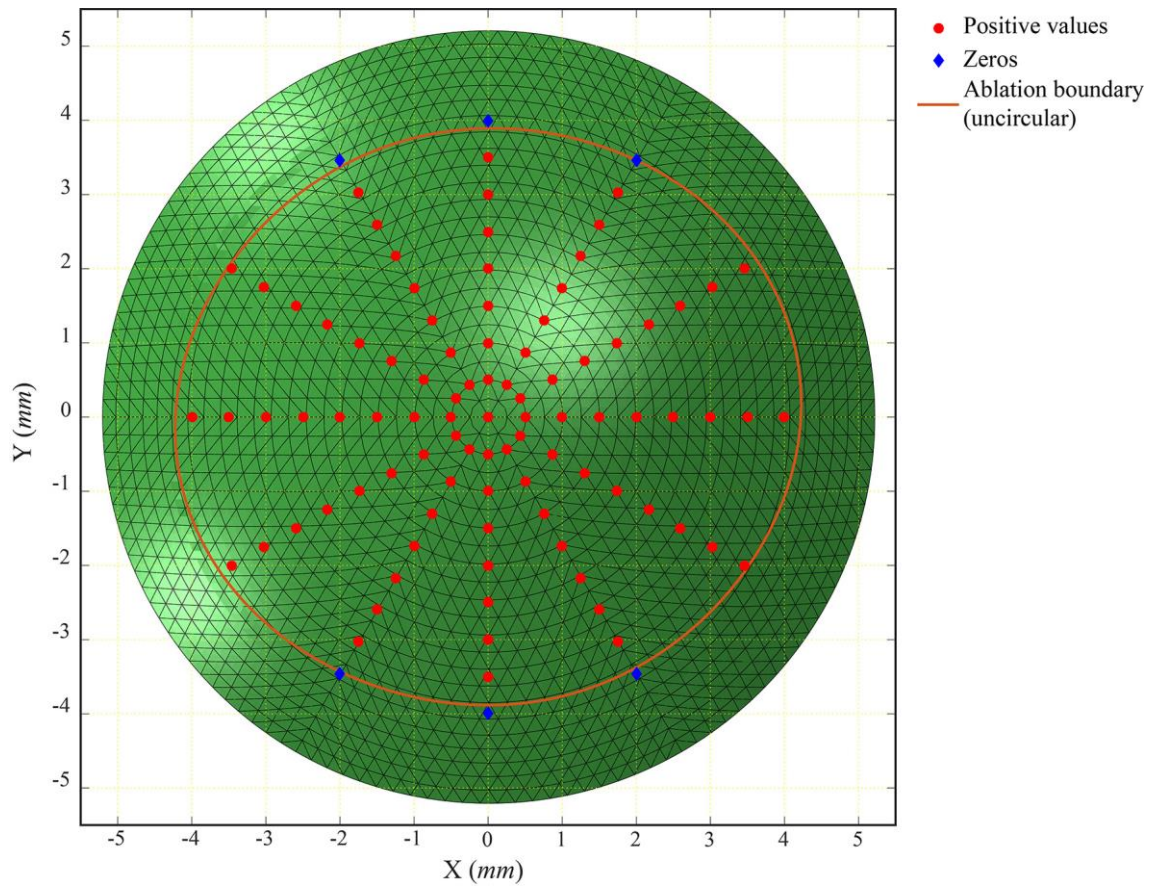


Figure 3-21. Ablation sample points and their locations as shown on the anterior corneal surface of the model. The ablation depth values at some peripheral locations are zeros (blue diamond), meaning laser ablation is not applied at these locations.

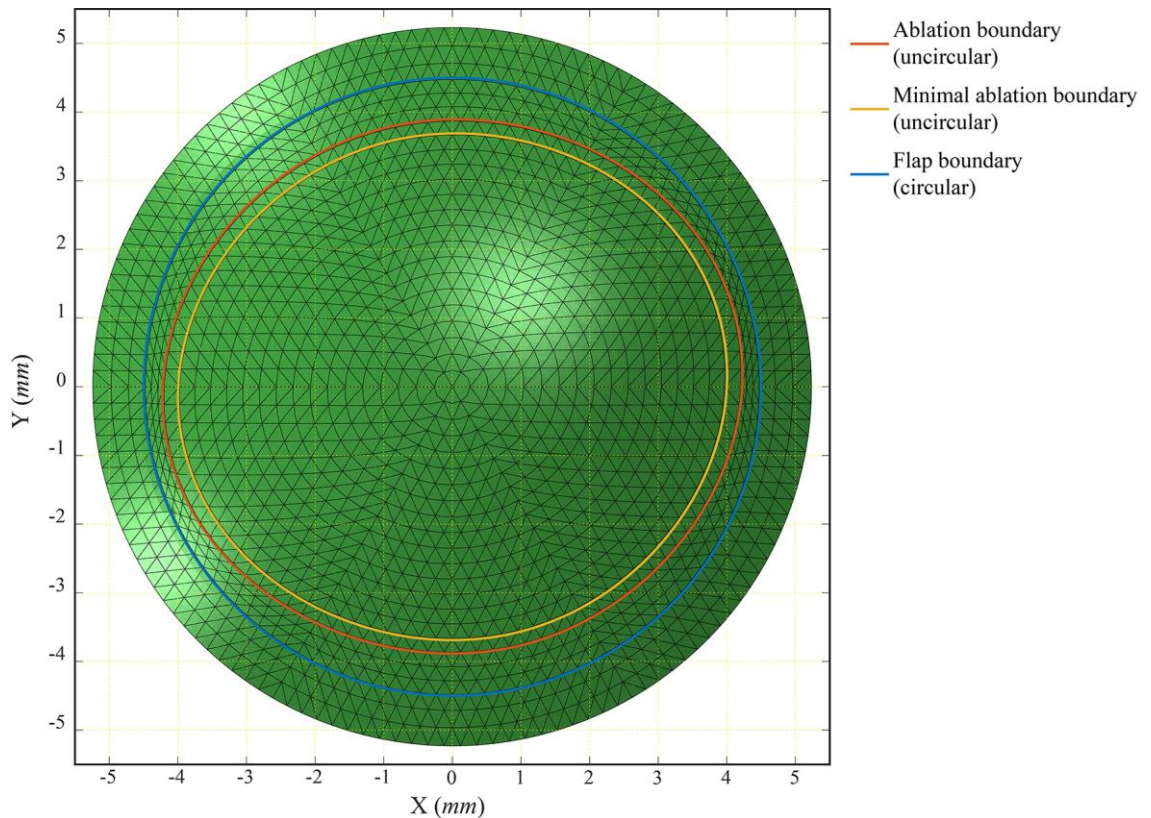


Figure 3-22. Re-configured corneal nodes to fit the ablation boundary. The central corneal rings are uncircular until the flap boundary, beyond which the rings remain regular and circular.

The reconfiguration of the corneal nodes may be avoided if the alternative approach described above is used, the process becomes as simple as identifying certain points inside the intact cornea that enclose the ablation thickness. Figure 3-23 has shown the identified points viewing from the front of the cornea in models with and without nodal re-arrangement. It should be noted that these points, which represent the posterior surface of the ablation profile, seemingly appear on the anterior corneal surface but they are in fact located inside the cornea as illustrated in Figure 3-20. In Figure 3-23A, the corneal nodes are re-configured to fit the ablation boundary and the identified points form complete rings (uncircular). In Figure 3-23B, the corneal nodes are regularly spaced in circular rings and the ablation boundary is only used to identify circularly spaced points that are inside the uncircular ablation boundary. The identified points rough cover the ablation region specified by the ablation boundary but appear to incompletely occupy some

peripheral rings. During the process of stress-free configuration, the nodal displacements of the identified points are interpolated using nearby nodes and included when computing the error estimate  $e_k$ .

No matter which way are used to locate the ablation depth, an adjusted profile can be obtained through the stress-free configuration. After determining the stress-free configuration, the adjusted ablation depth is removed to simulate the laser ablation in the surgical procedure. The layers above the ablation layer are moved downwards to close the gap while the rest of the model is kept unchanged.

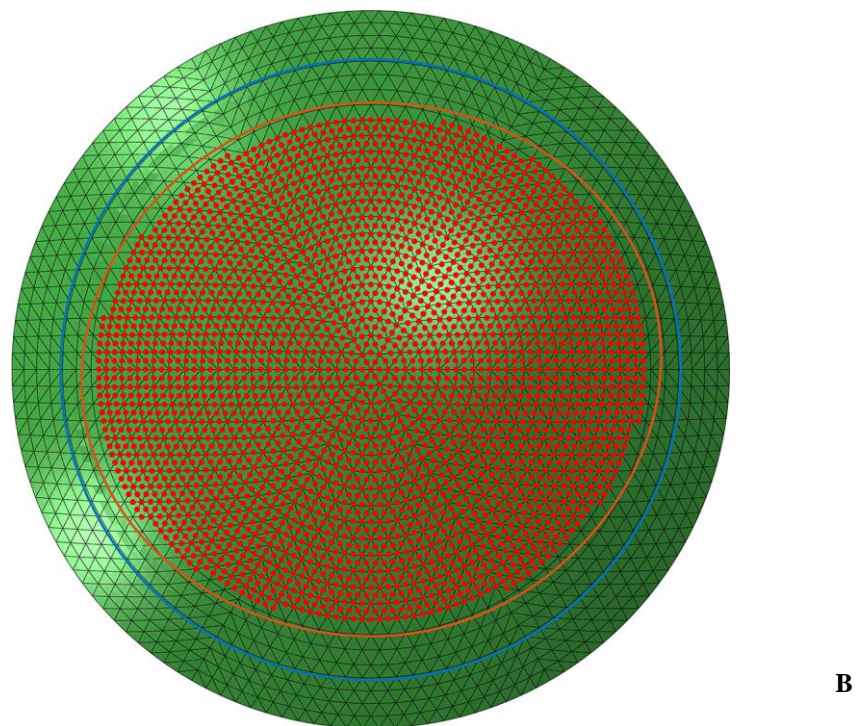
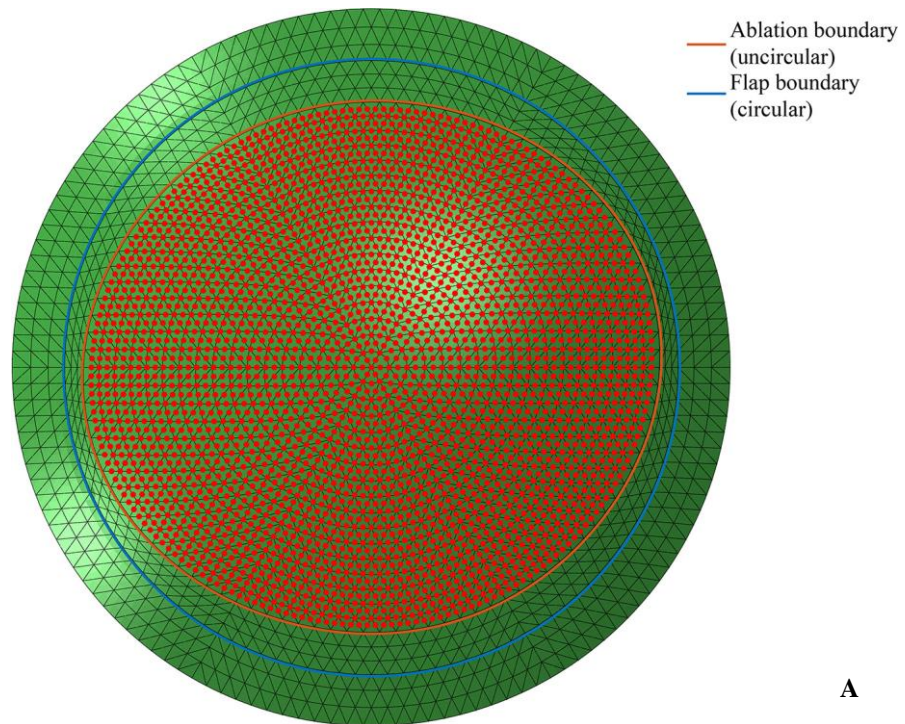


Figure 3-23. Locations (marked as red points) identified for adjustment of ablation depth as seen from the front of the cornea. **A:** The corneal nodes are re-configured according to the ablation boundary; **B:** Re-configuration of corneal nodes are not applied but the ablation boundary is still used to guide the identification of necessary points.

### 3.4.4 Definition of flap (for LASIK)/cap (for SMILE)

To closely mimic the actual situation in LASIK refractive surgery, the corneal flap is modelled and the flap thickness is obtained clinically. However, the measurements are also limited and they are only collected in two cross sections of the cornea based on Optical coherence tomography (OCT) images (Figure 3-24). Moreover, the data collection was done manually so the accuracy is low. As shown in Figure 3-25, the spatial plot of the flap thickness in z-x and z-y cross sections do not intersect with each other although they are expected to do so. Because of the limitations in both availability and accuracy, these flap data points are fitted to a set of second order Zernike polynomials which gives a rough estimate of the actual flap thickness (right figure of Figure 3-25).



Figure 3-24. An OCT image of a corneal cross section showing the boundary of flap



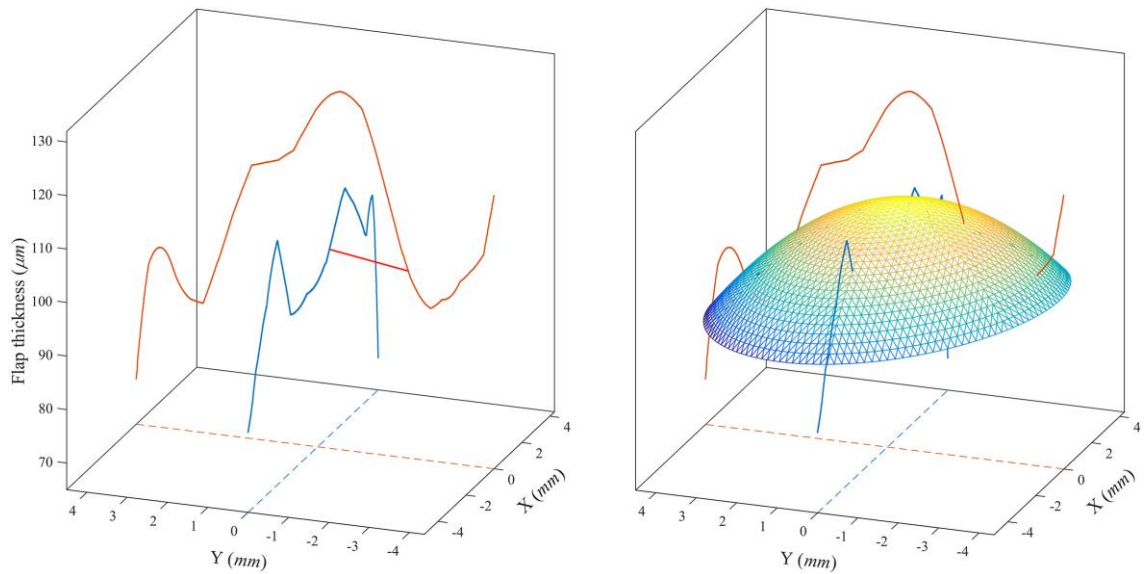


Figure 3-25. Plot of flap thickness in z-x and z-y cross-section and the 2<sup>nd</sup> order Zernike expression of the flap thickness distribution. In the left figure, the red line represents the closest distance of the two thickness curves.

Although the flap is only present after the cut, its thickness is embedded into the model before the stress-free configuration, enabling the location of ablation layer to be determined and making the design of flap afterwards easier. This does not change the structure of the model but just sets the thickness of the first layer (in cornea, the first two layers including the epithelium) according to the Zernike expression obtained above.

Once the ablation depth is subtracted and all upper layers are brought down accordingly, the central 9 mm diameter region of the first two corneal layers representing the flap are separated from the model and connected using multi-point constraints (MPC) to the rest of the model. This connection forms a hinge measuring about 4 mm in arc length as illustrated in Figure 3-26. A friction interaction is defined between the posterior flap surface and the underlying surface of the stroma. These parameters of flap diameter and hinge size are not patient-specific but are close to the clinically reported values [281].

In this study, the newer surgical procedure SMILE is also numerically studied and its only difference with LASIK is the flap connection to the rest of the cornea. In SMILE, the flap

becomes a cap and in contrast to the LASIK flap, the cap is connected to the rest of the model more completely with only a small separation used to model the small incision made to remove the corneal lenticule. The diameter of the SMILE cap is usually smaller than the LASIK flap as shown in Figure 3-26 but they are kept the same to allow direct comparison of model results. In addition, the size of the SMILE incision cut has been kept at 4mm, which is close to typical clinical practice [282].



Figure 3-26. Dimensions of LASIK flap and SMILE cap and the corresponding cut sizes

### 3.4.5 Wound healing

The effect of the wound healing process taking place after the surgical procedure has not been fully quantified. The studies on wound healing suggested that the adhesive tensile strength across the wound is much weaker compared to the rest of stroma [283] but the scarring of the surrounding tissue may lead to stiffness increases. In this study, a wound healing layer is designed in both LASIK and SMILE models, which measures 100  $\mu\text{m}$  in thickness and its stiffness is set proportional to the stroma thickness. The selection of a thickness of 100  $\mu\text{m}$  is based on informal discussion with Professor Julie Daniels at University College London. Moreover, the wound healing layer is assumed to cover the

whole region of flap/cap cut with uniform material properties for simplicity. The LASIK or SMILE model with a wound healing layer beneath the flap or cap is shown in Figure 3-27, it should be noted that the cornea has been thinned to model tissue removal. A parametric study is then carried out to find the optimal wound healing stiffness ratio which leads to the best fit of the simulated surgical outcomes with the actual clinical data. This parametric study is only doable for LASIK models, and therefore the wound healing stiffness in the SMILE models has adopted the optimal values found in the parametric study using LASIK models.

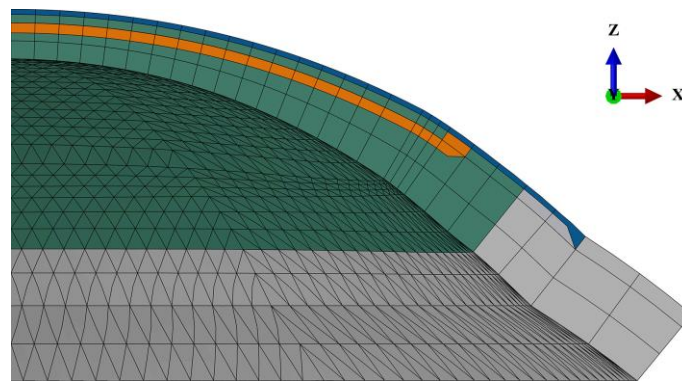


Figure 3-27. Model with a wound healing layer in orange

### 3.4.6 Summary of the simulation steps

In this study, both LASIK and SMILE procedures are modelled, they share the same steps until the definition of flap for LASIK and cap for SMILE. The only difference between the flap and the cap is their connection to the rest of the model. The simulation begins with the generation of an idealised model using a Visual Basic programme (Figure 3-28) and this model is used as a structural base, upon which each set of patient-specific data is used to create a model that meets the exact geometry of each eye in terms of corneal shape and axial length of the eye. An epithelium layer is introduced and assigned softer material behaviour compared to the corneal stroma. Having designed the first two layers to account for the flap thickness, an ablation layer is then located under the corneal flap and isolated

from the thickness of the stroma, this allows the adjustment of the ablation profile that is suitable for the relaxed model after obtaining the stress-free configuration. The adjustment of ablation profile can alternatively be achieved by introducing points that identify the posterior surface of the ablation layer. After the ablation depth is removed from the stroma, the flap or cap is moved downwards to close the gap with the rest of the tissue. In LASIK models, the flap measuring 9mm in diameter is separated from the model and only connected to the rest of the model by a hinge with an arc length about 4mm long. In SMILE models, the cap is connected to the model more completely, leaving an unconnected portion of the same size as the LASIK flap hinge. In both LASIK and SMILE models, a 100 micron thick wound healing layer is considered beneath the flap/cap and assigned different material behaviour. All these manipulations are done inside the MATLAB environment and the LASIK and SMILE models are submitted to the Abaqus solver for FEM analysis (application of IOP). To guide all this analysis, a Graphical User Interface (GUI) is built using MATLAB (Figure 3-29), it guides the user to select patient data and choose the simulation parameters. Based on user selections, the GUI builds the LASIK and/or SMILE models and calls Abaqus to do the FE analysis.

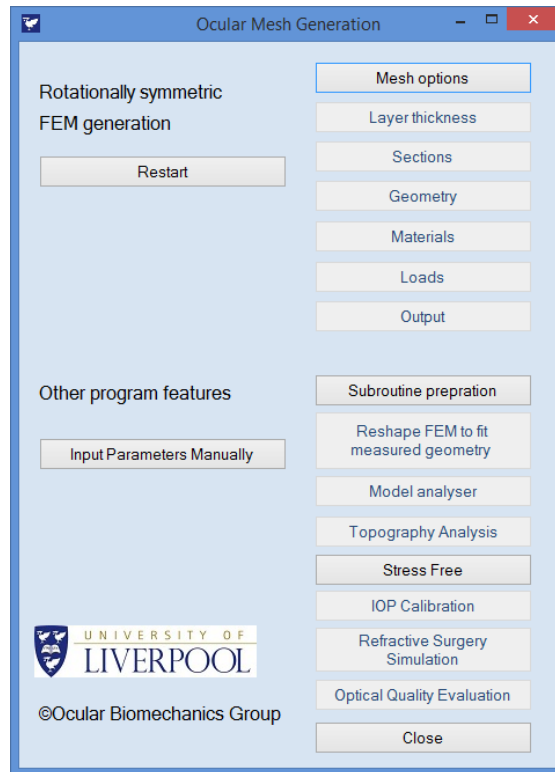


Figure 3-28. Visual Basic programme used to generate idealised models

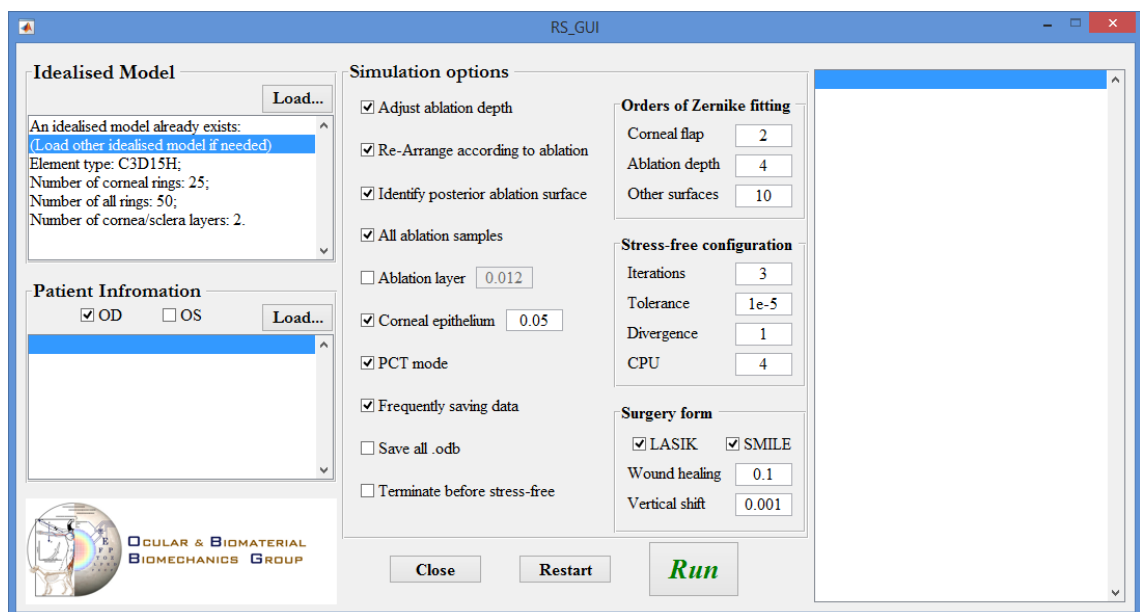


Figure 3-29. Graphical user interface under MATLAB environment that guides the patient-specific modelling of corneal refractive surgeries LASIK and SMILE

### **3.4.7 Mathematical simulation of LASIK**

In addition to the above steps of numerical simulation, for each set of patient-specific data, a mathematical simulation that considers no ocular biomechanical reaction to the surgical procedure is conducted. In this simulation, the ablation depth is simply subtracted from the corneal thickness measured preoperatively. The predicted postoperative topography from the mathematical simulation is then compared to the clinical topography and the results are used to validate the necessity of considering ocular biomechanics in refractive surgery modelling.

### **3.4.8 Simulation of tonometry**

Built upon the numerical models established in previous sections, the simulation of tonometry is also included in this thesis. The purpose of this study is to: 1) validate the capability of numerical models to reliably simulate tonometry and thus estimate the IOP, 2) reveal the effect of central corneal thickness on the IOP estimates by tonometry, and 3) study the influence of LASIK and SMILE procedures on the IOP estimates. To do so, three models are used for each patient-specific data set, namely model with full corneal thickness (INTACT), LASIK and SMILE models. Goldmann applanation tonometer (GAT) and Corvis ST (CVS) are included in the tonometry study.

GAT is a static and contact tonometry, and widely considered to be the gold standard IOP measuring technique. Based on the Imbert–Fick law, GAT measures the IOP as the external tonometry pressure subtracted by the effect of tear film tension along the tonometer edge [250]. To model GAT, as shown in Figure 3-30, a circular rigid body with a diameter 3.06 mm is introduced to simulate the tonometer and added to the existing models already established in previous sections (inflated by IOP). The rigid body is placed at the apex of the cornea and a friction contact is defined between the anterior

surface of the cornea and posterior surface of the tonometer to avoid penetration. A concentrated force is gradually applied to the centre of the tonometer to push it downwards against the cornea until complete appplanation is achieved. This process is done by a static FE analysis using Abaqus which records the force at appplanation. This force is then divided by the area of the tonometer ( $1.53^2 \pi$ ) to determine the external tonometry pressure. The effect of tear film tension is adopted from [250] as 0.45 mmHg, which is subtracted from the external tonometry pressure to determine the estimate of true IOP.

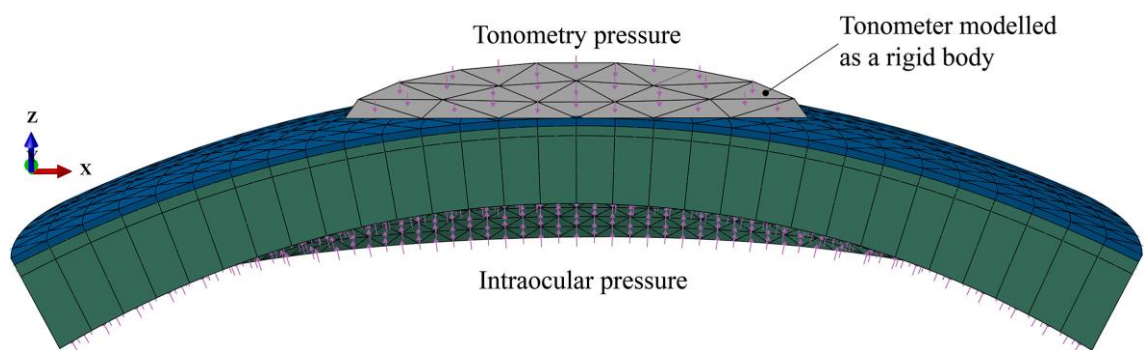


Figure 3-30. Schematic method to model GAT, showing in an INTACT model. The tonometry pressure is implemented by applying concentrated force in real simulation.

The recent CVS on the other hand is dynamic and non-contact, it is a very promising method with growing popularity because of its ability to not only measure the IOP but also characterise in vivo corneal biomechanics. An air-puff with duration of nearly 30 milliseconds is projected on the cornea and the magnitude of the pressure increases then decreases during the projection (Figure 3-31A). The pressure is precisely measured at the piston where the air-puff is jetted but this pressure will decline when the air-puff reaches the corneal surface. While it is difficult to measure the pressure on the cornea, a reduction ratio ( $95/182 \approx 0.522$ ) is suggested by the company as shown in Figure 3-31A. Further, the pressure in Figure 3-31A presents the pressure at the centre of the air-puff, the pressure across the cornea surface is not uniform, being the highest at the centre and

vanishing towards the periphery (Figure 3-31B). The air-puff pressure causes the corneal shape to deform from convex to concave and the time when this event take place is called applanation time 1 (AT1), which determines applanation pressure 1 (AP1) as shown in Figure 3-31A. AP1 is then converted to IOP estimate by a linear equation  $C1 \times AP1 + C2$  where  $C1$  and  $C2$  are constants. It should be noted that, the corneal shape will return to its original convex shape from concave when the air-puff pressure decrease to zero. To implement CVS in each patient-specific model, the rings within the central 3 mm radius of the anterior corneal surface are identified (Figure 3-32) and the air-puff pressure on each ring is computed based on the distance from its middle point to the corneal apex and the distribution profile in Figure 3-31B. Once the pressure distribution is defined, a dynamic FE analysis is performed using Abaqus and the AT1 is determined by monitoring the second derivative of the corneal apex in X direction (changing from negative to positive).

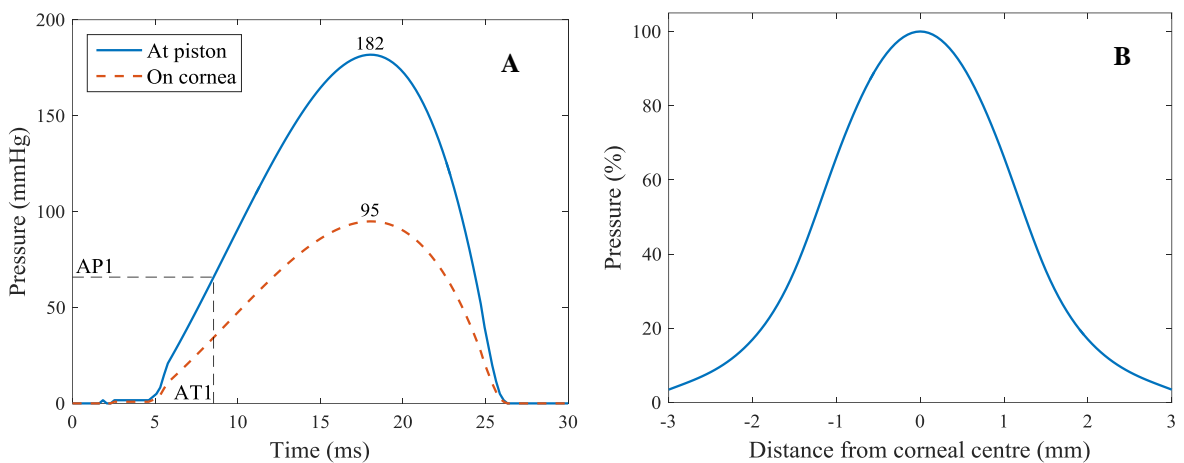


Figure 3-31. Temporal air-puff pressure profile over 30 ms (A) and spatial distribution of the pressure across corneal surface (B)



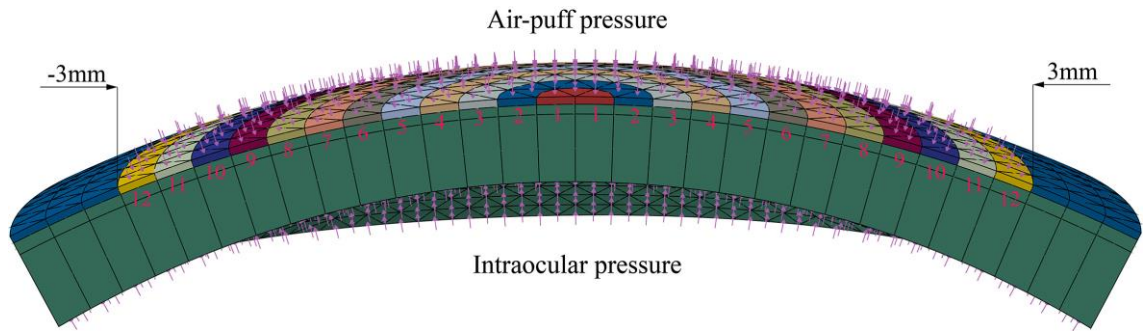


Figure 3-32. Schematic method to model CVS, showing in an INTACT model. The magnitudes of the air-puff pressure decrease from the centre (ring 1) to the periphery (till ring 12).

### 3.5 CONCLUDING REMARKS

In this chapter, the methodologies employed in the thesis have been highlighted, including (1) basic knowledge of orthogonal polynomials and the methods to calculate the polynomial coefficients for an arbitrary map represented by discrete points, (2) the mathematical statements of the topography matching problems for both pair-wise and multi-view registrations and the algorithms to achieve the solutions for these problems, and (3) the strategies and steps in the numerical simulation of corneal refractive surgery considering both LASIK and SMILE procedures and a simple mathematical simulation method, followed by numerical simulation of tonometry including GAT and CVS. These three main parts are set in a logical order. The topography fitting study aims to assess a series of orthogonal polynomials in terms of both reconstruction and prediction. The purpose of this practice is to derive explicit expressions of the discrete data points which are not only able to reproduce the points at known locations but also reliable enough to predict points that lay between the measured locations. The outcomes are beneficial to the following topography matching study when the algorithms need to find points on the central map that correspond to locations on the peripheral maps. The combination of topography fitting and ICP algorithm has never been done before and this has led to interesting results that will be presented in Chapter 5. Ideally, the combined map, which will have a much larger coverage than the standard single map, can be fitted to orthogonal

polynomials again and used to build patient-specific models for LASIK or SMILE. Unfortunately, the corneal topography data used in the numerical study only consist of a single central measurement for each eye. Nevertheless the outcomes of topography matching has prepared a necessary tool for future use once the required data becomes available. In this study, we had to continue the numerical simulation studies of LASIK and SMILE without taking the benefit of matching multiple topography maps of the cornea.

## CHAPTER 4

### RESULTS OF TOPOGRAPHY FITTING

---

#### 4.1 INTRODUCTION

Based on the theoretical background in Section 3.2, this chapter presents the results of topography fitting using topography data measured clinically. It begins with a comparison study on least squares estimation (LS) and orthogonal projection (OP) methods; the results of such study help determine the best suitable method for fitting of corneal topography. Then the performance of the orthogonal polynomials in reconstructing the measured topography maps is evaluated. This is followed by the assessment of various orthogonal polynomials in prediction of unmeasured locations and the potential risk of overfitting. In this study, the topography data are collected using a Pentacam videokeratographer and provided by Professor Pinakin Davey at Western University of Health Sciences, USA. The data include 200 normal and 174 keratoconic eyes and for each eye both anterior and posterior corneal surfaces are measured during the data collection process. The original topography, as a map, has a coverage of 14 mm in x and y directions, and a resolution of 0.1 mm, resulting in a 141×141 square grid. In practice, only certain central circular region of the original map is kept because of data incompleteness outside this region as shown in Figure 4-1. In this thesis, the central 5 mm radius is used.

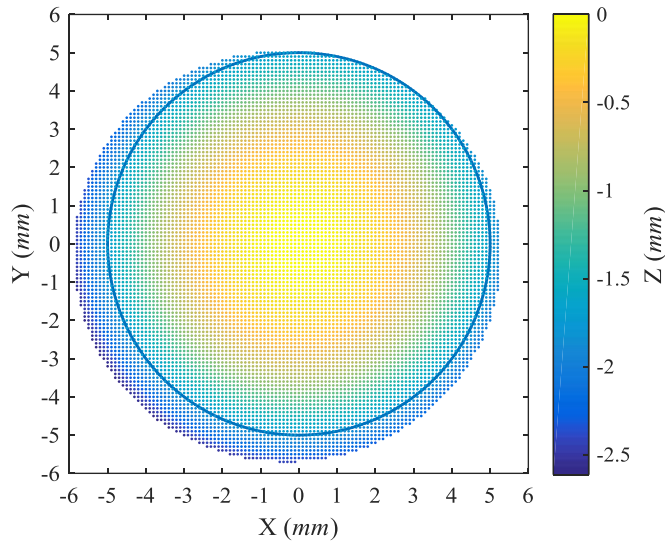


Figure 4-1. Typical Pentacam topography data viewed from the top. Colours of individual points reflect their z coordinates. The continuous circle in the figure has a radius of 5 mm.

## 4.2 OP vs. LS

One of the major differences in determining polynomial coefficients by LS optimisation and OP variants is that, for the former, the sample data are fitted to truncated features, the coefficients may not represent the real values if the number of features is insufficient and there will always be oscillation in values of the coefficients when the truncated number changes. To assess this underlying fact and the reliability of OP methods to evaluate the polynomial coefficients, a second order function  $z(x, y) = x^2 + y^2$  is fitted to a series of Zernike polynomials by both LS method and OP variants. Theoretically,  $z(x, y)$  can be explicitly expressed by only two terms of Zernike polynomials as  $z(x, y) = 0.5W_1(x, y) + 0.5W_5(x, y)$ , i.e. the coefficients of the 1<sup>st</sup> and 5<sup>th</sup> Zernike terms are both 0.5, while the coefficients of other terms should be zeros.

First, a  $60 \times 60$  unit square grid is used to sample  $z(x, y)$ , resulting in 2821 points in the unit circle. This set of 2821 points is fitted to Zernike series using orders from 2 to 50 and the coefficients are evaluated by LS method. It is obvious that order 2 is sufficient to fit this set of points based on the knowledge above because both the 1<sup>st</sup> and 5<sup>th</sup> Zernike

polynomials are included by order 2. When the order increases, new polynomials terms are added to the series, which sequentially changes the coefficients of the existing terms as the LS method takes no advantage of the orthogonality of the polynomials. Figure 4-2 shows errors of the first six Zernike coefficients ( $a_1, a_2, \dots, a_6$ ) computed by LS method expressed as absolute differences between the computed and theoretical values. It can be seen that the errors are trivial for all six coefficients and they change with increases in polynomial order. This happens because the orthogonality of the polynomials is not valid in a discrete manner such that the polynomial terms are no longer independent but coupling with each other. In the practice of fitting the aforesaid second order function, coefficients of higher order terms that should be zeros are no longer zeros, which forces coefficients of lower order terms to change, in order to cancel out the effect of non-zero higher order terms. However, the change in the coefficients are seen to be negligible.

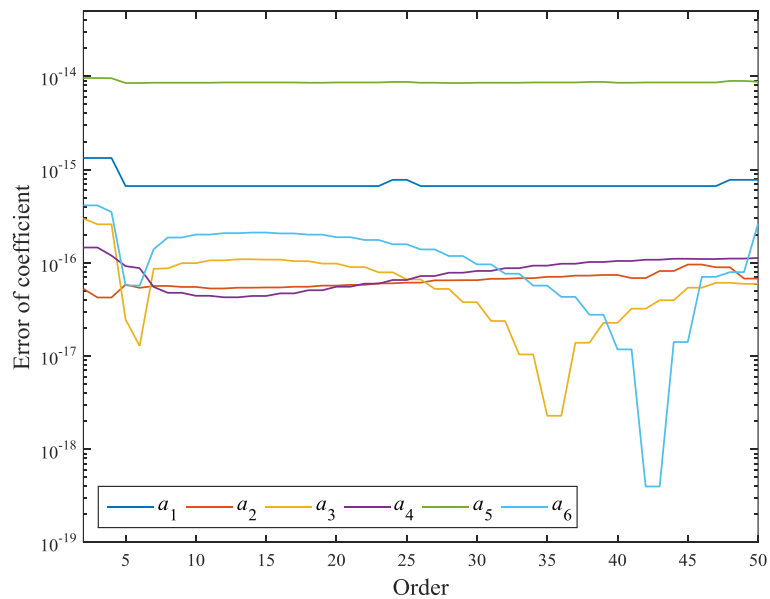


Figure 4-2. Vibration of coefficients as evaluated by the LS method while using different Zernike orders

In addition, to assess the reliability of OP variants in evaluating polynomials coefficients, square grids from  $15 \times 15$  to  $300 \times 300$  with increments of 15 points in both directions are used to sample the above second order function  $z(x, y) = x^2 + y^2$  and only points that lay

inside the unit circle are kept. Using these points (black and green) and boundary points (red) as shown in Figure 4-3, the unit circle are divided to triangles and/or squares as detailed in Section 3.2.2.

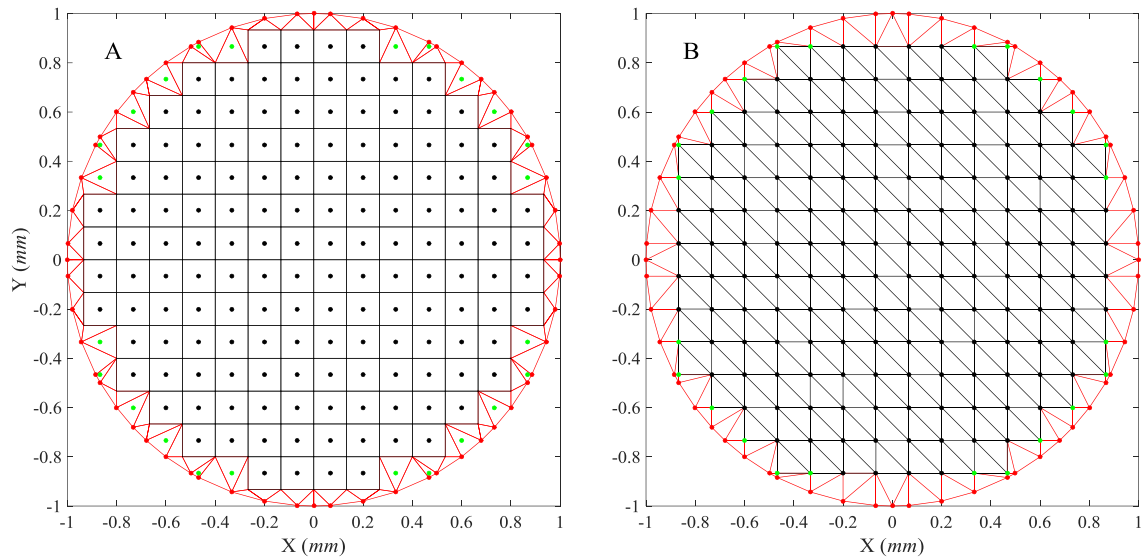


Figure 4-3. Discrete points and the squares and/or triangles representation of the unit circles. In representation A, the points are regarded as middle points of pixels and the green points are discarded because the corresponding pixels sit partly inside the unit circle. The same green points are kept in representation B, which is for INT variant of OP methods.

The first six Zernike coefficients, corresponding to order 2, are computed by variants of OP methods and also the LS method. The absolute errors of coefficients for the 1<sup>st</sup> and 5<sup>th</sup> Zernike terms along with the root mean square error of all the 6 coefficients with their true values are displayed in Figure 4-4. It can be seen that all OP variants tend to compute the coefficients more accurately with higher resolution. The zeroth order approximation (ZOA) approach obtains most inaccurate coefficients and the improvement of exact moments (EM) method over ZOA is not significant. It should also be noted that the behaviour of ZOA overlaps with that of EM when evaluating the first coefficients because the first Zernike polynomial term is a constant function. It then turns out that the interpolation extension of EM approach (INT) gives closest coefficient values to the exact ones because not only the polynomials are kept continuous but also the linear

approximation of the input surface reduces the difficulties of reconstruction. Nevertheless, even though the INT approach is reasonably good, the LS method estimates the true values remarkably better regardless of resolution as shown in Figure 4-4.

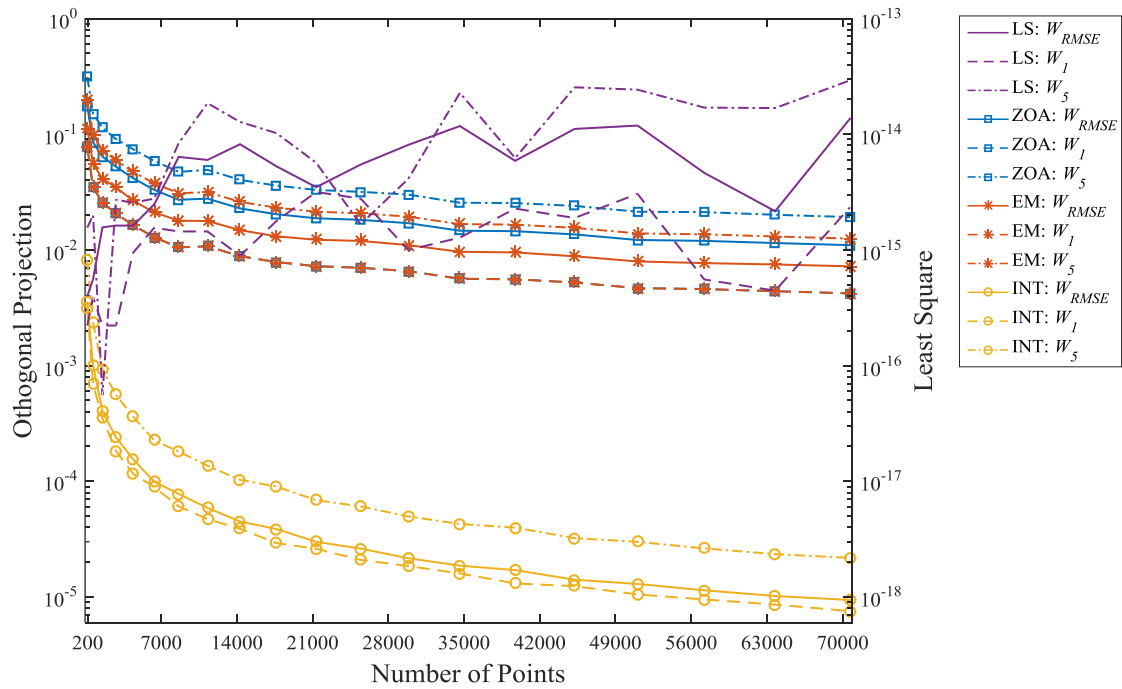


Figure 4-4. Absolute errors of the first and fifth Zernike polynomial coefficients and the root mean square error (RMSE) of all the first 6 coefficients with their true values (0.5 for both the first and fifth terms and 0 for the rest). The errors of coefficients by OP methods are plotted by the left axis while the ones for the LS method are displayed by the right axis for better clarity. The horizontal axis represents the number of points that are created by different grids.

Another important advantage of LS method over the OP method is its relatively fast speed. Once the polynomials are sampled at the same x and y coordinates, the whole set of coefficients are obtained by few matrix manipulations. On the other hand, except for the ZOA variant, both EM and INT variants of OP method involve computations of double integrals on finite areas of triangles and squares, which makes EM and INT variants computationally expensive especially for images or maps with a large number of points. Considering the fast speed of the LS method, its high accuracy and simplicity of implementation even when the polynomials are not sufficiently sampled (for example in

the square polynomials cases), the LS method is employed solely for the following test on clinical corneal topography.

### 4.3 TOPOGRAPHY RECONSTRUCTION

One anterior normal corneal topography is randomly chosen and the measurements within 5 mm radius (7845 data points) are extracted to test the reconstruction capability of all the polynomials mentioned in Section 3.2. For the square polynomials defined in Cartesian coordinates system, only the circular portion that maximally inscribes the original square domain is used to fit the surface. Figure 4-5 shows the goodness of each set of polynomials in terms of the reconstruction errors computed using Equation (3.26). It can be seen that there are only four trends even though 8 polynomial series are considered in total. The performance of Legendre polynomials (LPs) and Gegenbauer polynomials (GPs) perfectly overlaps that of the Zernike polynomials (ZPs). Further, the radial versions of LPs and GPs produce almost the same results as Orthogonal Fourier-Mellin polynomials (OFMPs). The performance patterns of these two groups are discussed later in Chapter 7.



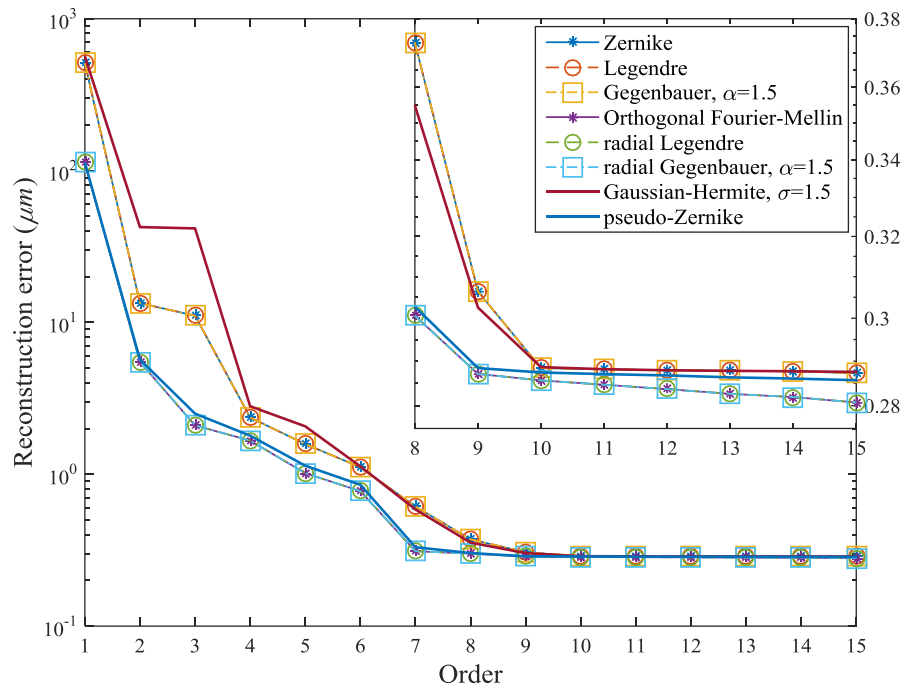


Figure 4-5. Reconstruction errors plotted against order for eight sets of polynomials, for one clinical anterior topography of a randomly chosen normal eye. For Gegenbauer polynomials and Gaussian-Hermite polynomials, only one scaling factor ( $\alpha$  or  $\sigma$ ) is included in this figure. An inset graph is added in the figure to show trivial difference in reconstruction errors of high orders.

It can be seen that all polynomials tend to fit this particular anterior corneal surface at almost the same accuracy level beyond order 10, while obvious differences are observed before this point. The OFMPs fit the surface the best at every order, followed by PZPs, ZPs and Gaussian-Hermite polynomials (GHPs). There is a cross point between ZPs and GHPs, clear superiority of ZPs are seen before order 6 but the GHPs begin to fit the surface slightly better after this order and tend to match ZPs in higher orders from 10. It should be noted that only  $\alpha = 1.5$  and  $\sigma = 1.5$  are used in Figure 4-5 for GPs and GHPs, respectively, where the parameters  $\alpha$  and  $\sigma$  are the scaling factors of the polynomials with smaller values turning the shapes of polynomials to local features. In fact, the set of LPs is a special case of GPs with  $\alpha = 0.5$ , and with its overlapping behaviour in Figure 4-5, it is easy to extend that GPs with different scaling factors but all defined on the same unit plane  $[-1,1]$  may also have the same performance as will be shown later. This extension however would not hold when the GHPs are concerned because GHPs are

defined as orthogonal on the infinite plane  $[-\infty, \infty]$  and the calculation of coefficients only uses data within the unit circle. The hypothesis of extension herein is supported by the results presented in Table 4-1 and Figure 4-6 where various scaling factors of GPs and GHPs are tested using the same topography map. For GPs, the reconstruction error is given from order 6 to 12; it can be seen that the scaling factor has no effect on the reconstruction error. But this is not true for GHPs where larger scaling factors (global features) tends to improve the reconstruction outcomes, Figure 4-6. The improvement by using larger scaling factors however becomes trivial beyond  $\sigma = 1.5$  thus only  $\sigma = 1.5$  is kept for further studies.

Table 4-1. Reconstruction errors ( $\mu\text{m}$ ) of GPs with different scaling factors  $\alpha$

$\alpha$ Order	0.3	0.6	0.9	1.2	1.5
6	1.113	1.113	1.113	1.113	1.113
7	0.613	0.613	0.613	0.613	0.613
8	0.373	0.373	0.373	0.373	0.373
9	0.306	0.306	0.306	0.306	0.306
10	0.288	0.288	0.288	0.288	0.288
11	0.288	0.288	0.288	0.288	0.288
12	0.288	0.288	0.288	0.288	0.288

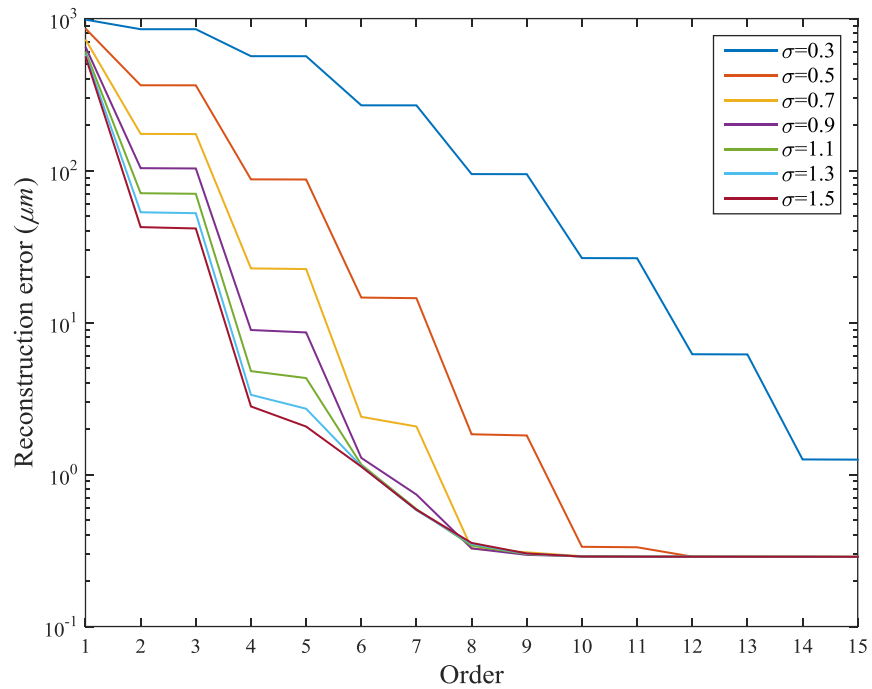


Figure 4-6. Reconstruction errors of Gaussian-Hermite polynomials with different scaling factors

With all results so far being given based on a single corneal map, the whole collection of topographies from the 200 normal and 174 keratoconic corneas including both anterior and posterior surfaces are added to the reconstruction test. Again, only measurements in the central 5 mm radius are kept and it should be mentioned that 14 posterior topographies of keratoconic corneas are discarded because there are missing measurements within the central 5 mm radius in these maps. Further, according to the overlapping results, only Zernike polynomials, pseudo-Zernike polynomials, Orthogonal Fourier-Mellin polynomials and Gaussian-Hermite polynomials with scaling factor  $\sigma = 1.5$  are kept and the reconstruction errors for orders 6 to 12 are given from Table 4-2 to Table 4-5, presented as mean  $\pm$  1 standard derivation.

Table 4-2. Reconstruction error ( $\mu\text{m}$ ) for Zernike polynomials, presented as mean  $\pm$  1 standard derivation.

Order	Anterior		Posterior	
	Normal	Keratoconic	Normal	Keratoconic
6	1.403 $\pm$ 0.573	2.772 $\pm$ 1.767	4.339 $\pm$ 1.752	7.905 $\pm$ 4.456
7	0.907 $\pm$ 0.402	1.674 $\pm$ 1.204	3.061 $\pm$ 1.28	5.101 $\pm$ 3.092
8	0.497 $\pm$ 0.198	0.901 $\pm$ 0.671	1.257 $\pm$ 0.684	2.118 $\pm$ 1.415
9	0.372 $\pm$ 0.106	0.591 $\pm$ 0.383	0.79 $\pm$ 0.465	1.25 $\pm$ 0.9
10	0.3 $\pm$ 0.035	0.387 $\pm$ 0.186	0.287 $\pm$ 0.001	0.287 $\pm$ 0.001
11	0.295 $\pm$ 0.023	0.352 $\pm$ 0.129	0.287 $\pm$ 0.001	0.287 $\pm$ 0.001
12	0.292 $\pm$ 0.013	0.331 $\pm$ 0.095	0.287 $\pm$ 0.001	0.287 $\pm$ 0.001

Table 4-3. Reconstruction error ( $\mu\text{m}$ ) for pseudo-Zernike polynomials, presented as mean  $\pm$  1 standard derivation.

Order	Anterior		Posterior	
	Normal	Keratoconic	Normal	Keratoconic
6	1.091 $\pm$ 0.509	1.822 $\pm$ 1.503	3.575 $\pm$ 1.766	5.633 $\pm$ 3.882
7	0.703 $\pm$ 0.371	1.168 $\pm$ 1	2.472 $\pm$ 1.27	3.739 $\pm$ 2.635
8	0.431 $\pm$ 0.17	0.66 $\pm$ 0.506	1.054 $\pm$ 0.629	1.563 $\pm$ 1.126
9	0.334 $\pm$ 0.079	0.442 $\pm$ 0.217	0.636 $\pm$ 0.444	0.909 $\pm$ 0.773
10	0.289 $\pm$ 0.008	0.309 $\pm$ 0.055	0.286 $\pm$ 0.001	0.286 $\pm$ 0.001
11	0.288 $\pm$ 0.005	0.3 $\pm$ 0.034	0.286 $\pm$ 0.001	0.286 $\pm$ 0.001
12	0.287 $\pm$ 0.003	0.294 $\pm$ 0.021	0.285 $\pm$ 0.001	0.286 $\pm$ 0.001

Table 4-4. Reconstruction error ( $\mu\text{m}$ ) for Orthogonal Fourier-Mellin polynomials, presented as mean  $\pm$  1 standard derivation.

Order	Anterior		Posterior	
	Normal	Keratoconic	Normal	Keratoconic
6	1.039 $\pm$ 0.502	1.709 $\pm$ 1.447	3.438 $\pm$ 1.746	5.354 $\pm$ 3.79
7	0.688 $\pm$ 0.368	1.116 $\pm$ 0.962	2.434 $\pm$ 1.262	3.658 $\pm$ 2.587
8	0.417 $\pm$ 0.163	0.619 $\pm$ 0.466	1.004 $\pm$ 0.625	1.459 $\pm$ 1.092
9	0.33 $\pm$ 0.077	0.426 $\pm$ 0.2	0.635 $\pm$ 0.445	0.907 $\pm$ 0.773
10	0.286 $\pm$ 0.004	0.294 $\pm$ 0.024	0.284 $\pm$ 0.002	0.284 $\pm$ 0.001
11	0.284 $\pm$ 0.003	0.289 $\pm$ 0.014	0.283 $\pm$ 0.002	0.284 $\pm$ 0.001
12	0.283 $\pm$ 0.002	0.286 $\pm$ 0.009	0.283 $\pm$ 0.002	0.283 $\pm$ 0.001

Table 4-5. Reconstruction error ( $\mu\text{m}$ ) for Gaussian-Hermite polynomials, presented as mean  $\pm$  1 standard derivation.

Order	Anterior		Posterior	
	Normal	Keratoconic	Normal	Keratoconic
6	$1.397 \pm 0.573$	$2.711 \pm 1.781$	$4.321 \pm 1.761$	$7.774 \pm 4.418$
7	$0.891 \pm 0.401$	$1.628 \pm 1.209$	$3.026 \pm 1.284$	$4.964 \pm 3.052$
8	$0.482 \pm 0.195$	$0.857 \pm 0.658$	$1.197 \pm 0.678$	$1.957 \pm 1.362$
9	$0.366 \pm 0.104$	$0.574 \pm 0.372$	$0.751 \pm 0.463$	$1.17 \pm 0.87$
10	$0.3 \pm 0.034$	$0.384 \pm 0.18$	$0.29 \pm 0.003$	$0.299 \pm 0.016$
11	$0.295 \pm 0.022$	$0.35 \pm 0.124$	$0.288 \pm 0.002$	$0.291 \pm 0.005$
12	$0.292 \pm 0.013$	$0.329 \pm 0.091$	$0.287 \pm 0.001$	$0.287 \pm 0.001$

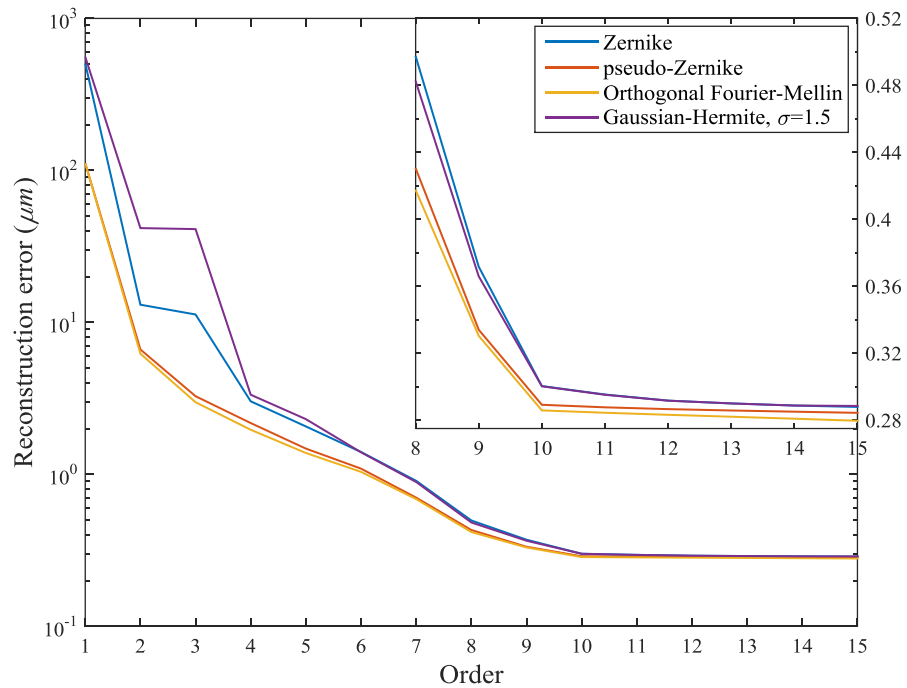


Figure 4-7. Mean reconstruction errors plotted for anterior normal corneal surfaces fitted by ZPs, PZPs, OFMPs and GHPs. An inset graph is added in the figure to show trivial difference in reconstruction errors of high orders.

The sequence of reconstruction goodness of the four polynomials are the same for all kinds of maps (anterior normal maps, anterior keratoconic maps, posterior normal maps and posterior keratoconic maps) and an example is given in Figure 4-7 for the anterior normal maps, showing mean reconstruction errors from order 1 to 15. It can be seen from Figure 4-7 that, on average, the OFMPs again fit topographies the best, followed by PZPs,

ZPs and GHPs. Further, GHPs still tend to match the behaviour of ZPs in orders larger than 10.

The reconstruction errors recorded from Table 4-2 to Table 4-5 also reveals that, in general for any particular set of polynomials, the anterior normal corneal surfaces tend to be fitted most accurately, followed by anterior keratoconic, posterior normal and finally posterior keratoconic surfaces. However, there is a cross-over at order 10, from which the posterior surfaces that appeared hard to fit by low order polynomials are fitted slightly better than anterior surfaces with order 10 and above. After the significant improvement in fitting of posterior surfaces from order 9 to 10, these surfaces are shown to be fitted almost equally well with order 10 and above, indicated by the very small standard derivation of the reconstruction errors in Table 4-2 to Table 4-5 and visualised by boxplots in Figure 4-8 for OFMPs.

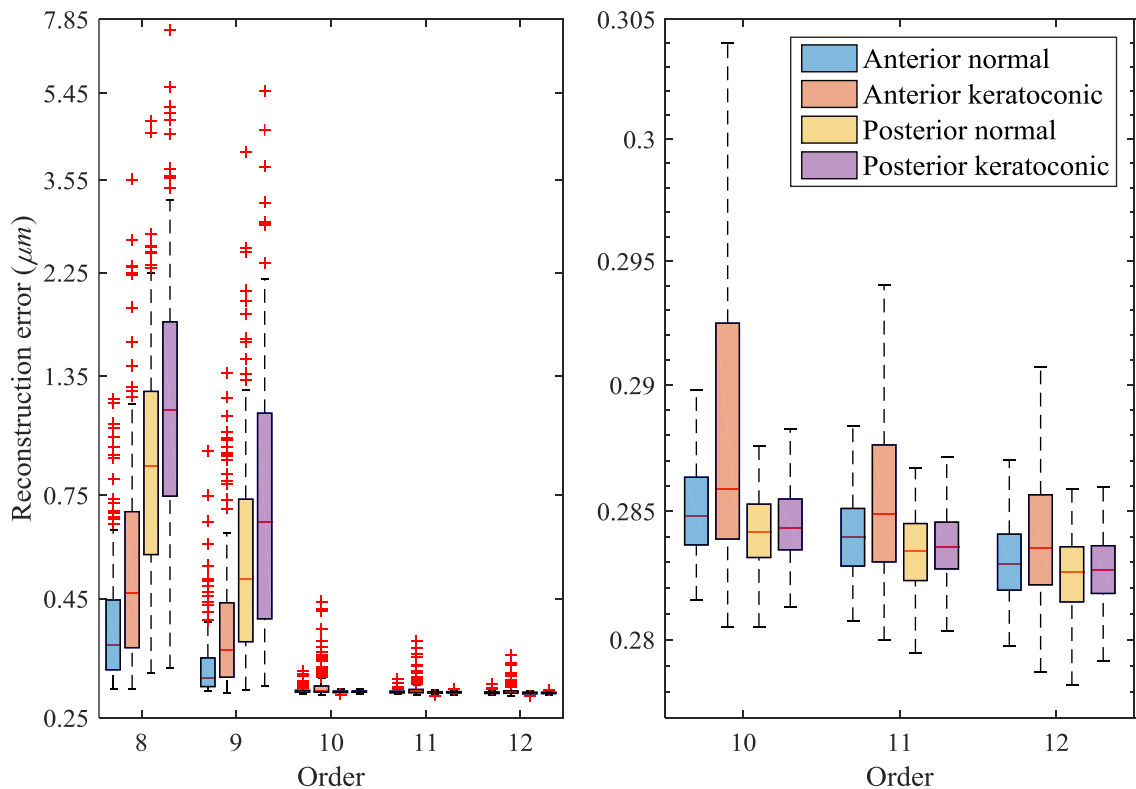


Figure 4-8. Boxplots of reconstruction errors by OFMPs from order 8 to 12 for anterior normal, anterior keratoconic, posterior normal and posterior keratoconic corneal surfaces. In the right figure, outliers are removed and only order 10 to 12 are included.

For each boxplot in Figure 4-8, the red line in the box marks the median of all the errors and the edges of the box are the 25th and 75th percentiles and the whiskers extend another 1.5 times of the length from the percentiles to the median. The whiskers length should cover approximately 99.3% of the data if they are normally distributed. The data outside the whisker reaches are considered outliers and marked with red plus symbols. It can be seen from Figure 4-8 that before order 10, the anterior normal corneal topographies are fitted most accurately, followed by anterior keratoconic, posterior normal and posterior keratoconic topographies. Similar numbers of outliers are found at this stage among all kinds of maps. The fits for posterior surfaces then seem to be significantly improved by order 10 as shown in the right figure of Figure 4-8, which is reflected by both the small magnitudes and narrow distributions of the reconstruction errors.

The cross-over behaviour above is believed to be caused by additional polynomials terms introduced by order 10 and above, which are complex and only helpful for complex surfaces while contribute little for simple surface, meanwhile, higher electronic noise level when measuring posterior surfaces makes the posterior surfaces noisier and thus more complex. Because of the same reason, the less noisy normal keratoconic topographies seem to benefit the least from high order polynomials features. However, it should be noted that using polynomials with very high orders to fit noisy topography is disadvantageous because significant amount of measurement noise is captured while in practice it is expected to be filtered. Although the posterior surfaces seem to be fitted remarkably well using high orders, their risks of overfitting may be significantly higher than the anterior surfaces. In Figure 4-9, the absolute magnitudes of ZPs coefficients for typical anterior normal, anterior keratoconic, posterior normal, posterior keratoconic corneal topographies are illustrated. ZPs have been selected for this example because their shapes are simpler and they have smaller number of terms for a given order. It can be

seen from the up-left of Figure 4-9 that the first and fifth terms seem to be most significant terms. By carefully looking at the feature shapes of ZPs in Figure 3-6, it is easy to understand that the first term tells the average distance of the data points to the reference plane passing through the apex. The fifth term generally determines how close the shape is to a sphere. For the keratoconic topographies including both anterior and posterior surfaces, the second and third features also have relatively big magnitudes; these terms generally tell how severe the surface is tilted and are bound to have bigger magnitude for keratoconic maps. The other sub-figures in Figure 4-9 shows the magnitudes of higher order terms decrease for all maps and collectively more high order terms are seen to have big magnitudes for posterior surfaces, and again this is believed to be caused by higher noisy levels in these maps. The anterior keratoconic map, although is less noisy, is more complex than the anterior normal map, so more high order polynomial terms are needed. However, the anterior keratoconic map is seen to benefit less from very high order terms than the posterior surfaces as shown in the bottom-right of Figure 4-9 since these terms tend to collect more noise-induced complex surface components existing in posterior surfaces, which is disadvantageous.



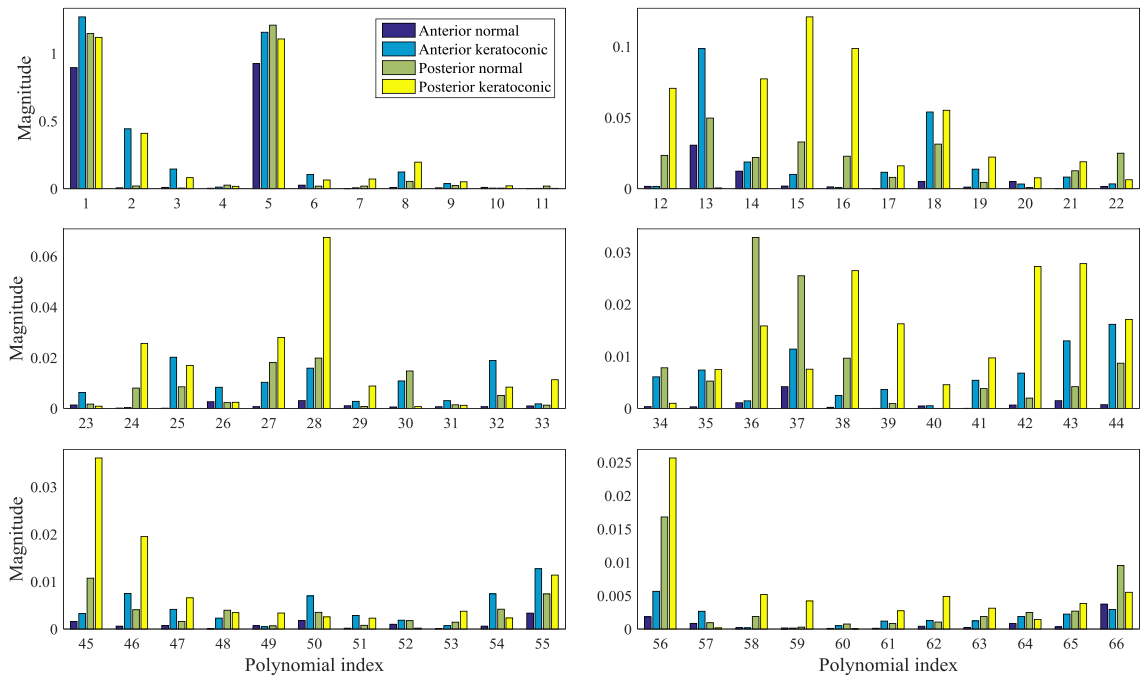


Figure 4-9. Magnitudes of coefficients for ZPs up to order 10 for typical anterior normal, anterior keratoconic, posterior normal and posterior keratoconic corneal topographies

#### 4.4 TOPOGRAPHY PREDICTION

As stated in the introduction, an important function of polynomials fitting is between-point interpolation. In addition to reconstruction, it is also of great importance to assess the reliability of the polynomials expression in predicting points between the measured points. To test this feature, the original data points of each topography map are divided into two sets; the first set is considered as the measured locations on the surface and used to reconstruct the surface. Once the polynomial coefficients are determined, the locations (x and y coordinates) of the second point set are used to predict the corresponding z coordinates, which are then compared to the actual measured values and the RMS error between the predicted and measured z coordinates denotes prediction error. An implementation of such a test is displayed in Figure 4-10 showing mean reconstruction and prediction errors for all 200 anterior normal corneal topographies. The original Pentacam topography as exported from the instrument usually has 0.1 mm spacing between measurements points. The reconstruction in Figure 4-10 selects the first set from

these original points such that the spacing becomes 0.2 mm resulting 1961 points, while the same number of points are randomly chosen from the rest of original points to assess goodness in prediction of the reconstructed surface based on the first data set. It can be seen from Figure 4-10 that even though the number of points in reconstruction has been reduced to a quarter of the original set, the reconstruction behaviour remains similar with Figure 4-7 where all original points are involved in the reconstruction process.

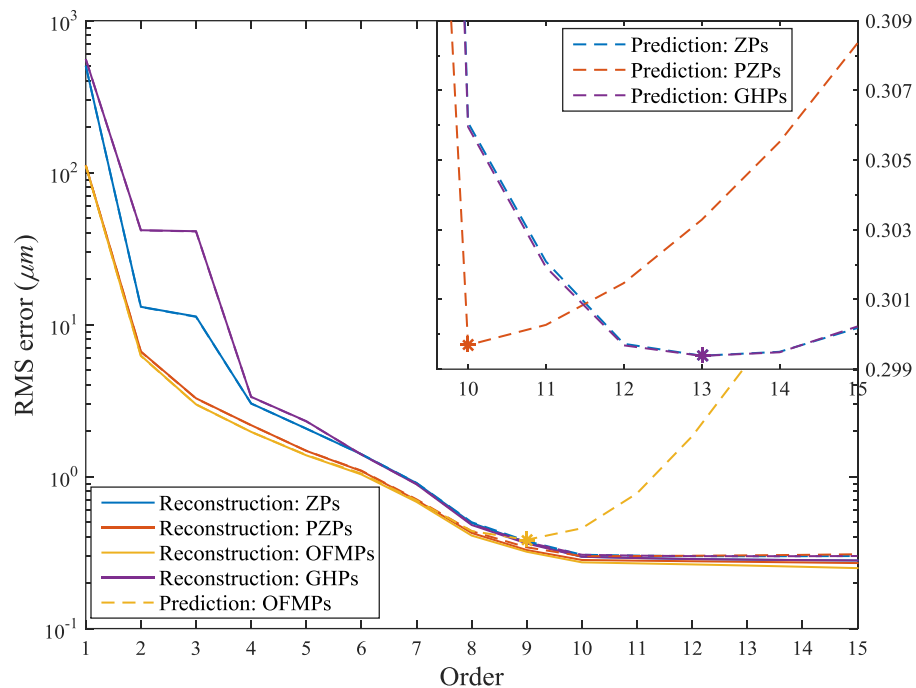


Figure 4-10. Mean reconstruction and prediction errors plotted for anterior normal corneal surfaces fitted by ZPs, PZPs, OFMPs and GHPs

More importantly, it is revealed in Figure 4-10 that overfitting of the original maps may occur where the prediction of nearby points may become worse beyond a certain polynomial order from which the prediction error begins to increase even if the reconstruction is being consistently improved. This phenomenon is due to the fact that the reconstruction by LS method is mere an optimisation that focuses only on the points that have been included in the calculations, while taking no account of how the reconstructed surface would be in the nearby area. With the increase in order, more

complex polynomial terms are included in the calculation, which on one hand improves the reconstruction outcomes of the included points but on the other hand increases the risk of vibrated or excessively curved nearby shapes around the points in this optimisation, creating the symptom of overfitting. It is also expected that the inflection of prediction curves that appear in Figure 4-10 could take place earlier (under smaller order) if the spacing of points in the reconstruction set decreases further beyond 0.2 mm. This is validated in Figure 4-11 where sparser sets are selected from the original data points for reconstruction and again same number of points are randomly chosen from the rest of the original data for assessment of prediction performance.

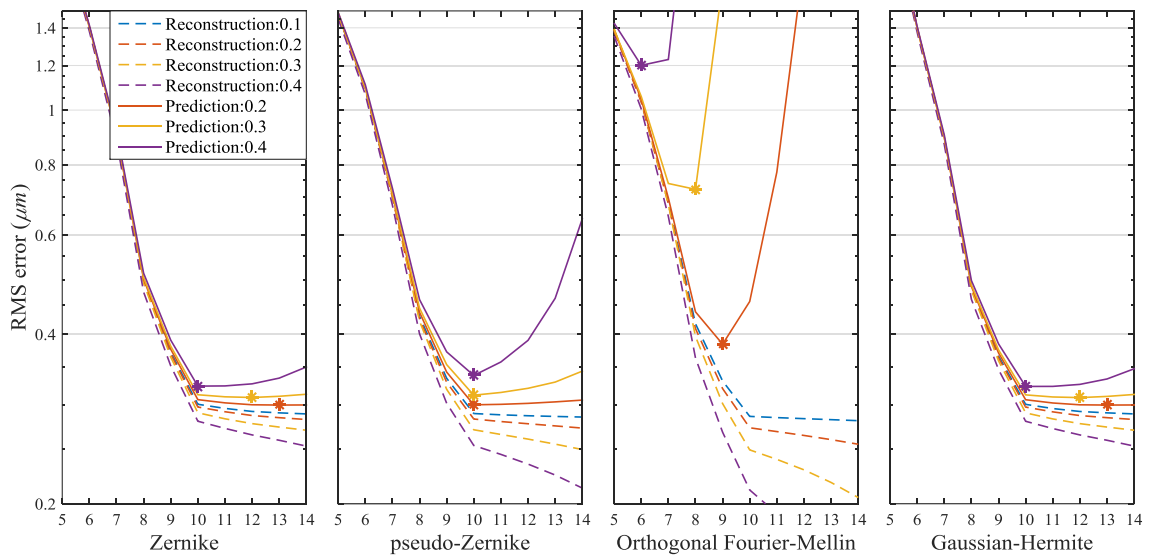


Figure 4-11. Mean reconstruction and prediction errors by ZPs, PZPs, OFMPs and GHPs using different sub-sets of the original anterior normal corneal topography as reconstruction sets

Except for the PZPs, the inflection orders of the prediction curves for ZPs, OFMPs and GHPs all move backwards with the increasing spacing of maps used for reconstruction. As a result, the best achieved prediction is worsened. Also illustrated in Figure 4-11, the reconstruction errors are seen to become smaller for sparser maps because of the reduced number of points employed in the optimisation.

It can also be seen from Figure 4-11 that the OFMPs seem to be most sensitive to the reduction of points when predicting nearby points around the ones used in reconstruction. This is believed to be introduced by rapidly increased complex terms in high order, which makes it easier for OFMPs to lead to a more complex reconstructed surface even though it passes through the measurements most accurately. While Figure 4-10 and Figure 4-11 are only concerned with the anterior normal corneal topographies, the inflection orders of the prediction errors and the corresponding error values including both reconstruction and prediction are given in Table 4-6 to Table 4-9 for all the four groups of topographies – anterior normal, anterior keratoconic, posterior normal and posterior keratoconic maps. In each table, the last column presents the ratios between prediction and reconstruction errors.

Table 4-6. Inflection orders of prediction curves and the corresponding prediction and reconstruction errors by various polynomials for **anterior normal** corneal topography. The errors are presented as mean  $\pm$  1 standard derivation and in  $\mu\text{m}$ .

	Spacing	Inflection order	Prediction error	Reconstruction error	Prediction/Reconstruction
ZPs	0.2 mm	13	$0.299 \pm 0.01$	$0.284 \pm 0.01$	1.053
	0.3 mm	12	$0.309 \pm 0.014$	$0.277 \pm 0.014$	1.112
	0.4 mm	10	$0.325 \pm 0.036$	$0.28 \pm 0.034$	1.160
PZPs	0.2 mm	10	$0.3 \pm 0.009$	$0.283 \pm 0.009$	1.060
	0.3 mm	10	$0.311 \pm 0.009$	$0.271 \pm 0.009$	1.151
	0.4 mm	10	$0.341 \pm 0.014$	$0.254 \pm 0.011$	1.344
OFMPs	0.2 mm	9	$0.38 \pm 0.077$	$0.32 \pm 0.078$	1.187
	0.3 mm	8	$0.742 \pm 0.244$	$0.396 \pm 0.163$	1.872
	0.4 mm	6	$1.297 \pm 0.629$	$1.005 \pm 0.494$	1.291
GHPs	0.2 mm	13	$0.299 \pm 0.01$	$0.284 \pm 0.01$	1.053
	0.3 mm	12	$0.308 \pm 0.013$	$0.277 \pm 0.013$	1.112
	0.4 mm	10	$0.325 \pm 0.035$	$0.28 \pm 0.033$	1.159

Table 4-7. Inflection orders of prediction curves and the corresponding prediction and reconstruction errors by various polynomials for **anterior keratoconic** corneal topography. The errors are presented as mean  $\pm$  1 standard derivation and in  $\mu\text{m}$ .

	Spacing	Inflection order	Prediction error	Reconstruction error	Prediction/Reconstruction
ZPs	0.2	15	$0.315 \pm 0.043$	$0.296 \pm 0.044$	1.063
	0.3	13	$0.337 \pm 0.066$	$0.3 \pm 0.067$	1.125
	0.4	12	$0.372 \pm 0.103$	$0.304 \pm 0.091$	1.227
PZPs	0.2	13	$0.308 \pm 0.015$	$0.28 \pm 0.014$	1.100
	0.3	11	$0.327 \pm 0.035$	$0.277 \pm 0.035$	1.177
	0.4	10	$0.363 \pm 0.059$	$0.275 \pm 0.056$	1.323
OFMPs	0.2	10	$0.471 \pm 0.12$	$0.281 \pm 0.023$	1.677
	0.3	8	$1.023 \pm 0.627$	$0.595 \pm 0.463$	1.718
	0.4	7	$2.076 \pm 1.818$	$1.059 \pm 0.93$	1.960
GHPs	0.2	15	$0.317 \pm 0.047$	$0.299 \pm 0.049$	1.061
	0.3	13	$0.336 \pm 0.064$	$0.299 \pm 0.065$	1.123
	0.4	12	$0.369 \pm 0.098$	$0.302 \pm 0.088$	1.221

Table 4-8. Inflection orders of prediction curves and the corresponding prediction and reconstruction errors by various polynomials for **posterior normal** corneal topography. The errors are presented as mean  $\pm$  1 standard derivation and in  $\mu\text{m}$ .

	Spacing	Inflection order	Prediction error	Reconstruction error	Prediction/Reconstruction
ZPs	0.2 mm	10	$0.293 \pm 0.003$	$0.284 \pm 0.002$	1.033
	0.3 mm	10	$0.299 \pm 0.005$	$0.277 \pm 0.005$	1.081
	0.4 mm	10	$0.31 \pm 0.008$	$0.269 \pm 0.006$	1.155
PZPs	0.2 mm	10	$0.297 \pm 0.004$	$0.28 \pm 0.003$	1.063
	0.3 mm	10	$0.308 \pm 0.006$	$0.268 \pm 0.005$	1.152
	0.4 mm	10	$0.337 \pm 0.013$	$0.251 \pm 0.006$	1.343
OFMPs	0.2 mm	10	$0.433 \pm 0.07$	$0.271 \pm 0.003$	1.598
	0.3 mm	8	$1.31 \pm 0.713$	$0.981 \pm 0.619$	1.335
	0.4 mm	7	$3.958 \pm 2.113$	$2.325 \pm 1.214$	1.702
GHPs	0.2 mm	11	$0.295 \pm 0.004$	$0.284 \pm 0.003$	1.039
	0.3 mm	10	$0.302 \pm 0.006$	$0.279 \pm 0.006$	1.080
	0.4 mm	10	$0.313 \pm 0.008$	$0.271 \pm 0.006$	1.155

Table 4-9. Inflection orders of prediction curves and the corresponding prediction and reconstruction errors by various polynomials for **posterior keratoconic** corneal topography. The errors are presented as mean  $\pm$  1 standard derivation and in  $\mu\text{m}$ .

	Spacing	Inflection order	Prediction error	Reconstruction error	Prediction/Reconstruction
ZPs	0.2 mm	10	$0.294 \pm 0.003$	$0.283 \pm 0.003$	1.038
	0.3 mm	10	$0.299 \pm 0.005$	$0.277 \pm 0.004$	1.079
	0.4 mm	10	$0.312 \pm 0.008$	$0.268 \pm 0.006$	1.164
PZPs	0.2 mm	10	$0.298 \pm 0.003$	$0.279 \pm 0.003$	1.066
	0.3 mm	10	$0.308 \pm 0.006$	$0.268 \pm 0.005$	1.151
	0.4 mm	10	$0.338 \pm 0.012$	$0.25 \pm 0.007$	1.350
OFMPs	0.2 mm	10	$0.438 \pm 0.065$	$0.271 \pm 0.003$	1.616
	0.3 mm	8	$1.805 \pm 1.205$	$1.427 \pm 1.076$	1.265
	0.4 mm	8	$4.914 \pm 2.342$	$1.309 \pm 0.986$	3.754
GHPs	0.2 mm	12	$0.296 \pm 0.003$	$0.282 \pm 0.003$	1.051
	0.3 mm	12	$0.304 \pm 0.006$	$0.273 \pm 0.005$	1.112
	0.4 mm	11	$0.321 \pm 0.011$	$0.267 \pm 0.008$	1.201

It can be seen that except for OFMPs, the inflection orders for ZPs, PZPs and GHPs are all no less than 10. The best achieved prediction errors at the inflection orders are always larger than the corresponding reconstruction errors (Prediction/Reconstruction ratio being larger than 1). To better present the sequence of goodness in prediction of all polynomials for all kinds of maps, the prediction errors at the inflection orders are displayed in Figure 4-12 with error bars showing standard derivations.

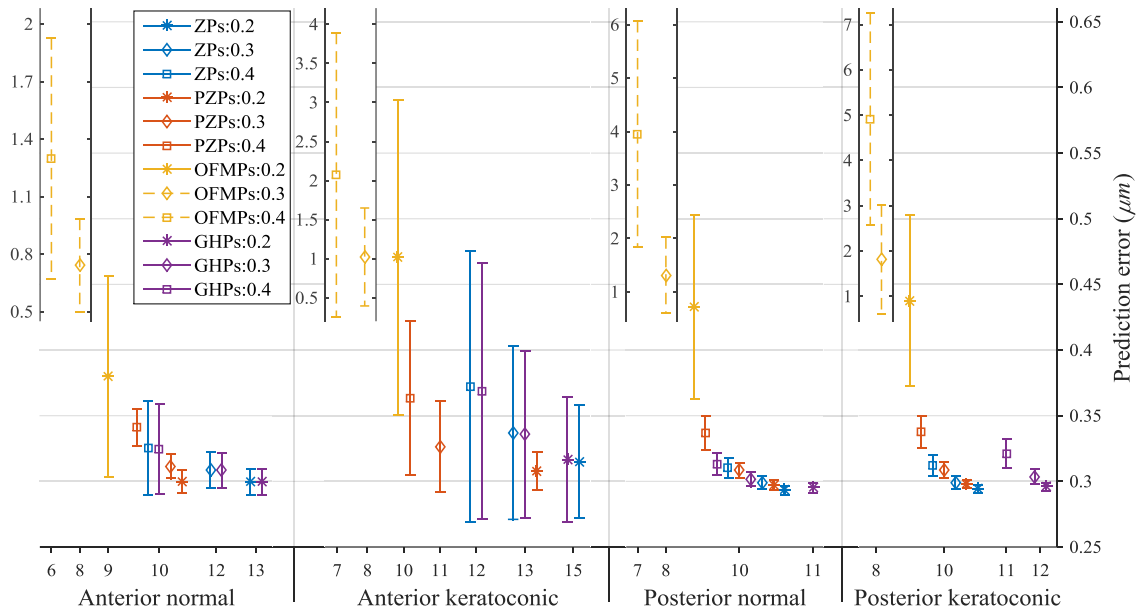


Figure 4-12. Inflection orders of prediction curves and the corresponding prediction errors by ZPs, PZPs, OFMPs and GHPs for anterior normal (first column), anterior keratoconic (second column), posterior normal (third column) and posterior keratoconic (last column) corneal topography. The horizontal axes represent the inflection order, from which the prediction error begins to increase. The prediction errors by OFMPs, when the data spacing in reconstruction is 0.3 mm and 0.4 mm, are much larger than the rest and thus are displayed at the up-left corner of each column in larger scales. The remaining prediction errors are displayed by a small scale showing on the very right side of the figure. All results in figure are in  $\mu\text{m}$ .

As expected, the sensitivity of OFMPs is obvious in all groups of topography, i.e. they begin to have difficulty in predicting nearby points in lower orders for all cases, and when the spacing increases further the inflection order always decreases for OFMPs. Further, the prediction error becomes larger than with other polynomials. In contrast, PZPs tend to be most stable for prediction with the inflection orders for PZPs being 10 for most cases. For all sets of polynomials, regardless of whether the inflection orders change or not, a constant trend is obtained in which the prediction error increases when the spacing of points in reconstruction set increases. It should be also noted that while the inflection orders are not less than 10 for all polynomials, the prediction errors for posterior surfaces are all smaller than that for anterior surfaces. This is consistent with the reconstruction behaviour revealed in Figure 4-8 that for polynomial orders of or higher than 10, the reconstruction errors for posterior surfaces are smaller than anterior surfaces. However, it should be borne in mind that using very high order polynomial terms to fit and predict

the noisier posterior surfaces may carry higher risks of overfitting. The trend above does not hold for cases where the inflection orders are less than 10 as happened only for OFMPs. Except for OFMPs of resolutions 0.3 mm and 0.4 mm, the best achieved prediction errors are very small, being less than 0.5  $\mu\text{m}$  on average, however wide range of prediction errors are seen for the anterior maps, being widest for anterior keratoconic maps.

#### 4.5 CONCLUDING REMARKS

This chapter has presented the results of topography fitting. A comparison study on two kinds of methods to estimate the polynomials' coefficients suggested that least-square (LS) method was more suitable for fitting corneal topography. While a good number of orthogonal polynomials were included in the study, some were seen to provide the same performance as for the well-known Zernike polynomials and the extensively studied OFMPs, commonly adopted in the image processing community. Only four orthogonal polynomials (ZPs, PZPs, OFMPs and GHPs) were then kept for fitting of all corneal topographies. The OFMPs were seen to outperform the others in fitting anterior and posterior topographies from both normal and keratoconic eyes. Anterior topographies can be fitted with reasonable accuracy easier but posterior topographies, which are expected to have lower measurement accuracy, may in return be fitted with smaller errors by higher order polynomials terms. However, it is not practical to increase the fitting order without caution as it is shown that the higher the fitting order is, the more problematic the prediction may become. The results of this chapter will be further discussed in Chapter 7.



## CHAPTER 5

### RESULTS OF TOPOGRAPHY MATCHING

---

#### 5.1 INTRODUCTION

The aim of topography matching study is to assess and further develop methods to combine corneal topographies collected from the different viewpoints (central and peripheral maps) in order to observe the entire corneal surface. Based on the methods given in Section 3.3, this chapter reports the achievements in matching and combining multiple topography maps.

The topography map, obtained using Medmont topographer in this study, covers a 12 mm diameter area and is presented by a 50×50 grid, resulting in a resolution of  $12/49 \approx 0.245 \text{ mm}$ . The coverage of the map is quite wide but the peripheral measurements appear to be problematic. As shown in Figure 5-1, an irregular flat area is highlighted and this irregular shape is believed to be caused by measurement inaccuracy. In fact, the validation of topographic data from current commercially available instruments is the subject of a considerable volume of literature, invariably showing a loss of repeatability and accuracy at the periphery [284-288]. During the topography measuring for this study, data were collected at least twice for both central and peripheral maps, which enables a repeatability study to address underlying repeatability and accuracy problem as mentioned above.

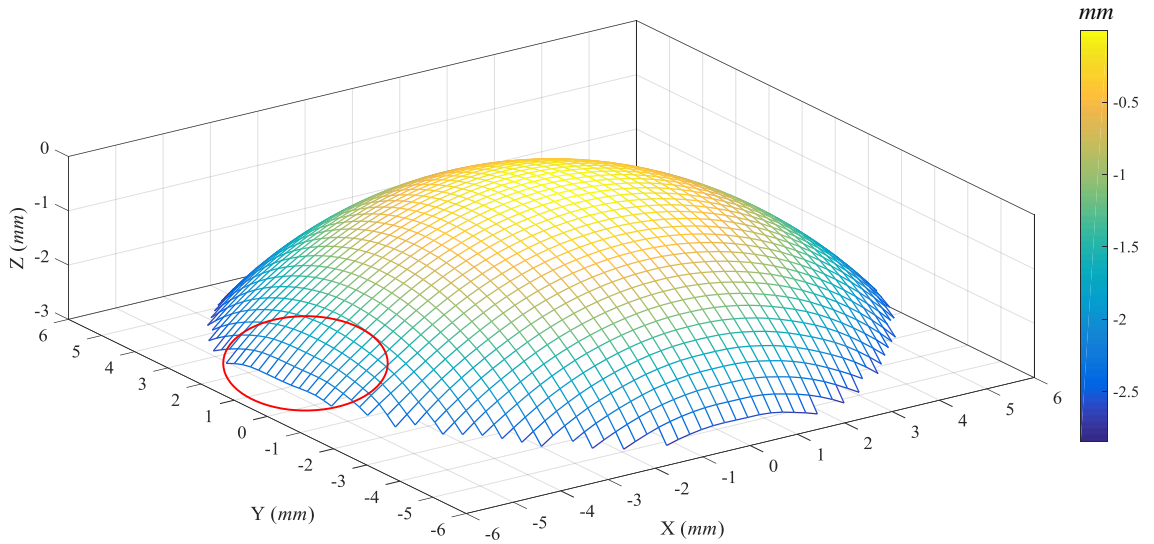


Figure 5-1. A typical central topography provided by Medmont E300, showing irregular peripheral shape

## 5.2 REPEATABILITY OF CLINICAL DATA

In the topography matching study, multiple measurements for each viewpoint led to the collection of 42 central and 74 peripheral data pairs. The topographies share the same x and y coordinates, meaning the repeatability can be assessed by comparing the z coordinates. For each data pair, a series of repeatability errors are computed as root mean square errors (RMSEs) in z values of points within circles of radii varying from minimal 0.245 mm (data resolution) to maximal 6 mm,

$$E_R = \frac{1}{m_R} \sum_{j=1}^{m_R} |z_{i_1}(j) - z_{i_2}(j)|; \quad i_1, i_2 = 1, 2, \dots; \quad i_1 \neq i_2 \quad (5.1)$$

where  $m_R$  is the number of points within a circle of radius  $R$ , and  $z_{i_1}, z_{i_2}$  are measured elevations with the same x, y coordinates.

It is shown in Figure 5-2 that the repeatability of the measurement decreases with distance from the centre towards the periphery. Also, peripheral maps are less repeatable than central maps. Although the repeatability test cannot fully reflect the collection accuracy, it does indicate that, in practice, only a subset of the measurement is usable.

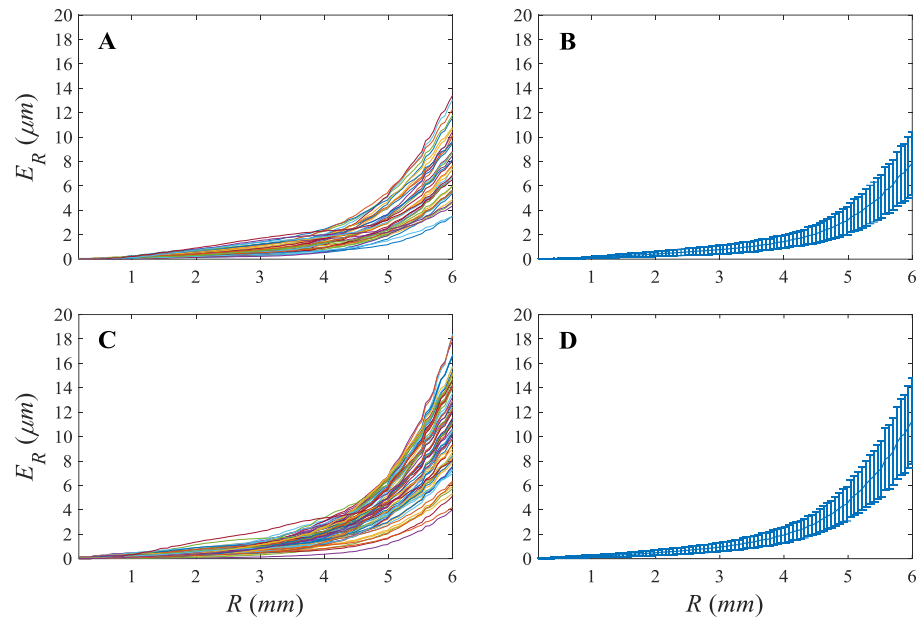


Figure 5-2. Repeatability tests of clinical height maps. **A, C**: individual plots for the 42 central and 74 peripheral map pairs respectively. **B, D**: corresponding mean curves with error bars  $\pm$  standard derivation.

### 5.3 DATA SETS AND EVALUATION METHODS

The repeatability study suggests that uncertain collection errors (e.g. noise) may decrease the repeatability and accuracy of clinical topography. To avoid these uncertain factors, a set of simulated pairs of central (static) and peripheral (dynamic) maps has been generated to carry out an initial comparative study of matching techniques. These maps are generated based on the same conic surface in Franklin et al. [109] (radius  $r_0 = 7.2 \text{ mm}$ , asphericity  $Q = -0.51$ ). To prevent the test set from being rotationally symmetric, the conic surfaces produced have been elongated in the X direction by a factor  $\sqrt{1.05}$ . The simulated maps have the same resolution as clinical data and cover 9 mm diameter circular regions, i.e. where the clinical data is deemed reasonably repeatable according to Figure 5-2, and with similar coverage to corneal topography available from videokeratography maps. The central map is generated directly from the conic surface equation, which is then transformed by pre-determined rigid-body transformations (rotation, translation) and the peripheral maps are generated using the transformed conic

equations. The transformations are designed to simulate typical clinical peripheral data overlapping with the central map.

Clinical collections include various uncertainties represented in this study by simulated and quasi-clinical data. In the first exercise the simulated elongated conic section above is considered with Gaussian random noise to represent measurement uncertainties (typically introduced by electronic noise and data processing procedures). In the second and third exercises clinical data is used. The central 9 mm diameter portion from a clinical 12 mm diameter central map measured from the front is taken to be the central map in both exercises. The original 12 mm diameter map is then shifted by the same pre-determined transformation as above to create the peripheral maps. In the second exercise, the peripheral map is obtained by interpolating the shifted original map on the same grid as the central map. In the third, points on the shifted original map that lie inside the central 9 mm diameter are directly kept as peripheral maps. This is different from what happens in practice, but the noisy measurement of the transformed map is retained (not smoothed by the interpolation process as in the second exercise).

The algorithms and methods in Section 3.3 are used to attempt to recover the transformation that has been applied to the peripheral maps. The convergence properties of Direct search (DS) and iterative closest point (ICP) registration methods were evaluated with the initial estimate set to  $\mathbf{r}_0 = (0.0 \ 0.0 \ 0.0 \ 0.0 \ 0.0 \ 0.0)^T$ . Closest-point (CP) and vertical and normal shooting (VS and NS) methods were included and Zernike polynomials were applied to fit the static map in VS and NS and to compute surface normals as needed. The order of the Zernike polynomials used in the study is primarily chosen as 10, i.e. 66 terms. The assessment of registration outcomes was achieved using the two error measurements defined below.

Alignment error ( $\mu\text{m}$ ): The root mean square (RMS) of distances (point-to-point or point-to-plane) of all pairs defined as,

$$E_a = \sqrt{\frac{1}{m} f(\mathbf{r})} \quad (5.2)$$

where  $f(\mathbf{r})$  is the objective function in the DS and ICP and  $m$  is number of all data pairs in the objective function.

Registration error: The RMS error between the computed transformation and the exact one.

$$E_r = \sqrt{\frac{1}{6} \sum_{i=1}^6 \|r_i - (r_e)_i\|^2} \quad (5.3)$$

where  $r_e$  denotes the exact transformation and  $(r_e)_i$  is the  $i$ th term.

#### 5.4 SIMULATED AND QUASI-CLINICAL EXERCISES

All the methods and algorithms were coded in MATLAB, and run on a standard personal computer with Intel Core i7 processor and 12 GB RAM. The convergence of the different registration methods for simulated and quasi-clinical surface pairs is evaluated in this section. A set of transformations were considered and the results were found to be similar, therefore only one case is given here. The registration outcomes for simulated surface pairs with no noise are presented in Figure 5-3, Figure 5-4, and Table 5-1. The closest point method is implemented using the closest pairs of discrete points on the two surfaces.

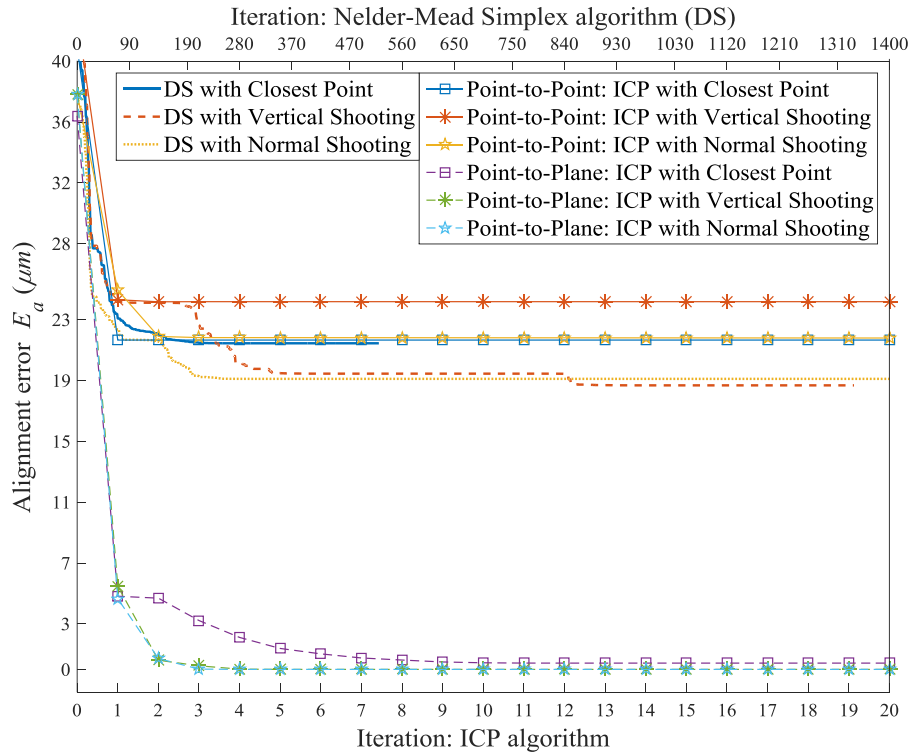


Figure 5-3. Convergence of registration algorithms, simulated surface with no noise,  $E_a$  vs. iteration.

It is clear that the ICP point-to-plane routines, implemented by equation (3.43) using the Levenberg-Marquardt (L-M) algorithm, give excellent results whereas the DS and ICP point-to-point routines converge with significant alignment and registration errors. This is due to inflexibility in the objective function that does not permit mutual sliding between the static and dynamic surfaces.

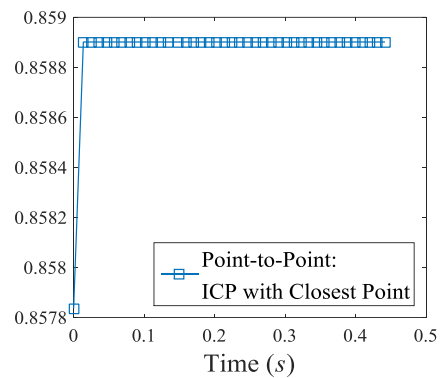
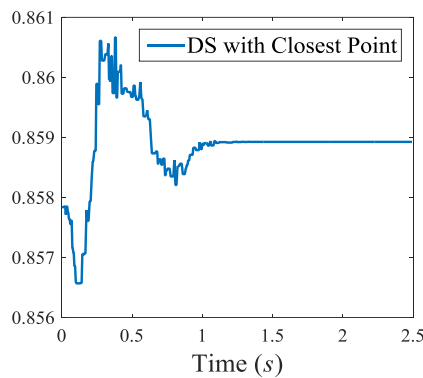
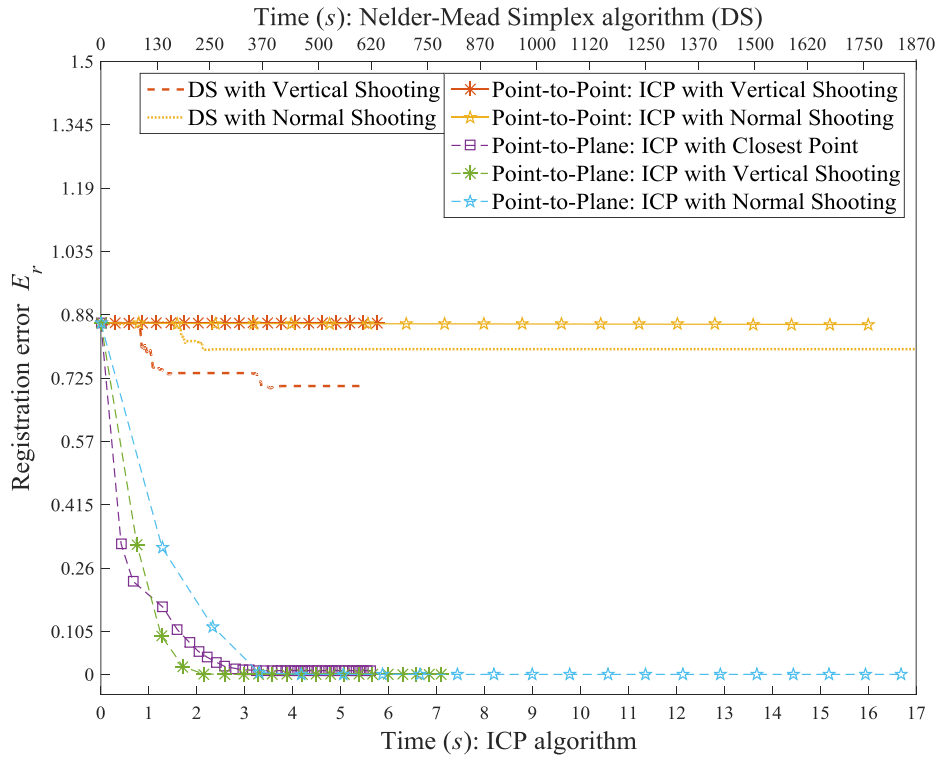


Figure 5-4. Convergence of registration algorithms, simulated surface with no noise,  $E_r$  vs. time. The closest-point variants of DS and ICP routines converge extremely rapidly and are shown separately in sub-figures on the lower left and right (respectively).

Table 5-1 shows that ICP variants with vertical and normal shooting produce perfect solutions in the absence of noise. The ICP point-to-plane CP variant converges very rapidly and gives very good results, but not quite as good as the point-to-plane VS and NS routines. The other routines all show significant errors and will not be considered further.

Table 5-1. Rigid-body transformation by various methods.

Exact	Direct Search method			Iterative Corresponding Point algorithm						
				<i>Point-to-point</i>			<i>Point-to-plane</i>			
	CP	VS	NS	CP	VS	NS	CP	VS	NS	
$\mathcal{G}_x$	-0.08	0.009	-0.022	0.007	0.009	0.008	0.007	-0.079	-0.08	-0.08
$\mathcal{G}_y$	-0.25	0.008	-0.037	-0.019	0.006	0.005	0.003	-0.247	-0.25	-0.25
$\mathcal{G}_z$	0.08	0.001	0.292	0.261	0.0	0.0	0.0	0.081	0.08	0.08
$t_x$	-2	-0.003	-0.376	-0.175	0.004	0.003	-0.007	-1.981	-2.0	-2.0
$t_y$	0.5	-0.002	0.121	-0.035	-0.005	-0.006	0.003	0.489	0.5	0.5
$t_z$	-0.3	-0.011	-0.036	-0.028	-0.026	-0.028	-0.027	-0.293	-0.3	-0.3
$E_r$		0.857	0.701	0.794	0.859	0.858	0.854	9.21E-03	6.29E-08	6.29E-08

A comparison of ICP point-to-plane CP, VS and NS routines based on minimisation using the Levenberg-Marquardt (L-M) algorithm and the linearisation/least-squares (LLS) approach is presented in Figure 5-5 and Table 5-2. In Figure 5-5, the CP convergence is illustrated in the first column, VS convergence in the second column and NS convergence in the third column. The solid curves show the results of simulated conic surfaces with added zero-mean Gaussian noise of standard deviation 2  $\mu\text{m}$  (close to the collection error of the topographer). The dash-dot and dotted curves correspond to the second and third exercises described towards the end of section ‘Data sets and evaluation methods’. Interpolation was carried out using biharmonic spline interpolation [260] in the second exercise. Registration outcomes are detailed in Table 5-2 where it is seen that the known transformation is recovered to the same (identical) high degree of accuracy by VS and NS methods when using L-M and LLS routines for all noisy data sets.



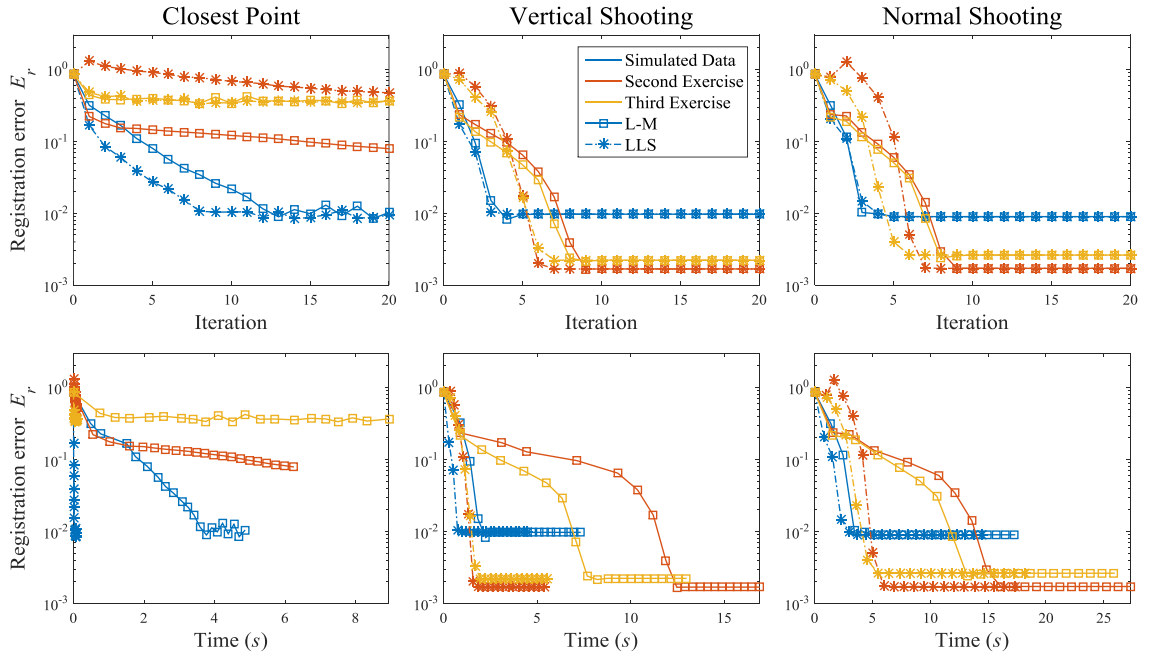


Figure 5-5. Convergence of ICP point-to-plane routines – noisy data, the registration errors are presented in log scale. In all figures, the data sets are distinguished by colours and L-M and LLS methods are distinguished by markers and line types.

Table 5-2. ICP point-to-plane transformations – noisy data

		Closest Point			Vertical Shooting			Normal Shooting			
Exact		Simulated Data	Second Exercise	Third Exercise	Simulated Data	Second Exercise	Third Exercise	Simulated Data	Second Exercise	Third Exercise	
L-M	$g_x$	-0.08	-0.078	-0.066	0.006	-0.083	-0.080	-0.081	-0.082	-0.080	-0.081
	$g_y$	-0.25	-0.247	-0.242	-0.183	-0.249	-0.250	-0.250	-0.250	-0.250	-0.250
	$g_z$	0.08	0.077	0.093	0.249	0.078	0.081	0.079	0.078	0.081	0.079
	$t_x$	-2	-1.977	-1.939	-1.392	-1.995	-2.003	-2.001	-1.998	-2.003	-2.001
	$t_y$	0.5	0.495	0.368	-0.355	0.523	0.497	0.505	0.522	0.497	0.506
	$t_z$	-0.3	-0.293	-0.276	-0.157	-0.300	-0.300	-0.301	-0.301	-0.300	-0.301
	$E_r$		1.029E-02	6.075E-02	4.401E-01	9.715E-03	1.683E-03	2.227E-03	8.987E-03	1.716E-03	2.625E-03
LLS	$E_r$		9.491E-03	3.548E-01	3.620E-01	9.715E-03	1.683E-03	2.227E-03	8.987E-03	1.716E-03	2.625E-03
	$g_x$	-0.08	-0.079	-0.006	-0.007	-0.083	-0.080	-0.081	-0.082	-0.080	-0.081
	$g_y$	-0.25	-0.247	-0.253	-0.159	-0.249	-0.250	-0.250	-0.250	-0.250	-0.250
	$g_z$	0.08	0.075	0.224	0.018	0.078	0.081	0.079	0.078	0.081	0.079
	$t_x$	-2	-1.979	-1.951	-1.255	-1.995	-2.003	-2.001	-1.998	-2.003	-2.001
	$t_y$	0.5	0.504	-0.352	0.070	0.523	0.497	0.505	0.522	0.497	0.506
	$t_z$	-0.3	-0.294	-0.278	-0.127	-0.300	-0.300	-0.301	-0.301	-0.300	-0.301

The L-M and LLS approaches generally converge successfully with the LLS routine converging fastest. The only exception is that of CP registration with clinical data, in which case neither method converges successfully. It is not possible to distinguish

between the VS and NS approaches, both of which produce excellent results. However, VS is simpler and faster than NS, so there seems to be no reason why NS would be preferred over VS.

## 5.5 CLINICAL DATA

In this section, clinical data in the form of measured central and peripheral maps described at the beginning of this chapter are used. 10 collections of one central map and four peripheral maps (superior, inferior, temporal, nasal) are selected from all available data, each collection leading to one combined map. It has already been demonstrated that points close to the periphery of both the central and peripheral maps are less accurate than points close to the centre. Thus, it would be expected that rejection of peripheral points on both maps should lead to better registration, but at the cost of reduced area of combined map. In the present investigation, central maps that vary in radius from 3.55 mm to 6 mm are considered. In each case of different central-map radius the peripheral-map radius is varied from 3.55 mm to the radius of the particular central map in question. The increment in radii for both central and peripheral maps is 0.245 mm. The ICP point-to-plane VS & LLS routine is used. It is shown in Figure 5-6 (upper-left) that, in general, the more peripheral measurements are rejected the smaller is the alignment error, but the increase in the size of combined map is lessened, as shown in the remaining sub-figures of Figure 5-6. It is also can be concluded that when the radius under consideration is below a certain value (e.g. radius 4.78 mm) the alignment error changes very little, and is quite small (around 1  $\mu\text{m}$ ).

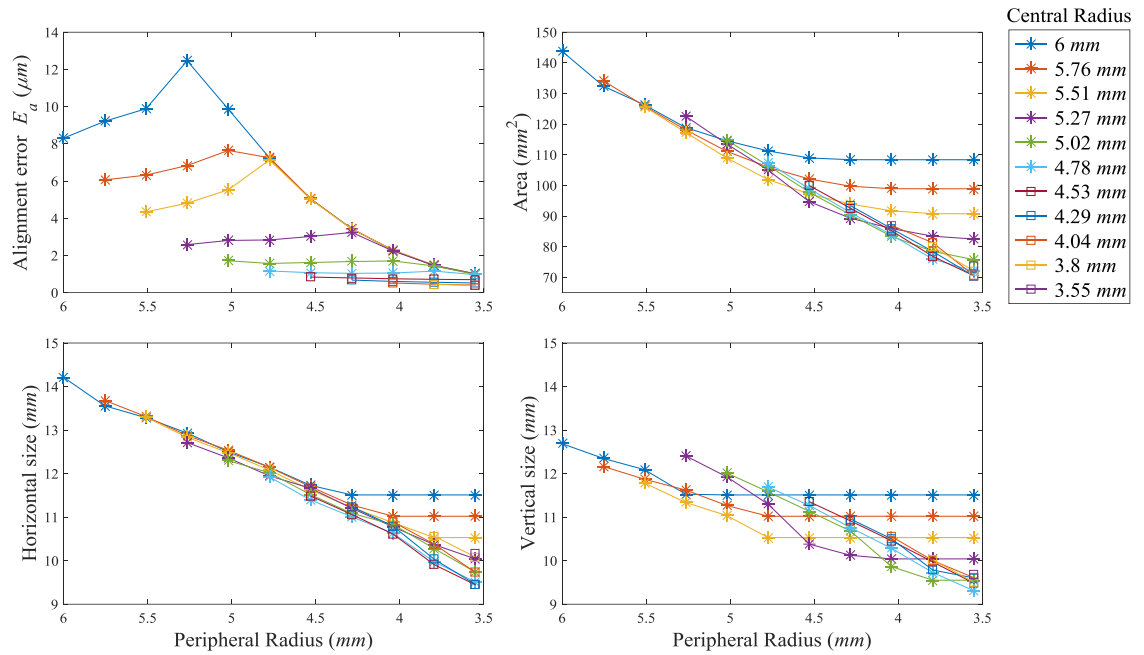


Figure 5-6. Registration outcomes of clinical maps for one collection. Alignment error of one pair of central and peripheral maps (upper left), combined area (upper right) and horizontal and vertical dimensions of the combined area (lower left and right) for different radii of central and peripheral maps.

The alignment error and dimensions of the combined map are detailed in Table 5-3 to Table 5-5. In Table 5-3, the four alignment errors concerning four peripheral maps in each map collection is averaged and the table lists the mean and standard deviation of this averaged value for the 10 map collections. Only pairs with radii no larger than 5.02 mm are given since the alignment errors beyond this radius are considered to be large. One particular example is that with central and peripheral map radii of 4.53 mm (i.e. diameter 9.06 mm) when the mean alignment error is found to be 1.40  $\mu\text{m}$  with standard deviation 0.92  $\mu\text{m}$ . In that case the mean dimension of 10 combined maps is 11.45 mm (standard deviation 0.29 mm) horizontally and 11.33 mm (standard deviation 0.40 mm) vertically. This result is comparable with the results reported by Franklin et al. [109]. One combined map for this example is displayed in Figure 5-7 having an increase in area of approximately 65% compared to the original central map.

Table 5-3. Alignment error ( $\mu\text{m}$ ), presented as mean  $\pm$  1 standard derivation.

		$R_c(\text{mm})$						
		5.02	4.78	4.53	4.29	4.04	3.8	3.55
$R_p(\text{mm})$	5.02	2.71 $\pm$ 1.41						
	4.78	2.97 $\pm$ 1.86	1.93 $\pm$ 1.20					
	4.53	2.81 $\pm$ 1.61	1.77 $\pm$ 1.06	1.40 $\pm$ 0.92				
	4.29	2.35 $\pm$ 1.34	1.61 $\pm$ 0.96	1.26 $\pm$ 0.84	1.06 $\pm$ 0.71			
	4.04	2.09 $\pm$ 1.32	1.45 $\pm$ 0.86	1.14 $\pm$ 0.80	0.96 $\pm$ 0.67	0.81 $\pm$ 0.57		
	3.80	1.78 $\pm$ 1.36	1.29 $\pm$ 0.88	0.99 $\pm$ 0.78	0.87 $\pm$ 0.71	0.73 $\pm$ 0.57	0.62 $\pm$ 0.53	
	3.55	1.54 $\pm$ 1.32	1.19 $\pm$ 0.92	0.95 $\pm$ 0.81	0.83 $\pm$ 0.74	0.78 $\pm$ 0.68	0.70 $\pm$ 0.76	0.56 $\pm$ 0.61

Table 5-4. Horizontal dimension (mm) of combined map, presented as mean  $\pm$  1 standard derivation.

		$R_c(\text{mm})$						
		5.02	4.78	4.53	4.29	4.04	3.8	3.55
$R_p(\text{mm})$	5.02	12.31 $\pm$ 0.25						
	4.78	11.91 $\pm$ 0.27	11.88 $\pm$ 0.28					
	4.53	11.48 $\pm$ 0.25	11.43 $\pm$ 0.31	11.45 $\pm$ 0.29				
	4.29	11.05 $\pm$ 0.23	11.03 $\pm$ 0.27	11.04 $\pm$ 0.30	11.08 $\pm$ 0.33			
	4.04	10.65 $\pm$ 0.27	10.60 $\pm$ 0.27	10.59 $\pm$ 0.27	10.66 $\pm$ 0.33	10.70 $\pm$ 0.37		
	3.80	10.18 $\pm$ 0.27	10.09 $\pm$ 0.29	10.08 $\pm$ 0.29	10.18 $\pm$ 0.30	10.28 $\pm$ 0.32	10.31 $\pm$ 0.35	
	3.55	9.76 $\pm$ 0.15	9.56 $\pm$ 0.26	9.51 $\pm$ 0.30	9.57 $\pm$ 0.37	9.51 $\pm$ 0.46	9.68 $\pm$ 0.59	9.63 $\pm$ 0.81

Table 5-5. Vertical dimension (mm) of combined map, presented as mean  $\pm$  1 standard derivation.

		$R_c(\text{mm})$						
		5.02	4.78	4.53	4.29	4.04	3.8	3.55
$R_p(\text{mm})$	5.02	12.11 $\pm$ 0.31						
	4.78	11.56 $\pm$ 0.28	11.77 $\pm$ 0.37					
	4.53	11.00 $\pm$ 0.34	11.36 $\pm$ 0.36	11.33 $\pm$ 0.40				
	4.29	10.70 $\pm$ 0.27	10.92 $\pm$ 0.35	10.97 $\pm$ 0.37	10.98 $\pm$ 0.36			
	4.04	10.17 $\pm$ 0.30	10.46 $\pm$ 0.35	10.50 $\pm$ 0.34	10.46 $\pm$ 0.33	10.61 $\pm$ 0.36		
	3.80	9.77 $\pm$ 0.27	9.99 $\pm$ 0.36	10.07 $\pm$ 0.36	10.03 $\pm$ 0.37	10.11 $\pm$ 0.35	10.25 $\pm$ 0.46	
	3.55	9.85 $\pm$ 0.92	9.59 $\pm$ 0.29	9.61 $\pm$ 0.36	9.63 $\pm$ 0.41	9.69 $\pm$ 0.36	9.77 $\pm$ 0.61	9.96 $\pm$ 1.13

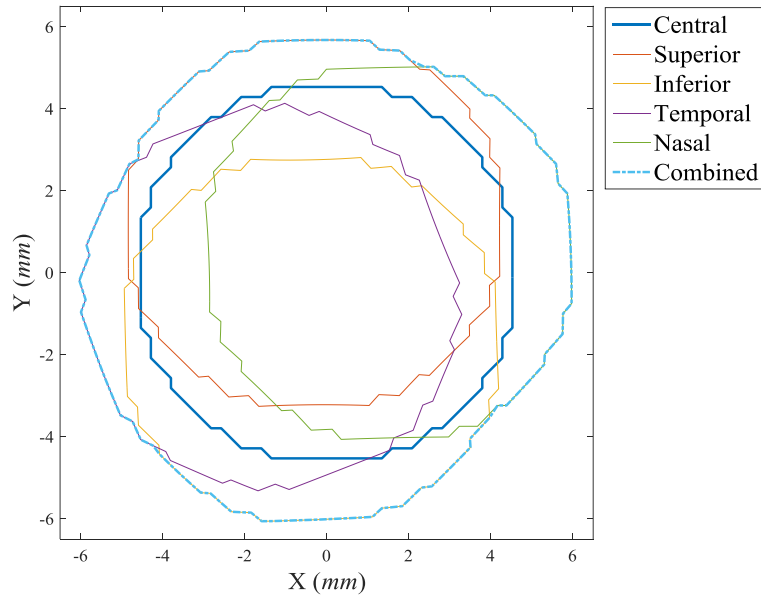


Figure 5-7. Area of the combined map.

## 5.6 BENEFITS OF MULTI-VIEW REGISTRATION

The aim of multi-view registration is to uniform the error distribution among all maps involved in the matching process, this includes errors between dynamic maps and the static map and those between pairs of dynamic maps. The 10 clinical map collections above, each including one central (static) map and four peripheral (dynamic) maps, were input to a multi-view iterative closest point (MICP) routine as described in Section 3.3.5. This time the MICP algorithm was employed to find the optimal transformation for all four dynamic maps at the same time. Only the central portion with 4.53 mm radius was kept for each topography map according to the results in pair-wise registration.

For each collection of one central and four peripheral maps, three tests were done. In the first, no initial guesses were provided to the MICP algorithm as in the ICP registration and Levenberg-Marquardt (LM) algorithm was used to solve Equation (3.55). In the second test, the extrapolation technique as described in the end of Section 3.3.5 was added. The mean MICP alignment errors of all the 10 cases are plotted in Figure 5-8 (blue and red curves) against the iteration sequence and computing time. It can be seen that the

extrapolation method typically introduced more vibrations in the converging path of the MICP algorithm but unfortunately it seemed to always predict the next iteration point too far from the current searching path and brought few benefits. The converging points with or without extrapolation were also seen to be identical among all cases in this study.

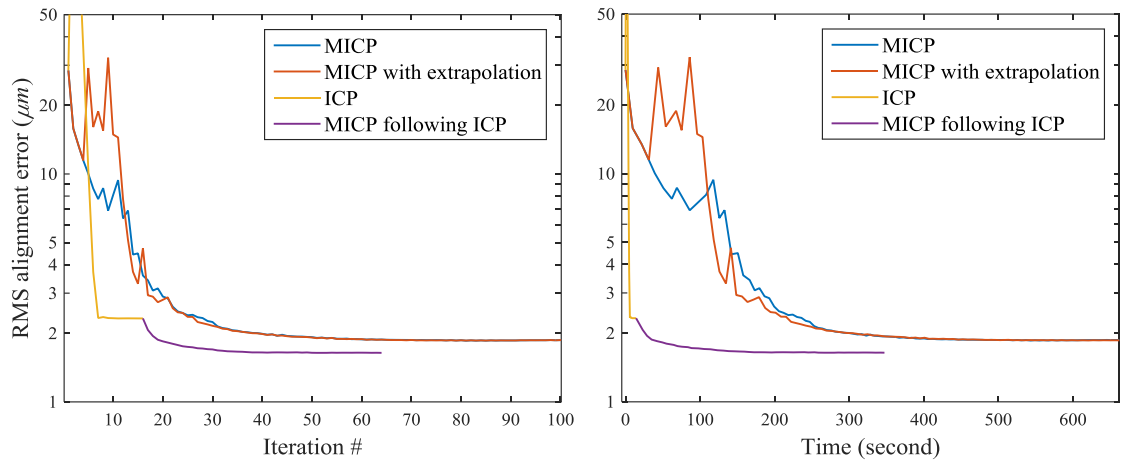


Figure 5-8. Convergence of MICP registration. The curves represent the mean MICP alignment error of all 10 cases in log scale. The error curves are plotted with respect to iteration number in the left figure, while with respect to computing time in the right figure.

In the third test, the results of the pair-wise registration were adopted as initial guess for the MICP algorithm and no extrapolation was included considering outcomes of the first two tests. To evaluate the superiority of the MICP algorithm over the ICP algorithm. A new set of alignment errors for the outcomes of ICP registration were computed. In details, the peripheral maps were transformed using the transformation found in every ICP iteration and the errors were then computed based on Equation (3.54). It should be noted that these recalculated errors are different from the ones in Table 5-3 where each value is the average error for the four pair-wise registrations (dynamic-to-static), while the errors between the dynamic maps were not taken into account. The mean of the recalculated errors of all the 10 cases are also plotted in Figure 5-8 (in yellow), followed by the mean error of MICP registration (in purple) that used the transformation found in the last ICP

registration as its initial point. These mean values of registration errors are detailed in Table 5-6 with the standard derivations.

Table 5-6. Overall alignment error ( $\mu\text{m}$ ), dynamic-to-static error ( $\mu\text{m}$ ) and dynamic-to-dynamic error ( $\mu\text{m}$ ), presented as mean  $\pm$  1 standard derivation.

	ICP	MICP		
		First test	Second test	Third test
Overall	$2.70 \pm 1.43$	$2.17 \pm 1.03$	$2.17 \pm 1.03$	$1.96 \pm 0.88$
Dynamic-to-static	$1.40 \pm 0.92$	$1.75 \pm 0.96$	$1.76 \pm 0.96$	$1.67 \pm 0.93$
Dynamic-to-dynamic	$2.52 \pm 2.13$	$2.01 \pm 1.33$	$2.01 \pm 1.33$	$1.88 \pm 1.13$

It is obvious from Figure 5-8 and Table 5-6 that, by simultaneously minimising both dynamic-to-static and dynamic-to-dynamic alignment errors, the MICP algorithm can improve the overall registration and this is particularly true when good initial guess is provided as in the third test where 27% decrease in mean overall registration error was observed. With no reasonable starting point, the MICP algorithm was seen in the first two tests to converge to a less improved point, moreover it took significantly longer. In Table 5-6, the dynamic-to-static errors represent the equivalent errors that are detailed in Table 5-3. It can be seen that to minimise the overall alignment error, the dynamic-to-static error is increased, this is because the pair-wise registration takes no consideration of relative alignment error among the dynamic maps, which usually leads to inconsistency among the dynamic maps and thus leave considerable residual dynamic-to-dynamic errors uncorrected. MICP algorithm instead tries to balance all error sources. On one hand, the accumulated dynamic-to-dynamic errors are reduced and on the other this inevitably increases the pair-wise registration error. This phenomenon is well reflected in Table 5-6 and further detailed in Figure 5-9 where each component in the MICP error metric are plotted separated. In each sub-figure of Figure 5-9, alignment error for one particular dynamic map to the static map is presented as blue bold curve, while its alignment errors

to the rest three dynamic maps were plotted in normal curves. The first several iterations with markers are the alignment errors computed by the results of the ICP algorithm and the rest are the MICP iterations. It can be seen that, for each dynamic map, the alignment errors with other dynamic maps are always bigger than the error with the static map (central map) in the stage of ICP registration because the relative information among the dynamic maps are ignored. The alignment errors are then seen to move closer in the MICP registration stage, balancing the error distribution across all maps.

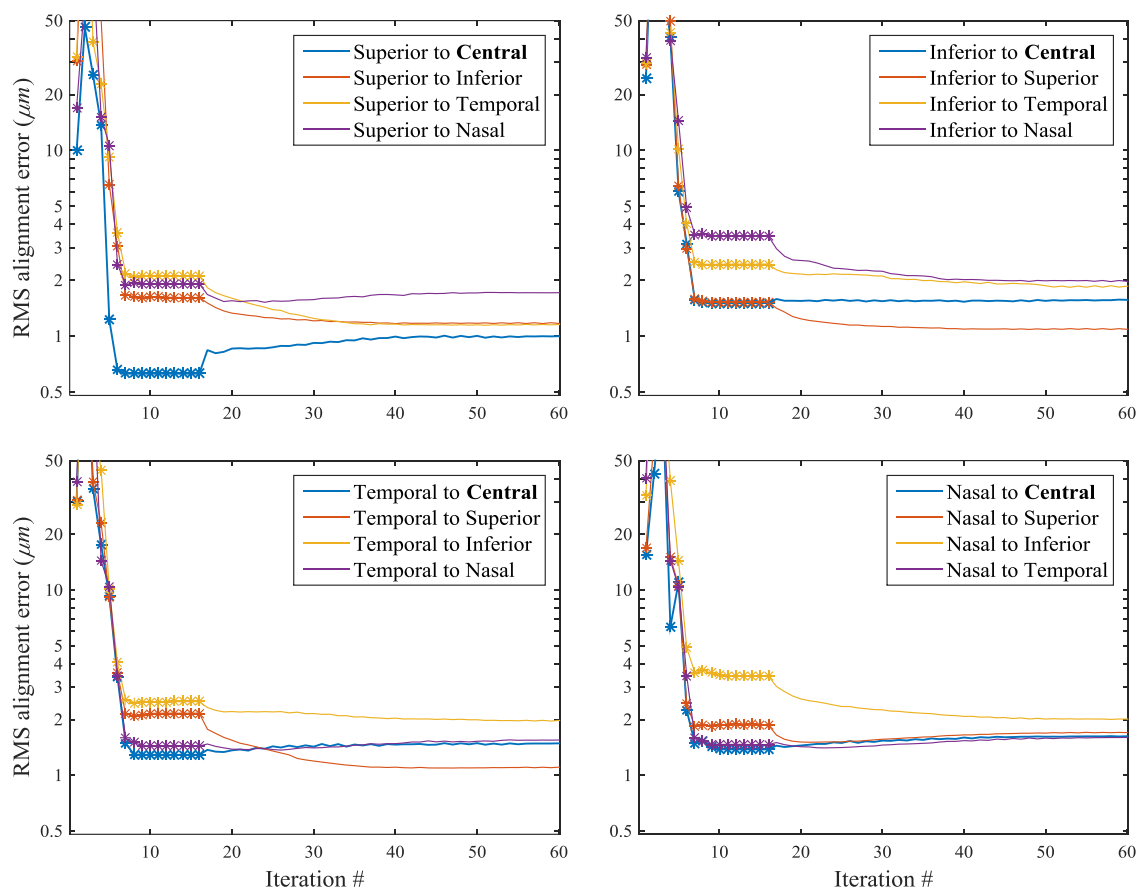


Figure 5-9. Individual alignment error between each pair of dynamic-to-static or dynamic-to-dynamic map along the convergence of the MICP registration. The first part of each curve with markers presents the individual alignment errors computed based on the results of ICP registration.

The results of MICP presented herein are all based on LM algorithm when solving minimisation (3.55). This is computationally more expensive compared to ICP algorithm where the closed-form solution for the minimisation is used. In the early stage of this



study of MICP, the approximated closed-form solution derived in Section 3.3.5 was attempted but unfortunately the results were less satisfying, largely due to the omission of higher order terms after linear approximation of sine and cosine functions.

## 5.7 CONCLUDING REMARKS

In this chapter, a repeatability study of Medmont topography is conducted showing obvious data unreliability to the periphery. Three sets of artificial data are then prepared for the test of various matching techniques given in Section 3.3. This leads to the favour of point-to-plane ICP algorithm using VS or NS mapping strategies, which produced consistently best results in all clinical tests. By matching the peripheral maps one by one to the central map, an area increase about 65% is achieved. Although the alignment errors through the favoured ICP algorithm are very small, it is then demonstrated that MICP algorithm can further refine the registration results of ICP algorithm by minimising alignment errors both between peripheral and central maps and peripheral maps themselves. Although the reduction in overall alignment errors contributed by MICP is not significant, the error distribution across all maps are indeed uniformed and this is advantageous to eliminate the inconsistency that may occur in pair-wise ICP registration. The drawback of MICP however is its computing costs. To solve an error matrix that has been enlarged 16 times and without a closed-form solution, the MICP can take significantly longer than ICP especially when no reasonable initial guess is provided. The results presented in this chapter enables further discussion on topography matching in Chapter 7.

## CHAPTER 6

### RESULTS OF NUMERICAL SIMULATION

---

#### 6.1 INTRODUCTION

A major goal of numerical simulation of corneal refractive surgery is to predict the biomechanical reaction of the ocular tissue, especially the cornea, to the surgical procedure. The goodness of the numerical prediction can be assessed by evaluating the differences between the predicted and measured postoperative corneal topographies. In addition, with the geometric shapes of the anterior and posterior corneal surfaces known and their relative positions determined by the central corneal thickness (CCT), it is also possible to compute the corneal refractive power, which is commonly used in clinical practice. Therefore, the difference in refractive powers computed using predicted and measured postoperative topographies can also be a measurement of the goodness of the numerical simulation.

This chapter reports the outcomes of numerical simulation as follows. First, an initial study on the model structure is conducted to evaluate the effect of different mesh density and the superiority of various methods for ablation adjustment. This initial study determines an optical model structure that is both reliable and computationally efficient and chooses a single ablation adjustment strategy for all patient-specific modelling. Second, the results of the parametric study on wound healing stiffness are presented. A comparison between the numerical modelling and mathematical simulation (where biomechanical effects of surgery are ignored) is then reported and followed by the outcomes of the simulation of SMILE procedure in comparison to LASIK. The results of tonometry simulation are presented as the last part.

## 6.2 STRUCTURAL STUDY

In an initial study of the modelling structure, one set of clinical data is randomly chosen. As detailed in Table 6-1, a total of 6 model settings are included. The first three simulations use the same approach for ablation adjustment, that is, the anterior corneal nodes are re-arranged to account for the ablation boundary and a new layer is added for the ablation depth. The models in these simulations are only different in the number of layers and scleral rings (Figure 6-1 and Figure 6-2). Compared to the third simulation, the fourth only marks the location of the ablation (more precisely its posterior surface) without adding a visible layer, however the anterior corneal nodes are also re-arranged as simulations one to three (referred to Figure 3-23A). The fifth simulation then eliminates the node re-arrangement as happened in the first four simulations while still marks the necessary locations within the cornea to identify the ablation depth (referred to Figure 3-23B). In the final simulation, neither the node re-arrangement nor the identification of the ablation depth is included. In this simulation, the ablation depth is not adjusted, but directly adopted from the clinical measurements.

Table 6-1. Six model settings tested in an initial study. The epithelial and ablation layers are not accounted for the number of layers herein.

	Simulations					
	<b>1</b>	<b>2</b>	<b>3</b>	<b>4</b>	<b>5</b>	<b>6</b>
Number of corneal rings	25	25	25	25	25	25
Number of all rings	70	50	50	50	50	50
Number of layers	3	3	2	2	2	2
Re-arranging corneal nodes	Yes	Yes	Yes	Yes	No	No
Ablation layer	Yes	Yes	Yes	No	No	No
Marking ablation	No	No	No	Yes	Yes	No

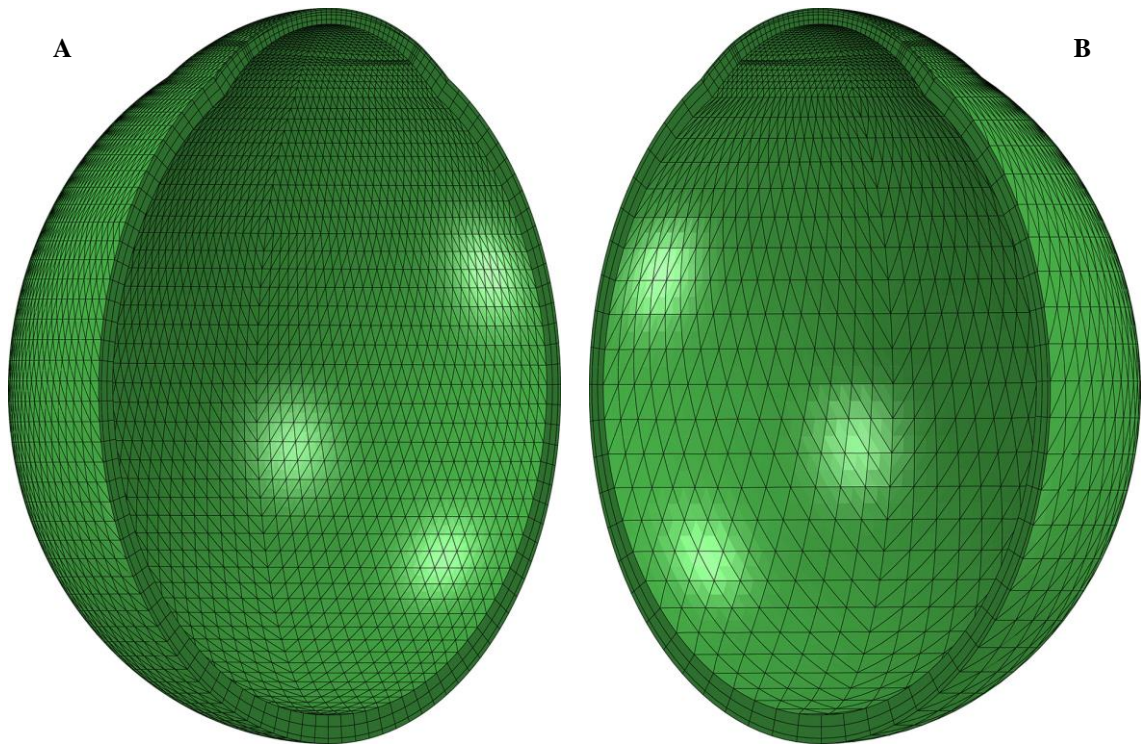


Figure 6-1. Models in simulation 1(left) and 2 (right), showing different numbers of scleral rings

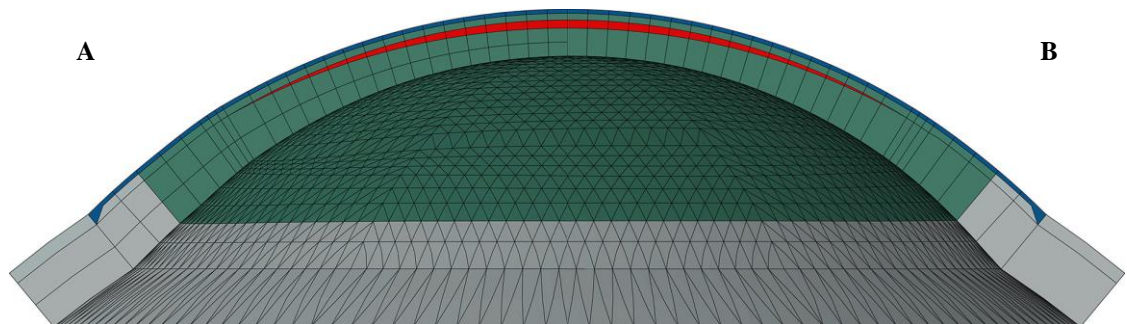


Figure 6-2. Cross-sectional views of models in simulation 2 with three layers (left) and simulation 3 with two layers (right)

A static analysis of each model is performed using Abaqus, bringing the IOP to the measured value for this particular patient. This is regarded as an initial loading and the displacements of all nodes are monitored and the nodes in three particular locations (corneal apex, limbal node with maximal x coordinates and posterior scleral pole) are listed in Table 6-2. Using the results of this analysis, a stress-free configuration is carried out as described in Section 3.4.2. The displacements of the same nodes from the stressed

configuration to the achieved stress-free configuration are recorded and again shown in Table 6-2 (in italic). In addition, the tissue thickness at these locations are calculated.

Table 6-2. Displacements and thickness values at three model nodes after an initial loading and stress-free configuration (italic values). The values in the table are all in  $\mu m$ . The thickness at the corneal apex, the limbus and the posterior pole of the sclera before any FE analysis are  $571 \mu m$ ,  $861.4 \mu m$ , and  $1033.7 \mu m$ , respectively.

		Simulations					
		1	2	3	4	5	6
Corneal centre	Displacement	242.5 <i>235.1</i>	242.2 <i>234.8</i>	242.3 <i>234.9</i>	242.3 <i>234.9</i>	245.0 <i>237.0</i>	245.0 <i>237.0</i>
	Thickness	541.1 <i>601.9</i>	541.1 <i>601.9</i>	541.1 <i>601.9</i>	541.1 <i>601.9</i>	541.2 <i>601.7</i>	541.2 <i>601.7</i>
Limbus	Displacement	149.4 <i>145.1</i>	149.2 <i>144.9</i>	149.2 <i>144.9</i>	149.2 <i>144.9</i>	156.8 <i>152.7</i>	156.8 <i>152.7</i>
	Thickness	840.8 <i>882.2</i>	840.7 <i>882.3</i>	840.7 <i>882.3</i>	840.7 <i>882.3</i>	840 <i>883</i>	840 <i>883</i>
Posterior pole	Displacement	151.9 <i>145.5</i>	152 <i>145.7</i>	152 <i>145.6</i>	152 <i>145.6</i>	152 <i>145.6</i>	152 <i>145.6</i>
	Thickness	1005.5 <i>1062</i>	1005.6 <i>1062</i>	1005.6 <i>1062</i>	1005.6 <i>1062</i>	1005.6 <i>1062</i>	1005.6 <i>1062</i>

It is evident from Table 6-2 that the different mesh settings of model layers and scleral rings almost have no effect on the simulation results as seen in the first three cases. In the fourth simulation, although the ablation layer is not visible, the locations corresponding to the nodes in the ablation layer in the third model are identified and contributed to the stress-free configuration. It is seen in Table 6-2 that this simplification does not change the results of the stress-free configuration. By comparing simulations 4 and 5, it can be seen that re-arranging corneal nodes does cause some effect but this is trivial. The difference in displacement caused by nodal arrangement is about 3 microns at the corneal apex and bigger at the limbal node, being around 8 microns. It should also be noted that the displacement of the polar node in the sclera shows no obvious difference among all 6 simulations. After the initial loading (application of IOP), the thickness at the three locations decreased because of the compression introduced by inflation. The differences in thickness reduction among all 6 simulations are trivial. This is also true in the thickness

increase in developing the stress-free configuration where the release of IOP causes relaxation of the tissue and thus increases in tissue thickness.

The simulations continue to remove the ablation depth in the stress-free configuration using either the adjusted ablation depth (obtained along with the stress-free configurations) or the original clinical data as in the sixth simulation. The models with the corneal thickness being modified and thinned after tissue removal are inflated by the IOP using static analysis in Abaqus and in all these simulations, the stiffness of the wound healing zone is set to be same as the stromal stiffness. The final inflated model in the first and fifth simulations are illustrated in Figure 6-3 and Figure 6-4 where the colour in the figures represent the amount of stress in the tissue.

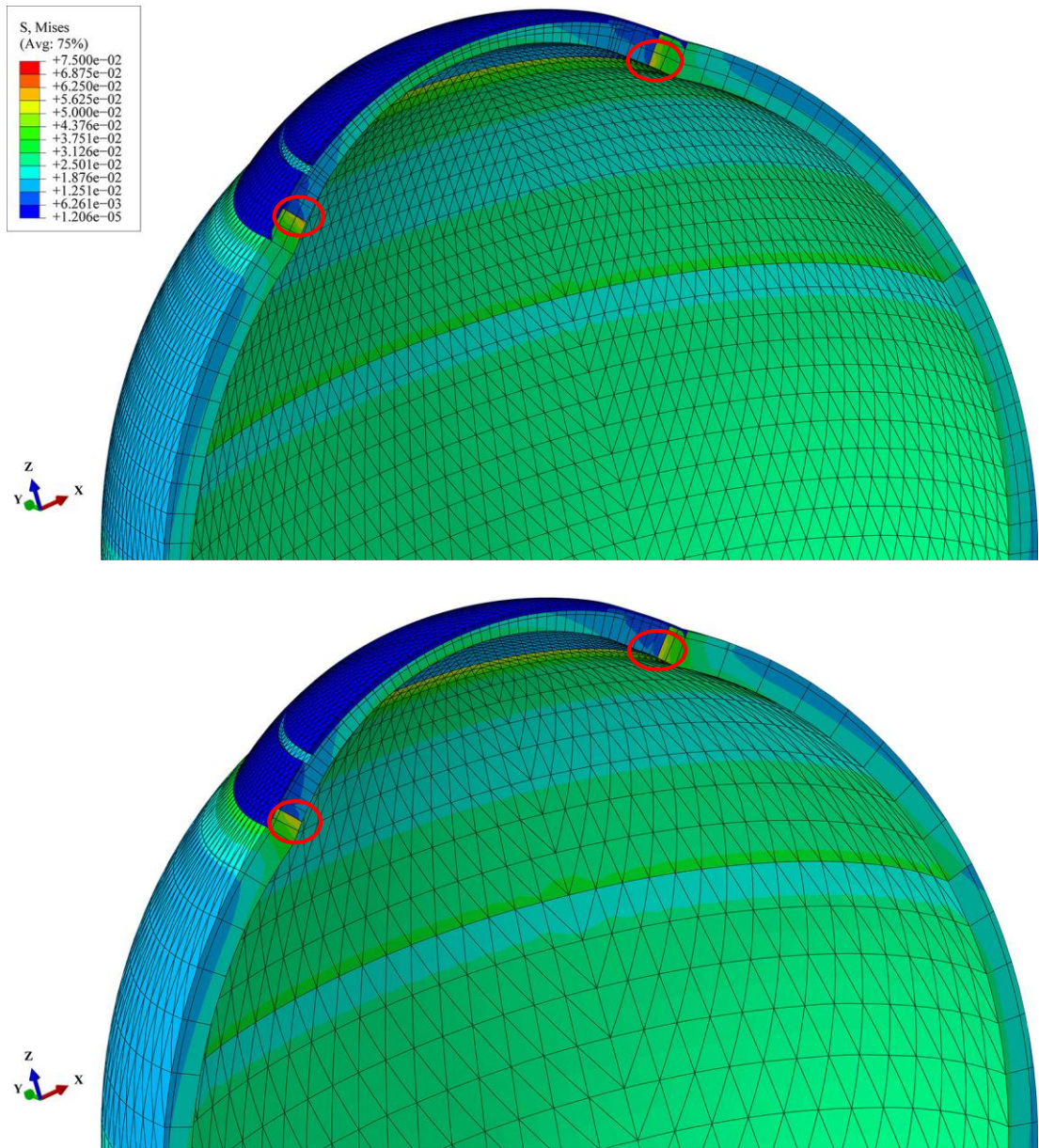


Figure 6-3. Cross-sectional views of models used in simulations 1 and 5. Red circles in the figures mark the regions with maximal stress.

It can be seen from Figure 6-3 that even if the model structures are different, the two inflated models share almost identical stress patterns. In both models, there are clear gaps at the flap edges and these are largest opposite the sites of the hinges. In Figure 6-4, it can be seen that the flap carries almost no stress except for the hinge zone. In simulation 1, the central corneal rings are not circular because the nodes are reconfigured to meet the ablation depth and the need to build a layer for the ablation depth. It should be noted that in both Figure 6-3 and Figure 6-4 noticeable stress concentration can be found, which is

located in the transition zone from the limbus to the cornea (Figure 6-3, marked by red circles) and the two sides of the flap hinge (Figure 6-4, marked by red circles). Although this may not change the corneal deformation behaviour, local mesh refinement may be helpful to eliminate the observed stress concentration.

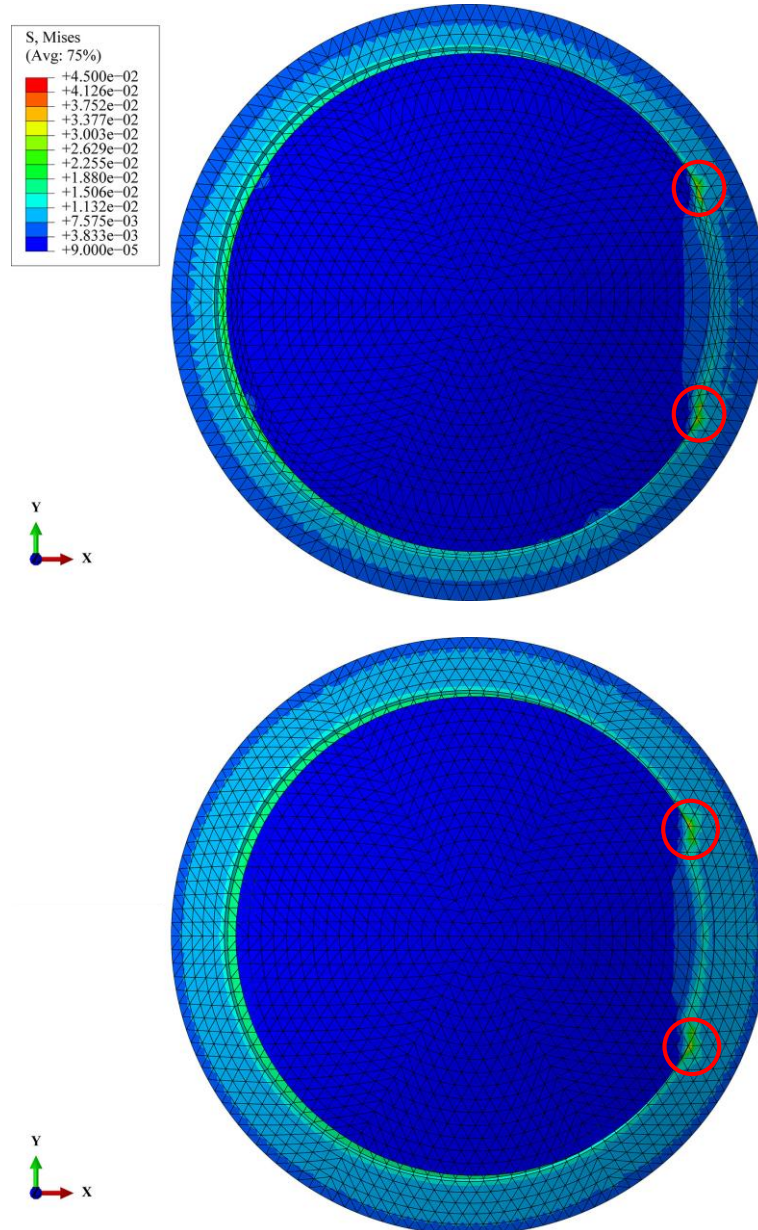


Figure 6-4. Top views of models used in simulations 1 and 5. The corneal flap bears significantly less stress compared to the rest of the cornea and the only obviously stressed part is the flap hinge. Red circles in the figures mark the regions with maximal stress.

The anterior corneal surfaces of all 6 inflated models are extracted and compared to the clinical anterior corneal topography. The difference between the simulated and clinical



anterior corneal surfaces are calculated as root mean square error (RMSE) of z coordinates. To do this calculation, the clinical topography is fitted to Zernike polynomials of order 10, and the locations on the clinical topography that are corresponding to the same x and y coordinates of the simulated anterior surface are sampled using the Zernike expression, which would allow the actual calculation of the RMSE. Only nodes in the central 3.5 mm radius are included and the calculated RMSE are listed in Table 6-3.

Table 6-3. Surface fit with the clinical measurements for the 6 simulations. The root mean square errors in this table are in  $\mu m$ .

	Simulations					
	1	2	3	4	5	6
RSME	5.89	5.89	5.90	5.93	5.72	8.33

It can be seen from Table 6-3 that the final outcomes of the simulated postoperative anterior surfaces differ from the clinical measurements with similar amounts in the first 4 simulations. This difference in topography is slightly smaller in the fifth simulation and increased significantly in the last simulation. The slight difference of RMSE in the fifth simulation relative to the first four cases could be caused by the different layout of the corneal nodes such that the ablation depth is sampled at different locations from the 4<sup>th</sup> order Zernike expression for the ablation depth. This means different sampling errors may occur because the Zernike expression itself is a rough approximation of the actual ablation depth that is applied in clinical practice and this approximation carries fitting errors. In this particular case, the RMSE is smaller in the fifth case but this may not be the same for another set of clinical data from a different patient. Nevertheless, the effect of the ablation adjustment is obvious when comparing the last simulation to the rest. In this simulation, the ablation adjustment is not implemented, and as a result a noticeable increase (46% in comparison with the fifth simulation) in RMSE is observed and this is believed to be

caused by applying an ablation depth pattern in a stressed fashion on a stress-free configuration. In Figure 6-5, the error distributions in surface fit for the 6 simulations are plotted in 3D. It can be seen that the distributions for the first five cases are almost identical, while obvious pattern change is seen in the last case.

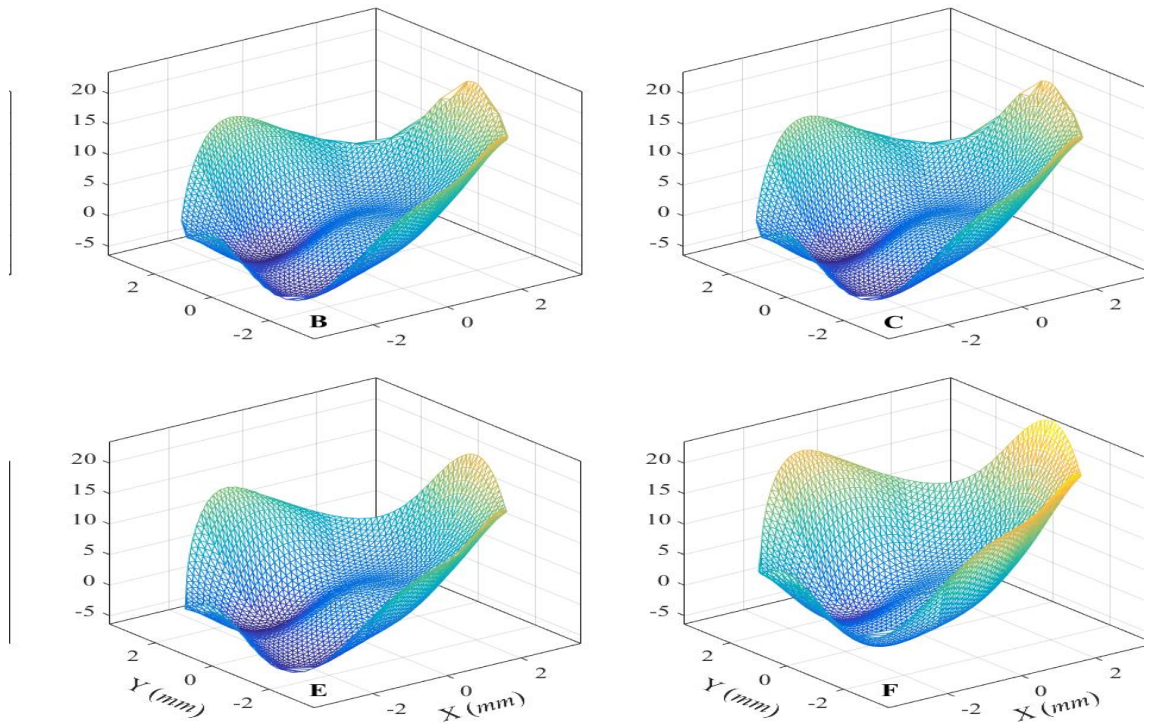


Figure 6-5. Distributions of errors in surface fit with the clinical measurements for the 6 simulations. Sub-figures **A** to **F** are for simulations 1 to 6.

The outcome of this initial structural study suggests that reducing the number of layers and element sizes of the sclera do not affect the output of the FE analysis and the two approaches of ablation adjustment lead to almost identical simulation results. The nodal re-arrangement of the central cornea, to account for the ablation boundary, does not guarantee a closer fit with the clinical postoperative outcomes because the available measurements of the ablation depth are limited such that the low order Zernike expression may have considerable discrepancy with the actual ablation that is applied in the patient eye. This Zernike expression may thus only predict a rough boundary of the actual

ablation profile. For this reason, re-arrangement of the central corneal nodes has not been conducted in all subsequent studies for reasons of simplicity.

### 6.3 PARAMETRIC STUDY OF WOUND HEALING

Using the outcome of the initial study, each of the 60 sets of patient data is used to create a patient-specific numerical surgery model. This step includes modification of an idealised model to fit the patient topography data, creation of a stress-free configuration based on the patient IOP measurement, reduction of corneal thickness by an adjusted ablation depth and inflation of the resulting model after defining the flap and the wound healing zone. The parametric study on wound healing aims to evaluate effect of the wound healing stiffness on the simulation outcome in terms of fitting error between the numerically predicted and clinically measured anterior corneal surfaces. In this parametric study, the varying stiffness of the wound healing layer is controlled by the value of parameter  $\mu_1$  of the stromal material. In details, the value of parameter  $\mu_1$  of the wound healing layer is set proportional to that of the stroma, the ratio of  $\mu_1$  between the wound healing layer and the stromal layer is called stiffness ratio because it acts as a scaling factor of the tangential modulus of the material. In each case, the surface fit is quantified by the RMSE as described earlier in the initial study, but this time five RMSEs are considered for five values of radius of the central area over which the quality of topography match is assessed. This area varies in diameter between 3 and 7 mm. The mean errors are plotted in Figure 6-6 and detailed in Table 6-4 with standard derivation.

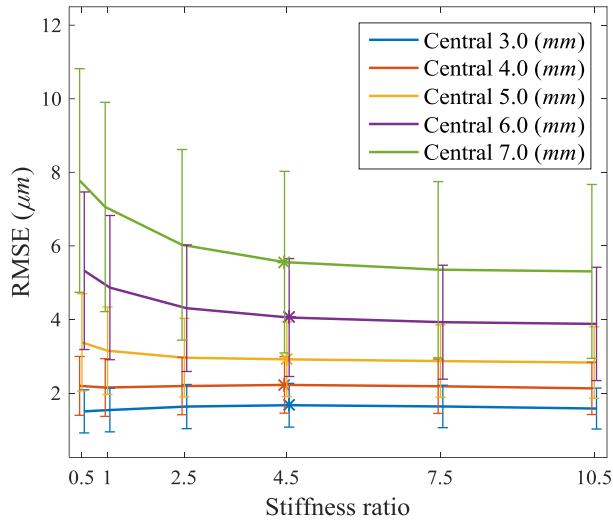


Figure 6-6. Average root mean square errors between 60 numerically predicted and clinically postoperative anterior corneal surfaces, with error bars representing  $\pm 1$  standard derivation. The errors are plotted against the stiffness ratio of the wound healing with the value 1.0 meaning the same stiffness as the stroma outside the wound healing area.

Table 6-4. Average root mean square errors between 60 numerically predicted and clinically postoperative anterior corneal surfaces, presented as mean  $\pm 1$  standard derivation. The unit of the values is  $\mu m$ .

Comparison diameter	Stiffness ratio					
	0.5	1	2.5	4.5	7.5	10.5
3 mm	1.50 $\pm$ 0.59	1.54 $\pm$ 0.59	1.63 $\pm$ 0.60	1.67 $\pm$ 0.60	1.64 $\pm$ 0.58	1.58 $\pm$ 0.56
4 mm	2.20 $\pm$ 0.80	2.15 $\pm$ 0.78	2.19 $\pm$ 0.78	2.22 $\pm$ 0.77	2.19 $\pm$ 0.74	2.13 $\pm$ 0.71
5 mm	3.38 $\pm$ 1.32	3.15 $\pm$ 1.19	2.96 $\pm$ 1.07	2.92 $\pm$ 1.02	2.87 $\pm$ 0.98	2.83 $\pm$ 0.97
6 mm	5.33 $\pm$ 2.14	4.87 $\pm$ 1.96	4.31 $\pm$ 1.72	4.05 $\pm$ 1.60	3.93 $\pm$ 1.55	3.88 $\pm$ 1.54
7 mm	7.78 $\pm$ 3.04	7.06 $\pm$ 2.84	6.03 $\pm$ 2.59	5.56 $\pm$ 2.47	5.35 $\pm$ 2.39	5.31 $\pm$ 2.36

Figure 6-6 shows that the mean errors increase with radius and they are less than 2 microns in the central 3mm diameter area. On the other hand, the fits in the central 3mm and 4mm do not seem to change much with different levels of wound healing stiffness, Table 6-4. The errors computed in areas with larger diameters (5mm, 6mm and 7mm) show a clear trend that the fit between predicted and measured surfaces becomes better with higher stiffness in wound healing zone. The decrease in fitting errors, however, changes very little when the stiffness is larger than 4.5. In Figure 6-7, the typical error distribution over the corneal surface is plotted in 3D for one set of clinical data. In the

figure, positive values mean the clinically measured topography is above the predicted topography and vice versa. When the wound healing stiffness is higher, it is expected to contribute more resistance against the intraocular pressure and thus the cornea becomes less inflated, therefore flatter. This, as a result, brings the predicted surface closer to the clinical surface. Again it is shown in Figure 6-7 that there is a trivial difference in error distribution when the wound stiffness ratio goes beyond 4.5. For these reasons, the optimal wound healing stiffness in the current modelling setting is chosen as 4.5 times the stiffness in the rest of the stroma.

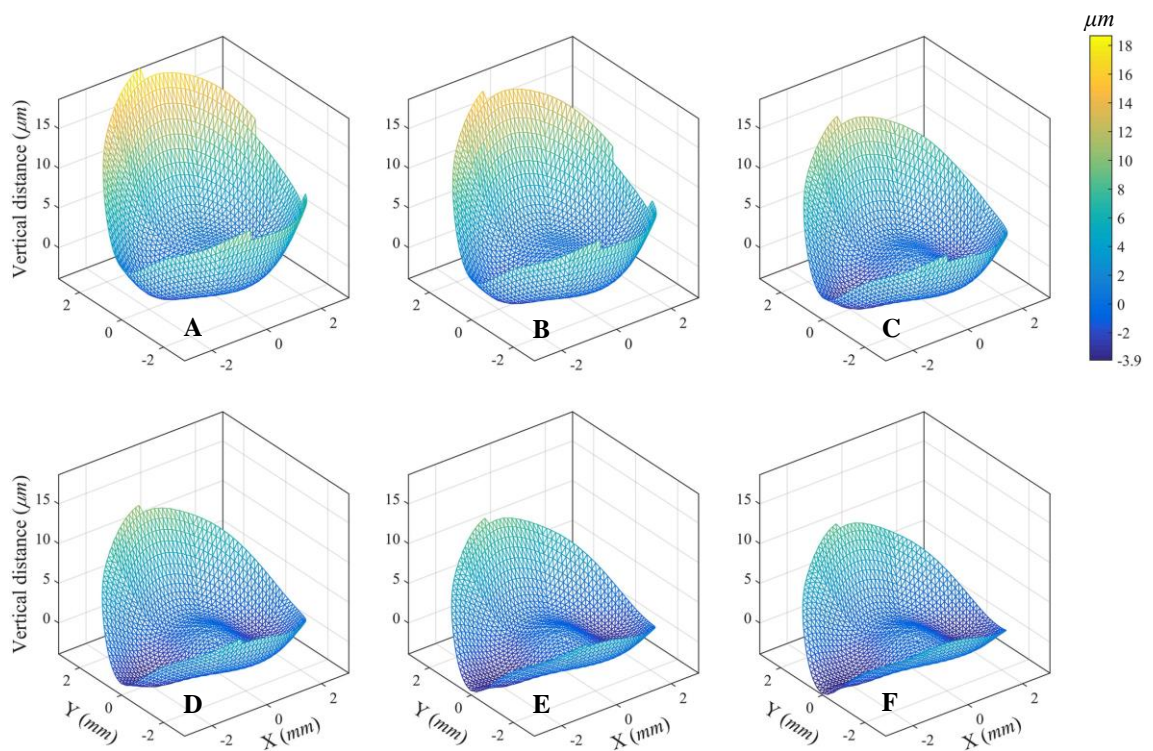


Figure 6-7. A typical example of distribution of error in surface fit between the predicted and measured postoperative anterior corneal surfaces. Sub-figures **A** to **F** are for stiffness ratios from 0.5 to 10.5 as listed in Table 6-4.

It should be noted the RMSEs vary largely among the 60 cases as seen in Figure 6-6 and detailed in Table 6-4, which raises high levels of uncertainty in selecting the optimal wound healing stiffness ratio. In Figure 6-8, individual RMSEs (considering 7mm diameter) for all the 60 numerical cases are plotted against wound healing stiffness ratio. It can be seen that, although vary notably, the RMSE for each case shares similar trend

and changes very little beyond ratio 4.5. The choice of optimal wound healing stiffness ratio of 4.5 is thus deemed reasonable because of the uniform trend of RMSEs in individual cases. The large range of RMSE among cases may have been caused by other error sources such as topography and ablation fitting errors, this will be further discussed in Chapter 7 and future work with more accurate clinical data may be necessary.

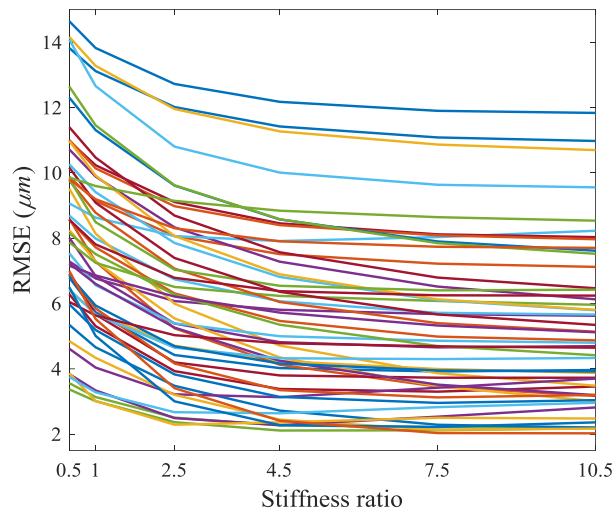


Figure 6-8. Individual root mean square errors between 60 numerically predicted and clinically postoperative anterior corneal surfaces, considering the central 7mm diameter.

#### 6.4 EFFECT OF CONSIDERING SURGERY-RELATED STIFFNESS CHANGES

From the parametric study in the last section, it is shown that numerical simulations that consider the surgery-related stiffness changes in the cornea can produce postoperative surgical results that are close to the clinical measurements. In this section, the previous simulation results, based on a wound healing stiffness ratio of 4.5, are compared to the simple mathematical prediction of the surgery where the biomechanical changes in cornea are ignored. This simpler simulation therefore predicts the postoperative corneal topographies by subtracting ablation depth profile directly from the anterior corneal surface. The same Zernike fitting of the ablation depth is used here to enable direct comparison of results. The fit between the predicted and measured surfaces again are computed in 5 diameters as shown Figure 6-9, which shows the distributions of RMSE of

all 60 numerical simulation cases and corresponding mathematical simulations. For each boxplot in Figure 6-9, the red line in the box marks the median of the 60 errors, the edges of the box are the 25<sup>th</sup> and 75<sup>th</sup> percentiles and the whiskers extend another 1.5 times the length from the percentiles to the median. It can be seen that the errors are almost normally distributed and only one outlier is identified for all these distributions. The fits with clinical measurement using numerical simulation are seen superior in all comparison diameters. In addition to the boxplots, the average errors and the standard derivations are given in Table 6-5.

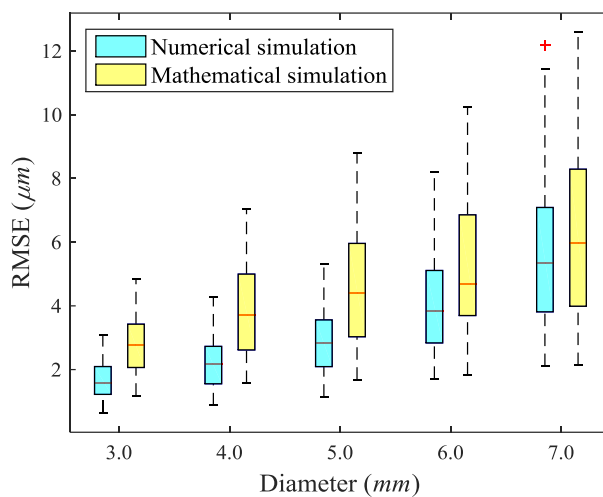


Figure 6-9. Box plot of the RMSE for both numerical and mathematical simulations, showing the RMSE distribution among all patient-specific cases.

Table 6-5. Average root mean square errors for both numerical and mathematical simulations, presented as mean  $\pm$  1 standard derivation. All values are in  $\mu m$ .

Simulations	Comparison diameter				
	3 mm	4 mm	5 mm	6 mm	7 mm
Numerical	$1.67 \pm 0.60$	$2.22 \pm 0.77$	$2.92 \pm 1.02$	$4.05 \pm 1.60$	$5.56 \pm 2.47$
Mathematical	$2.77 \pm 0.90$	$3.83 \pm 1.37$	$4.53 \pm 1.75$	$5.18 \pm 2.09$	$6.31 \pm 2.76$

It can be seen from Table 6-5 that both the mean errors and standard derivations for the numerical simulation cases are smaller than the mathematical results. To evaluate the overall simulation outcome compared to the clinical ones, the refractive powers are

calculated using clinical topographies both preoperatively and postoperatively, as well as using the numerically and mathematically predicted topographies postoperatively.

The calculation considers both anterior and posterior corneal topographies and is done using ray tracing. For each case, a bundle of parallel light rays with a diameter of 7mm is traced through cornea. The light refraction is modelled on both corneal surfaces and the amount of refraction is computed by Snell's law. When the light rays reach the cornea, they are convergently refracted by its anterior surface because the refraction index increases from 1 in the air to 1.376 in the cornea. A slight divergent refraction is then caused by the small reduction in refraction index in the aqueous humour, being 1.336. The surface normal needed for the calculation of refraction angles are computed using Zernike expressions (order 10) of the surfaces and the average focal length  $f$  of all rays referenced to the anterior corneal surface [289] is converted to the equivalent refractive power by  $n/f$  where  $n$  is the refraction index of the aqueous humour and  $f$  is in unit of metre. The converted refractive powers are recorded in Table 6-6 and the linear regression plots are shown in Figure 6-10 comparing the correlation of predicted postoperative refractive powers both numerically and mathematically with the clinical measurements.

Table 6-6. Average refractive powers computed using clinical and predicted corneal topographies, presented in mean  $\pm$  1 standard derivation. All values are in dioptr (D).

Preoperative	Postoperative		
	Clinical	Numerical	Mathematical
42.49 $\pm$ 1.35	38.15 $\pm$ 1.79	38.14 $\pm$ 1.78	37.30 $\pm$ 1.90

From Table 6-6, it can be seen that all means of postoperative power are smaller than the mean power calculated using preoperative clinical data. The actual clinically achieved postoperative powers are higher than both numerical and mathematical results but the numerical simulations are observed to produce closer results than mathematical



simulations. It should be noted however that the calculated refractive power values through mathematical simulations would have been the target of the actual surgery plan. This expected refractive power was not achieved clinically because the biomechanical reaction of the cornea following surgery led to a modified corneal shape such that a myopic shift occurred as reflected by the bigger refractive power that was actually achieved. The numerical simulation has taken the biomechanical effect into account and managed to predict closely the clinical outcomes. This closer outcome of numerical simulation is detailed in Figure 6-10 where linear regressions between the predicted and measured postoperative refractive powers are sought. The linear correlations confirmed that numerical simulations produced better fit of postoperative power than corresponding mathematical simulations.

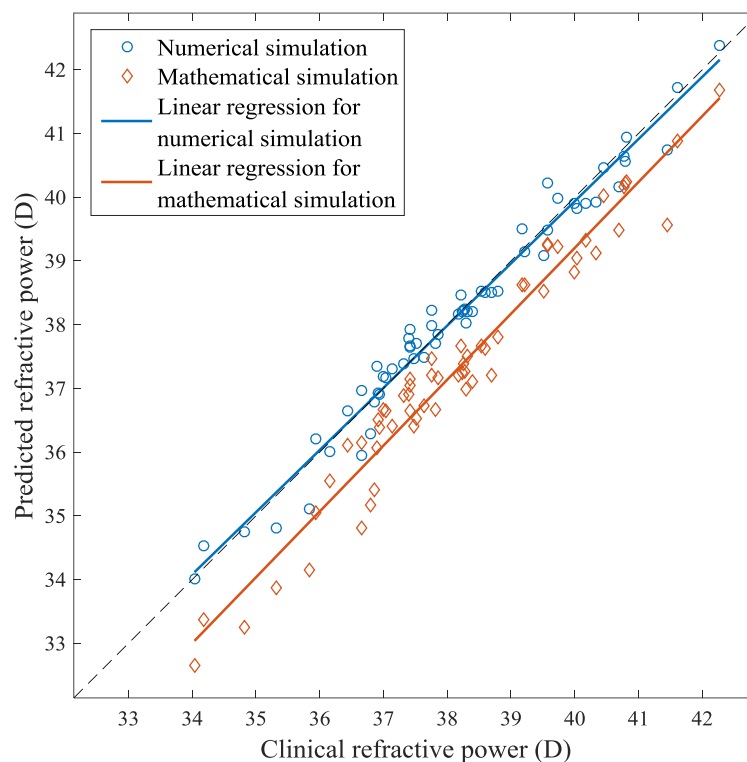


Figure 6-10. Linear correlation between the refractive powers predicted by numerical and mathematical simulations, and the clinical refractive powers

Having calculated preoperative and postoperative refractive powers, it is now worth evaluating the achieved refractive correction, which is the surgically induced refractive power change and calculated by subtracting the preoperative refractive power from the postoperative refractive power. The results are detailed in Table 6-7 and the Bland-Altman plots are presented in Figure 6-11 to show the agreement between predicted and measured refractive corrections.

Table 6-7. Average refractive corrections obtained clinically and predicted numerically and mathematically. Also listed are the differences between predicted corrections and the clinically achieved corrections.

	Clinical	Numerical	Mathematical
Refractive correction	$-4.34 \pm 1.05$	$-4.36 \pm 1.01$	$-5.20 \pm 1.25$
Difference with clinical	-	$-0.02 \pm 0.30$	$-0.86 \pm 0.42$

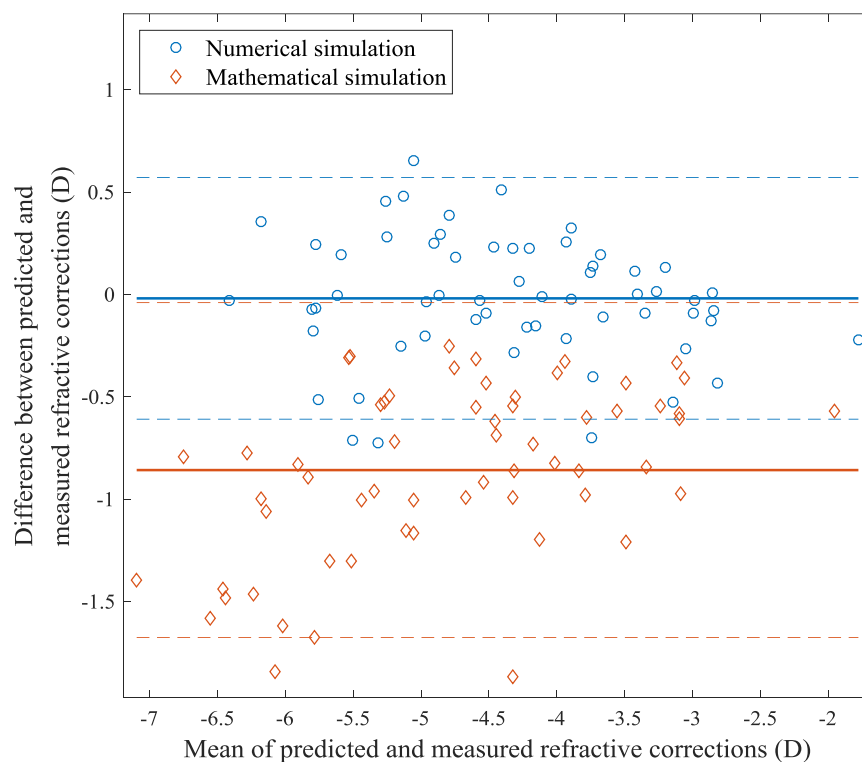


Figure 6-11. Bland-Altman plots for predicted and measured refractive correction. The continuous lines mark the means of differences, while the dashed lines present the 95% confidence limits.

As expected, the achieved clinical refractive correction is less than the attempted correction as represented by the mathematical simulation (Table 6-7). The results also tell

that for the purpose of predicting the surgical outcomes, numerical simulation appears to be superior. The refractive correction obtained in the numerical simulations agreed with the clinical outcomes to a higher level as shown Figure 6-11. This is presented by the closer mean difference to zero and the narrower 95% confidence limits.

## 6.5 LASIK vs. SMILE

In this part of the study, the 60 sets of LASIK FE models have been modified to simulate the SMILE procedure in order to investigate the differences in outcome between the two procedures. As stated in Chapter 3, SMILE models differ from the LASIK models in only the definitions of flap (LASIK) and cap (SMILE). The SMILE cap is assumed to have the same size as the LASIK flap to enable direct comparison of results. In Figure 6-12 and Figure 6-13, the inflated LASIK and SMILE models built for a typical patient are presented. In the figures, the colour contours represent stress in the tissue caused by the inflation. It is shown from Figure 6-12 that the SMILE cap contributes more in resisting the IOP, while the corneal flap in the LASIK model makes almost no contribution (bluer colour). Compared to the gap between the flap and the rest of cornea at the opposite side to the hinge, the opening in the SMILE cut is considerably smaller. In Figure 6-13, the flap and cap are removed to display the stress distribution of underlying tissue. The area beneath the flap is seen to be more stressed than the area beneath the cap. This is expected because corneal flap is not functional in this inflation process.

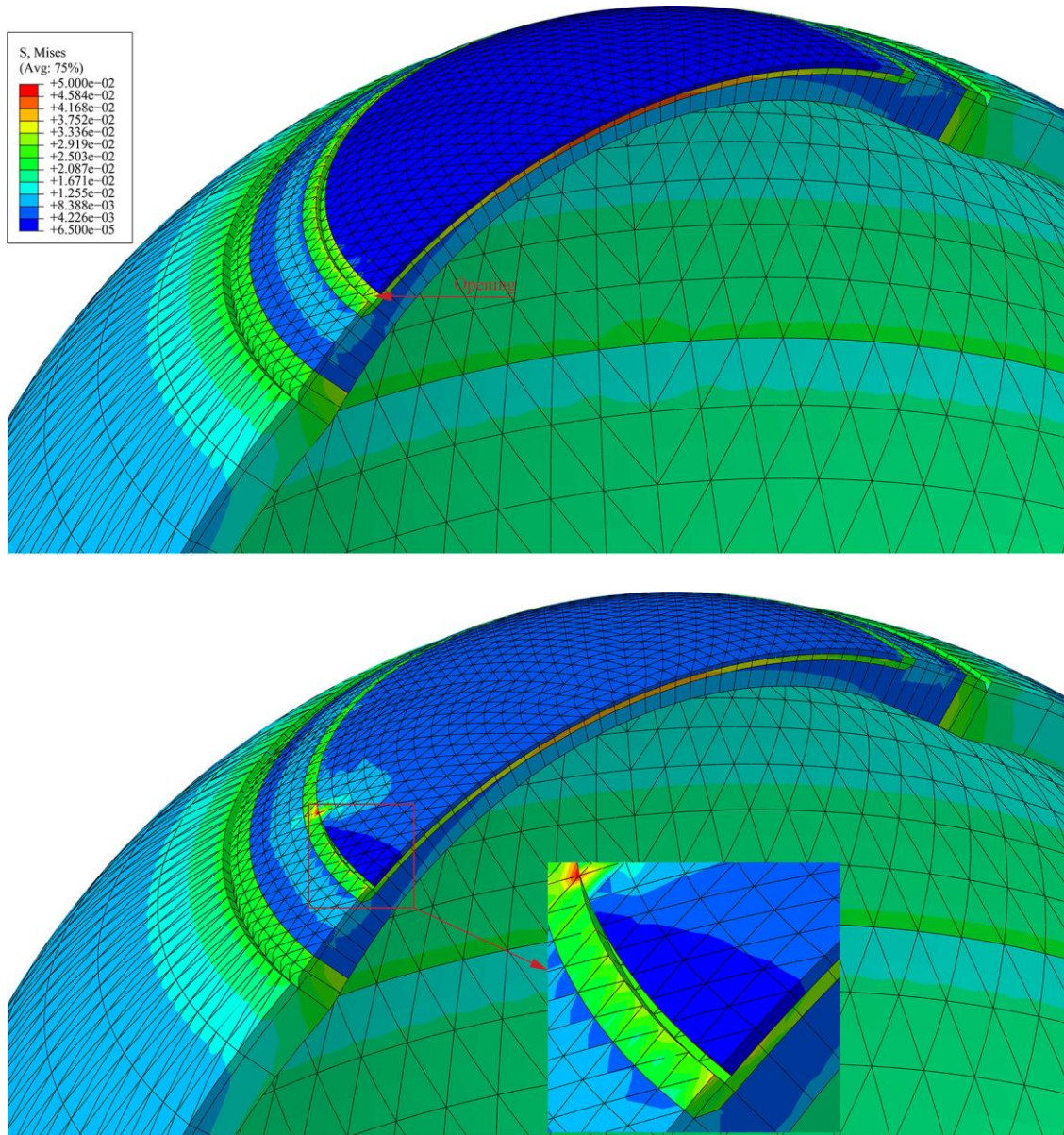


Figure 6-12. Cross section of inflated LASIK (top figure) and SMILE (bottom figure) models using one typical set of patient data. The contour colours represent the stress in the tissue. The epithelium layers are removed in both models.

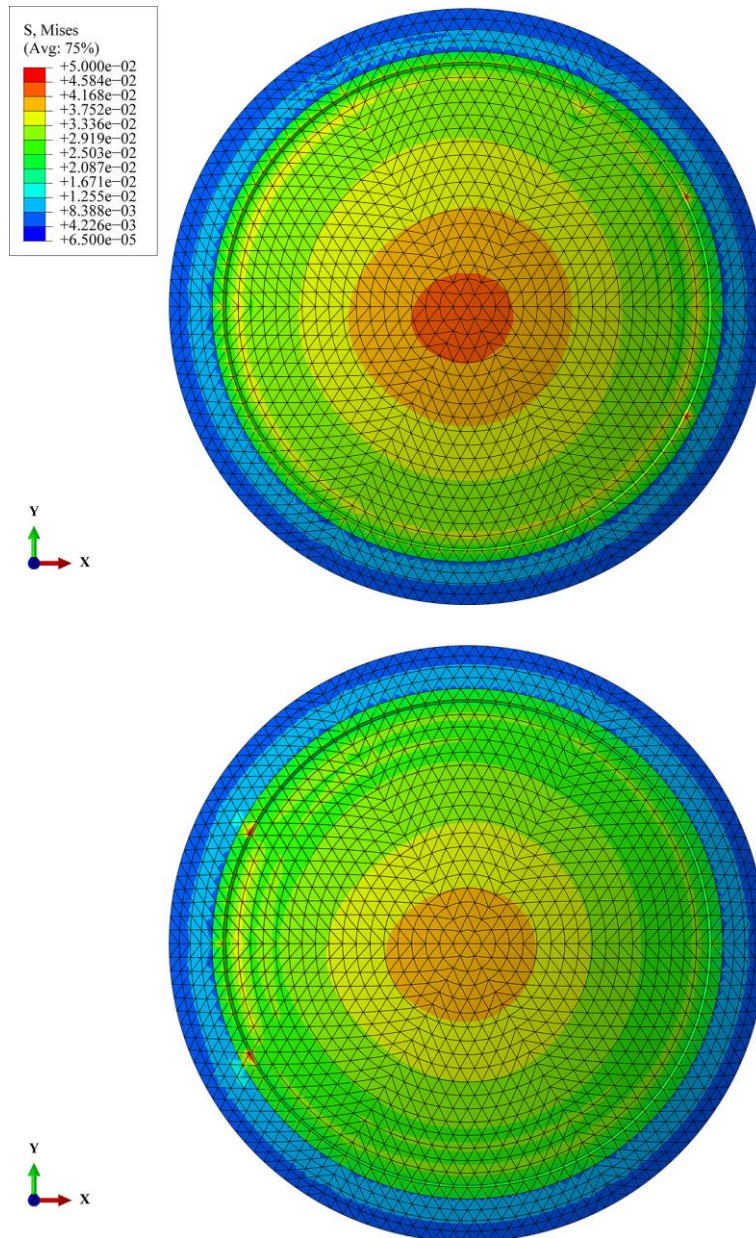


Figure 6-13. Top view of inflated LASIK (top figure) and SMILE (bottom figure) models using one typical set of patient data. The contour colours represent the stress in the tissue. The epithelium and flap layers are removed in both models.

Without the contribution of flap in bearing the internal pressure, it is expected the cornea (especially the central cornea) in LASIK would undergo larger displacement under the same IOP. This is supported by Figure 6-14 where it is shown that corneal apex underwent more displacement in the LASIK models compared to the SMILE models, while the limbal displacement, which should not be affected much by corneal action, show no

obvious difference. Combined, these results should lead to more curved corneal shapes in the LASIK models and hence less correction for myopia.

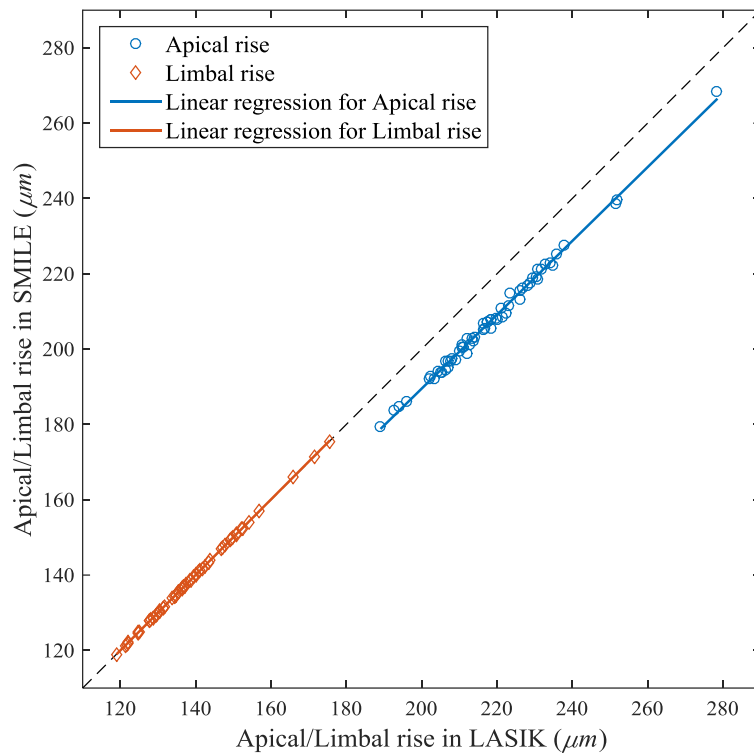


Figure 6-14. Linear correlation of corneal apical rise and limbal rise in LASIK and SMILE models

In Figure 6-14, the limbal point is chosen as the right node from the z-x cross section (limbal nodes with maximal x coordinates), and it is necessary to examine the symmetric property of the cornea behaviour because the cuts for flap and cap are asymmetric, leading possibly to some asymmetric corneal behaviour under IOP. The results in Figure 6-15 and Figure 6-16 show that this effect is negligible with almost perfect agreement between the right and left, superior and inferior limbal rises. In LASIK, the hinged flap, although carries little stress at the hinge, may have contributed too little to affect overall symmetric corneal behaviour. On the other hand, the SMILE cap is only separated from the rest of model by a small incision, and this also seems to have a negligible effect in changing the symmetric corneal behaviour.

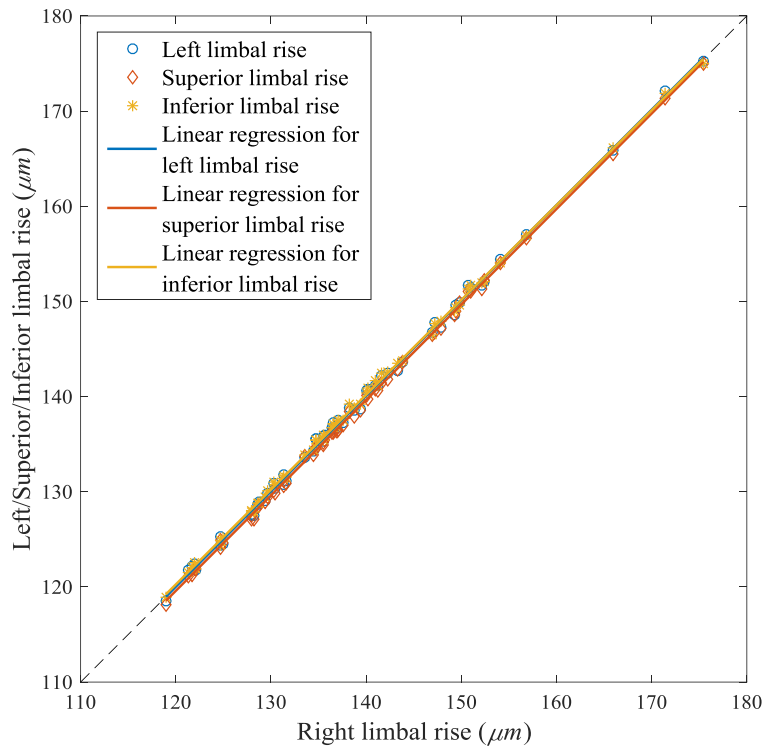


Figure 6-15. Linear correlation of limbal rises in **LASIK** models between the right and left, superior and inferior limbal nodes

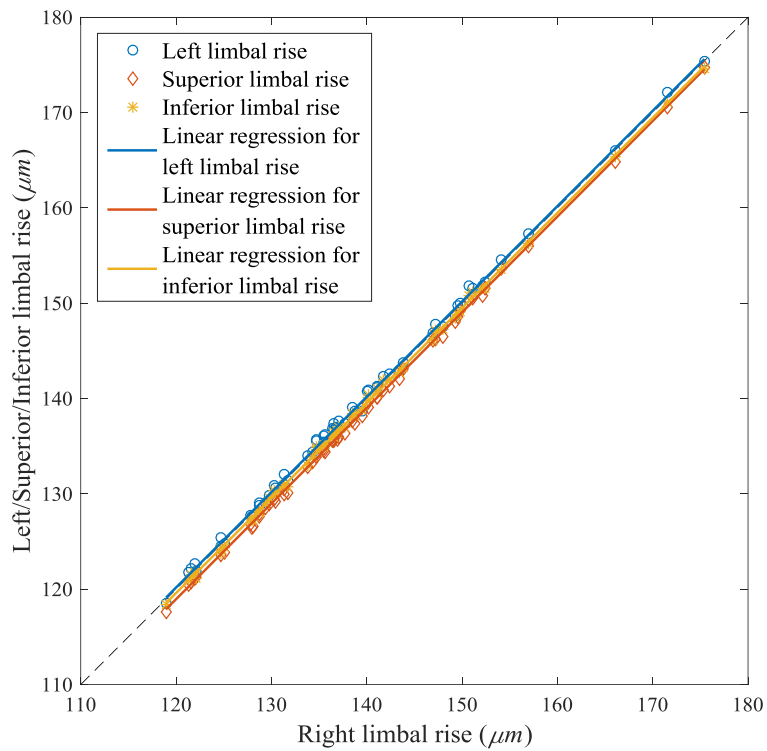


Figure 6-16. Linear correlation of limbal rises in **SMILE** models between the right and left, superior and inferior limbal nodes

Having been acknowledged that the more curved corneal shapes may be obtained in LASIK models (thus greater refractive powers), it is worth validating this by mean of refractive powers. Following the same ray tracing approach as stated in Section 6.4, the corneal refractive powers of the SMILE models are computed and compared to that of the LASIK models which have been given earlier. In addition, the refractive powers in models before application of IOP are also computed. The average values are given in Table 6-8. It can be seen from Table 6-8 that corneal refractive powers after application of IOP are increased by small amounts in both LASIK and SMILE models. The values for LASIK and SMILE are very close, however they are seen to be slightly larger in SMILE models, which is out of expectation because the corneal shapes in SMILE models under IOP are expected to be less curved thus carry less refractive powers. This phenomenon is discussed later in Chapter 7.

Table 6-8. Average corneal refractive powers computed using corneal topographies before and after application of IOP in LASIK and SMILE models

Without IOP	Under IOP	
	LASIK	SMILE
36.18 ± 2.20	36.84 ± 1.85	36.94 ± 1.84

It should be noted that, even though it seems like the SMILE offers slightly less myopic correction (with higher residual refractive power), the greater corneal movement outwards in the LASIK models should be considered. As such, there will be an additional myopic shift in LASIK models compared to the SMILE correspondence, which lessens the myopic correction of LASIK. Combined, the myopic correction of the LASIK should be less than that of the SMILE.



## 6.6 TONOMETRY

The LASIK and SMILE models established in this thesis have enabled numerical study of tonometry to evaluate the influence of surgical applications on the IOP estimates using the Goldmann applanation tonometer (GAT) and Corvis ST (CVS). The IOP estimates  $IOP_{GAT}$  for GAT and  $IOP_{CVS}$  for CVS using INTACT (with preoperative corneal thickness), LASIK and SMILE models are obtained following the methods described in Section 3.4.8 and listed in Table 6-9.

Table 6-9. Average IOP estimates by GAT and CVS using INTACT, LASIK and SMILE models, presented as mean  $\pm$  1 standard derivation. Also listed are the ratio between the estimated IOP and the true IOP. IOP values are in mmHg.

True IOP	Estimated by GAT			Estimated by CVS		
	INTACT	LASIK	SMILE	INTACT	LASIK	SMILE
$16.91 \pm 1.99$	$17.25 \pm 2.14$	$13.12 \pm 1.94$	$13.27 \pm 1.99$	$21.59 \pm 3.60$	$16.59 \pm 3.72$	$16.18 \pm 3.68$
	$1.02 \pm 0.05$	$0.78 \pm 0.07$	$0.78 \pm 0.07$	$1.27 \pm 0.13$	$0.97 \pm 0.15$	$0.95 \pm 0.15$

Very close IOP estimates compared to the true values are obtained in INTACT models by GAT; it can be seen from Table 6-9 that there is only 2% overestimation by average. Using the same INTACT models, the CVS leads to a mean overestimation of 27%. This notably larger overestimation is discussed in Chapter 7. From Table 6-9, it is evident that surgical applications have significant effect on tonometry. Significant reduction in IOP estimates are found from INTACT to LASIK and SMILE models which takes place in both GAT and CVS studies and is visualised in Figure 6-17 to Figure 6-18. In GAT, the reductions rates are 23.9% and 23.0% for LASIK and SMILE, and these become 23.2% and 25.1% in CVS. All these reduction rates are very similar.

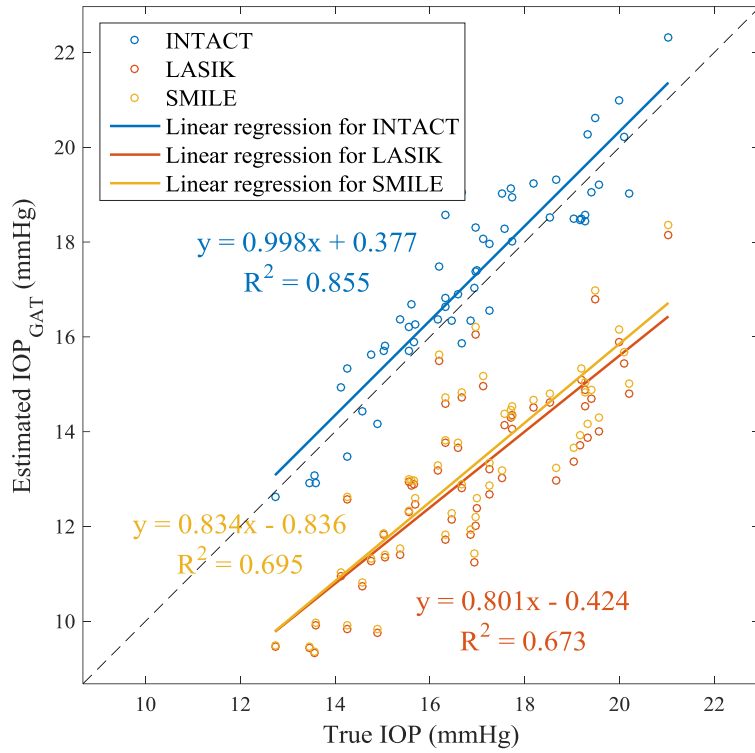


Figure 6-17. Linear correlation of true IOP and estimated IOP<sub>GAT</sub>

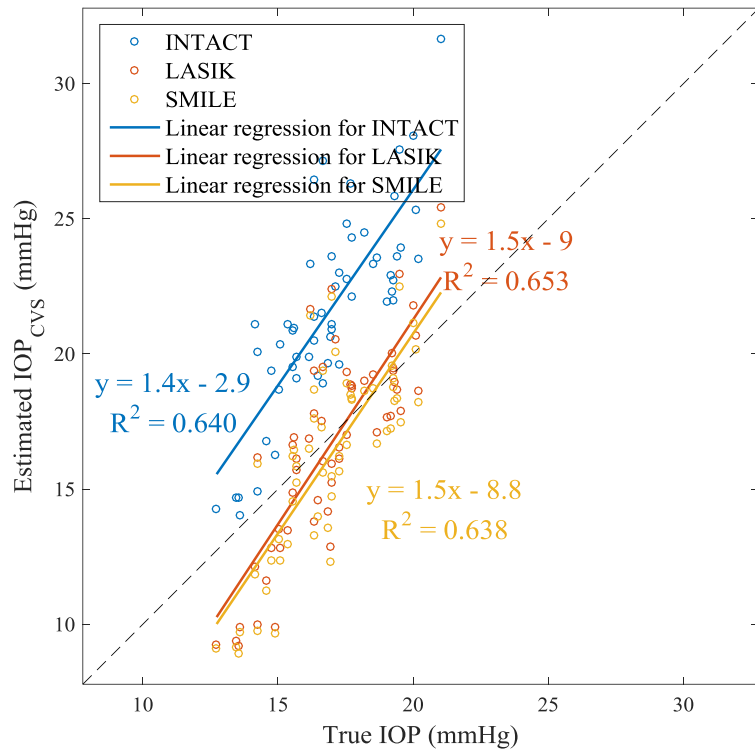


Figure 6-18. Linear correlation of true IOP and estimated IOP<sub>CVS</sub>

Being indirect method to measure IOP, GAT and CVS are reported to be influenced by the corneal thickness. The linear relations between the central corneal thickness (CCT) and ratio between estimated IOP and true IOP are sought in Figure 6-19 and Figure 6-20 for GAT and CVS, respectively. In the figures, the CCT values for LASIK and SMILE models are obtained by subtracting the central ablation depth from the CCT values for INTACT models. It is seen that CCT is highly related with the ratios; thicker CCT values tend to result in overestimation of true IOP and vice versa. With the CCT being reduced in LASIK and SMILE models, the IOP values estimated by GAT and CVS are both reduced significantly.

It should be noted, although the LASIK and SMILE models are different in corneal integrity, the IOP estimates by both GAT and CVS differ little between LASIK and SMILE as seen from Figure 6-17 to Figure 6-20. This suggests that the corneal resistance against tonometric pressure remains similar after LASIK and SMILE procedures.

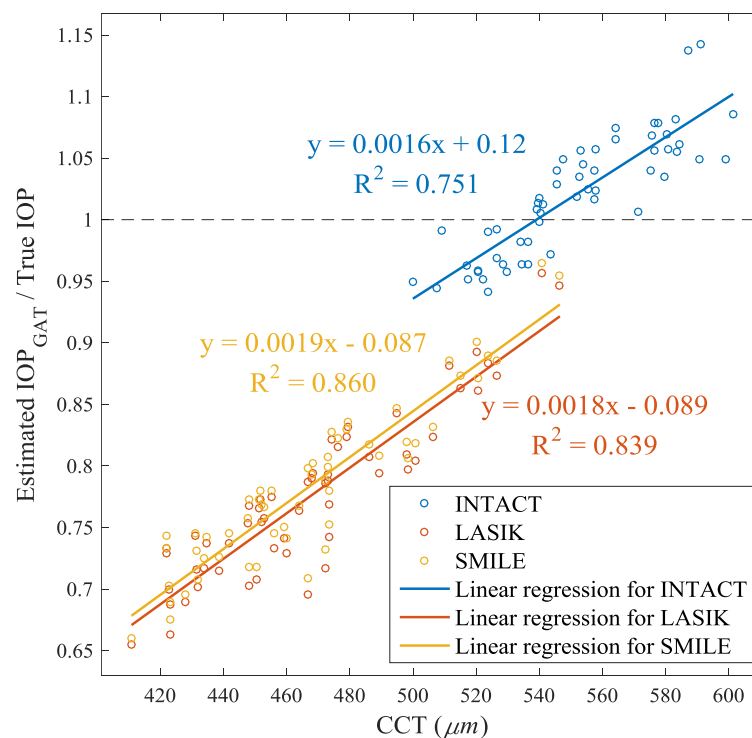


Figure 6-19. Linear correlation of CCT and ratio between estimated IOP<sub>GAT</sub> and true IOP

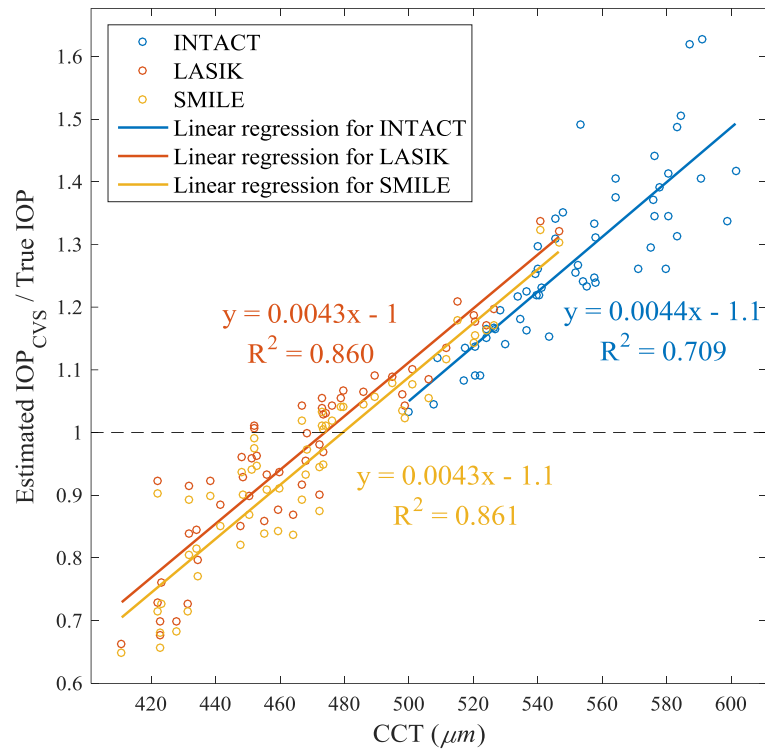


Figure 6-20. Linear correlation of CCT and ratio between estimated  $IOP_{CVS}$  and true IOP

## 6.7 CONCLUDING REMARKS

In this chapter, an initial study considering the modelling strategies are included, leading to a reasonable mesh approach and ablation adjustment method. Using the results of this initial study, 60 sets of patient data are used to conduct a parametric study on wound healing, the outcomes of which show that the wound healing zone needed to be at least 4.5 times as stiff as the rest of the stroma to produce a reasonable fit with the measured postoperative outcomes. With this optimal stiffness ratio, the models can closely predict the clinical surgical outcomes and show significant advantages over the simple mathematical simulation of refractive surgery where the biomechanical effect of the surgery is ignored. This reliability of numerical simulation has supported later a comparative study between the LASIK and SMILE procedures, revealing that greater impact is introduced by LASIK procedure. This greater impact is then shown to have little

effect on the IOP estimates by GAT and CVS. The outcomes and results of this chapter will be discussed in Chapter 7.

## CHAPTER 7

### OVERALL DISCUSSION AND CONCLUSION

---

#### 7.1 INTRODUCTION

The results presented in the last three chapters concerning topography fitting, topography matching and numerical simulation of refractive surgery are discussed in this chapter. Overall conclusions are then given, followed by recommendations for future work.

#### 7.2 OVERALL DISCUSSION

##### 7.2.1 Topography fitting

The topography fitting study is concerned with the fitting of corneal topography to polynomials, it assessed various polynomials that are either well-known in the ocular community or extensively studied in the image processing field.

The reliability and capability of these polynomials in representing surfaces are mainly determined by the forms of the polynomial terms and the number of terms associated with the polynomial order. The core step of this representation is the estimation of coefficients for individual polynomial terms. In this thesis, two major approaches are considered, namely Orthogonal Projection (OP) and Least squares (LS) methods. A comparison between these methods suggested that the LS method, which has been used as the standard routine in ocular community, is more accurate than the main variants of the OP method. There are three variants of OP, namely zero order approximation (ZOA), exact moment (EM) and interpolation extension of EM (INT). The ZOA variant discretises the orthogonal polynomials to cope with the discrete points, while the EM variant treats the discrete points input as a piecewise-constant function which in theory should result in

better estimation of the coefficients. However, the superiority of EM over ZOA is not significant, and it is the INT variant that improves, to a large extent, the accuracy of the computed coefficients because it approximates the surface as piecewise-linear function. A common problem for OP variants is that they all need a sufficient number of data points in the orthogonal domain. In addition, the EM and INT variants need to evaluate a large number of double integrals on triangles or squares, making them computationally expensive especially for the INT variant (three times the amount of integrals compared to EM). It is because of this inefficiency of the OP method that only LS method is solely employed to fit clinical data in this study.

The reconstruction results based on clinical topographies indicate that the conventionally used Zernike polynomials (ZPs) may not be the best option for fitting of optical surfaces such as the one considered in this paper – corneal elevation map. In fact, the set of ZPs appear to be among the worst fitting options if the reconstruction error is considered.

The square polynomials such as Legendre polynomials (LPs) and Gegenbauer polynomials (GPs) with various scaling factors, although are only kept within a circular portion inside the complete square domain, match the fitting performance of ZPs at all orders. This can be explained by looking at the explicit expressions in Table 7-1 where ZPs have been expressed in a Cartesian coordinates system. It is easy to derive that the optimisation problems expressed by Equation (3.22) using either ZPs, LPs or GPs reduce to the same optimisation problem involving  $Z(x_d, y_d) = \sum a_{n,m} x_d^n y_d^m + \varepsilon_d$  because all of them consist of same general polynomial terms. It is natural to understand that the radial versions of LPs and GPs match OFMPs for the same reason that the optimisation problems based on these polynomials reduce to a single optimisation problem.

Table 7-1. Explicit expressions of ZPs in Cartesian system, LPs and GPs.

ZPs (Cartesian[290])	LPs	GPs	General polynomials
1	1	1	1
$x$	$x$	$2\alpha x$	$x$
$y$	$y$	$2\alpha y$	$y$
$2xy$	$(3x^2 - 1)/2$	$2\alpha(\alpha + 1)x^2 - \alpha$	$x^2$
$2x^2 + 2y^2 - 1$	$xy$	$4\alpha^2 xy$	$xy$
$-x^2 + y^2$	$(3y^2 - 1)/2$	$2\alpha(\alpha + 1)y^2 - \alpha$	$y^2$

The OFMPs, although have been used for a considerable period in pattern recognition and character identification, have not been adopted in the ocular community for representation of corneal topography. The studies in this thesis have shown that the OFMPs always fit the target surfaces best at all orders considered. This is believed to be because the radial polynomial of OFMPs is independent of the angular frequency such that for a certain order, the OFMPs have more polynomial terms and thus offer greater fitting power. Following OFMPs in performance is the set of PZPs, which also lead to significantly smaller reconstruction errors compared to ZPs, this is believed mainly because PZPs also have more polynomial terms than ZPs for the same order as listed in Table 3-2. The GHPs have a scaling factor and can change from local features to global features, and are orthogonal on the infinite plane due to the exponential term in their expressions. The results show that the GHPs also tend to match ZPs at high order when the global features of GHPs are used.

Further to the above comparisons, it is also revealed that the anterior surfaces of normal corneas can be fitted relatively easily, followed by anterior surfaces of keratoconic corneas, and posterior surfaces of both normal and keratoconic corneas. The anterior surfaces are commonly believed to be more accurately measured but keratoconic corneas typically have more complex shapes, which increase the difficulties in polynomial fitting. The posterior surfaces for both normal and keratoconic corneas are normally noisy



because of limitations of the measurement instruments. Higher order polynomials are needed to fit these noisy surfaces and the fitting outcomes may in turn be better than the less noisy anterior surfaces because those higher order complex polynomials features may be only helpful for the noisy and thus more complex surfaces.

Considering that the main purpose of polynomial fitting is estimating locations on the corneal surface that are not measured, a series of prediction tests have been included in this study. The results indicate that even though the reconstruction outcomes are continuously improved when increasing the polynomial order, the prediction of nearby locations by the reconstructed surface may be erroneous. For most polynomials except OFMPs, order 10 is shown to be a safe threshold for prediction, at which both the reconstruction and prediction errors are small enough (around  $0.3\mu\text{m}$ ). The prediction behaviour of OFMPs is very sensitive to the data resolution in reconstruction, and this may be due to the fact that for the same order, OFMPs have more complex terms. But fortunately, if the data resolution is not too low, the prediction by OFMPs is also acceptable. The studies show that the minimal prediction errors of OFMPs for resolution  $0.2\text{ mm}$ , although are larger than that of other polynomials, are still less than  $0.5\mu\text{m}$ . It should also be noted that the prediction test in this study can only be implemented with a spacing distance starting at  $0.2\text{mm}$ , which is double that of the original measurements. The prediction error based on the original spacing of  $0.1\text{mm}$ , although is not able to be assessed in this thesis, is expected to be smaller.

The prediction practice above can be cast as an interpolation problem. One can easily relate this to various choices of interpolation algorithm such as linear, spline interpolation methods and so forth. Considering this, the prediction exercises in Chapter 4 are repeated using several standard interpolation methods and the results are listed in Table 7-2 to

Table 7-5, where the best achieved prediction errors for each map have been extracted from Chapter 4 for comparison. Four standard interpolation methods are included, namely linear interpolation, natural neighbour interpolation, cubic spline and biharmonic spline interpolation. It can be seen that the biharmonic spline interpolation method resulted in the best prediction outcomes among the four methods but the prediction errors of interpolation methods are all bigger than the polynomial fitting approach for all kinds of maps with all resolutions. The prediction by interpolation becomes significantly worse with increase in the spacing (especially for posterior surfaces) while remains similar by polynomial fitting. There is a clear superiority of performance by interpolation methods in anterior normal corneal topography, followed by anterior keratoconic, posterior normal and posterior keratoconic corneal topography, respectively.

Table 7-2. Prediction errors by polynomial fitting and various standard interpolation methods for **anterior normal** corneal topography. The errors are presented as mean  $\pm$  1 standard derivation and in  $\mu\text{m}$ .

Spacing	Polynomial fitting	Interpolation			
		Linear	Natural neighbour	Cubic spline	Biharmonic spline
0.2	0.295 $\pm$ 0.006	9.04 $\pm$ 0.494	3.75 $\pm$ 0.185	2.368 $\pm$ 0.098	0.367 $\pm$ 0.007
0.3	0.302 $\pm$ 0.009	3.167 $\pm$ 0.16	3.362 $\pm$ 0.168	5.233 $\pm$ 0.233	0.397 $\pm$ 0.023
0.4	0.317 $\pm$ 0.015	6.703 $\pm$ 0.352	6.907 $\pm$ 0.358	9.852 $\pm$ 0.412	0.483 $\pm$ 0.057

Table 7-3. Prediction errors by polynomial fitting and various standard interpolation methods for **anterior keratoconic** corneal topography. The errors are presented as mean  $\pm$  1 standard derivation and in  $\mu\text{m}$ .

Spacing	Polynomial fitting	Interpolation			
		Linear	Natural neighbour	Cubic spline	Biharmonic spline
0.2	0.3 $\pm$ 0.012	9.173 $\pm$ 0.701	3.792 $\pm$ 0.239	2.424 $\pm$ 0.145	0.377 $\pm$ 0.026
0.3	0.312 $\pm$ 0.023	3.253 $\pm$ 0.209	3.453 $\pm$ 0.217	5.088 $\pm$ 0.405	0.432 $\pm$ 0.076
0.4	0.339 $\pm$ 0.051	6.946 $\pm$ 0.506	7.148 $\pm$ 0.509	9.934 $\pm$ 0.647	0.6 $\pm$ 0.2

Table 7-4. Prediction errors by polynomial fitting and various standard interpolation methods for **posterior normal** corneal topography. The errors are presented as mean  $\pm$  1 standard derivation and in  $\mu\text{m}$ .

Spacing	Polynomial fitting	Interpolation			
		Linear	Natural neighbour	Cubic spline	Biharmonic spline
0.2	0.293 $\pm$ 0.003	12.079 $\pm$ 1.307	4.916 $\pm$ 0.374	3.003 $\pm$ 0.162	0.378 $\pm$ 0.013
0.3	0.299 $\pm$ 0.005	4.188 $\pm$ 0.314	4.443 $\pm$ 0.325	6.547 $\pm$ 0.398	0.434 $\pm$ 0.043
0.4	0.31 $\pm$ 0.007	8.804 $\pm$ 0.74	9.075 $\pm$ 0.745	12.514 $\pm$ 0.683	0.651 $\pm$ 0.148

Table 7-5. Prediction errors by polynomial fitting and various standard interpolation methods for **posterior keratoconic** corneal topography. The errors are presented as mean  $\pm$  1 standard derivation and in  $\mu\text{m}$ .

Spacing	Polynomial fitting	Interpolation			
		Linear	Natural neighbour	Cubic spline	Biharmonic spline
0.2	0.294 $\pm$ 0.003	12.367 $\pm$ 1.794	5.047 $\pm$ 0.482	3.102 $\pm$ 0.21	0.412 $\pm$ 0.053
0.3	0.299 $\pm$ 0.005	4.323 $\pm$ 0.449	4.591 $\pm$ 0.462	6.503 $\pm$ 0.547	0.556 $\pm$ 0.175
0.4	0.312 $\pm$ 0.008	9.19 $\pm$ 1.074	9.463 $\pm$ 1.077	12.721 $\pm$ 0.941	0.938 $\pm$ 0.39

In Figure 7-1, the number of maps that were best predicted by various sets of polynomials are presented by histogram plots. The polynomial orders for all polynomial sets at which the best prediction occurred are also illustrated. It can be seen that the ZPs performed the best in prediction, followed by GHPs and PZPs, it is not surprising that OFMPs never produced best prediction for any maps. Because of the fact that the GHPs matched ZPs at high order, it is reasonable to combine their contributions in prediction. In fact, among all maps that were best predicted by GHPs, the prediction errors by ZPs were only  $8.02e^{-7} \mu\text{m}$  larger than that of the GHPs on average with a standard derivation of  $1.52e^{-6} \mu\text{m}$ .

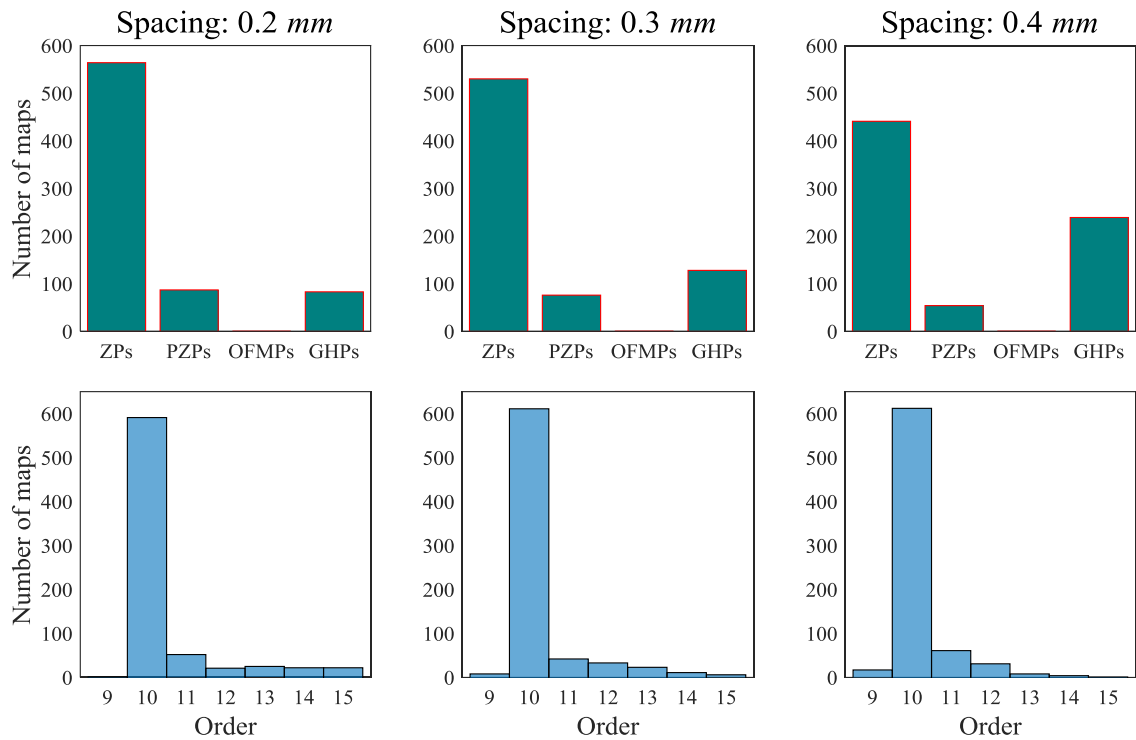


Figure 7-1. The set of polynomials that achieves best prediction and the corresponding polynomial order for all topography maps

The comparison here has consolidated the superiority of orthogonal polynomials in prediction of corneal topography over various standard interpolation algorithms. Further, it is also seen in Figure 7-1 that the majority of the maps were best predicted by order 10. This order has been shown to be an important order, beyond which the reconstruction errors (as presented in Chapter 4) tend to improve relatively little and the prediction errors gradually increase. This particular behaviour, which exists in all polynomials is believed to be related to the map radius used in the reconstruction. The maps used so far in both reconstruction and prediction studies all had radii 5 mm. Figure 7-2 shows the reconstruction errors of maps with smaller coverage, ZPs are used in this particular example. The maps used herein come from the same original Pentacam data but smaller central portions are kept for reconstruction. Also, an additional group of maps with a larger spacing (0.2 mm) is extracted. In Figure 7-2, central portions with radii from 3.0 mm to 5.0 mm are used and distinguished by different colours. In addition the two

spacings are discriminated by line types. As shown in Figure 7-2, the order, at which the reconstruction becomes stable tends to be smaller for smaller maps. If this order is called the stable order, it is shown that the stable order decreased to 6 when the radius of the map was 3.0 mm. On the other hand, even though larger spacing results in fewer data points in the reconstruction and leads to slightly smaller reconstruction error, this seems not to change the stable order, which agrees well with the results shown in Figure 4-11 where spacings 0.3 mm and 0.4 mm were additionally included and were not seen to change the corresponding stable orders.

The reduction of stable order shown in Figure 7-2 will potentially cause the inflection of prediction error to take place earlier. This is validated in Figure 7-3, in addition to the reconstruction test using maps with resolution 0.2 mm, the prediction is also made following the same approach in Chapter 4. Figure 7-3 shows the results for OFMPs because the inflection of prediction is most obvious using this set of polynomials. The solid curves now present the reconstruction errors and the dashed curves are the corresponding prediction errors. The inflection point on the prediction error curves are marked and it is evident that the inflection order reduces consistently with the stable order.

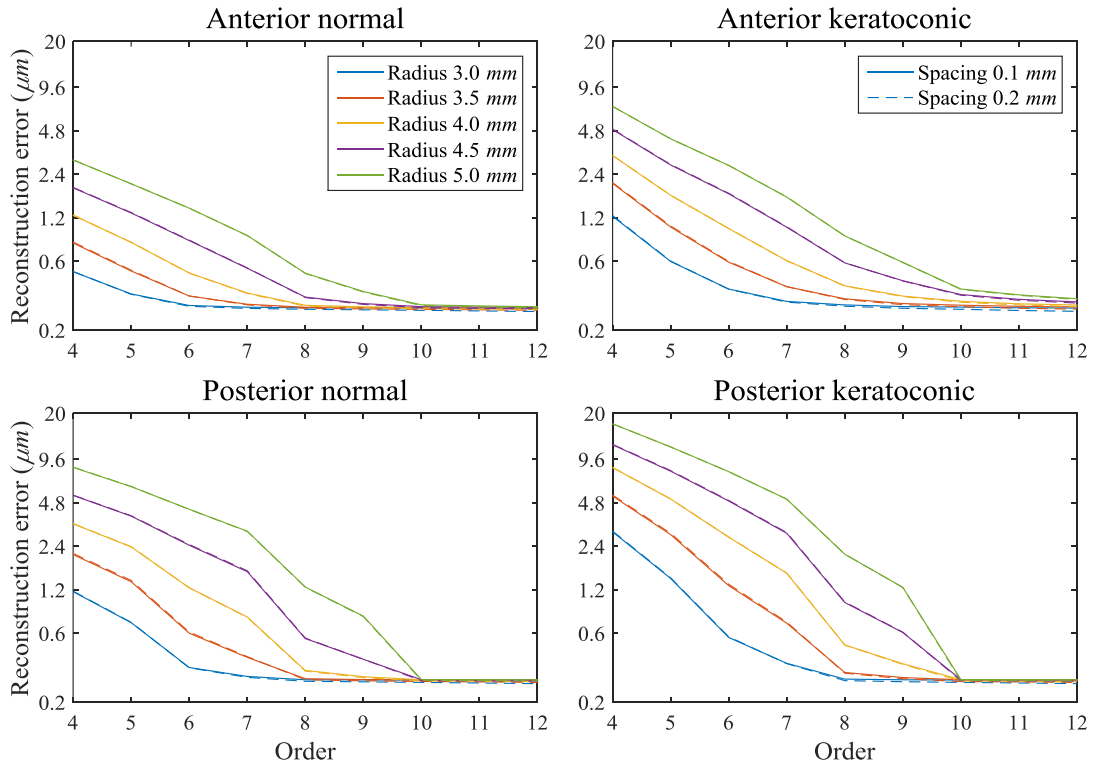


Figure 7-2. Mean reconstruction errors for maps with different radii and resolutions, the reconstruction is by ZPs.

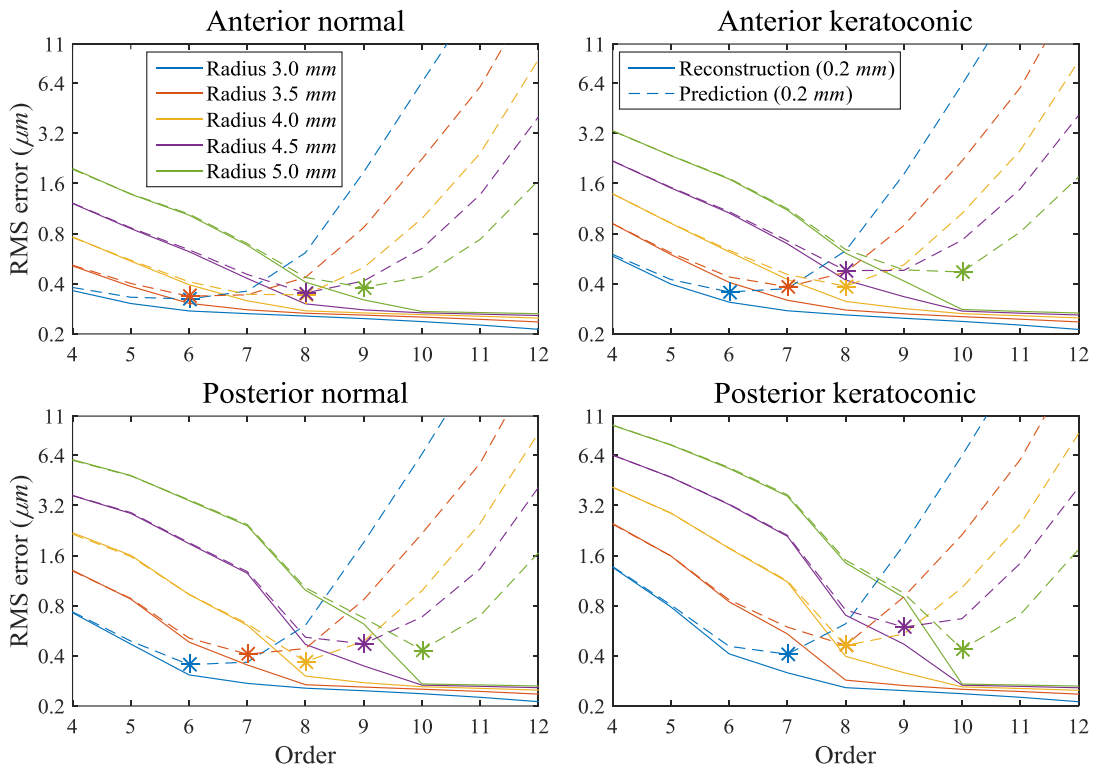


Figure 7-3. Mean reconstruction and prediction errors for maps with different radii and resolution 0.2 mm, the reconstruction and prediction are by OFMPs. The asterisks represent reflection orders.

### 7.2.2 Topography matching

The topography matching is concerned with the problem of combining multiple corneal topographies to form a single map covering the entire cornea. Direct search (DS) and several variants of the iterative closest point (ICP) algorithm are implemented and tested. Convergence of the DS and point-to-point ICP approaches results in significant registration and alignment errors even in the case of noise-free simulated data. This is due to an over-constrained objective function which insists on tying multiple sets of paired points on the static and dynamic maps. However, the point-to-plane ICP routines release this constraint by allowing the dynamic surface to slide over the static surface.

The Nelder-Mead (NM) simplex algorithm was employed in the DS method because of its simplicity. The NM algorithm uses the values of the objective functions only without numerical or analytical gradients and other higher order derivatives information, it is classified as a direct search algorithm and belongs to local and unconstrained minimisation algorithms. It would be reasonable to consider other algorithms such as quasi-newton and interior-point algorithms or more sophisticated global approaches such as genetic algorithm, particle swarm optimisation and simulated annealing optimisation. The commercial Matlab software has provided a good number of optimisation tools including all of the aforementioned candidates and the coding of DS method in this study has enabled easy adoption of new optimisation methods to solve the same problem. In addition to the results reported in Table 5-1 of DS using NM algorithm, several other optimisation algorithms are attempted to implement the DS method with vertical shooting mapping. These algorithms are local approaches including quasi-newton (QN), interior-point (IP), sequential quadratic programming (SQP), active-set (AS) and global approaches including pattern search (PS), particle swarm optimisation (PSO), genetic algorithm (GA) and simulated annealing (SA). The rigid-body transformation obtained

using these algorithms (including that obtained using NM as presented in Table 5-1) is detailed in Table 7-6. Indeed, some optimisation methods, additionally attempted here, result in better matching outcomes (bold and italic) but they are generally costly in terms of computational time and the results are still not comparable to the more efficient ICP variants. It should be noted that the built-in default settings are used herein for all standard optimisation methods. Also, it is well known that the performances of these methods (especially the local approaches) are significantly influenced by initial/starting points and they may unexpectedly fall in local minima. However, a further detailed discussion is outside the scope of this thesis and it is unlikely that the DS method with any standard optimisation approach could match the speed and accuracy of the ICP variants.

Table 7-6. Rigid-body transformation by DS method fulfilled by various optimisation algorithms

Exact	Local optimisation algorithms					Global optimisation algorithms				
	NM	QN	IP	SQP	AS	PS	PSO	GA	SA	
$g_x$	-0.08	-0.022	6.4E-08	-0.088	-0.173	<i>-0.026</i>	-0.004	<i>-0.190</i>	<i>-0.091</i>	-0.154
$g_y$	-0.25	-0.037	2.9E-07	0.026	0.019	<i>-0.257</i>	0.029	<i>-0.208</i>	<i>-0.013</i>	0.252
$g_z$	0.08	0.292	-3.8E-10	0.002	-0.041	<i>0.054</i>	-0.079	<i>0.205</i>	<i>0.075</i>	-0.185
$t_x$	-2	-0.376	6.0E-07	0.000	0.000	<i>-2.017</i>	0.029	<i>-1.893</i>	<i>-0.335</i>	1.761
$t_y$	0.5	0.121	8.4E-09	0.731	1.377	<i>0.137</i>	0.070	<i>1.114</i>	<i>0.733</i>	0.878
$t_z$	-0.3	-0.036	-1.8E-08	-0.042	-0.129	<i>-0.290</i>	-0.011	<i>-0.338</i>	<i>-0.048</i>	-0.285
$E_r$		0.701	0.858	0.837	0.903	<b><i>0.150</i></b>	0.866	<b><i>0.264</i></b>	<b><i>0.701</i></b>	1.561

There are two main ICP algorithms, point-to-point and point-to-plane, and for each of these there are three variants, closest point (CP), vertical shooting (VS) and normal shooting (NS). The CP routine is based on paired discrete points on the two surfaces. The VS and NS methods rely respectively on vertical or normal rays projected from the dynamic surface to intersect with the static surface. This defines the corresponding points on the two maps and requires the continuous definition of the two surfaces - for construction of the normals and for determining the points of intersection. In the present



study, the continuous surface definition is achieved using orthogonal Zernike polynomials.

The practical application of fitting the series of Zernike polynomials to sets of discrete points requires truncation, which is known to be beneficial in that measurement noise, present in the high-order (high spatial frequency) terms, is eliminated. The effects of Zernike fitting can be seen in Figure 7-4 where the CP variant of the ICP algorithm is used. The points with zero-mean Gaussian noise are adjusted to lie on the Zernike-fitted surfaces. It is seen that smooth convergence of the registration error is achieved when Zernike fitting is applied whereas a persistent oscillation is seen when noisy data is used directly.

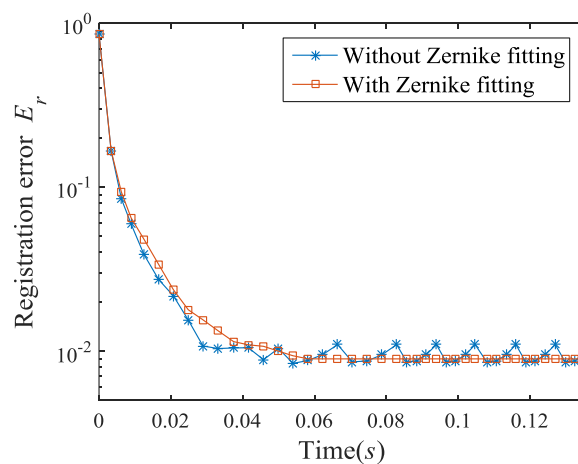


Figure 7-4. The influence of Zernike fitting on the performance of the ICP CP routine, the registration errors are presented in log scale.

The ICP point-to-plane CP variant results in small registration errors in the cases of noise-free, noisy and clinical data with a known numerically applied transformation. This error might be further reduced by increasing the resolution of the measured data – as is achievable with most currently available modern topographers such as the Pentacam used in the topography fitting study. Excellent results are obtained by VS and NS point-to-plane ICP algorithms for simulated noisy data and clinical data with known numerical

transformation. These algorithms also result in acceptably small alignment errors when using full clinical data (both central and peripheral maps), typically  $\mu(E_a) = 1.40 \mu m$ ,  $\sigma(E_a) = 0.92 \mu m$  for central and peripheral maps of 4.53mm radii. An increase in area of around 65% was achieved after combining the central map with four peripheral maps.

The topography matching results achieved in this study are comparable with those reported by Franklin et al. [109], however the preferred ICP variant has significant advantages over the approach proposed by Franklin et al. First, it only takes a few seconds to register all peripheral maps to the central map using ICP algorithm while the optimisation process presented by Franklin may take hours. Even though the computing power nowadays has been dramatically improved, it is unlikely that this would speed up Franklin's approach to match the ICP algorithm. Second, the use of Zernike polynomials in the ICP algorithm overcomes the difficulty in finding reliable corresponding points and acts as a noise filter which enables quick convergence and accurate matching.

The topography matching study used topography maps from the Medmont E300 topographer and only a limited number of maps were included in this study. However the algorithms in this study should also be applicable to topographies provided by other instruments. In fact, two sets of central and peripheral topographies were obtained from Wenzhou Medical University recently and these topography maps were collected using the Pentacam topographer. The VS and point-to-plane variant of the pair-wise ICP algorithm was used to match the peripheral maps to the central map in each set and the alignment errors were plotted in Figure 7-5. Only the central area with a 4 mm radius was kept for all the maps because the large area beyond this radius had missing measurements. The mean alignment error of all the pair-wise matching was  $1.02 \mu m$  with a standard derivation of  $0.13 \mu m$ . Figure 7-6 and Figure 7-7 have shown the combined maps in 3D

and X-Y views. It is evident that significant increases in map coverage have been achieved for both sets of data. The practice here has provided strong support to results reported in Chapter 5 for Medmont data and confidence in applying the matching algorithms to topography maps from other instruments.

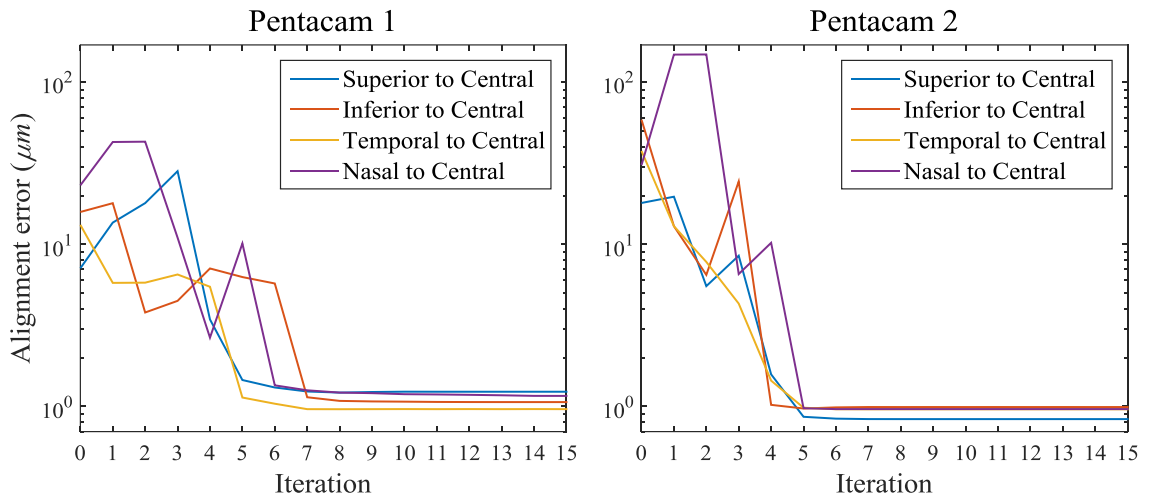


Figure 7-5. Alignment errors of two sets of Pentacam topographies

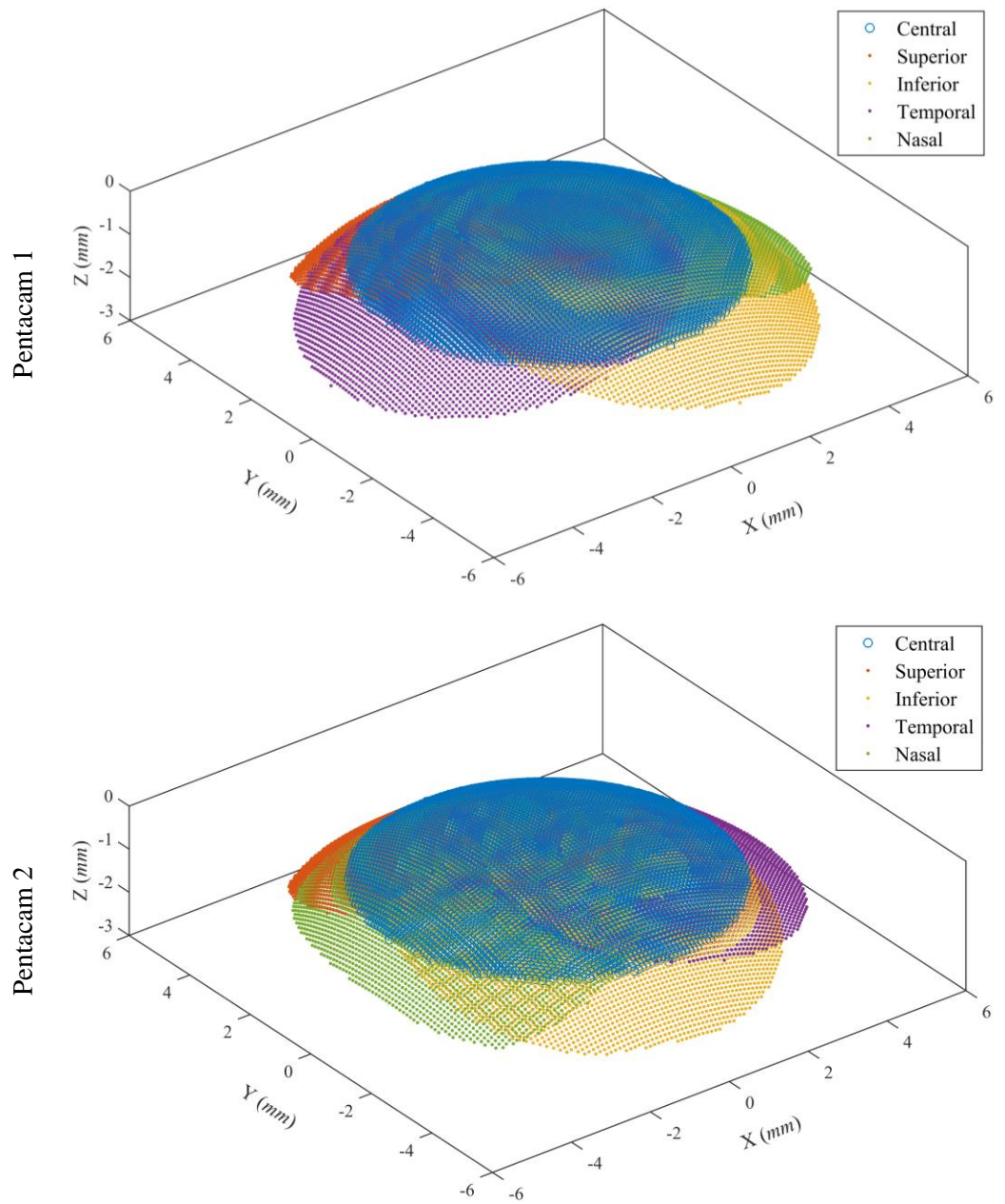


Figure 7-6. The maps in registration, shown in 3D

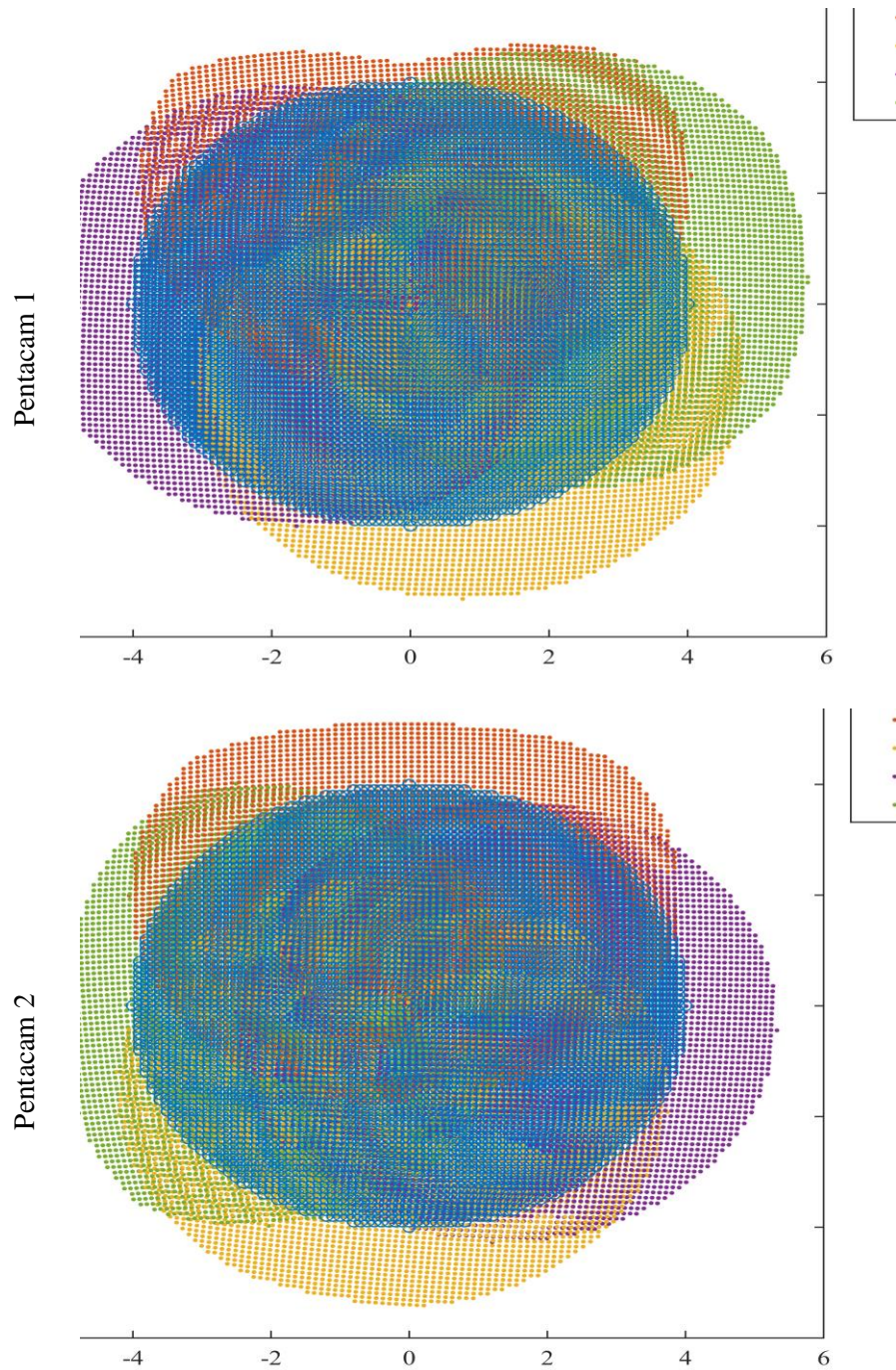


Figure 7-7. The maps in registration, shown in X-Y views

### 7.2.3 Numerical simulation

The numerical simulation of refractive surgery has concentrated on the most commonly used LASIK procedure and was later extended to cover the new, promising SMILE procedure.

Special efforts were taken to closely model these surgical forms such as accurate adoption of patient-specific topography, representative consideration of LASIK flap and SMILE cap, and realistic adjustment of the ablation depth profile. Many recent studies tried to model refractive surgeries patient-specifically [201, 203, 207, 216], however even though they managed to adopt patient-specific topography, none had successfully covered the relatively free LASIK flap and accurate ablation profile that would have been applied in the clinical practice, making them unable to produce reasonable prediction of the postoperative outcome. The numerical simulation of LASIK procedure in this study has relied on a more complete set of patient-specific data including corneal topography maps, ocular axial length, corneal flap thickness distribution and laser ablation profile. These data enabled a more representative simulation of the LASIK procedure and its validation in comparison to the clinical postoperative topography. The good match of numerically predicted and clinically measured postoperative outcomes made it possible to conduct simulation of the SMILE procedure and later the numerical study on effects of corneal surgical applications on tonometry. According to the author's knowledge, numerical studies of tonometry after LASIK and SMILE surgeries are still lacking in the literature.

In this thesis, all numerical models consisted of both the cornea and sclera such that the need to approximate the boundary conditions in the limbus was eliminated. A comprehensive and representative modelling strategy was designed, which involved using a VB programme to generate the idealised model and a Matlab GUI to navigate the main simulation steps including adoption of clinical measurements to create clinical models, stress-free configurations, simulation of laser tissue ablation and generation of LASIK and SMILE models. An efficient and accurate modelling structure was determined through an initial study concerning mesh density, nodal arrangement and methods of ablation adjustment. Even though the nodal rearrangement in the cornea is

not adopted for large scale patient-specific modelling studies, it remains a good candidate for future studies when the actual ablation profile is provided more accurately. The adjustment of ablation was shown to be necessary and resulted in nearly 50% improvement in fit between the simulated and clinically measured postoperative anterior corneal topography.

The wound healing immediate after surgery is believed to significantly contribute to the discrepancy between the attempted and achieved surgical outcomes. In this project, a parametric study on stiffness of the wound healing zone was carried out and indicated that the stiffness of the wound healing layer is at least 4.5 times as stiff as the natural stroma. This finding, at first glance, seems to contradict some results that have been published by other researchers. On one hand, Schmack et al. [283] found that the cohesive tensile strength between corneal wound surfaces was significantly weaker than between stromal lamellae. On the other hand, it is well known that IOP measurement after the LASIK procedure is generally smaller than the measurement taken before the surgery, indicating an overall corneal softening. However, the reduction in cohesive tensile strength does not mean softening of corneal wound but may just indicate inadequate connection between the wound surfaces. Further, there are mainly two factors after surgery that have potential to change the overall corneal stiffness or resistance to internal and external forces, these two factors are corneal thickness thinning and material stiffness change of the wound layer. In LASIK, corneal thickness thinning includes not only the thickness of ablated tissue but also the thickness of the flap because the flap, once cut, would lose almost its entire ability to bear internal and external loadings. Obviously, the thickness thinning will decrease the overall stiffness of the cornea. However, the corneal wound layer with a potentially increased material stiffness, increases the overall stiffness of the cornea.

Current instruments such as GAT and Corvis ST use contact and non-contact tonometry techniques to estimate the IOP. An external pressure is caused by the tonometry methods and the response of the cornea to this pressure is dominated by its flexural or bending stiffness, which is reliant on the sum of  $E_i I_i$  for all corneal layers [219], where  $E_i$  is the Young's modulus (taken as 0.5 MPa for stroma) and  $I_i = t_i^3/12 + t_i z_i^2$  is the second moment of area, with  $t_i$  being the thickness of the  $i$ th layer and  $z_i$  being distance from mid-thickness of the  $i$ th layer to the corneal mid-thickness. Before the surgery, the cornea is modelled by epithelial and stromal layers and these change into a wound healing layer with thickness 0.1 mm and a thinned stromal layer. Using the relevant thickness values in each patient-specific model, the flexural stiffness before and after the simulation of LASIK procedure is calculated and detailed in Table 7-7 and Figure 7-8. For comparison, the membrane (in-plane) stiffness, expressed as sum of  $E_i t_i$ , is also included and detailed in Table 7-8 and Figure 7-9.

Table 7-7. Estimated bending stiffness (MPa) before and after LASIK surgery and the changes presented by mean  $\pm$  1 standard derivation

		Stiffness	Change of stiffness	Change in percentage (%)
Before surgery		$6.18e^{-3} \pm 9.18e^{-4}$		
	0.5	$1.44e^{-3} \pm 5.03e^{-4}$	$-4.74e^{-3} \pm 6.28e^{-4}$	$-77.1 \pm 5.7$
	1	$1.95e^{-3} \pm 6.42e^{-4}$	$-4.23e^{-3} \pm 5.97e^{-4}$	$-69 \pm 7.1$
After surgery/ Stiffness ratio	2.5	$2.91e^{-3} \pm 9.40e^{-4}$	$-3.28e^{-3} \pm 6.38e^{-4}$	$-53.7 \pm 10.4$
	4.5	$3.60e^{-3} \pm 1.18e^{-3}$	$-2.59e^{-3} \pm 7.59e^{-4}$	$-42.7 \pm 13.1$
	7.5	$4.19e^{-3} \pm 1.37e^{-3}$	$-2.00e^{-3} \pm 8.98e^{-4}$	$-33.3 \pm 15.3$
	10.5	$4.57e^{-3} \pm 1.49e^{-3}$	$-1.62e^{-3} \pm 9.89e^{-4}$	$-27.3 \pm 16.5$



Table 7-8. Estimated membrane stiffness (MPa) before and after LASIK surgery and the changes presented by mean  $\pm$  1 standard derivation

		Stiffness	Change of stiffness	Change in percentage (%)
Before surgery		$2.63e^{-1} \pm 1.33e^{-2}$		
	0.5	$1.53e^{-1} \pm 1.93e^{-2}$	$-1.10e^{-1} \pm 1.20e^{-2}$	$-42 \pm 5.3$
	1	$1.78e^{-1} \pm 1.93e^{-2}$	$-8.53e^{-2} \pm 1.20e^{-2}$	$-32.5 \pm 5$
After surgery/ Stiffness ratio	2.5	$2.53e^{-1} \pm 1.93e^{-2}$	$-1.03e^{-2} \pm 1.20e^{-2}$	$-4 \pm 4.5$
	4.5	$3.53e^{-1} \pm 1.93e^{-2}$	$8.97e^{-2} \pm 1.20e^{-2}$	$34.1 \pm 4.5$
	7.5	$5.03e^{-1} \pm 1.93e^{-2}$	$2.40e^{-1} \pm 1.20e^{-2}$	$91.2 \pm 5.9$
	10.5	$6.53e^{-1} \pm 1.93e^{-2}$	$3.90e^{-1} \pm 1.20e^{-2}$	$148.2 \pm 8.1$

It is shown in Table 7-7 that the mean bending stiffness values all decreased after surgery. Visually in Figure 7-8, it is seen that the majority of bending stiffness values calculated after surgery have reduced relative to the values before surgery. There is a clear trend that the bending stiffness become larger when stiffer material is used for the wound healing layer and the overall corneal softening in terms of bending stiffness is believed to be dominated by the corneal thinning caused by cutting of flap and tissue removal. On the other hand, the wound healing layer is seen to contribute more in change of membrane stiffness before and after surgery. As detailed in Table 7-8 and illustrated in Figure 7-9, when the wound healing layer is relatively soft, the membrane stiffness declines postoperatively. It then becomes larger than that of the preoperative calculation and this begins to take place when the stiffness ratio of the wound healing layer is 2.5 in some cases as shown in Figure 7-9.

These results make it evident that the stiffening of wound healing layer is not large enough to compensate for the softening effect of corneal thinning. Therefore, a combined effect could be a decline in IOP measurement after surgery.

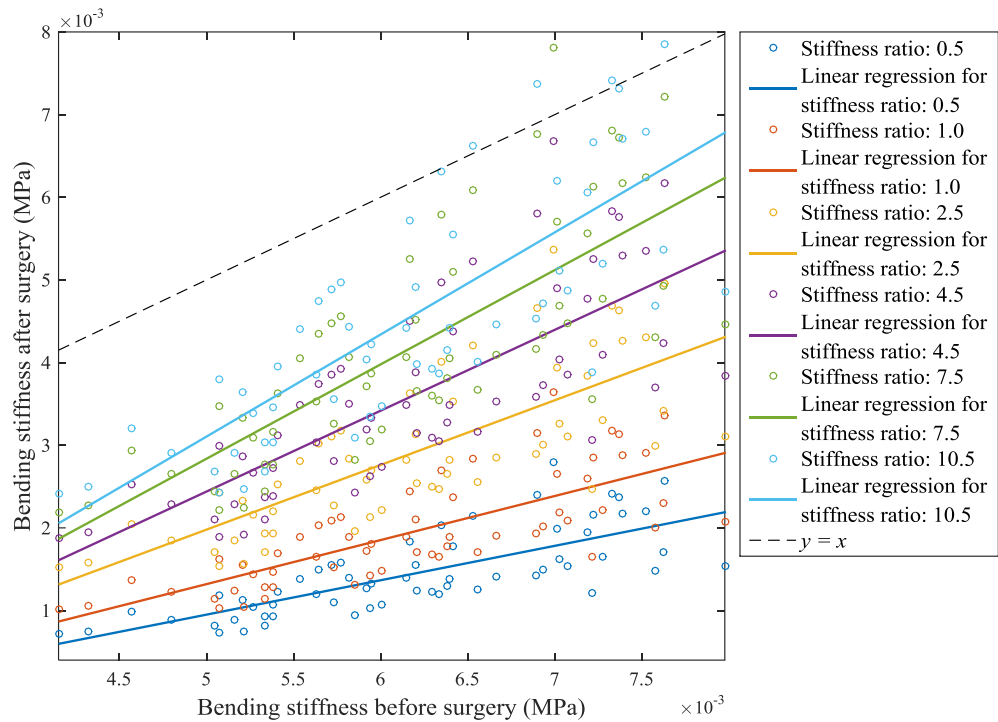


Figure 7-8. Estimated bending stiffness (MPa) before and after LASIK surgery and their approximated linear relationships

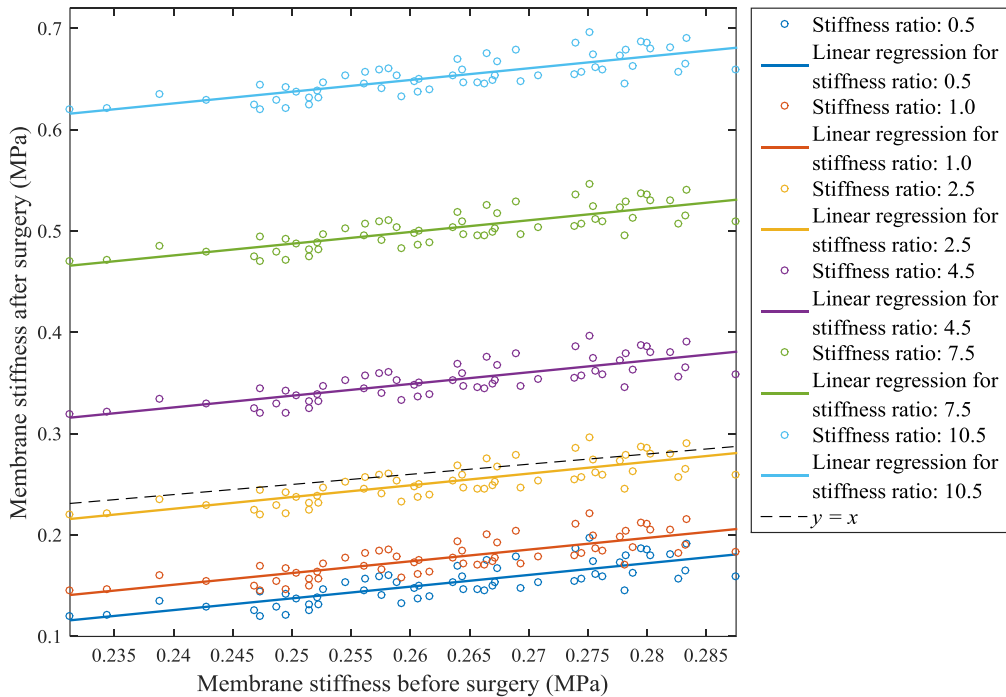


Figure 7-9. Estimated membrane stiffness (MPa) before and after LASIK surgery and their approximated linear relationships

The studies on topography analysis (especially topography fitting) has provided a foundation for numerical simulation when dealing with discrete data sets. The studies

include adjustment of the idealised model to build eye-specific clinical models. The corneal topography and thickness maps are fitted by Zernike polynomials up to order 10, where order 4 is used for ablation data and 2 for corneal flap measurements. Table 7-9 shows the fitting errors of these data. The corneal topography and thickness maps are fitted accurately with errors being around 0.3  $\mu\text{m}$ . Limited by the number of measurement points for the ablation profile and corneal flap, lower order Zernike polynomials were used to fit these data, resulting in significantly larger fitting errors compared to the more complete topography and thickness maps.

Table 7-9. Surface fitting errors by Zernike polynomials for corneal topography, thickness maps, ablation depth data and flap thickness. The errors are represented by mean  $\pm$  1 standard derivation and in  $\mu\text{m}$ .

Corneal topography	Corneal thickness	Ablation depth	Flap thickness
0.34 $\pm$ 0.03	0.33 $\pm$ 0.03	2.75 $\pm$ 1.31	5.96 $\pm$ 1.75

The linear correlations between these fitting errors and the RMSE of the predicted and measured anterior corneal topography are sought in Figure 7-10 and the results are based on numerical models with wound healing stiffness set to 4.5 times the stiffness of the stroma. It is seen that there exists notable correlation between the ablation fitting error and the RMSE of simulation while no obvious correlation is found for surface fitting for corneal topography, corneal thickness map and the flap thickness. The larger fitting error of the ablation depth is largely due to the limited number of available data points such that fitting these points with high order polynomials may be problematic as reported in the prediction study in the topography fitting chapter. As a consequence, the ablation profile used in the actual simulation serves only as rough approximation of the clinical profile, which may have restricted the numerical simulation in predicting the surgical outcomes. Further, it is expected that the numerical simulation can produce better prediction of the clinical outcome if the ablation profile information is provided more

completely such that the actual tissue removal as would be applied clinically can be mimicked more closely.

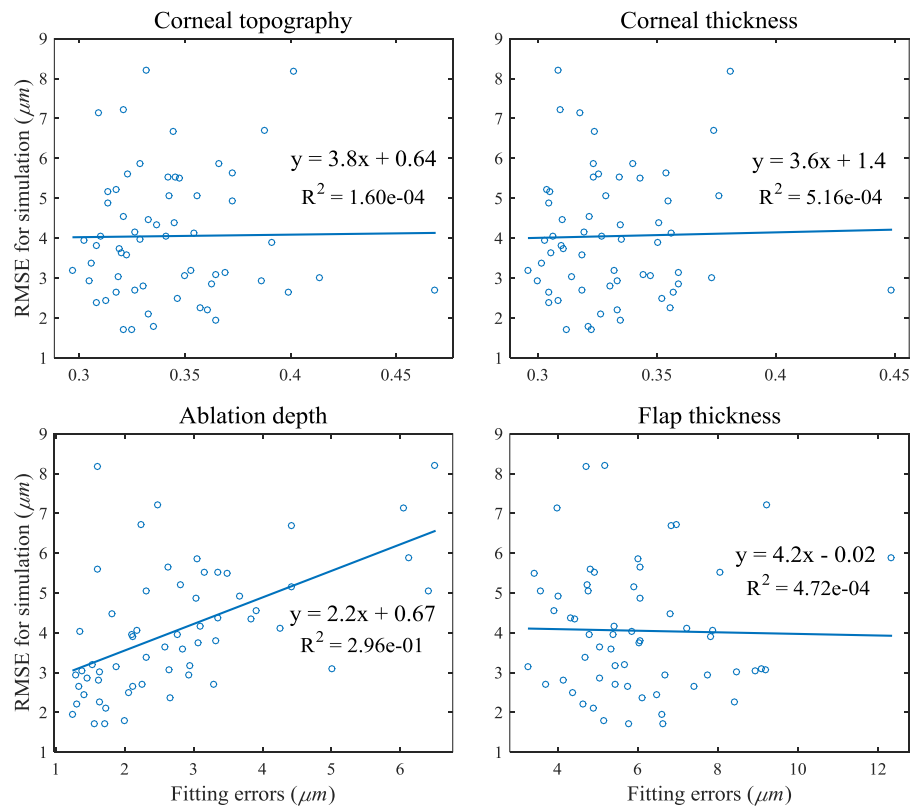


Figure 7-10. Linear correlations between various fitting errors and the RMSE of numerically predicted and clinically measured anterior corneal topography within the central 3 mm radius

However, regardless of the limitations of clinical data, the numerical simulation has been demonstrated to be superior to simple mathematical simulation which does not take the corneal biomechanical performance into account. Both the shape of the postoperative anterior corneal surface and the estimated corneal refractive power were predicted more accurately by numerical simulation and this had provided confidence of using numerical methods to simulate other surgical procedures. Following this route, the SMILE procedure was studied and the results showed that the SMILE procedure had less impact on the corneal integrity. Less stress was caused by the internal pressure (IOP) following SMILE and the corneal apex underwent less displacement compared to LASIK models. The difference in impact of LASIK and SMILE procedures was localised at the central

portion of the cornea as similar stresses and nodal displacements were found at the limbus. This finding suggested that SMILE indeed could reduce the risks of ectasia, which was a complication that mainly seen after LASIK procedure. The cornea was expected to deform more in LASIK and lead to more curved shape, which would result in higher refractive power. Interestingly however, the refractive power of the cornea after LASIK procedure was showed to be slightly lower than that after SMILE. This unexpected phenomenon can be explained by examining the shapes of the anterior corneal surfaces after both LASIK and SMILE surgery as shown in Figure 7-11 for one eye.

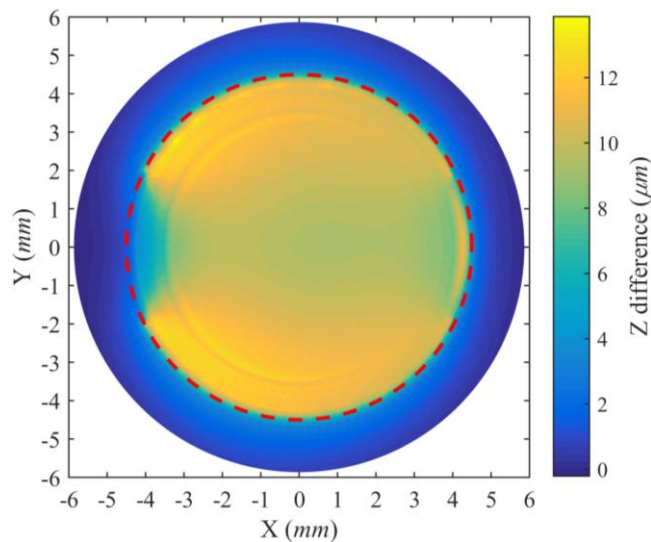


Figure 7-11. Vertical difference in anterior surfaces of LASIK and SMILE models for one eye. Positive value means the surface of LASIK model is above that of SMILE model. The red dashed circle marks the region of flap/cap.

In Figure 7-11, the vertical difference in anterior corneal surfaces of LASIK and SMILE models for a typical eye is visualised by subtracting the z coordinates of anterior nodes of the inflated SMILE model from that of the corresponding LASIK model, Zernike fitting of anterior surface of the LASIK model is employed to do such subtraction. The positive values thus mean the anterior surface of the LASIK model is located above that of the SMILE model. As expected, the two surfaces are very close at the limbus indicating similar deformation at the limbus in both models, which is consistent with the results

reported in Figure 6-14 to Figure 6-16. Interesting phenomenon is seen inside the region of flap/cap as marked by a red dashed circle in Figure 7-11. Although all nodes inside the flap region in the LASIK model underwent larger displacements, the difference profile is asymmetric. In the X direction (flap hinge is located at the right side), differences in z coordinates tended to be less towards the periphery, which indicated the surface of the LASIK model was more curved in this direction. However, the opposite was observed in the Y direction, indicating flatter surface of the LASIK model. This is because in the LASIK model, the flap thickness was totally free in Y direction whereas the SMILE cap was connected to the stroma. Consequently, the flap thickness was not thinned while the corresponding thickness in the cap was considerably reduced. The more curved shape in X direction tended to result in higher refractive power in the LASIK model but this was cancelled out in the Y direction. It was this cancellation that in turn led to slight lower overall refractive power in the LASIK model.

In myopic correction, lower residual refractive power means greater refractive correction. However, greater corneal movement outwards in the LASIK model would in turn cause larger myopic shift, lessening the myopic correction to a larger extent, compared to SMILE. In other words, given that the difference in residual refractive powers of LASIK and SMILE models is trivial, the LASIK model should have produced less myopic correction.

In addition to the study of corneal biomechanical behaviour following LASIK and SMILE procedures as discussed above, this project has also investigated the Goldmann tonometry (GAT) and the newer Corvis ST (CVS). An intact model with full thickness equal to preoperative measurement for each eye was included as a reference model. It was shown that using this reference model, very close estimates of the true IOP were obtained for

GAT but notably larger readings were achieved for CVS. Even though CVS was clinically reported to estimate higher IOP readings compared to GAT [247], the larger readings obtained in this project might also be caused by imperfections in the simulation process. In the CVS simulation, the maximal pressure applied on the cornea was not directly measured but roughly assumed to be 95 mmHg. However, other studies used higher maximal pressure on the cornea for example in [233], being about 110 mmHg. If this pressure is adopted in the model herein, the appplanation will take place earlier (smaller appplanation time 1 (AT1)). Given that appplanation pressure 1 (AP1) is determined using piston pressure rather than the pressure on cornea as shown in Figure 3-31, a smaller AP1 may be obtained using a smaller AT1, which consequently leads to smaller IOP readings.

The influence of central corneal thickness (CCT) on the IOP reading was obvious. The ratio between the estimated and true IOP appeared to be larger with thicker corneas. Also observed was the reduction in IOP readings for LASIK and SMILE models, compared to the reference intact model. This is consistent with clinical studies [256, 258, 259]. The difference in readings for LASIK and SMILE however was trivial. This indicates that even though corneal integrity is better preserved in SMILE procedure, the bending stiffness of the cornea after SMILE remains similar with the post-LASIK cornea.

### **7.3 CONCLUSIONS**

This thesis aims to provide a predictive tool for refractive surgery by finite element modelling. Patient-specific numerical models are built based on clinical data, and topography analysis, including fitting and matching, is essential for creation of these numerical models.

In the topography fitting study, various sets of orthogonal polynomials and methods to compute the polynomials' coefficients are compared. According to the author's

knowledge, this is the first study to assess the predictive behaviour of various polynomials. The variants of OP method and LS method are described and applied to fit a simple second order function. The results show that the LS method is superior to the OP variants in terms of accuracy and calculation speed. Among all the polynomials considered, OFMPs are the most successful in representing corneal elevation maps, they fit/reconstruct the discrete measurements best and always achieve better accuracy. Although they are generally more sensitive to data resolution when predicting nearby locations, this can be avoided by using as many as data points in the reconstruction to prevent local oscillation of the reconstructed surface caused by high order polynomials. On the other hand, the commonly used ZPs are shown to have the worst accuracy in reconstruction but show high reliability in prediction. However, this higher reliability in prediction is only obvious when dealing with low resolution data. In summary, OFMPs has been shown to be a very promising tool for representing corneal topography. They reconstruct the discrete corneal topography best and also provide reliable prediction of unmeasured locations.

In the topography matching study, portions of corneal topography are combined by image registration. DS and ICP methods are described and applied to simulated and real clinical data. The DS and point-to-point ICP routines are based on an objective function that aims to reduce the distance between corresponding points that are established at the beginning and do not change. This introduces a 'hard' constraint resulting in persistent registration and alignment errors. The point-to-plane ICP routine releases this constraint by allowing the dynamic map to slide over the static map. It requires interpolation of the target (static) map, which is achieved using a truncated series of Zernike polynomials due to their good performance in prediction especially for maps with few measurements. It is found to produce excellent results in simulation studies and high-quality results when applied to



real clinical data. The point-to-plane ICP algorithm is available in several forms but in this study consistently best results were produced by vertical or normal shooting (VS or NS). It is found to be robust to measurement noise and insensitive to the chosen starting values of the transformation parameters.

In the numerical simulation study, finite element modelling has been employed to simulate LASIK and SMILE procedures. The study has developed a complete process using customised Visual Basic and Matlab user interfaces to build idealised and patient-specific models and navigate the numerical modelling of LASIK and SMILE procedures. The process has considered tissue separation between the flap or cap and the rest of the stroma, and effect of stromal wound healing introduced by the laser cut. Through a parametric study on stiffness of stromal wound, it is demonstrated that the wound layer would have a stiffness that is 4.5 times that of the stroma. The numerical simulation was demonstrated to be superior to mathematical simulation that consider no biomechanics of the eye, in terms of not only the better fit with the clinical outcome but also the ability to visualise the biomechanical impact of the surgical procedure on the eye, which enables the numerical comparison between different procedures as implied in this thesis between LASIK and SMILE. It is revealed that LASIK procedure is more invasive to the eye, making the postoperative cornea more vulnerable. With the LASIK flap contributing significantly less load-carrying capability against internal pressure compared with the SMILE cap, the cornea is seen to be more stressed under IOP and this was most obvious in the central part of cornea. However, the visual outcomes in terms of refractive power is shown to be similar in post-LASIK and post-SMILE corneas.

Goldmann tonometry and Corvis ST are studied in this thesis using established LASIK and SMILE models as well as intact models with preoperative corneal thickness.

Reasonable IOP readings are obtained, showing significantly decreased values after LASIK and SMILE procedures, largely due to the reduction of corneal thickness. The estimates of IOP are seen to be similar after LASIK and SMILE procedures.

The studies presented in this thesis have potentials to assist clinical planning of future refractive surgery. For the 60 clinical cases studied in this thesis, notable myopic shift in comparison to the planned refractive correction was observed and this was accurately predicted by the numerical models. In practice, a numerical model can be generated for each patient using preoperative topography and the postoperative outcome can be predicted by the numerical method presented in this thesis using the existing ablation profile. By comparing the predicted and planned refractive corrections, an updated ablation profile can be found which should lead to an actual correction that is close to the planned one.

#### **7.4 FUTURE RESEARCH AND RECOMMENDATIONS**

In this thesis, efforts have been made to understand the corneal topography and to study the LASIK and SMILE procedures numerically based on clinical data. There are still spaces and gaps in the research and some of them are outlined in this section.

##### **7.4.1 Topography fitting against noise in the map**

The topography fitting study has demonstrated that the corneal topography can be fitted with very high accuracy in terms of both reconstruction and prediction, being about  $0.3 \mu\text{m}$ . The measurements of posterior surfaces are usually thought to be noisier because of the electronic noise of the videokeratographer. This motivates a useful extension to consider the effect of noise level on the outcome of polynomials fitting, which can be done for instance, using artificial topography with added Gaussian noise.

#### 7.4.2 Multi-view ICP (MICP)

The multi-view extension of ICP, MICP, was shown to be useful to eliminate the inconsistency between the peripheral maps registered by ICP. The current method to solve the minimisation in the MICP algorithm is based on Levenberg-Marquardt (LM) algorithm which is computationally expensive in spite of good performance. The closed-form solution derived in this thesis was shown to have convergence problem possibly due to the linearisation of angular components and omission of subsequent high order (second order) terms. A quasi-closed form may be possible to only linearise the angular components but solve the resulting error metric numerically. This is practical because the linearisation has been demonstrated to be acceptable in the ICP algorithm and the problem in the MICP algorithm may be solely caused by the omission of high order terms. This quasi-closed form is expected to be faster than the LM algorithm.

In addition, the acceleration method for the MICP algorithm should be explored further. Current results showed that the acceleration method always updated the solution incorrectly, creating fluctuation in the searching path. It should be noted that only one updating criterion has been considered, the fluctuation is usually caused by inappropriate criterion and the situation when using other criterion remains unknown.

Further study on MICP is meaningful and should be tested on other matching problems such as combine scleral surfaces. The insignificant benefit of MICP in this thesis may be because the topography maps used were measured relative accurately and they were simple shapes, such that the inconsistency left by ICP was trivial. The performance of MICP on matching more complex or noisy surfaces should be more pronounced.

### **7.4.3 Ablation profile**

In the numerical simulation of LASIK surgery, the ablation profile provided for modelling use was roughly given as samples of the actual profile with about 90 data points. This may have largely restricted the accuracy in prediction of the patient-specific models. Moreover, this profile is usually not possible to obtain due to commercial confidentiality. A possible way to overcome this problem is to fit the limited number data points to several known formulas for designing ablation profile. These formulas include the classic Munnerlyn formula and its improved variants, wavefront-optimised algorithm and so forth [192, 291-293].

### **7.4.4 Local mesh refinement**

As mentioned in Chapter 6, stress concentration may occur in some regions of the model. This is particularly obvious in transition regions where stiff and soft tissues are connected, e.g. regions connecting the limbus and the cornea. The stress concentration phenomenon is also observed at the two sides of LASIK flap hinge and SMILE incision. To eliminate the stress concentration in these regions, local mesh refinement may be practical. Although this is not believed to change the deformation behaviour of the eye globe, it may solve some convergence problems when running the models.

### **7.4.5 Anisotropy of ocular tissue**

The fibrous cornea and sclera have been observed to be anisotropic [68, 294], which was not accounted for in numerical modelling presented in this thesis. This may limit the accuracy of the current model in presenting the actual corneal and scleral behaviour against internal and external pressures. The embedding of anisotropic material model into the current model may benefit from the research on comprehensive material model of

cornea within the Ocular and Biomaterial Biomechanics Group (OBBG) which considers the spatial variation in orientation of collagen fibrils in the stroma [278].

#### **7.4.6 Simulation of stromal wound**

An optimal stiffness ratio between the stromal wound and the stroma was considered to be 4.5. In fact the surface fit between the predicted and measured postoperative anterior corneal topography was seen to be continuously improved with stiffer wound healing layer and the ratios considered in this study was as high as 10.5. The stiffness ratio is a ratio applied to the Ogden parameter  $\mu$ , which means only  $\mu$  is changed. It might be useful to consider the change in another parameter  $\alpha$  at the same time and this could be done employing inverse modelling techniques.

Besides, a significant limitation of the numerical models in this thesis is that the wound healing layer has been assumed a planner thickness of 100  $\mu\text{m}$  and uniform stiffness across the wound zone. Many clinical studies have demonstrated that the wound healing is remarkably more active in the LASIK flap margin [50, 59, 283, 295, 296], suggesting significant stiffness variation across the wound healing zone from the periphery to the centre.

The effect of edge-localised wound healing layer on the corneal deformation behaviour is investigated using one typical set of clinical data. In addition to results for the complete wound healing layer as reported in Chapter 6, two models with different edge-localised wound healing layers are studied. In each model, certain area of central region in the old wound healing layer is set the same material properties as the stroma, as a result, the new wound healing layer exhibits an annular shape. The areas of the resulting wound healing zones are 72% and 36% of the complete zone. The initial results in terms of refractive powers are listed in Table 7-10 and the displacement differences of the anterior cornea

between the two new models and the one with complete wound healing layer is illustrated in Figure 7-12.

Table 7-10. Effect of edge-localised wound healing layer on the refractive power predicted by numerical model

Clinical	Numerical: Wound healing layer coverage		
	<i>Complete (100%)</i>	Edge-localised 1 (72%)	Edge-localised 2 (36%)
37.41	37.66	39.34	38.03

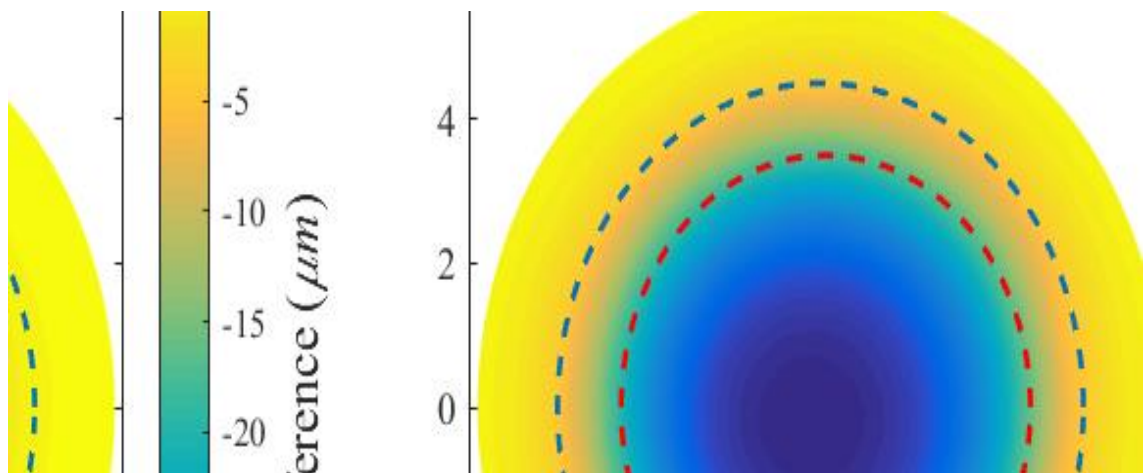


Figure 7-12. Displacement difference of anterior corneal surfaces between the models with edge-localised wound healing layers and the one with complete wound healing layer. Negative values mean that the anterior corneal surface of the model with complete wound healing layer is beneath that of the model with edge-localised wound healing layer. The blue dashed circle marks the complete wound healing zone while the red marks the inner radius of the annular wound healing zone in the two new models.

It can be seen from Table 7-10 that, by setting certain area of the central wound healing zone to softer stiffness as the stroma, the central cornea is seen to undergo greater deformation, resulting in a larger refractive power. Moreover, the cornea is more curved when using an edge-localised wound zone with a larger area. This is expected because the corneal steepening is localised more centrally in model with edge-localised wound healing layer that leaves smaller central area of softer stiffness. From Figure 7-12, it is obvious that the displacement differences of the central cornea (2 mm diameter) between

the new models with the old model are similar, however the difference is localised more centrally for the first new model, creating a steeper resulting corneal shape.

This initial study shows that the edge-localised wound healing pattern does have some effects on the modelling results but it needs more investigation. With more experimental studies on corneal wound layer in the future, the creation of a more representative wound healing layer with regionally varying material properties may be possible.

#### **7.4.7 Layered structure of the cornea**

The cornea is currently modelled as a bulk of tissue and even it is divided to several layers, the layers are connected with each other. However, the cornea is known to be weak in bearing shear force because of its layered structure. For an inflation practice, the effect of shear stiffness may be negligible, but for simulation of tonometry, this effect may be significant. Further study on tonometry should consider the layered structure of the cornea for better outcome. This can be done by modelling friction interaction between corneal layers or defining inter-lamellar adhesive strength via adhesion elements as done in [219].

#### **7.4.8 Material properties of the sclera**

Studies have shown that the stiffness of the sclera increases with age [276] but may decrease in myopic (especially highly myopic) eyes and this tends to be more obvious in the posterior sclera [297-299]. However, the material properties of the sclera are obtained by inverse modelling using donor sclera aged 50 or above while average age of the patients is about 28 years old in this study, indicating a limitation of the numerical studies in this thesis.

Although the sclera is only considered as a boundary support to the cornea, its material stiffness may change the deformation behaviour of the cornea. An investigation in effects

of varying scleral material properties on corneal deformation has been carried out using the same patient data as in the study of edge-localised wound healing layer above. The scleral stiffness is set proportional to that in the models reported in Chapter 6, and similarly refractive powers and displacement of the anterior corneal surface is compared to the old model. The resulting refractive powers are given in Table 7-11 and the displacement difference is visualised in Figure 7-13. It is obvious that softer sclera tends to create weaker boundary condition in the limbus such that the peripheral corneal is allowed to deform with greater freedom, leading to a flatter corneal shape.

Table 7-11. Effect of varying sclera material properties on the refractive power predicted by numerical model

Clinical	Numerical: Scleral stiffness ratio				
	0.50	0.75	1.00	1.50	2.00
37.41	37.32	37.51	37.66	37.90	38.09



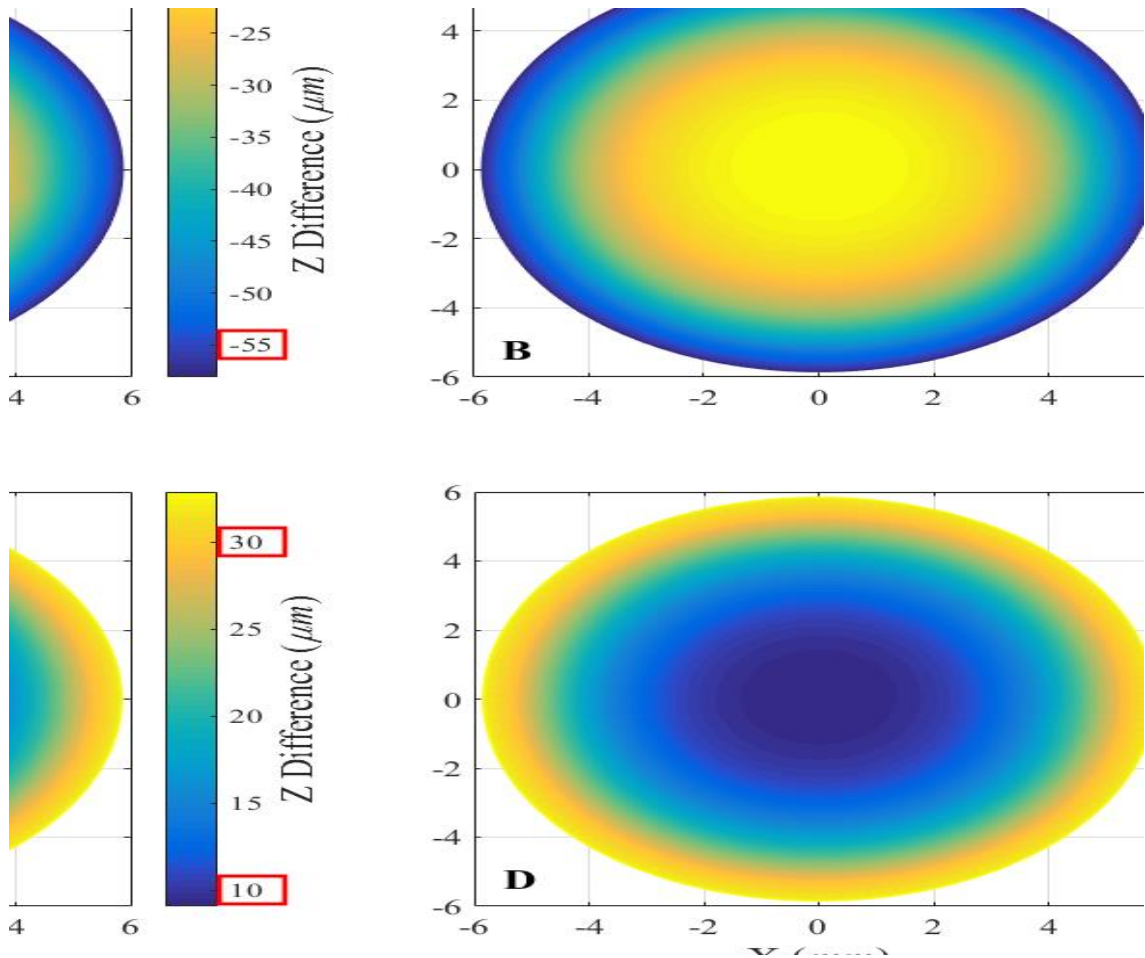


Figure 7-13. Displacement difference of anterior corneal surfaces between the models with softer (**A, B**) or stiffer (**C, D**) scleral material properties and the one with reference material properties. Negative values mean that the anterior corneal surface of the model with reference stiffness is beneath that of the models with softer or stiffer scleral material properties. Positive values thus mean the contrast. Similar pattern is seen in each row but the two sub-figures have different scales as marked by red squares.

Further to the study above, the possible regional softening of the sclera in myopic eye is studied. Based on the values published in [297], the stiffness of the equatorial and posterior sclera is reduced by 8% and 15%, respectively. The stiffness of the anterior sclera is kept the same as in the old model. From Table 7-12 and Figure 7-14, it can be seen that this manipulation has little effect on the corneal behaviour.

Table 7-12. Effect of reduced stiffness in equatorial and posterior sclera on the refractive power predicted by numerical model. Numerical 1 is for model with reference scleral material properties as in previous chapters, while Numerical 2 is for model with reduced stiffness in equatorial and posterior sclera. The refractive powers are rounded to the fourth digit to appreciate the difference.

Clinical	Numerical 1	Numerical 2
37.4121	37.6572	37.6568

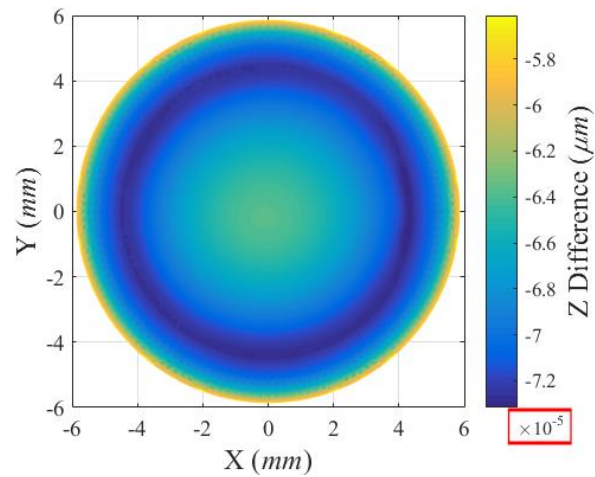


Figure 7-14. Displacement difference of anterior corneal surfaces between the model with reduced equatorial and posterior scleral stiffness and the one with reference material properties. Meaning of the values in this figure is the same as in Figure 7-13.

The studies above on scleral material stiffness indicate the need of further investigation in effects of varying scleral material properties on corneal biomechanical behaviour, and particularly the emphasis should be on the age-related variation of scleral material properties. Given that in vivo characterisation of scleral material properties is somehow impossible at present, a reduction of scleral stiffness in younger eye may be practical.

## REFERENCES

---

- [1] A. J. Bron, R. C. Tripathi, B. J. Tripathi, and E. Wolff, *Wolff's anatomy of the eye and orbit*, London; New York: Chapman & Hall Medical, 1997.
- [2] R. Wojciechowski, "Nature and nurture: the complex genetics of myopia and refractive error," *Clinical Genetics*, vol. 79, no. 4, pp. 301-320, Apr, 2011.
- [3] I. G. Morgan, K. Ohno-Matsui, and S. M. Saw, "Myopia," *The Lancet*, vol. 379, no. 9827, pp. 1739-1748, May, 2012.
- [4] M. Lombardo, and G. Lombardo, "Wave aberration of human eyes and new descriptors of image optical quality and visual performance," *Journal of Cataract and Refractive Surgery*, vol. 36, no. 2, pp. 313-331, Feb, 2010.
- [5] N. Ferrero, "Leonardo Da Vinci: Of the eye. An original new translation from Codex D," *American Journal of Ophthalmology*, vol. 35, no. 4, pp. 507-521, 1952.
- [6] K. S. Na, S. H. Chung, J. K. Kim, E. J. Jang, N. R. Lee, and C. K. Joo, "Comparison of LASIK and Surface Ablation by Using Propensity Score Analysis: A Multicenter Study in Korea," *Investigative Ophthalmology & Visual Science*, vol. 53, no. 11, pp. 7116-7121, Oct, 2012.
- [7] K. D. Solomon, L. E. F. de Castro, H. P. Sandoval, J. M. Biber, B. Groat, K. D. Neff, M. S. Ying, J. W. French, E. D. Donnenfeld, R. L. Lindstrom, and L. S. T. F. Joint, "LASIK World Literature Review: Quality of Life and Patient Satisfaction," *Ophthalmology*, vol. 116, no. 4, pp. 691-701, Apr, 2009.
- [8] S. M. MacRae, J. Schwiegerling, and R. Snyder, "Customized corneal ablation and super vision," *Journal of Refractive Surgery*, vol. 16, no. 2, pp. S230-S235, Mar-Apr, 2000.

- [9] C. Roberts, "Biomechanics of the cornea and wavefront-guided laser refractive surgery," *Journal of Refractive Surgery*, vol. 18, no. 5, pp. S589-S592, Sep-Oct, 2002.
- [10] I. Lipshitz, "Thirty-four challenges to meet before excimer laser technology can achieve super vision," *Journal of Refractive Surgery*, vol. 18, no. 6, pp. 740-743, Nov-Dec, 2002.
- [11] C. R. Ethier, M. Johnson, and J. Ruberti, "Ocular biomechanics and biotransport," *Annual Review of Biomedical Engineering*, vol. 6, pp. 249-273, 2004.
- [12] H. Gray, S. Standring, and N. R. Borley, *Gray's anatomy : the anatomical basis of clinical practice*, Edinburgh: Churchill Livingstone Elsevier, 2008.
- [13] H. Hashemi, A. H. Kashi, A. Fotouhi, and K. Mohammad, "Distribution of intraocular pressure in healthy Iranian individuals: the Tehran Eye Study," *British Journal of Ophthalmology*, vol. 89, no. 6, pp. 652-657, Jun, 2005.
- [14] Y. Shiose, Y. Kitazawa, S. Tsukahara, T. Akamatsu, K. Mizokami, R. Futa, H. Katsushima, and H. Kosaki, "Epidemiology of glaucoma in Japan - a nationwide glaucoma survey," *Japanese Journal of Ophthalmology*, vol. 35, no. 2, pp. 133-155, 1991.
- [15] A. Sommer, J. M. Tielsch, J. Katz, H. A. Quigley, J. D. Gottsch, J. Javitt, and K. Singh, "Relationship between Intraocular-Pressure and Primary Open Angle Glaucoma among White and Black-Americans - the Baltimore Eye Survey," *Archives of Ophthalmology*, vol. 109, no. 8, pp. 1090-1095, Aug, 1991.
- [16] B. E. Klein, R. Klein, and K. L. Linton, "Intraocular pressure in an American community. The Beaver Dam Eye Study," *Invest Ophthalmol Vis Sci*, vol. 33, no. 7, pp. 2224-8, Jun, 1992.

- [17] M. C. Leske, A. M. S. Connell, S. Y. Wu, L. Hyman, and A. P. Schachat, "Distribution of intraocular pressure - The Barbados Eye Study," *Archives of Ophthalmology*, vol. 115, no. 8, pp. 1051-1057, Aug, 1997.
- [18] S. Y. Wu, and M. C. Leske, "Associations with intraocular pressure in the Barbados Eye Study," *Archives of Ophthalmology*, vol. 115, no. 12, pp. 1572-1576, Dec, 1997.
- [19] L. M. Weih, B. N. Mukesh, C. A. McCarty, and H. R. Taylor, "Association of demographic, familial, medical, and ocular factors with intraocular pressure," *Archives of Ophthalmology*, vol. 119, no. 6, pp. 875-880, Jun, 2001.
- [20] J. S. Lee, S. H. Lee, B. S. Oum, J. S. Chung, B. M. Cho, and J. W. Hong, "Relationship between intraocular pressure and systemic health parameters in a Korean population," *Clinical and Experimental Ophthalmology*, vol. 30, no. 4, pp. 237-241, Aug, 2002.
- [21] J. H. K. Liu, A. J. Sit, and R. N. Weinreb, "Variation of 24-hour intraocular pressure in healthy individuals - Right eye versus left eye," *Ophthalmology*, vol. 112, no. 10, pp. 1670-1675, Oct, 2005.
- [22] A. J. Sit, "Continuous Monitoring of Intraocular Pressure Rationale and Progress Toward A Clinical Device," *Journal of Glaucoma*, vol. 18, no. 4, pp. 272-279, Apr-May, 2009.
- [23] E. M. Hoffmann, F.-H. Grus, and N. Pfeiffer, "Intraocular pressure and ocular pulse amplitude using dynamic contour tonometry and contact lens tonometry," *BMC ophthalmology*, vol. 4, pp. 4, 2004, 2004.
- [24] A. I. Dastiridou, H. S. Ginis, D. De Brouwere, M. K. Tsilimbaris, and I. G. Pallikaris, "Ocular Rigidity, Ocular Pulse Amplitude, and Pulsatile Ocular Blood

- Flow: The Effect of Intraocular Pressure,” *Investigative Ophthalmology & Visual Science*, vol. 50, no. 12, pp. 5718-5722, Dec, 2009.
- [25] K. Anderson, A. El-Sheikh, and T. Newson, “Application of structural analysis to the mechanical behaviour of the cornea,” *Journal of the Royal Society Interface*, vol. 1, no. 1, pp. 3-15, Nov, 2004.
- [26] P. M. Kiely, G. Smith, and L. G. Carney, “The mean shape of the human cornea,” *Optica Acta*, vol. 29, no. 8, pp. 1027-1040, 1982.
- [27] T. Saude, *Ocular anatomy and physiology*, Oxford; Boston: Blackwell Scientific Publications, 1993.
- [28] S. A. Klein, and R. B. Mandell, “Shape and refractive powers in corneal topography,” *Investigative Ophthalmology & Visual Science*, vol. 36, no. 10, pp. 2096-2109, Sep, 1995.
- [29] A. Guirao, and P. Artal, “Corneal wave aberration from videokeratography: accuracy and limitations of the procedure,” *Journal of the Optical Society of America a-Optics Image Science and Vision*, vol. 17, no. 6, pp. 955-965, Jun, 2000.
- [30] J. Schwiegerling, and J. E. Greivenkamp, “Using corneal height maps and polynomial decomposition to determine corneal aberrations,” *Optometry and Vision Science*, vol. 74, no. 11, pp. 906-916, Nov, 1997.
- [31] J. Schwiegerling, and J. E. Greivenkamp, “Keratoconus detection based on videokeratoscopic height data,” *Optometry and Vision Science*, vol. 73, no. 12, pp. 721-728, Dec, 1996.
- [32] D. R. Iskander, M. J. Collins, and B. Davis, “Optimal modeling of corneal surfaces with Zernike polynomials,” *Ieee Transactions on Biomedical Engineering*, vol. 48, no. 1, pp. 87-95, Jan, 2001.

- [33] A. J. Kanellopoulos, "Topography-guided custom retreatments in 27 symptomatic eyes," *Journal of Refractive Surgery*, vol. 21, no. 5, pp. S513-S518, Sep-Oct, 2005.
- [34] W. Tang, M. J. Collins, L. Carney, and B. Davis, "The accuracy and precision performance of four videokeratoscopes in measuring test surfaces," *Optometry and Vision Science*, vol. 77, no. 9, pp. 483-491, Sep, 2000.
- [35] T. Swartz, L. Marten, and M. Wang, "Measuring the cornea: the latest developments in corneal topography," *Current Opinion in Ophthalmology*, vol. 18, no. 4, pp. 325-333, Jul, 2007.
- [36] J. J. Rozema, K. Wouters, D. G. P. Mathysen, and M. J. Tassignon, "Overview of the Repeatability, Reproducibility, and Agreement of the Biometry Values Provided by Various Ophthalmic Devices," *American Journal of Ophthalmology*, vol. 158, no. 6, pp. 1111-1120, Dec, 2014.
- [37] H. S. Dua, L. A. Faraj, D. G. Said, T. Gray, and J. Lowe, "Human Corneal Anatomy Redefined A Novel Pre-Descemet's Layer (Dua's Layer)," *Ophthalmology*, vol. 120, no. 9, pp. 1778-1785, Sep, 2013.
- [38] H. D. McKee, L. C. D. Irion, F. M. Carley, A. K. Brahma, M. R. Jafarinasab, M. Rahmati-Kamel, M. R. Kanavi, and S. Feizi, "Re: Dua et al.: Human corneal anatomy redefined: a novel pre-Descemet layer (Dua's layer) (Ophthalmology 2013;120:1778-85)," *Ophthalmology*, vol. 121, no. 5, pp. E24-E25, May, 2014.
- [39] H. S. Dua, L. A. Faraj, D. G. Said, T. Gray, and J. Lowe, "Re: Dua et al.: Human corneal anatomy redefined: a novel pre-Descemet layer (Dua's layer) (Ophthalmology 2013;120:1778-85) Reply," *Ophthalmology*, vol. 121, no. 5, pp. E25-E26, May, 2014.
- [40] J. R. Hassell, and D. E. Birk, "The molecular basis of corneal transparency," *Experimental Eye Research*, vol. 91, no. 3, pp. 326-335, Sep, 2010.

- [41] K. M. Meek, and C. Boote, "The organization of collagen in the corneal stroma," *Experimental Eye Research*, vol. 78, no. 3, pp. 503-512, Mar, 2004.
- [42] L. J. Muller, E. Pels, L. Schurmans, and G. Vrensen, "A new three-dimensional model of the organization of proteoglycans and collagen fibrils in the human corneal stroma," *Experimental Eye Research*, vol. 78, no. 3, pp. 493-501, Mar, 2004.
- [43] J. V. Jester, T. Moller-Pedersen, J. Y. Huang, C. M. Sax, W. T. Kays, H. D. Cavanagh, W. M. Petroll, and J. Piatigorsky, "The cellular basis of corneal transparency: evidence for 'corneal crystallins'," *Journal of Cell Science*, vol. 112, no. 5, pp. 613-622, Mar, 1999.
- [44] D. H. Geroski, M. Matsuda, R. W. Yee, H. F. Edelhauser, and J. Sugar, "Pump function of the human corneal endothelium. Effects of age and cornea guttata," *Ophthalmology*, vol. 92, no. 6, pp. 759-763, 1985.
- [45] U. Schlötzer-Schrehardt, and F. E. Kruse, "Anatomy and Physiology: Considerations in Relation to Transplantation," *Corneal Transplantation*, J. Hjortdal, ed., Switzerland: Springer International Publishing, 2016.
- [46] A. J. Bron, "The architecture of the corneal stroma," *British Journal of Ophthalmology*, vol. 85, no. 4, pp. 379-381, Apr, 2001.
- [47] L. J. Muller, E. Pels, and G. Vrensen, "The specific architecture of the anterior stroma accounts for maintenance of corneal curvature," *British Journal of Ophthalmology*, vol. 85, no. 4, pp. 437-443, Apr, 2001.
- [48] A. J. Quantock, M. Winkler, G. J. Parfitt, R. D. Young, D. J. Brown, C. Boote, and J. V. Jester, "From nano to macro: Studying the hierarchical structure of the corneal extracellular matrix," *Experimental Eye Research*, vol. 133, pp. 81-99, Apr, 2015.



- [49] S. E. Wilson, "Analysis of the keratocyte apoptosis, keratocyte proliferation, and myofibroblast transformation responses after photorefractive keratectomy and laser in situ keratomileusis," *Transactions of the American Ophthalmological Society*, vol. 100, pp. 411-33, 2002, 2002.
- [50] M. V. Netto, R. R. Mohan, R. Ambrosio, A. E. K. Hutcheon, J. D. Zieske, and S. E. Wilson, "Wound healing in the cornea - A review of refractive surgery complications and new prospects for therapy," *Cornea*, vol. 24, no. 5, pp. 509-522, Jul, 2005.
- [51] D. W. DelMonte, and T. Kim, "Anatomy and physiology of the cornea," *Journal of Cataract and Refractive Surgery*, vol. 37, no. 3, pp. 588-598, Mar, 2011.
- [52] L. Lu, P. S. Reinach, and W. W. Y. Kao, "Corneal epithelial wound healing," *Experimental Biology and Medicine*, vol. 226, no. 7, pp. 653-664, Jul, 2001.
- [53] L. Spadea, D. Giammaria, and P. Trabucco, "Corneal wound healing after laser vision correction," *British Journal of Ophthalmology*, vol. 100, no. 1, pp. 28-33, Jan, 2016.
- [54] J. Imanishi, K. Kamiyama, I. Iguchi, M. Kita, C. Sotozono, and S. Kinoshita, "Growth factors: Importance in wound healing and maintenance of transparency of the cornea," *Progress in Retinal and Eye Research*, vol. 19, no. 1, pp. 113-129, Jan, 2000.
- [55] J. V. Jester, and H. C. Jin, "Modulation of cultured corneal keratocyte phenotype by growth factors/cytokines control in vitro contractility and extracellular matrix contraction," *Experimental Eye Research*, vol. 77, no. 5, pp. 581-592, Nov, 2003.
- [56] J. V. Jester, D. Brown, A. Pappa, and V. Vasiliou, "Myofibroblast Differentiation Modulates Keratocyte Crystallin Protein Expression, Concentration, and Cellular

- Light Scattering,” *Investigative Ophthalmology & Visual Science*, vol. 53, no. 2, pp. 770-778, Feb, 2012.
- [57] F. L. Barbosa, S. S. Chaurasia, H. Kaur, F. W. de Medeiros, V. Agrawal, and S. E. Wilson, “Stromal interleukin-1 expression in the cornea after haze-associated injury,” *Experimental Eye Research*, vol. 91, no. 3, pp. 456-461, Sep, 2010.
- [58] C. Cintron, L. C. Hassinger, C. L. Kublin, and D. J. Cannon, “Biochemical and ultrastructural changes in collagen during corneal wound healing,” *Journal of Ultrastructure Research*, vol. 65, no. 1, pp. 13-22, 1978.
- [59] W. J. Dupps, and S. E. Wilson, “Biomechanics and wound healing in the cornea,” *Experimental Eye Research*, vol. 83, no. 4, pp. 709-720, Oct, 2006.
- [60] J. V. Jester, W. M. Petroll, and H. D. Cavanagh, “Corneal stromal wound healing in refractive surgery: the role of myofibroblasts,” *Progress in Retinal and Eye Research*, vol. 18, no. 3, pp. 311-356, May, 1999.
- [61] D. T. Azar, J.-H. Chang, and K. Y. Han, “Wound healing after keratorefractive surgery: review of biological and optical considerations,” *Cornea*, vol. 31 Suppl 1, pp. S9-19, 2012, 2012.
- [62] A. Elsheikh, “Finite Element Modeling of Corneal Biomechanical Behavior,” *Journal of Refractive Surgery*, vol. 26, no. 4, pp. 289-300, Apr, 2010.
- [63] M. R. Bryant, and P. J. McDonnell, “Constitutive laws for biomechanical modeling of refractive surgery,” *Journal of Biomechanical Engineering-Transactions of the Asme*, vol. 118, no. 4, pp. 473-481, Nov, 1996.
- [64] A. Elsheikh, B. Geraghty, P. Rama, M. Campanelli, and K. M. Meek, “Characterization of age- related variation in corneal biomechanical properties,” *Journal of the Royal Society Interface*, vol. 7, no. 51, pp. 1475-1485, Oct, 2010.

- [65] A. Daxer, K. Misof, B. Grabner, A. Ettl, and P. Fratzl, "Collagen fibrils in the human corneal stroma: Structure and aging," *Investigative Ophthalmology & Visual Science*, vol. 39, no. 3, pp. 644-648, Mar, 1998.
- [66] A. Elsheikh, D. F. Wang, M. Brown, P. Rama, M. Campanelli, and D. Pye, "Assessment of corneal biomechanical properties and their variation with age," *Current Eye Research*, vol. 32, no. 1, pp. 11-19, Jan, 2007.
- [67] J. W. Ruberti, A. S. Roy, and C. J. Roberts, "Corneal Biomechanics and Biomaterials," *Annual Review of Biomedical Engineering, Vol 13*, Annual Review of Biomedical Engineering M. L. Yarmush, J. S. Duncan and M. L. Gray, eds., pp. 269-295, Palo Alto: Annual Reviews, 2011.
- [68] A. Elsheikh, M. Brown, D. Alhasso, P. Rama, M. Campanelli, and D. Garway-Heath, "Experimental assessment of corneal anisotropy," *Journal of Refractive Surgery*, vol. 24, no. 2, pp. 178-187, Feb, 2008.
- [69] D. A. Atchison, and G. Smith, *Optics of the human eye*, Oxford; Boston: Butterworth-Heinemann, 2000.
- [70] L. F. Garner, C. S. Ooi, and G. Smith, "Refractive index of the crystalline lens in young and aged eyes," *Clinical and Experimental Optometry*, vol. 81, no. 4, pp. 145-150, 1998.
- [71] N. Maeda, "Wavefront technology in ophthalmology," *Current opinion in ophthalmology*, vol. 12, no. 4, pp. 294-9, 2001, 2001.
- [72] B. Howland, and H. C. Howland, "Subjective measurement of high order aberrations of the eye," *Science*, vol. 193, no. 4253, pp. 580-582, 1976.
- [73] J. Schwiegerling, "Theoretical limits to visual performance," *Survey of Ophthalmology*, vol. 45, no. 2, pp. 139-146, Sep-Oct, 2000.

- [74] A. S. Marathay, and J. F. McCalmont, "Physical Optics: Diffraction," *Handbook of optics: Volume 1, Geometrical and physical optics, polarized light, components and instruments*, M. Bass and V. N. Mahajan, eds., New York: McGraw-Hill Professional, 2009.
- [75] P. Artal, A. Guirao, E. Berrio, and D. R. Williams, "Compensation of corneal aberrations by the internal optics in the human eye," *Journal of Vision*, vol. 1, no. 1, pp. 8, 2001.
- [76] J. Taberero, A. Benito, E. Alcon, and P. Artal, "Mechanism of compensation of aberrations in the human eye," *Journal of the Optical Society of America a-Optics Image Science and Vision*, vol. 24, no. 10, pp. 3274-3283, Oct, 2007.
- [77] G. R. Mello, K. M. Rocha, M. R. Santhiago, D. Smadja, and R. R. Krueger, "Applications of wavefront technology," *Journal of Cataract and Refractive Surgery*, vol. 38, no. 9, pp. 1671-1683, Sep, 2012.
- [78] N. Maeda, "Clinical applications of wavefront aberrometry - a review," *Clinical and Experimental Ophthalmology*, vol. 37, no. 1, pp. 118-129, Jan-Feb, 2009.
- [79] v. F. Zernike, "Beugungstheorie des schneidenver-fahrens und seiner verbesserten form, der phasenkontrastmethode," *Physica*, vol. 1, no. 7-12, pp. 689-704, 5//, 1934.
- [80] J. Schwiegerling, J. E. Greivenkamp, and J. M. Miller, "Representation of Videokeratoscopic Height Data with Zernike Polynomials," *Journal of the Optical Society of America a-Optics Image Science and Vision*, vol. 12, no. 10, pp. 2105-2113, Oct, 1995.
- [81] W. Lotmar, "Theoretical Eye Model with Aspherics," *Journal of the Optical Society of America*, vol. 61, no. 11, pp. 1522-&, 1971.

- [82] M. A. Halstead, B. A. Barsky, S. A. Klein, and R. B. Mandell, "A Spline Surface Algorithm for Reconstruction of Corneal Topography from a Videokeratographic Reflection Pattern," *Optometry and Vision Science*, vol. 72, no. 11, pp. 821-827, Nov, 1995.
- [83] M. Ares, and S. Royo, "Comparison of cubic B-spline and Zernike-fitting techniques in complex wavefront reconstruction," *Applied Optics*, vol. 45, no. 27, pp. 6954-6964, Sep, 2006.
- [84] Z. X. Zhu, E. Janunts, T. Eppig, T. Sauer, and A. Langenbucher, "Iteratively re-weighted bi-cubic spline representation of corneal topography and its comparison to the standard methods," *Zeitschrift Fur Medizinische Physik*, vol. 20, no. 4, pp. 287-298, 2010.
- [85] J. A. Corbin, S. Klein, and C. van de Pol, "Measuring effects of refractive surgery on corneas using Taylor series polynomials," *Ophthalmic Technologies IX, Proceedings Of, Proceedings of the Society of Photo-Optical Instrumentation Engineers (Spie)* P. O. Rol, K. M. Joos, F. Manns, B. E. Stuck and M. Belkin, eds., pp. 46-52, Bellingham: Spie-Int Soc Optical Engineering, 1999.
- [86] L. N. Thibos, R. A. Applegate, J. T. Schwiegerling, R. Webb, and V. S. T. Members, "Standards for reporting the optical aberrations of eyes," *Journal of Refractive Surgery*, vol. 18, no. 5, pp. S652-S660, Sep-Oct, 2002.
- [87] M. K. Smolek, and S. D. Klyce, "Zernike polynomial fitting fails to represent all visually significant corneal aberrations," *Investigative Ophthalmology & Visual Science*, vol. 44, no. 11, pp. 4676-4681, Nov, 2003.
- [88] D. R. Iskander, M. R. Moreland, M. J. Collins, and B. Davis, "Modeling of corneal surfaces with radial polynomials," *Ieee Transactions on Biomedical Engineering*, vol. 49, no. 4, pp. 320-328, Apr, 2002.

- [89] A. Soumelidis, Z. Fazekas, F. Schipp, and Ieee, "Geometrical description of quasi-hemispherical and calotte-like surfaces using discretised argument-transformed Chebyshev-polynomials," *2005 44th Ieee Conference on Decision and Control & European Control Conference, Vols 1-8*, IEEE Conference on Decision and Control, pp. 1619-1624, New York: Ieee, 2005.
- [90] Z. Hongqing, L. Min, S. Huazhong, Z. Jin, and Z. Hui, "Representation of Videokeratographic Height Data Using a Set of Discrete Tchebichef Orthogonal Polynomials," *International Journal of Signal Processing, Image Processing & Pattern Recognition*, vol. 3, no. 3, pp. 13-28, 2010.
- [91] A. Martinez-Finkelstein, A. M. Delgado, G. M. Castro, A. Zarzo, and J. L. Alio, "Comparative Analysis of Some Modal Reconstruction Methods of the Shape of the Cornea from Corneal Elevation Data," *Investigative Ophthalmology & Visual Science*, vol. 50, no. 12, pp. 5639-5645, Dec, 2009.
- [92] J. Espinosa, D. Mas, J. Perez, and C. Illueca, "Optical surface reconstruction technique through combination of zonal and modal fitting," *Journal of Biomedical Optics*, vol. 15, no. 2, pp. 7, Mar-Apr, 2010.
- [93] K. M. Hosny, "Image representation using accurate orthogonal Gegenbauer moments," *Pattern Recognition Letters*, vol. 32, no. 6, pp. 795-804, Apr, 2011.
- [94] S. X. Liao, and M. Pawlak, "On image analysis by moments," *Ieee Transactions on Pattern Analysis and Machine Intelligence*, vol. 18, no. 3, pp. 254-266, Mar, 1996.
- [95] J. Shen, *Orthogonal Gaussian-Hermite moments for image characterization*, Bellingham: Spie - Int Soc Optical Engineering, 1997.

- [96] Y. L. Sheng, and L. X. Shen, "Orthogonal Fourier-Mellin Moments for Invariant Pattern-Recognition," *Journal of the Optical Society of America a-Optics Image Science and Vision*, vol. 11, no. 6, pp. 1748-1757, Jun, 1994.
- [97] C. H. Teh, and R. T. Chin, "On Image-Analysis by the Methods of Moments," *Ieee Transactions on Pattern Analysis and Machine Intelligence*, vol. 10, no. 4, pp. 496-513, Jul, 1988.
- [98] J. Schwiegerling, "Modal reconstruction methods with Zernike polynomials," *Journal of Refractive Surgery*, vol. 21, no. 5, pp. S552-S557, Sep-Oct, 2005.
- [99] L. Kotoulas, and I. Andreadis, "Accurate calculation of image moments," *Ieee Transactions on Image Processing*, vol. 16, no. 8, pp. 2028-2037, Aug, 2007.
- [100] R. Mukundan, S. H. Ong, and P. A. Lee, "Image analysis by Tchebichef moments," *Ieee Transactions on Image Processing*, vol. 10, no. 9, pp. 1357-1364, Sep, 2001.
- [101] R. Mukundan, "Radial Tchebichef invariants for pattern recognition," *Tencon 2005 - 2005 Ieee Region 10 Conference, Vols 1-5, TENCON-IEEE Region 10 Conference Proceedings*, pp. 2088-2093, New York: Ieee, 2006.
- [102] P. T. Yap, R. Paramesran, and S. H. Ong, "Image analysis by Krawtchouk moments," *Ieee Transactions on Image Processing*, vol. 12, no. 11, pp. 1367-1377, Nov, 2003.
- [103] P. T. Yap, R. Paramesran, and S. H. Ong, "Image analysis using Hahn moments," *Ieee Transactions on Pattern Analysis and Machine Intelligence*, vol. 29, no. 11, pp. 2057-2062, Nov, 2007.
- [104] H. Zhu, M. Liu, H. Shu, H. Zhang, and L. Luo, "General form for obtaining discrete orthogonal moments," *Iet Image Processing*, vol. 4, no. 5, pp. 335-352, Oct, 2010.

- [105] C. W. Chong, P. Raveendran, and R. Mukundan, "A comparative analysis of algorithms for fast computation of Zernike moments," *Pattern Recognition*, vol. 36, no. 3, pp. 731-742, Mar, 2003.
- [106] Y. Mejia-Barbosa, and D. Malacara-Hernandez, "A review of methods for measuring corneal topography," *Optometry and Vision Science*, vol. 78, no. 4, pp. 240-253, Apr, 2001.
- [107] M. W. Belin, and C. D. Ratliff, "Evaluating data acquisition and smoothing functions of currently available videokeratoscopes," *Journal of Cataract and Refractive Surgery*, vol. 22, no. 4, pp. 421-426, May, 1996.
- [108] B. R. Jani, and L. B. Szczotka, "Efficiency and accuracy of two computerized topography software systems for fitting rigid gas permeable contact lenses," *CLAO Journal*, vol. 26, no. 2, pp. 91-96, April, 2000.
- [109] R. J. Franklin, M. R. Morelande, D. R. Iskander, M. J. Collins, and B. A. Davis, "Combining central and peripheral videokeratoscope maps to investigate total corneal topography," *Eye & Contact Lens*, vol. 32, no. 1, pp. 27-32, 2006, 2006.
- [110] A. Elsheikh, and D. Wang, "Numerical modelling of corneal biomechanical behaviour," *Computer Methods in Biomechanics and Biomedical Engineering*, vol. 10, no. 2, pp. 85-95, Apr, 2007.
- [111] C. W. Lau, and S. A. Klein, "Viewing more corneal surface splicing of multiple videokeratographs," *Investigative Ophthalmology & Visual Science*, vol. 37, no. 3, pp. 2569-2569, Feb 15, 1996.
- [112] F. Shevlin, S. A. Klein, R. B. Mandell, and T. Carney, "Evaluation of entire-cornea topography measurement." pp. 259-265.



- [113] B. A. Barsky, S. A. Klein, and D. D. Garcia, "Gaussian power with cylinder vector field representation for corneal topography maps," *Optometry and Vision Science*, vol. 74, no. 11, pp. 917-925, Nov, 1997.
- [114] R. J. Campbell, and P. J. Flynn, "A survey of free-form object representation and recognition techniques," *Computer Vision and Image Understanding*, vol. 81, no. 2, pp. 166-210, Feb, 2001.
- [115] J. P. W. Pluim, J. B. A. Maintz, and M. A. Viergever, "Mutual-information-based registration of medical images: A survey," *Ieee Transactions on Medical Imaging*, vol. 22, no. 8, pp. 986-1004, Aug, 2003.
- [116] J. Salvi, C. Matabosch, D. Fofi, and J. Forest, "A review of recent range image registration methods with accuracy evaluation," *Image and Vision Computing*, vol. 25, no. 5, pp. 578-596, May 1, 2007.
- [117] Y. Chen, and G. Medioni, "Object modeling by registration of multiple range images," *IEEE International Conference on Robotics and Automation*. pp. 2724-2729, 1991.
- [118] P. J. Besl, and N. D. Mckay, "A method for registration of 3-D shapes," *IEEE Transactions on Pattern Analysis and Machine Intelligence*, vol. 14, no. 2, pp. 239-256, Feb, 1992.
- [119] S. Rusinkiewicz, and M. Levoy, "Efficient variants of the ICP algorithm." pp. 145-152, 2001.
- [120] R. Bergevin, M. Soucy, H. Gagnon, and D. Laurendeau, "Towards a general multi-view registration technique," *Ieee Transactions on Pattern Analysis and Machine Intelligence*, vol. 18, no. 5, pp. 540-547, May, 1996.
- [121] A. J. Stoddart, and A. Hilton, "Registration of multiple point sets." pp. 40-44.

- [122] R. Benjema, and F. Schmitt, "A solution for the registration of multiple 3D point sets using unit quaternions," *LECTURE NOTES IN COMPUTER SCIENCE*, no. 1407, pp. 34-50, //, 1998.
- [123] P. J. Neugebauer, "Reconstruction of real-world objects via simultaneous registration and robust combination of multiple range images," *International Journal of Shape Modeling*, vol. 03, no. 01n02, pp. 71-90, 1997.
- [124] D. W. Marquardt, "An algorithm for least-squares estimation of nonlinear parameters," *Journal of the Society for Industrial and Applied Mathematics*, vol. 11, no. 2, pp. 431-441, 1963.
- [125] D. F. Huber, and M. Hebert, "Fully automatic registration of multiple 3D data sets," *Image and Vision Computing*, vol. 21, no. 7, pp. 637-650, Jul, 2003.
- [126] G. C. Sharp, S. W. Lee, and D. K. Wehe, "Multiview registration of 3D scenes by minimizing error between coordinate frames," *Ieee Transactions on Pattern Analysis and Machine Intelligence*, vol. 26, no. 8, pp. 1037-1050, Aug, 2004.
- [127] C. Matabosch, E. Battle, D. Fofi, and J. Salvi, "A variant of point-to-plane registration including cycle minimization," *Photogrammetric Computer Vision*, pp. 20-22, 2006.
- [128] S. M. MacRae, R. R. Krueger, and R. A. Applegate, *Customized corneal ablation : the quest for superVision*, Thorofare, N.J.: Slack, 2001.
- [129] U. Fares, M. A. Al-Aqaba, A. M. Otri, and H. S. Dua, "A Review of Refractive Surgery," *European Ophthalmic Review*, vol. 5, no. 1, pp. 50-55, 2011.
- [130] L. J. Kugler, and M. X. Wang, "Lasers in refractive surgery: history, present, and future," *Applied Optics*, vol. 49, no. 25, pp. F1-F9, Sep, 2010.
- [131] U. Vogt, "Kersley lecture: eye believe in contact lenses: contact lenses and/or refractive surgery," *Eye & contact lens*, vol. 29, no. 4, pp. 201-6, 2003, 2003.

- [132] H. Snellen, "Die richtung des hauptmeridiane des astigmatishen auges," *Albrecht von Graefes Archiv für klinische und experimentelle Ophthalmologie*, vol. 15, pp. 199-207, 1869.
- [133] C. McAlinden, "Corneal refractive surgery: past to present," *Clinical and Experimental Optometry*, vol. 95, no. 4, pp. 386-398, Jul, 2012.
- [134] L. J. Lans, "Experimentelle Untersuchungen über Entstehung von Astigmatismus durch nicht-perforirende Corneawunden," *Albrecht von Graefes Archiv für Ophthalmologie*, vol. 45, no. 1, pp. 117-152, Mar, 1898.
- [135] T. Sato, "Treatment of conical cornea (incision of Descemet's membrane)," *Acta Soc. Opth. (Jap.)*, vol. 43, pp. 541, 1939.
- [136] T. Sato, "Posterior incision of cornea: Surgical treatment for conical cornea and astigmatism," *American Journal of Ophthalmology*, vol. 33, no. 6, pp. 943-948, 1950.
- [137] T. Sato, K. Akiyama, and H. Shibata, "A new surgical approach to myopia," *American Journal of Ophthalmology*, vol. 36, no. 6, pp. 823-829, 1953.
- [138] F. S. Yenaliyev, "Experience of surgical treatment of myopia," *Vestnik Oftalmologii*, no. 3, pp. 52-55, 1979.
- [139] S. N. Fyodorov, and V. V. Durnev, "Operation of dosaged dissection of corneal circular ligament in cases of myopia of mild degree," *Annals of Ophthalmology*, vol. 11, no. 12, pp. 1885-1889, 1979.
- [140] S. N. Fyodorov, V. V. Durnevv, A. I. Ivashina, and V. B. Gudechkov, "Calculation method of effectiveness of anterior keratotomy in surgical correction of myopia," *Surgery for Anomalies in Ocular Refraction*, S. N. Fyodorov, ed., pp. 114-121, Moscow: The Moscow Research Institute of Ocular Microsurgery, 1981.

- [141] V. V. Durnevv, "Characteristics of surgical correction of myopia after 16 and 32 peripheral anterior radial nonperforating incisions," *Surgery for Anomalies in Ocular Refraction*, S. N. Fyodorov, ed., pp. 33-35, Moscow: The Moscow Research Institute of Ocular Microsurgery, 1981.
- [142] G. O. Waring, M. J. Lynn, B. Fielding, P. A. Asbell, H. D. Balyeat, E. A. Cohen, W. Culbertson, D. J. Doughman, P. Fecko, M. B. McDonald, R. E. Smith, and L. B. Wilson, "Results of the Prospective Evaluation of Radial Keratotomy (PERK) Study 4 years after surgery for myopia. Perk Study Group.," *Jama-Journal of the American Medical Association*, vol. 263, no. 8, pp. 1083-1091, Feb, 1990.
- [143] G. O. Waring, M. J. Lynn, and P. J. McDonnell, "Results of the prospective evaluation of radial keratotomy (PERK) study 10 years after surgery," *Archives of Ophthalmology*, vol. 112, no. 10, pp. 1298-1308, Oct, 1994.
- [144] P. J. McDonnell, A. Nizam, M. J. Lynn, and G. O. Waring, "Morning-to-evening change in refraction, corneal curvature, and visual acuity 11 years after radial keratotomy in the prospective evaluation of radial keratotomy study. The PERK Study Group.," *Ophthalmology*, vol. 103, no. 2, pp. 233-239, Feb, 1996.
- [145] C. S. Fong, "Refractive surgery: the future of perfect vision?," *SMJ Singapore Medical Journal*, vol. 48, no. 8, pp. 709-718, Aug, 2007.
- [146] J. I. Barraquer, "Queratoplastia refractiva," *Estudios e Informaciones Oftalmológicas*, vol. 10, pp. 1-21, 1949.
- [147] J. I. Barraquer, "The history and evolution of keratomileusis," *International Ophthalmology Clinics*, vol. 36, no. 4, pp. 1-7, Fal, 1996.
- [148] J. I. Barraquer, "Keratomileusis," *International surgery*, vol. 48, no. 2, pp. 103-17, 1967, 1967.

- [149] C. A. Swinger, and J. I. Barraquer, "Keratophakia and keratomileusis--clinical results," *Ophthalmology*, vol. 88, no. 8, pp. 709-715, August, 1981.
- [150] J. H. Krumeich, "Indications, techniques, and complications of myopic keratomileusis," *International ophthalmology clinics*, vol. 23, no. 3, pp. 75-92, 1983, 1983.
- [151] D. J. Schanzlin, J. V. Jester, and E. Kay, "Cryolathe Corneal Injury," *Cornea*, vol. 2, no. 1, pp. 57-68, 1983.
- [152] C. A. Swinger, J. Krumeich, and D. Cassiday, "Planar Lamellar Refractive Keratoplasty," *Journal of Refractive Surgery*, vol. 2, no. 1, pp. 17, January, 1986.
- [153] E. Y. Zavala, J. Krumeich, and P. S. Binder, "Laboratory evaluation of freeze vs nonfreeze lamellar refractive keratoplasty," *Archives of Ophthalmology*, vol. 105, no. 8, pp. 1125-1128, Aug, 1987.
- [154] E. Y. Zavala, J. Krumeich, and P. S. Binder, "Clinical pathology of non-freeze lamellar refractive keratoplasty," *Cornea*, vol. 7, no. 3, pp. 223-230, 1988.
- [155] L. A. Ruiz, and J. J. Rowsey, "In situ keratomileusis," *Investigative Ophthalmology and Visual Science*, vol. 29, no. ABSTR. ISSUE, pp. 392, 1988.
- [156] J. Taboada, G. W. Mikesell, and R. D. Reed, "Response of the corneal epithelium to KrF excimer laser pulses," *Health Physics*, vol. 40, no. 5, pp. 677-683, 1981.
- [157] S. L. Trokel, R. Srinivasan, and B. Braren, "Excimer laser surgery of the cornea," *American Journal of Ophthalmology*, vol. 96, no. 6, pp. 710-715, 1983.
- [158] A. M. Cotliar, H. D. Schubert, E. R. Mandel, and S. L. Trokel, "Excimer laser radial keratotomy," *Ophthalmology*, vol. 92, no. 2, pp. 206-208, 1985.
- [159] J. Marshall, S. Trokel, S. Rothery, and R. R. Krueger, "A comparative study of corneal incisions induced by diamond and steel knives and two ultraviolet

- radiations from an excimer laser," *British Journal of Ophthalmology*, vol. 70, no. 7, pp. 482-501, Jul, 1986.
- [160] T. Seiler, T. Bende, and J. Wollensak, "Correction of astigmatism with the excimer laser [German]," *Klinische Monatsblätter Fur Augenheilkunde*, vol. 191, no. 3, pp. 179-183, Sep, 1987.
- [161] M. B. McDonald, J. M. Frantz, S. D. Klyce, B. Salmeron, R. W. Beuerman, C. R. Munneryn, T. N. Clapham, S. J. Koons, and H. E. Kaufman, "One-year refractive results of central photorefractive keratectomy for myopia in the nonhuman primate cornea," *Archives of Ophthalmology*, vol. 108, no. 1, pp. 40-47, Jan, 1990.
- [162] L. Buratto, M. Ferrari, and P. Rama, "Excimer laser intrastromal keratomileusis," *American Journal of Ophthalmology*, vol. 113, no. 3, pp. 291-295, Mar, 1992.
- [163] I. G. Pallikaris, M. E. Papatzanaki, E. Z. Stathi, O. Frenschock, and A. Georgiadis, "Laser in situ keratomileusis," *Lasers in Surgery and Medicine*, vol. 10, no. 5, pp. 463-468, 1990.
- [164] B. Zuberbuhler, S. Tuft, D. Gartry, and D. Spokes, "Refractive Corneal Surgery," *Corneal Surgery : Essential Techniques*, B. Zuberbuhler, S. Tuft, D. Gartry and D. Spokes, eds., p. 105, Berlin; New York: Springer-Verlag Berlin Heidelberg, 2013.
- [165] J. V. Jester, "Refractive Surgical Wound Healing Mechanisms Revisited: A Glimpse at the Future of LASEK," *LASEK, PRK, and excimer laser stromal surface ablation*, D. T. Azar, M. Camellin and R. W. Yee, eds., pp. 300-311, New York: Marcel Dekker, 2005.
- [166] L. Buratto, S. Slade, and M. Tavolato, "Complications," *LASIK : the evolution of refractive surgery*, L. Buratto, S. Slade and M. Tavolato, eds., pp. 57-70, Thorofare, NJ: SLACK, 2012.

- [167] G. Sutton, M. Lawless, and C. Hodge, "Laser in situ keratomileusis in 2012: a review," *Clinical and Experimental Optometry*, vol. 97, no. 1, pp. 18-29, Jan, 2014.
- [168] C. M, and C. M, "LASEK technique promising after 1 year of experience," *Ocular Surgery News*, vol. 18, no. 1, pp. 14-17, 2000.
- [169] I. G. Pallikaris, I. I. Naoumidi, M. I. Kalyvianaki, and V. J. Katsanevaki, "Epi-LASIK: comparative histological evaluation of mechanical and alcohol-assisted epithelial separation," *Journal of cataract and refractive surgery*, vol. 29, no. 8, pp. 1496-501, 2003, 2003.
- [170] C. D. Reilly, V. Panday, V. Lazos, and B. R. Mittelstaedt, "PRK vs LASEK vs Epi-LASIK: a comparison of corneal haze, postoperative pain and visual recovery in moderate to high myopia," *Nepalese journal of ophthalmology : a biannual peer-reviewed academic journal of the Nepal Ophthalmic Society : NEPJOPH*, vol. 2, no. 2, pp. 97-104, 2010, 2010.
- [171] S. H. Chung, and E. Mazur, "Surgical applications of femtosecond lasers," *Journal of Biophotonics*, vol. 2, no. 10, pp. 557-572, Oct, 2009.
- [172] I. Ratkay-Traub, T. Juhasz, C. Horvath, C. Suarez, K. Kiss, I. Ferincz, and R. Kurtz, "Ultra-short pulse (femtosecond) laser surgery: initial use in LASIK flap creation," *Ophthalmology clinics of North America*, vol. 14, no. 2, pp. 347-55, viii-ix, 2001, 2001.
- [173] W. Sekundo, K. S. Kunert, and M. Blum, "Small incision corneal refractive surgery using the small incision lenticule extraction (SMILE) procedure for the correction of myopia and myopic astigmatism: results of a 6 month prospective study," *British Journal of Ophthalmology*, vol. 95, no. 3, pp. 335-339, Mar, 2011.

- [174] K. Konig, H. Liang, M. W. Berns, and B. J. Tromberg, "Cell damage in near-infrared multimode optical traps as a result of multiphoton absorption," *Optics Letters*, vol. 21, no. 14, pp. 1090-1092, Jul, 1996.
- [175] T. Juhasz, H. Frieder, R. M. Kurtz, C. Horvath, J. F. Bille, and G. Mourou, "Corneal refractive surgery with femtosecond lasers," *Ieee Journal of Selected Topics in Quantum Electronics*, vol. 5, no. 4, pp. 902-910, Jul-Aug, 1999.
- [176] M. R. Santhiago, N. Kara, and G. O. Waring, "Microkeratome versus femtosecond flaps: accuracy and complications," *Current Opinion in Ophthalmology*, vol. 25, no. 4, pp. 270-274, Jul, 2014.
- [177] J. B. M. D. Randleman, "Femtosecond LASIK Flaps: Excellent, but Superior?," *Journal of Refractive Surgery*, vol. 28, no. 1, pp. 9-10, Jan, 2012.
- [178] S. H. Chen, Y. F. Feng, A. Stojanovic, M. R. Jankov, and Q. M. Wang, "IntraLase Femtosecond Laser vs Mechanical Microkeratomes in LASIK for Myopia: A Systematic Review and Meta-analysis," *Journal of Refractive Surgery*, vol. 28, no. 1, pp. 15-24, Jan, 2012.
- [179] M. Moshirfar, M. V. McCaughey, D. Z. Reinstein, R. Shah, L. Santiago-Caban, and C. R. Fenzl, "Small-incision lenticule extraction," *Journal of Cataract and Refractive Surgery*, vol. 41, no. 3, pp. 652-665, Mar, 2015.
- [180] A. S. Roy, W. J. Dupps, and C. J. Roberts, "Comparison of biomechanical effects of small-incision lenticule extraction and laser in situ keratomileusis: Finite-element analysis," *Journal of Cataract and Refractive Surgery*, vol. 40, no. 6, pp. 971-980, Jun, 2014.
- [181] A. C. Murray, L. Jones, A. C. Milne, C. M. Fraser, T. Lourenco, and J. M. Burr, *A systematic review of the safety and efficacy of elective photorefractive surgery*



*for the correction of refractive error*: National Institute for Health and Clinical Excellence, 2005.

- [182] M. Dirani, T. Couper, J. Yau, E. K. Ang, F. M. A. Islam, G. R. Snibson, R. B. Vajpayee, and P. N. Baird, "Long-term refractive outcomes and stability after excimer laser surgery for myopia," *Journal of Cataract and Refractive Surgery*, vol. 36, no. 10, pp. 1709-1717, Oct, 2010.
- [183] S. C. Schallhorn, E. C. Amesbury, and D. J. Tanzer, "Avoidance, recognition, and management of LASIK complications," *American Journal of Ophthalmology*, vol. 141, no. 4, pp. 733-739, Apr, 2006.
- [184] J. A. Davison, and S. C. Johnson, "Intraoperative Complications of LASIK Flaps Using the IntraLase Femtosecond Laser in 3009 Cases," *Journal of Refractive Surgery*, vol. 26, no. 11, pp. 851-857, Nov, 2010.
- [185] M. O'Doherty, C. Kirwan, M. O'Keeffe, and J. O'Doherty, "Postoperative pain following Epi-LASIK, LASEK, and PRK for myopia," *Journal of Refractive Surgery*, vol. 23, no. 2, pp. 133-138, Feb, 2007.
- [186] B. Zuberbuhler, S. Tuft, D. Gartry, and D. Spokes, "Refractive Corneal Surgery," *Corneal Surgery : Essential Techniques*, B. Zuberbuhler, S. Tuft, D. Gartry and D. Spokes, eds., pp. 116-126, Berlin; New York: Springer-Verlag Berlin Heidelberg, 2013.
- [187] M. A. Lawless, and R. J. Potvin, "Fulfilling the promise of laser refractive surgery," *Journal of Refractive Surgery*, vol. 22, no. 9, pp. S965-S968, Nov, 2006.
- [188] C. R. Munnerlyn, S. J. Koons, and J. Marshall, "Photorefractive Keratectomy - A Technique For Laser Refractive Surgery," *Journal of Cataract and Refractive Surgery*, vol. 14, no. 1, pp. 46-52, Jan, 1988.

- [189] S. Marcos, S. Barbero, L. Llorente, and J. Merayo-Llodes, "Optical response to LASIK surgery for myopia from total and corneal aberration measurements," *Investigative Ophthalmology & Visual Science*, vol. 42, no. 13, pp. 3349-3356, Dec, 2001.
- [190] G. Yoon, S. MacRae, D. R. Williams, and I. G. Cox, "Causes of spherical aberration induced by laser refractive surgery," *Journal of Cataract and Refractive Surgery*, vol. 31, no. 1, pp. 127-135, Jan, 2005.
- [191] A. Benito, M. Redondo, and P. Artal, "Laser In Situ Keratomileusis Disrupts the Aberration Compensation Mechanism of the Human Eye," *American Journal of Ophthalmology*, vol. 147, no. 3, pp. 424-431, Mar, 2009.
- [192] M. Mrochen, C. Donitzky, C. Wullner, and J. Loffler, "Wavefront-optimized ablation profiles: Theoretical background," *Journal of Cataract and Refractive Surgery*, vol. 30, no. 4, pp. 775-785, Apr, 2004.
- [193] T. A. Pasquali, D. Smadja, M. J. Savetsky, G. H. R. Mello, F. Alkhaldeh, and R. R. Krueger, "Long-term follow-up after laser vision correction in physicians: Quality of life and patient satisfaction," *Journal of Cataract and Refractive Surgery*, vol. 40, no. 3, pp. 395-402, Mar, 2014.
- [194] D. Z. Reinstein, T. J. Archer, and M. Gobbe, "The History of LASIK," *Journal of Refractive Surgery*, vol. 28, no. 4, pp. 291-298, Apr, 2012.
- [195] B. U. Tan, T. L. Purcell, L. F. Torres, and D. J. Schanzlin, "New surgical approaches to the management of keratoconus and post-LASIK ectasia," *Transactions of the American Ophthalmological Society*, vol. 104, pp. 212-20, 2006, 2006.
- [196] R. W. Clough, "The finite element in plane stress analysis," in 2nd ASCE Conference on Electronic Computations, Pittsburgh, PA, 1960.

- [197] O. C. Zienkiewicz, R. L. Taylor, and J. Z. Zhu, *Finite element method: its basis and fundamentals*, 7th ed., Amsterdam; Boston: Butterworth-Heinemann, 2013.
- [198] D. C. Fernandez, A. M. Niaz, R. M. Kurtz, G. P. Djotyan, and T. Juhasz, "Finite element analysis applied to cornea reshaping," *Journal of Biomedical Optics*, vol. 10, no. 6, pp. 11, Nov-Dec, 2005.
- [199] V. Alastrue, B. Calvo, E. Pena, and M. Doblare, "Biomechanical modeling of refractive corneal surgery," *Journal of Biomechanical Engineering-Transactions of the Asme*, vol. 128, no. 1, pp. 150-160, Feb, 2006.
- [200] C. Deenadayalu, B. Mobasher, S. D. Rajan, and G. W. Hall, "Refractive change induced by the LASIK flap in a biomechanical finite element model," *Journal of Refractive Surgery*, vol. 22, no. 3, pp. 286-292, Mar, 2006.
- [201] A. Pandolfi, G. Fotia, and F. Manganiello, "Finite element simulations of laser refractive corneal surgery," *Engineering with Computers*, vol. 25, no. 1, pp. 15-24, Jan, 2009.
- [202] A. S. Roy, and W. J. Dupps, "Effects of Altered Corneal Stiffness on Native and Postoperative LASIK Corneal Biomechanical Behavior: A Whole-eye Finite Element Analysis," *Journal of Refractive Surgery*, vol. 25, no. 10, pp. 875-887, Oct, 2009.
- [203] A. S. Roy, and W. J. Dupps, "Patient-Specific Modeling of Corneal Refractive Surgery Outcomes and Inverse Estimation of Elastic Property Changes," *Journal of Biomechanical Engineering-Transactions of the Asme*, vol. 133, no. 1, pp. 10, Jan, 2011.
- [204] H. P. Studer, H. Riedwyl, C. A. Amstutz, J. V. M. Hanson, and P. Buchler, "Patient-specific finite-element simulation of the human cornea: A clinical

- validation study on cataract surgery,” *Journal of Biomechanics*, vol. 46, no. 4, pp. 751-758, Feb, 2013.
- [205] P. Sanchez, K. Moutsouris, and A. Pandolfi, “Biomechanical and optical behavior of human corneas before and after photorefractive keratectomy,” *Journal of Cataract and Refractive Surgery*, vol. 40, no. 6, pp. 905-917, Jun, 2014.
- [206] A. Sinha Roy, W. J. Dupps, Jr., and C. J. Roberts, “Comparison of biomechanical effects of small-incision lenticule extraction and laser in situ keratomileusis: finite-element analysis,” *Journal of cataract and refractive surgery*, vol. 40, no. 6, pp. 971-80, 2014, 2014.
- [207] I. Simonini, and A. Pandolfi, “Customized Finite Element Modelling of the Human Cornea,” *Plos One*, vol. 10, no. 6, pp. 23, Jun, 2015.
- [208] H. P. Studer, K. R. Pradhan, D. Z. Reinstein, E. Businaro, T. J. Archer, M. Gobbe, and C. J. Roberts, “Biomechanical Modeling of Femtosecond Laser Keyhole Endokeratophakia Surgery,” *Journal of Refractive Surgery*, vol. 31, no. 7, pp. 480-486, Jul, 2015.
- [209] R. P. Vito, T. J. Shin, and B. E. McCarey, “A mechanical model of the cornea: the effects of physiological and surgical factors on radial keratotomy surgery,” *Refractive & corneal surgery*, vol. 5, no. 2, pp. 82-8, 1989, 1989.
- [210] P. M. Pinsky, and D. V. Datye, “A microstructurally-based finite-element model of the incised human cornea,” *Journal of Biomechanics*, vol. 24, no. 10, pp. 907-922, 1991.
- [211] S. A. Velinsky, and M. R. Bryant, “On the computer-aided and optimal design of keratorefractive surgery,” *Refractive & corneal surgery*, vol. 8, no. 2, pp. 173-82, 1992, 1992.

- [212] W. Gray, W. E. Sponsel, F. W. Scribbick, A. R. Stern, C. E. Weiss, S. L. Groth, and J. D. Walker, "Numerical Modeling of Paintball Impact Ocular Trauma: Identification of Progressive Injury Mechanisms," *Investigative Ophthalmology & Visual Science*, vol. 52, no. 10, pp. 7506-7513, Sep, 2011.
- [213] A. A. Weaver, E. A. Kennedy, S. M. Duma, and J. D. Stitzel, "Evaluation of Different Projectiles in Matched Experimental Eye Impact Simulations," *Journal of Biomechanical Engineering-Transactions of the Asme*, vol. 133, no. 3, pp. 10, Mar, 2011.
- [214] S. J. Mousavi, N. Nassiri, N. Masoumi, N. Nassiri, M. Majdi-N, S. Farzaneh, A. R. Djalilian, and G. A. Peyman, "Finite Element Analysis of Blunt Foreign Body Impact on the Cornea After PRK and LASIK," *Journal of Refractive Surgery*, vol. 28, no. 1, pp. 59-64, Jan, 2012.
- [215] A. S. Roy, and W. J. Dupps, "Patient-Specific Computational Modeling of Keratoconus Progression and Differential Responses to Collagen Cross-linking," *Investigative Ophthalmology & Visual Science*, vol. 52, no. 12, pp. 9174-9187, Nov, 2011.
- [216] F. Cavas-Martinez, D. G. Fernandez-Pacheco, E. De la Cruz-Sanchez, J. N. Martinez, F. J. F. Canavate, A. Vega-Estrada, A. B. Plaza-Puche, and J. L. Alio, "Geometrical Custom Modeling of Human Cornea In Vivo and Its Use for the Diagnosis of Corneal Ectasia," *Plos One*, vol. 9, no. 10, pp. 12, Oct, 2014.
- [217] I. Seven, A. S. Roy, and W. J. Dupps, "Patterned corneal collagen crosslinking for astigmatism: Computational modeling study," *Journal of Cataract and Refractive Surgery*, vol. 40, no. 6, pp. 943-953, Jun, 2014.
- [218] L. A. Carvalho, M. Prado, R. H. Cunha, A. C. Neto, A. Paranhos, P. Schor, and W. Chamon, "Keratoconus prediction using a finite element model of the cornea

- with local biomechanical properties,” *Arquivos Brasileiros De Oftalmologia*, vol. 72, no. 2, pp. 139-145, Mar-Apr, 2009.
- [219] A. Elsheikh, S. Ross, D. Alhasso, and P. Rama, “Numerical Study of the Effect of Corneal Layered Structure on Ocular Biomechanics,” *Current Eye Research*, vol. 34, no. 1, pp. 26-35, 2009.
- [220] A. Elsheikh, A. Joda, A. Abass, and D. Garway-Heath, “Assessment of the Ocular Response Analyzer as an Instrument for Measurement of Intraocular Pressure and Corneal Biomechanics,” *Current Eye Research*, 2014.
- [221] Z. L. Han, C. Tao, D. Zhou, Y. Sun, C. Q. Zhou, Q. S. Ren, and C. J. Roberts, “Air Puff Induced Corneal Vibrations: Theoretical Simulations and Clinical Observations,” *Journal of Refractive Surgery*, vol. 30, no. 3, pp. 208-213, Mar, 2014.
- [222] M. A. Ariza-Gracia, J. F. Zurita, D. P. Pinero, J. F. Rodriguez-Matas, and B. Calvo, “Coupled Biomechanical Response of the Cornea Assessed by Non-Contact Tonometry. A Simulation Study,” *Plos One*, vol. 10, no. 3, pp. 15, Mar, 2015.
- [223] A. Sinha Roy, M. Kurian, H. Matalia, and R. Shetty, “Air-puff associated quantification of non-linear biomechanical properties of the human cornea in vivo,” *Journal of the mechanical behavior of biomedical materials*, vol. 48, pp. 173-82, 2015 Aug (Epub 2015 Apr, 2015).
- [224] M. H. Abyaneh, R. D. Wildman, I. A. Ashcroft, and P. D. Ruiz, “A hybrid approach to determining cornea mechanical properties in vivo using a combination of nano-indentation and inverse finite element analysis,” *Journal of the Mechanical Behavior of Biomedical Materials*, vol. 27, pp. 239-248, Nov, 2013.

- [225] S. Evans, and S. Avril, "Identification of material parameters through inverse finite element modelling," *Computer Methods in Biomechanics and Biomedical Engineering*, vol. 15, no. 1, pp. 1-2, 2012.
- [226] S. Kok, N. Botha, and H. M. Inglis, "Calibrating corneal material model parameters using only inflation data: An ill-posed problem," *International Journal for Numerical Methods in Biomedical Engineering*, vol. 30, no. 12, pp. 1460-1475, Dec, 2014.
- [227] T. D. Nguyen, and B. L. Boyce, "An inverse finite element method for determining the anisotropic properties of the cornea," *Biomechanics and Modeling in Mechanobiology*, vol. 10, no. 3, pp. 323-337, Jun, 2011.
- [228] A. S. Roy, K. M. Rocha, J. B. Randleman, R. D. Stulting, and W. J. Dupps, "Inverse computational analysis of in vivo corneal elastic modulus change after collagen crosslinking for keratoconus," *Experimental Eye Research*, vol. 113, pp. 92-104, Aug, 2013.
- [229] H. Studer, H. Riedwyl, and P. Buchler, "Importance of multiple loading scenarios for the identification of material coefficients of the human cornea," *Computer Methods in Biomechanics and Biomedical Engineering*, vol. 15, no. 1, pp. 93-99, 2012.
- [230] M. A. Lago, M. J. Ruperez, F. Martinez-Martinez, C. Monserrat, E. Larra, J. L. Guell, and C. Peris-Martinez, "A new methodology for the in vivo estimation of the elastic constants that characterize the patient-specific biomechanical behavior of the human cornea," *Journal of Biomechanics*, vol. 48, no. 1, pp. 38-43, Jan, 2015.

- [231] T. D. Nguyen, R. E. Jones, and B. L. Boyce, "A nonlinear anisotropic viscoelastic model for the tensile behavior of the corneal stroma," *Journal of Biomechanical Engineering-Transactions of the Asme*, vol. 130, no. 4, pp. 10, Aug, 2008.
- [232] L. Yoo, J. Reed, A. Shin, J. Kung, J. K. Gimzewski, V. Poukens, R. A. Goldberg, R. Mancini, M. Taban, R. Moy, and J. L. Demer, "Characterization of Ocular Tissues Using Microindentation and Hertzian Viscoelastic Models," *Investigative Ophthalmology & Visual Science*, vol. 52, no. 6, pp. 3475-3482, May, 2011.
- [233] S. Kling, N. Bekesi, C. Dorronsoro, D. Pascual, and S. Marcos, "Corneal Viscoelastic Properties from Finite-Element Analysis of In Vivo Air-Puff Deformation," *Plos One*, vol. 9, no. 8, pp. 12, Aug, 2014.
- [234] Kobayash.As, S. L. Y. Woo, C. Lawrence, and W. A. Schlegel, "Analysis of corneo-scleral shell by method of direct stiffness," *Journal of Biomechanics*, vol. 4, no. 5, pp. 323-&, 1971.
- [235] K. A. Buzard, "Introduction to biomechanics of the cornea," *Refractive & corneal surgery*, vol. 8, no. 2, pp. 127-38, 1992, 1992.
- [236] N. Katsube, R. T. Wang, E. Okuma, and C. Roberts, "Biomechanical response of the cornea to phototherapeutic keratectomy when treated as a fluid-filled porous material," *Journal of Refractive Surgery*, vol. 18, no. 5, pp. S593-S597, Sep-Oct, 2002.
- [237] A. Pandolfi, and F. Manganiello, "A model for the human cornea: constitutive formulation and numerical analysis," *Biomechanics and Modeling in Mechanobiology*, vol. 5, no. 4, pp. 237-246, Nov, 2006.
- [238] A. Pandolfi, and G. A. Holzapfel, "Three-Dimensional Modeling and Computational Analysis of the Human Cornea Considering Distributed Collagen



- Fibril Orientations,” *Journal of Biomechanical Engineering-Transactions of the Asme*, vol. 130, no. 6, pp. 12, Dec, 2008.
- [239] M. R. Bryant, S. A. Velinsky, M. E. Plesha, and G. P. Clarke, “Computer-aided surgical design in refractive keratotomy,” *CLAO Journal*, vol. 13, no. 4, pp. 238-242, 1987.
- [240] W. Srodka, and D. R. Iskander, “Optically inspired biomechanical model of the human eyeball,” *Journal of Biomedical Optics*, vol. 13, no. 4, pp. 8, Jul-Aug, 2008.
- [241] R. Amini, and V. H. Barocas, “Anterior Chamber Angle Opening during Corneoscleral Indentation: The Mechanism of Whole Eye Globe Deformation and the Importance of the Limbus,” *Investigative Ophthalmology & Visual Science*, vol. 50, no. 11, pp. 5288-5294, Nov, 2009.
- [242] C. Kniestedt, O. Punjabi, S. Lin, and R. L. Stamper, “Tonometry Through the Ages,” *Survey of Ophthalmology*, vol. 53, no. 6, pp. 568-591, Nov-Dec, 2008.
- [243] R. L. Stamper, “A History of Intraocular Pressure and Its Measurement,” *Optometry and Vision Science*, vol. 88, no. 1, pp. E16-E28, Jan, 2011.
- [244] J. M. Martinez-de-la-Casa, J. Garcia-Feijoo, A. Fernandez-Vidal, C. Mendez-Hernandez, and J. Garcia-Sanchez, “Ocular response analyzer versus Goldmann applanation tonometry for intraocular pressure measurements,” *Investigative Ophthalmology & Visual Science*, vol. 47, no. 10, pp. 4410-4414, Oct, 2006.
- [245] O. S. Punjabi, C. Kniestedt, R. L. Stamper, and S. C. Lin, “Dynamic contour tonometry: principle and use,” *Clinical and Experimental Ophthalmology*, vol. 34, no. 9, pp. 837-840, Dec, 2006.
- [246] S. Bak-Nielsen, I. B. Pedersen, A. Ivarsen, and J. Hjortdal, “Repeatability, Reproducibility, and Age Dependency of Dynamic Scheimpflug-Based

- Pneumotonometer and Its Correlation With a Dynamic Bidirectional Pneumotonometry Device,” *Cornea*, vol. 34, no. 1, pp. 71-77, Jan, 2015.
- [247] M. Lanza, S. Iaccarino, M. Cennamo, C. Irregolare, V. Romano, and U. A. G. Carnevale, “Comparison between Corvis and other tonometers in healthy eyes,” *Contact Lens & Anterior Eye*, vol. 38, no. 2, pp. 94-98, Apr, 2015.
- [248] B. A. Francis, A. Hsieh, M. Y. Lai, V. Chopra, F. Pena, S. Azen, R. Varma, and G. Los Angeles Latino Eye Study, “Effects of corneal thickness, corneal curvature, and intraocular pressure level on Goldmann applanation tonometry and dynamic contour tonomet,” *Ophthalmology*, vol. 114, no. 1, pp. 20-26, Jan, 2007.
- [249] E. Chihara, “Assessment of true intraocular pressure: The gap between theory and practical data,” *Survey of Ophthalmology*, vol. 53, no. 3, pp. 203-218, May-Jun, 2008.
- [250] A. Elsheikh, D. F. Wang, A. Kotecha, M. Brown, and D. Garway-Heath, “Evaluation of goldmann applanation tonometry using a nonlinear finite element ocular model,” *Annals of Biomedical Engineering*, vol. 34, no. 10, pp. 1628-1640, Oct, 2006.
- [251] K. Saleh, V. Unger, A. Dietzel, D. Heydenreich, R. GroSsjohann, C. Jurgens, F. Tost, and J. Haueisen, “Mechanical Eye Model for Evaluating Intraocular Pressure Measurements,” *Biomedical Engineering Letters (BMEL)*, vol. 4, no. 4, pp. 396-402, 2014.
- [252] A. Elsheikh, D. Alhasso, P. Gunvant, and D. Garway-Heath, “Multiparameter Correction Equation for Goldmann Applanation Tonometry,” *Optometry and Vision Science*, vol. 88, no. 1, pp. E102-E112, Jan, 2011.

- [253] P. G. Davey, A. Elsheikh, and D. F. Garway-Heath, "Clinical evaluation of multiparameter correction equations for Goldmann applanation tonometry," *Eye*, vol. 27, no. 5, pp. 621-629, May, 2013.
- [254] A. A. Joda, M. M. S. Shervin, D. Kook, and A. Elsheikh, "Development and validation of a correction equation for Corvis tonometry," *Computer Methods in Biomechanics and Biomedical Engineering*, 2015.
- [255] H. Svedberg, E. Chen, and H. Hamberg-Nystrom, "Changes in corneal thickness and curvature after different excimer laser photorefractive procedures and their impact on intraocular pressure measurements," *Graefes Archive for Clinical and Experimental Ophthalmology*, vol. 243, no. 12, pp. 1218-1220, Dec, 2005.
- [256] A. S. H. Tsai, and S. C. Loon, "Intraocular pressure assessment after laser in situ keratomileusis: a review," *Clinical and Experimental Ophthalmology*, vol. 40, no. 3, pp. 295-304, Apr, 2012.
- [257] W. J. Yao, and A. S. Crossan, "An update on postrefractive surgery intraocular pressure determination," *Current Opinion in Ophthalmology*, vol. 25, no. 4, pp. 258-263, Jul, 2014.
- [258] J. X. Hong, Z. Q. Yu, C. H. Jiang, X. T. Zhou, Z. G. Liu, X. H. Sun, and J. J. Xu, "Corvis ST Tonometer for Measuring Postoperative IOP in LASIK Patients," *Optometry and Vision Science*, vol. 92, no. 5, pp. 589-595, May, 2015.
- [259] J. M. Schallhorn, S. C. Schallhorn, and Y. Ou, "Factors that Influence Intraocular Pressure Changes after Myopic and Hyperopic LASIK and Photorefractive Keratectomy," *Ophthalmology*, vol. 122, no. 3, pp. 471-479, Mar, 2015.
- [260] D. T. Sandwell, "Biharmonic spline interpolation of Geos-3 and seasat altimeter data," *Geophysical Research Letters*, vol. 14, no. 2, pp. 139-142, Feb, 1987.

- [261] S. X. Liao, and M. Pawlak, "On the accuracy of Zernike moments for image analysis," *Ieee Transactions on Pattern Analysis and Machine Intelligence*, vol. 20, no. 12, pp. 1358-1364, Dec, 1998.
- [262] K. M. Hosny, "Fast computation of accurate Gaussian-Hermite moments for image processing applications," *Digital Signal Processing*, vol. 22, no. 3, pp. 476-485, May, 2012.
- [263] L. F. Shampine, "MATLAB program for quadrature in 2D," *Applied Mathematics and Computation*, vol. 202, no. 1, pp. 266-274, Aug, 2008.
- [264] S. Y. Park, and M. Subbarao, "An accurate and fast point-to-plane registration technique," *Pattern Recognition Letters*, vol. 24, no. 16, pp. 2967-2976, Dec, 2003.
- [265] G. Turk, and M. Levoy, "Zippered polygon meshes from range images," *21st annual conference on Computer graphics and interactive techniques*. pp. 311-318, 1994.
- [266] J. A. Nelder, and R. Mead, "A simplex-method for function minimization," *Computer Journal*, vol. 7, no. 4, pp. 308-313, 1965.
- [267] J. C. Lagarias, J. A. Reeds, M. H. Wright, and P. E. Wright, "Convergence properties of the Nelder-Mead simplex method in low dimensions," *Siam Journal on Optimization*, vol. 9, no. 1, pp. 112-147, Dec 21, 1998.
- [268] J. Frédéric Bonnans, J. Charles Gilbert, C. Lemaréchal, and C. A. Sagastizábal, *Numerical optimization: Theoretical and practical aspects*: Springer Berlin Heidelberg, 2006.
- [269] K. S. Arun, T. S. Huang, and S. D. Blostein, "Least-squares fitting of two 3-d point sets," *IEEE transactions on pattern analysis and machine intelligence*, vol. 9, no. 5, pp. 698-700, 1987, 1987.

- [270] B. K. P. Horn, "Closed-form solution of absolute orientation using unit quaternions," *Journal of the Optical Society of America a-Optics Image Science and Vision*, vol. 4, no. 4, pp. 629-642, Apr, 1987.
- [271] B. K. P. Horn, H. M. Hilden, and S. Negahdaripour, "Closed-form solution of absolute orientation using orthonormal matrices," *Journal of the Optical Society of America a-Optics Image Science and Vision*, vol. 5, no. 7, pp. 1127-1135, Jul, 1988.
- [272] M. W. Walker, L. Shao, and R. A. Volz, "Estimating 3-D location parameters using dual number quaternions," *Cvgip-Image Understanding*, vol. 54, no. 3, pp. 358-367, Nov, 1991.
- [273] D. W. Eggert, A. Lorusso, and R. B. Fischer, "Estimating 3-D rigid body transformations: A comparison of four major algorithms," *Machine Vision and Applications*, vol. 9, no. 5-6, pp. 272-290, 1997.
- [274] S. Umeyama, "Least-squares estimation of transformation parameters between two point patterns," *IEEE Transactions on Pattern Analysis and Machine Intelligence*, vol. 13, no. 4, pp. 376-380, Apr, 1991.
- [275] A. W. Fitzgibbon, "Robust registration of 2D and 3D point sets," *Image and Vision Computing*, vol. 21, no. 13-14, pp. 1145-1153, Dec 1, 2003.
- [276] A. Elsheikh, B. Geraghty, D. Alhasso, J. Knappett, M. Campanelli, and P. Rama, "Regional variation in the biomechanical properties of the human sclera," *Experimental Eye Research*, vol. 90, no. 5, pp. 624-633, May, 2010.
- [277] R. W. Ogden, *Non-linear elastic deformations*, Chichester; New York: E. Horwood; Halsted Press, 1984.
- [278] C. Whitford, H. Studer, C. Boote, K. M. Meek, and A. Elsheikh, "Biomechanical model of the human cornea: Considering shear stiffness and regional variation of

- collagen anisotropy and density,” *Journal of the Mechanical Behavior of Biomedical Materials*, vol. 42, pp. 76-87, Feb, 2015.
- [279] A. Elsheikh, D. AlhasSo, and P. Rama, “Assessment of the epithelium's contribution to corneal biomechanics,” *Experimental Eye Research*, vol. 86, no. 2, pp. 445-451, Feb, 2008.
- [280] A. Elsheikh, C. Whitford, R. Hamarashid, W. Kassem, A. Joda, and P. Buchler, “Stress free configuration of the human eye,” *Medical Engineering & Physics*, vol. 35, no. 2, pp. 211-216, Feb, 2013.
- [281] I. M. Aslanides, N. S. Tsiklis, N. I. Astyrakakis, I. G. Pallikaris, and M. R. Jankov, “LASIK flap characteristics using the Moria M2 microkeratome with the 90- $\mu$ m single use head,” *Journal of Refractive Surgery*, vol. 23, no. 1, pp. 45-49, Jan, 2007.
- [282] P. Verdaguer, M. A. El-Husseiny, D. Elies, O. Gris, F. Manero, M. Biarnés, and J. L. Güell, “Small incision lenticule extraction (SMILE) procedure for the correction of myopia and myopic astigmatism,” *Journal of Emmetropia*, vol. 4, pp. 191-196, 2013.
- [283] I. Schmack, D. G. Dawson, B. E. McCarey, G. O. Waring, H. E. Grossniklaus, and H. F. Edelhauser, “Cohesive tensile strength of human LASIK wounds with histologic, ultrastructural, and clinical correlations,” *Journal of Refractive Surgery*, vol. 21, no. 5, pp. 433-445, Sep-Oct, 2005.
- [284] M. R. Lattimore, Jr., S. Kaupp, S. Schallhorn, and R. t. Lewis, “Orbscan pachymetry: implications of a repeated measures and diurnal variation analysis,” *Ophthalmology*, vol. 106, no. 5, pp. 977-81, May, 1999.

- [285] G. Cairns, C. N. J. McGhee, M. J. Collins, H. Owens, and G. D. Gamble, "Accuracy of Orbscan II slit-scanning elevation topography," *Journal of Cataract and Refractive Surgery*, vol. 28, no. 12, pp. 2181-2187, Dec, 2002.
- [286] J. M. Gonzalez-Meijome, A. Cervino, E. Yebra-Pimentel, and M. A. Parafita, "Central and peripheral corneal thickness measurement with Orbscan II and topographical ultrasound pachymetry," *Journal of Cataract and Refractive Surgery*, vol. 29, no. 1, pp. 125-132, Jan, 2003.
- [287] G. Cairns, and C. N. J. McGhee, "Orbscan computerized topography: Attributes, applications, and limitations," *Journal of Cataract and Refractive Surgery*, vol. 31, no. 1, pp. 205-220, Jan, 2005.
- [288] H. Shankar, D. Taranath, C. T. Santhirathelagan, and K. Pesudovs, "Anterior segment biometry with the Pentacam: Comprehensive assessment of repeatability of automated measurements," *Journal of Cataract and Refractive Surgery*, vol. 34, no. 1, pp. 103-113, Jan, 2008.
- [289] L. Wang, A. M. Mahmoud, B. L. Anderson, D. D. Koch, and C. J. Roberts, "Total Corneal Power Estimation: Ray Tracing Method versus Gaussian Optics Formula," *Investigative Ophthalmology & Visual Science*, vol. 52, no. 3, pp. 1716-1722, Mar, 2011.
- [290] P. Novak, J. Novak, and A. Miks, "Fast and robust computation of Cartesian derivatives of Zernike polynomials," *Optics and Lasers in Engineering*, vol. 52, pp. 7-12, Jan, 2014.
- [291] F. Manns, A. Ho, J. M. Parel, and W. Culbertson, "Ablation profiles for wavefront-guided correction of myopia and primary spherical aberration," *Journal of Cataract and Refractive Surgery*, vol. 28, no. 5, pp. 766-774, May, 2002.

- [292] A. W. Chang, A. C. Tsang, J. E. Contreras, P. D. Huynh, C. J. Calvano, T. C. Crnic-Rein, and E. H. Thall, "Corneal tissue ablation depth and the Munnerlyn formula," *Journal of Cataract and Refractive Surgery*, vol. 29, no. 6, pp. 1204-1210, Jun, 2003.
- [293] R. G. Anera, C. Villa, J. R. Jimenez, R. Gutierrez, and L. J. del Barco, "Differences between real and predicted corneal shapes after aspherical corneal ablation," *Applied Optics*, vol. 44, no. 21, pp. 4528-4532, Jul, 2005.
- [294] P. M. Pinsky, D. van der Heide, and D. Chernyak, "Computational modeling of mechanical anisotropy in the cornea and sclera," *Journal of Cataract and Refractive Surgery*, vol. 31, no. 1, pp. 136-145, Jan, 2005.
- [295] D. G. Dawson, T. R. Kramer, H. E. Grossniklaus, G. O. Waring, and H. F. Edelhauser, "Histologic, ultrastructural, and immuno fluorescent evaluation of human laser-assisted in situ keratomileusis corneal wounds," *Archives of Ophthalmology*, vol. 123, no. 6, pp. 741-756, Jun, 2005.
- [296] S. G. Priglinger, C. A. May, C. S. Alge, A. Wolf, A. S. Neubauer, C. Haritoglou, A. Kampik, and U. Welge-Lussen, "Immunohistochemical findings after LASIK confirm in vitro LASIK model," *Cornea*, vol. 25, no. 3, pp. 331-335, Apr, 2006.
- [297] J. R. Phillips, and N. A. McBrien, "Form deprivation myopia: elastic properties of sclera," *Ophthalmic and Physiological Optics*, vol. 15, no. 5, pp. 357-362, Sep, 1995.
- [298] J. T. Siegwart, and T. T. Norton, "Regulation of the mechanical properties of tree shrew sclera by the visual environment," *Vision Research*, vol. 39, no. 2, pp. 387-407, Jan, 1999.



- [299] N. A. McBrien, A. I. Jobling, and A. Gentle, "Biomechanics of the Sclera in Myopia: Extracellular and Cellular Factors," *Optometry and Vision Science*, vol. 86, no. 1, pp. 23-30, Jan, 2009.